MAGMATIC VOLATILE CONTENTS AND EXPLOSIVE CINDER CONE ERUPTIONS IN THE HIGH CASCADES: RECENT VOLCANISM IN CENTRAL OREGON AND NORTHERN CALIFORNIA

by

DANIEL M. RUSCITTO

A DISSERTATION

Presented to the Department of Geological Sciences
and the Graduate School of the University of Oregon
in partial fulfillment of the requirements
for the degree of
Doctor of Philosophy

March 2011

DISSERTATION APPROVAL PAGE

Student: Daniel M. Ruscitto

Title: Magmatic Volatile Contents and Explosive Cinder Cone Eruptions in the High Cascades: Recent Volcanism in Central Oregon and Northern California

This dissertation has been accepted and approved in partial fulfillment of the requirements for the Doctor of Philosophy degree in the Department of Geological Sciences by:

Dr. Paul J. Wallace	Chair and Advisor
Dr. Katharine Cashman	Member
Dr. Ilya Bindeman	Member
Dr. Richard Taylor	Outside Member

and

Richard Linton	Vice President for Research and Graduate Studies/Dean of the Graduate School

Original approval signatures are on file with the University of Oregon Graduate School.

Degree awarded March 2011

DISSERTATION ABSTRACT

Daniel M. Ruscitto

Doctor of Philosophy

Department of Geological Sciences

March 2011

Title: Magmatic Volatile Contents and Explosive Cinder Cone Eruptions in the High Cascades: Recent Volcanism in Central Oregon and Northern California

Approved: _____

Dr. Paul J. Wallace

Volatile components (H_2O, CO_2, S, Cl) dissolved in magmas influence all aspects of volcanic activity from magma formation to eruption explosivity. Understanding the behavior of volatiles is critical for both mitigating volcanic hazards and attaining a deeper understanding of large-scale geodynamic processes. This work relates the dissolved volatile contents in olivine-hosted melt inclusions from young volcanics in the Central Oregon and Northern California Cascades to inferred magmatic processes at depth and subsequent eruptive activity at the surface.

Cinder cone eruptions are the dominant form of Holocene volcanism in the Central Oregon segment of the High Cascades. Detailed field study of deposits from three cinder cones in Central Oregon reveals physical and compositional similarities to explosive historic eruptions characterized as violent strombolian. This work has important implications for future hazard assessments in the region. Based on melt inclusion data, pre-eruptive volatile contents for seven calc-alkaline cinder cones vary from 1.7–3.6 wt.% H_2O, 1200–2100 ppm S, and 500–1200 ppm Cl. Subarc mantle temperatures inferred from H_2O and trace elements are similar to or slightly warmer than temperatures in other arcs, consistent with a young and hot incoming plate.

High-magnesium andesites (HMA) are relatively rare but potentially important in the formation of continental crust. Melt inclusions from a well-studied example of HMA from near Mt. Shasta, CA were examined because petrographic evidence for magma mixing has stimulated a recent debate over the origin of HMA magmas. High volatile

contents (3.5–5.6 wt.% H_2O, 830–2900 ppm S, 1590–2580 ppm Cl), primitive host crystals, and compositional similarities with experiments suggest that these inclusions represent mantle-derived magmas.

The Cascades arc is the global end member, warm-slab subduction zone. Primitive magma compositions from the Cascades are compared to data for arcs spanning the global range in slab thermal state to examine systematic differences in slab-derived components added to the mantle wedge. H_2O/Ce, Cl/Nb, and Ba/La ratios negatively correlate with inferred slab surface temperatures predicted by geodynamic models. Slab components become increasingly solute-rich as slab surface temperatures increase from ~550 to 950°C at 120 km depth.

This dissertation includes previously published and unpublished co-authored material.

CURRICULUM VITAE

NAME OF AUTHOR: Daniel M. Ruscitto

GRADUATE AND UNDERGRADUATE SCHOOLS ATTENDED:

University of Oregon, Eugene
University of Minnesota, Minneapolis
Union College, Schenectady, New York

DEGREES AWARDED:

Doctor of Philosophy, Geological Sciences, 2011, University of Oregon
Master of Science, Geology & Geophysics, 2006, University of Minnesota
Bachelor of Science, Geology, 2003, Union College

AREAS OF SPECIAL INTEREST:

Igneous Petrology and Geochemistry
Volcanology

GRANTS, AWARDS, AND HONORS:

Weiser Scholarship, University of Oregon, 2010

Marthe E. Smith Memorial Science Fellowship, University of Oregon, 2008

Kleinman Grant for Volcano Research, USGS Cascades Volcano Observatory, 2008

Parke D. Snavely, Jr. Cascadia Research Award, Geological Society of America, 2008

National Science Foundation Travel Grant: EAR-0824339, NSF, 2008

Goldschmidt Student Travel Grant, Geochemical Society, 2008

Lloyd Staples Fellowship, University of Oregon, 2007, 2008

Thomas F. Andrews Fellowship, University of Minnesota, 2005

American Federation of Mineralogical Societies Scholarship, American Federation of Mineralogical Societies, 2003, 2004

Magna cum Laude, Union College, 2003

Departmental Honors, Union College Geology Department, 2003

E.S.C. Smith Prize, Union College, 2003

Union College Research Fellowship, Union College, 2002

Ed Fitz Memorial Scholarship, Schenectady Alumni of Union College, 1999-2002

Schenectady Sons of Italy Scholarship, Sons of Italy, 1999

PUBLICATIONS:

Ruscitto, D.M., Wallace, P.J., Johnson, E.R., Kent, A.J.R., Bindeman, I.N., 2010a. Volatile contents of mafic magmas from cinder cones in the Central Oregon High Cascades: implications for magma formation and mantle conditions in a hot arc. Earth Planet Sci Lett. 298, 153–161. doi:10.1016/j.epsl.2010.07.037

Ruscitto, D.M., Wallace, P.J., Kent, A.J.R., 2010b, in press. Revisiting the compositions and volatile contents of olivine-hosted melt inclusions from the Mount Shasta region: implications for the formation of high-Mg andesites. Contrib. Mineral. Petrol. doi: 10.1007/s00410-010-0587-y.

Hollocher, K., Quintin L., Ruscitto D., 2002. Geochemistry and source of the Saratoga Springs. In, McClelland, J. and Karabinos, P., editors, New York State Geological Association, Field Trip Guidebook, Lake George, New York, Trip C11, p. C11–1 to C11–15.

ACKNOWLEDGMENTS

I would first like to thank my advisor, Paul Wallace, for inviting me to work on a great project focused in the Cascades. I appreciated his patience, guidance, and support throughout my graduate career at the University of Oregon. In particular, his collaborative outlook and encouragement to pursue projects involving other investigators within and outside the department was refreshing. I would also like to thank Kathy Cashman, a secondary advisor, committee member, and outstanding teacher in both the field and the lecture hall. Ilya Bindeman, another committee member, also provided me with generous advice, honest feedback and served as an impressive role model. I would also like to thank my outside committee member, Richard Taylor, for taking the time to be a part of this process and for his enthusiasm regarding my projects.

I would like to thank Sara Auer, Bob Bonine, Isolde Belien, Nick Deardorff, Natalia Deligne, Daniele McKay, John Nangle, Laura Pioli, and the Hoodoo Ski Resort for assistance in the field. Thanks also to Varina Smith, who helped out considerably in the lab. I especially would like to thank John Donovan for assistance on the electron probe, Andy Ungerer and Adam Kent for assistance with LA-ICP-MS analyses, Rick Conrey for providing whole-rock XRF and ICP-MS data, and Jim Palandri for assistance with oxygen isotope analyses. I greatly appreciate the many helpful discussions that I had over the years with Bill Leeman, Tim Grove, and Martin Streck. Maxim Portnyagin, Katie Kelley, and Martin Streck provided thorough and constructive reviews of Chapter III. I would like to thank Fred Anderson and Martin Streck for providing the samples for and helpful reviews of Chapter IV. Regarding Chapter IV, I would especially like to thank Bruce Watson for providing the initial code for the diffusion model in addition to his support and guidance during the modification process. I also appreciate help from Glenn Gaetani and Stephen Parman and the thoughtful reviews by Glenn, Jay Barr, Martin Streck, and Tim Grove. All of this work was funded by grants to Paul Wallace, Adam Kent, Kathy Cashman, and Ilya Bindeman from the National Science Foundation.

Finally, I would like to thank my extended family and friends for their support during my graduate career. I am particularly indebted to my wife, Tammy Sargent

Ruscitto, who supported me throughout. She has been my rock, supporting me during the good times and pushing me through the bad. None of this would have been possible without her encouragement and love. I am also thankful to my parents and grandparents for sacrificing to provide my brother and I with limitless opportunities. Lastly, I thank my new son, Franklin Dominic, for showing me what is truly important.

To my family, who have shown me the importance of hard work.

TABLE OF CONTENTS

LIST OF FIGURES

Figure Page

Chapter II

Chapter III

Chapter IV

LIST OF TABLES

CHAPTER I
INTRODUCTION

1.1. Overview of the Cascades and Subduction

The Cascades volcanic arc stretches 1250 km from northern California to southwestern British Columbia and consists of over 2300 Quaternary volcanic edifices (Hildreth, 2007). This belt of volcanic activity is part of the semi-continuous 'Ring of Fire' that extends around the margin of the Pacific Ocean and results from subduction. Subduction zones are destructive plate margins that occur where tectonic plates of different densities collide and the less dense plate (e.g., North America) is forced over the denser slab (e.g., Juan de Fuca). These regions are colloquially known as 'Subduction Factories' and have been central in the geochemical evolution of the Earth (Tatsumi, 2005). During subduction, increasing temperatures and pressures reduce the stability of hydrous minerals in the descending slab. The near-continuous dehydration reactions within the subducting slab release H_2O and mobile elements into the overlying mantle (e.g., Schmidt & Poli, 1998). The presence of H_2O (the most abundant volatile component) causes melting by depressing the mantle solidus, decreasing the temperature required to initiate melting. Hydrous melts buoyantly ascend from the mantle source into the overlying crust and either stall and crystallize or migrate up to the surface, where eruption explosivity is driven by decompression-induced volatile exsolution (primarily H_2O and CO_2); a process analogous to uncorking a bottle of champagne.

Volatiles are important, yet ephemeral, components in magma because their low solubilities at surface pressures generally leave eruption products (lava and tephra) degassed (Holloway & Blank, 1994). The strong solubility dependence on pressure results in exsolution of a vapor phase along with an accompanying increase in melt liquidus temperature (inducing crystallization) as a magma undergoes decompression. Melt inclusions form as magma ascends and begins to crystallize, and the growing crystals trap small parcels of the parent melt within their structures. Certain crystals, particularly olivine, act as pressure vessels and preserve relatively undegassed and volatile-rich compositions that are unavailable at the surface (Anderson, 1974; Schiano,

2003). During eruptions, crystals are ejected from the vent along with tephra. Transport through the colder atmosphere rapidly quenches melt inclusions into glass within the host crystals and the dissolved volatiles can then be analyzed.

The Cascades arc, in particular, is an optimal study area to examine volcanic processes. It is an active volcanic arc situated in a heavily populated and developed country, easily accessed by a well-developed road network. More importantly, the nearby volcanic vents and lava fields are both young and numerous. Detailed mapping and extensive previous research provide a comprehensive framework for the geologic history of this region. (e.g., McBirney, 1978; Hughes, 1990; Taylor, 1990; Bacon et al., 1997; Conrey et al., 1997; Hildreth, 2007). The Cascade arc represents a 'warm-slab' extreme environment in the global spectrum of subduction zones (Kirby et al., 2002). It has been assumed to be relatively dry, because magmas have low concentrations of slab-recycled trace elements that suggest a low H_2O flux from the subducted plate (e.g., Leeman et al., 1990). A comprehensive understanding of subduction zone processes requires the evaluation of magmatic volatile contents over a wide range of subduction parameters (e.g., slab age, dip angle, plate velocity) and the Cascades arc provides an important contrast to other well-studied subduction zones.

1.2. Scientific Approach and Dissertation Organization

This dissertation integrates geochemical measurements and thermodynamic principles with physical and field-based observations to investigate both deep- (mantle melting, slab recycling) and shallow-level (eruption, degassing) magmatic processes. Following the introduction, this dissertation consists of four stand-alone chapters presented as separate manuscripts. Two separate but interrelated aspects of the dissertation are (1) understanding the relationships between pre-eruptive magmatic volatile contents and eruption activity in cinder cones from Central Oregon and Northern California (Chapters II and IV) (2) investigating volatile recycling and the role of volatiles on magma generation a 'warm-slab' subduction environment (Chapters III and V). The primary foci of Chapters II, III, and IV are small cinder cones (total volume <1 km^3) rather than the prominent high peaks (e.g., Mt. Hood, Mt. Rainier, Three Sisters) of the Cascades because the high peaks represent only a small fraction of active volcanism

(Hildreth, 2007). Moreover, cinder cone eruptions are the most common form of continental volcanism on Earth and are produced by eruptions of small, isolated magma batches. These small eruptions have potentially bypassed crustal mixing and assimilation processes that complicate interpretations of eruption products from larger, long-lived volcanoes (Leeman et al., 1990; Hildreth, 2007). Therefore, mafic cinder cone compositions are best suited for studying mantle-source compositions and magma formation.

In Chapter II, "Degassing Patterns and Eruption Processes of Cinder Cones in Central Oregon: A Melt Inclusion Perspective", I first document the eruptive histories of three recent (≤ 3000 yrs b.p.) cinder cones in Central Oregon by relating olivine-hosted melt inclusion compositions and volatile contents to their stratigraphic positions. We find that the Central Oregon magmas are surprisingly volatile-rich (up to 4 wt.% H_2O), and that the eruptions share chemical and physical similarities to the well-documented, historic eruptions at Jorullo (1759–1774) and Paricutin (1943–1952) in Mexico (e.g., Luhr, 2001; Johnson et al., 2008; Pioli et al., 2008; Erlund et al., 2009). I expand the Central Oregon dataset in Chapter III, "Volatile contents of mafic magmas from cinder cones in the Central Oregon High Cascades: Implications for magma formation and mantle conditions in a hot arc", to include seven additional cones. This dataset is then used to infer the volatile contents of primary, mantle-derived magmas from Central Oregon and relate these to conditions of formation in the mantle wedge beneath this segment of the arc. Chapter IV, "Revisiting the compositions and volatile contents of olivine-hosted melt inclusions from the Mount Shasta region: Implications for the formation of high-Mg andesites", examines the origins and pre-eruptive history of a particularly important magma composition found in the High Cascades of Northern California. The chapter challenges the conclusions of recent work (Streck et al. 2007) and supports previous interpretations (e.g., Anderson, 1974; Grove et al., 2005) that this magma represents a near-primary, volatile-rich melt derived from the mantle. This chapter also includes a detailed discussion concerning post-entrapment modification processes affecting olivine-hosted melt inclusions. A global dataset of volatile contents for primitive arc magmas is assembled using data from the preceding three chapters and supplemented by the literature in Chapter V, "Global Variations in Arc-related Magmatic

Volatile Contents". This study examines volatile contents from arcs representing the global range in subduction zone thermal parameter, a proxy for pressure-temperature path experienced by the downgoing slab. The slab-fluid geothermometer of Plank et al. (2009) is employed as a geochemical means of testing slab surface temperatures that have been predicted by geodynamic models (Syracuse et al., 2010). A final summary chapter follows the main dissertation and synthesizes the important findings in the preceding studies.

I am the first author on all of the chapters presented in this dissertation, and I performed all laboratory, analytical, and field-based work unless explicitly stated. Chapter II is in preparation and will be submitted to the *Journal of Volcanology and Geothermal Research* with Dr. Paul Wallace (advisor), Daniele McKay (UO Ph.D. Candidate), and Dr. Kathy Cashman (committee member) as coauthors. Drs. Paul Wallace and Kathy Cashman provided editorial assistance and all three coauthors participated in fieldwork and sample collection. Chapter III has been published in *Earth and Planetary Science Letters* with Drs. Paul Wallace (advisor), Emily Johnson (University of Tasmania), Adam Kent (Oregon State University), and Ilya Bindeman (committee member). All coauthors assisted with editing. Dr. Kent assisted with LA-ICP-MS analyses at Oregon State University, and Dr. Bindeman assisted with oxygen isotope analyses at the University of Oregon. Dr. Emily Johnson provided the melt inclusion dataset for Blue Lake Crater. Chapter IV has been published in *Contributions to Mineralogy and Petrology* with Drs. Paul Wallace (advisor) and Adam Kent (Oregon State University). Both coauthors assisted with editing and Dr. Kent also assisted with LA-ICP-MS analyses at Oregon State University. Dr. Wallace collected the tephra samples. Chapter V is in preparation in the style of *Earth and Planetary Science Letters* and will be coauthored with Dr. Paul Wallace (advisor), who provided editorial assistance.

CHAPTER II
DEGASSING PATTERNS AND ERUPTION PROCESSES OF CINDER CONES IN CENTRAL OREGON: A MELT INCLUSION PERSPECTIVE

This chapter includes co-authored material with Dr. P.J. Wallace, D. McKay, and Dr. K. Cashman. The laboratory work was performed entirely by me and the writing is entirely mine. Drs. Wallace and Cashman provided editorial assistance.

2.1. Introduction

Mafic cinder cones are the most common continental volcanic landforms and are found in diverse tectonic settings (e.g., convergent margins, back-arc regions, continental rift zones, in addition to surrounding larger volcanic edifices). Total volumes of erupted material (cone, lava, and tephra) from individual eruptions are typically small ($\leq$1 km^3), but these edifices are often found in large (100s–1000s km^2) volcanic fields consisting of 10s to 100s of vents (Connor & Conway, 2000; Valentine et al., 2006). Eruptive styles range from Strombolian to Violent Strombolian explosions capable of dispersing tephra over great distances (>100 km^2) (Walker, 1973; Pioli et al., 2008; Valentine & Gregg, 2008). While generally not life-threatening, the abundance and proximity of cinder cone vents to populated areas (e.g., Mexico City, Mexico; Auckland, New Zealand) present a threat to surrounding communities and an eruption may cause significant economic disruptions to the local area for over a decade (Ort et al., 2008). Quaternary volcanism in the Oregon Cascades has produced an extensive volcanic field (~1054 vents in ~9500 km^2) dominated by cinder cones, small shields and fissure-fed lava flows (Hildreth, 2007). Despite these abundances, few investigations have been focused on hazards associated with explosive mafic volcanism in the Cascades.

Exsolution of dissolved volatiles (predominantly H_2O and CO_2) provides the necessary acceleration to drive explosive eruptions (e.g., Parfitt & Wilson, 1995; Cashman et al., 2000; Wallace & Anderson, 2000; Houghton & Gonnermann, 2008).

Extensive vesiculation accompanies magma decompression because of the strong pressure dependence of H_2O and CO_2 solubilities in silicate melts (Holloway & Blank, 1994). An additional consequence, however, is that the extremely low solubilities of these gases at surface pressures leave eruption products devoid of these important components. Melt inclusions, or tiny pockets of glass trapped within phenocrysts, may preserve the original (pre-eruptive) volatile content of the magma (e.g., Anderson, 1974; Anderson & Brown, 1993; Cervantes & Wallace, 2003). For this reason, several previous studies have used melt inclusions to examine the relationships between volatile degassing and eruption styles (e.g., Roggensack et al., 1997; Luhr, 2001; Cervantes & Wallace, 2003; Blundy & Cashman, 2005; Spilliaert et al., 2006; Johnson et al., 2008; Erlund et al., 2009).

In this study, we use olivine-hosted melt inclusions to determine the pre-eruptive volatile contents of mafic magmas erupted in the Central Oregon High Cascades and relate these to eruption styles inferred from the deposits. We find that monogenetic eruptions in Central Oregon have chemical and physical similarities to the Violent Strombolian eruptions of Jorullo (1759–1774) and Paricutin (1943–1952) in Mexico (e.g., Luhr, 2001; Johnson et al., 2008; Pioli et al., 2008; Erlund et al., 2009). These results are somewhat unexpected because mafic magmas in the Cascades (north of Shasta) have traditionally been considered volatile-poor because they have low concentrations of slab-recycled trace elements (e.g., Leeman et al., 1990). This work (along with the recent results of Ruscitto et al., 2010a) shows that this view is erroneous and that mafic eruptions in Central Oregon have the potential to be more explosive than previously realized.

2.2. Geological Setting

Volcanism in the Central Oregon Cascades is associated with subduction of the Juan de Fuca plate beneath Western North America. The rate of orthogonal convergence between the subducting slab (Farallon/Juan de Fuca) and Central Oregon has decreased since ~40 Ma (Priest, 1990; Taylor, 1990). A corresponding increase in obliquity of subduction has produced clockwise rotation of the Oregon forearc (Wells, 1990; Wells & Simpson, 2001), ultimately causing intra-arc, E-W extension along the crest of the

Central Oregon High Cascades that has been propagating northward since ~5–8 Ma (Priest, 1990; Taylor, 1990; Wells, 1990; Conrey et al., 2000). Regional extension has promoted the ascent and eruption of small, isolated batches of basaltic and basaltic andesite magmas as cinder cone and fissure eruptions along pre-existing faults (Hughes & Taylor, 1986). As a consequence, Central Oregon has experienced the highest mafic output in the entire Cascades arc over the last 2 Ma, and monogenetic cinder cone eruptions have constituted the dominant form of volcanic activity during the Holocene (Sherrod & Smith, 1990; Sherrod et al., 2004; Hildreth, 2007). The focus of this study is the tephra deposits of three recent (≤ 3000 yr b.p.) cinder cone eruptions in the Central Oregon Cascades: Four-in-One, Collier Cone, and Sand Mountain (Figure 1).

2.2.1. Depositional Characteristics and Inferred Eruption Histories

We examined and described the tephra deposits associated with three recent mafic eruptions in the Central Oregon Cascades by digging trenches, auguring pits and exposing natural outcrops (Figure 1). Representative stratigraphic sections of the deposits are shown in Figure 2, and detailed descriptions of the main units are presented in Table 1. The primary focus of this study, however, is to examine the relationships between olivine-hosted melt inclusion compositions (volatiles in particular) over the course of explosive activity for these three mafic eruptions. Therefore, a general overview of the depositional characteristics and inferred styles of eruption will be presented before focusing on the melt inclusion compositions. The styles of explosive activity reported are based on areal extents of tephra dispersal, stratigraphic layering, and clast size distributions. All three eruptions produced at least one scoria cone, each with associated lava flows to the west and a tephra blanket deposited to the east, consistent with the prevailing wind directions in this region.

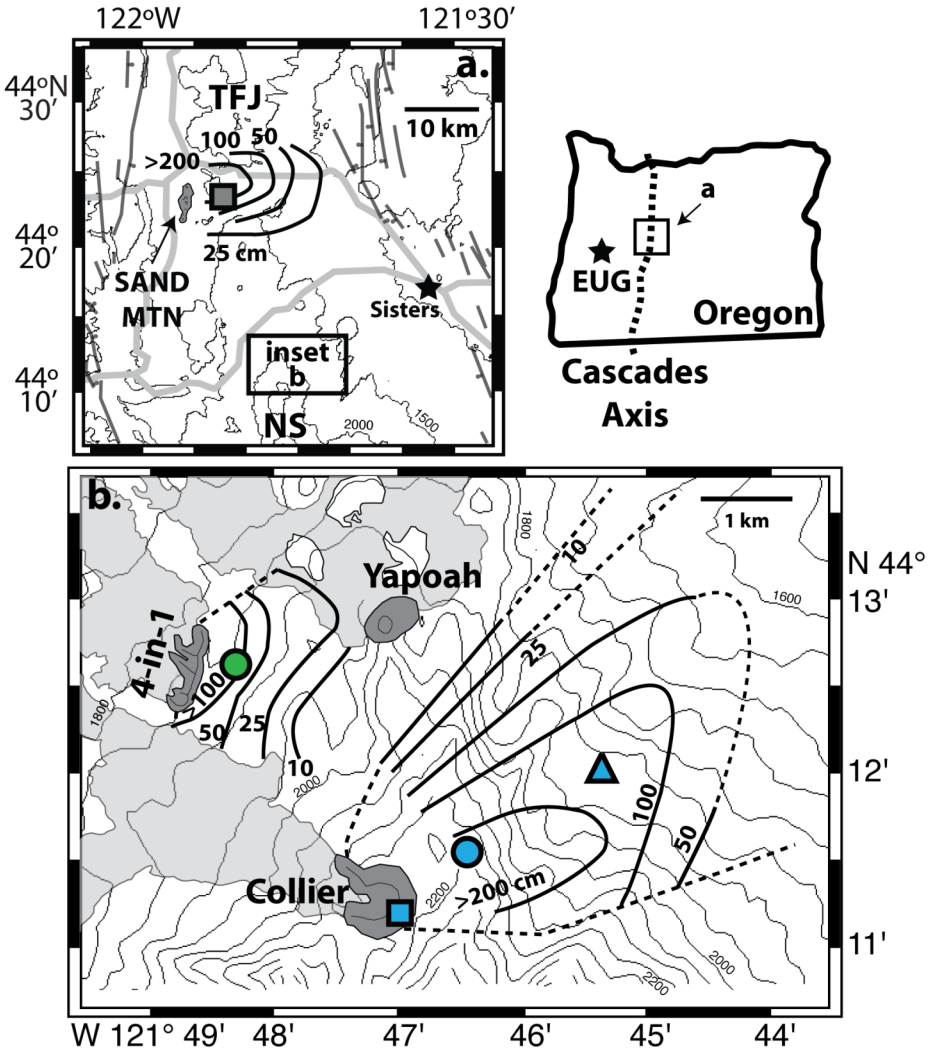

Figure 1. (a) Topographic map of the Santiam-McKenzie Pass region of the Central Oregon Cascades (area highlighted in overview map to right) showing preliminary isopach lines for tephra deposits from Sand Mountain (labeled composite cone; D. McKay, personal communication) and sample location (square) relative to Collier and 4-in-1 cones (inset b). The town of Sisters (black star) and major highways (thick gray), and prominent graben-bounding normal faults are also shown. (b) Isopach lines for 4-in-1 and Collier Cone deposits are shown in panel (b). Three sample localities from Collier Cone (square, circle, triangle) and one locality from 4-in-1 (circle) tephra deposits are shown. Lava flows associated with both 4-in-1 and Collier vents flow towards the east (light gray shaded areas). Nearby Yapoah cone and associated lava flow are also highlighted.

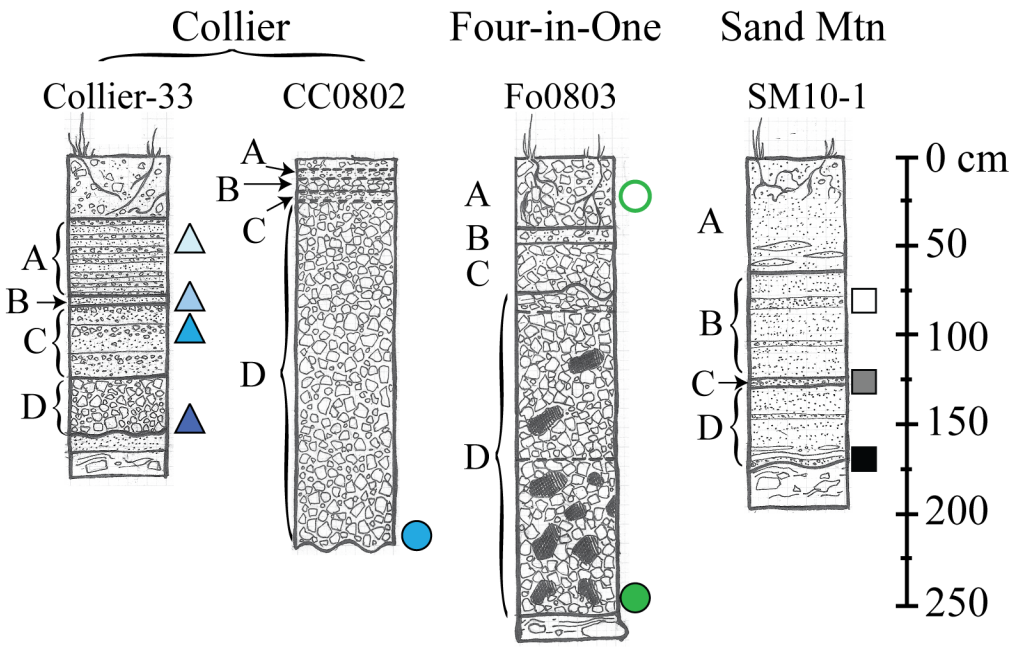

Figure 2. Representative stratigraphic columns for Collier Cone (Collier-33, CC0802), Four-in-One (Fo0803), and Sand Mountain (SM10-1) tephra deposits. Units are labeled to the left of each column and corresponding sample symbols are located to the right. The base of the deposit CC0802 was not reached. Deposit CC0802 is inferred to be equivalent to unit D of Collier-33. Complete unit descriptions are provided in Table 1.

2.2.1.1. Four-in-One

The Four-in-One 'cone' consists of four contiguous vents aligned N 10° E on the northern flank of North Sister volcano. This eruption represents the smallest of the three studied eruptions, producing only ~0.005 km^3 of lava and tephra. The scoria cones are all breached to the NW towards a basaltic andesite to andesitic lava flow that extends ~4 km. The lava flow is moderately porphyritic (predominantly plagioclase and olivine) and contains rare rhyolitic xenoliths. A modest tephra apron (minimum tephra volume ~0.0008 km^3; Figure 1) mantles the eastern side of the cone complex, rapidly decreasing to <10 cm thickness at ~2 km away from the vent. The tephra deposit lies stratigraphically above both the nearby Yapoah lava flow and discontinuous lenses of fine white ash interpreted to be from the 2000–2300 yr b.p. Rock Mesa-Devil's Hill eruption to the south (Sherrod et al., 2004). A single radiocarbon age of 1910 ±200 (calendar) yr b.p. has been obtained from charred vegetation in the basal portion of the tephra apron (Sherrod et al., 2004). The massive character of the deposit and the limited

areal dispersal of coarse scoria and glassy bombs suggest a Strombolian phase of activity (Walker, 1973; Valentine & Gregg, 2008). The small volume of erupted material and lack of significant internal unconformities or disturbed units suggests that explosive activity at Four-in-One was relatively short-lived (days to weeks).

2.2.1.2. Collier Cone

Collier Cone is a 75 m high cinder cone on the NW flank of North Sister (~3 km NW of summit). The cone is breached to the NW where it fed a predominantly basaltic andesite to andesite lava flow that extended 14 km into the White Branch Valley. The lava comprises multiple emplacement units that vary in phenocryst (olivine, plagioclase, ±clinopyroxene) abundances and contain both troctolite xenoliths (~90 vol.% high An plagioclase; interpreted to be mafic cumulates), and silicic xenoliths that are similar in composition to the nearby Obsidian Cliffs (Schick, 1994; Sherrod et al., 2004). The lava flows partially cover the southern extent of the tephra apron of Four-in-One (Figure 1), showing that this eruption followed that of Four-in-One. A radiocarbon age of 1511 ±108 calendar yrs b.p. was obtained from of charred material beneath tephra blanket (Sherrod et al., 2004). The total volume of lava and tephra erupted from Collier is ~0.04–0.05 km^3, (based on isopach maps; lava volume from Deardorff & Cashman, 2009) approximately an order of magnitude larger than that erupted at Four-in-One. A moderate-sized tephra blanket (minimum volume ~0.007 km^3; Figure 1) was deposited to the NE, across the crest of the High Cascades. The deposit maintains a >1 m thickness up to ~3 km away from the vent. To the east of the Cascades crest, the deposit sits stratigraphically above crystal-rich ash deposits of Yapoah and a paleosol containing discontinuous lenses of fine, white ash interpreted to be from the Rock Mesa-Devil's Hill eruption.

The tephra record from Collier is considerably more complex than the Four-in-One record and comprises three main units that are best exposed at distal locations (e.g., Collier-33; Figure 2). The basal unit (Collier-33D) is a laterally continuous layer of massive, crystal-poor, coarse (up to 3–4 cm) vesicular lapilli containing sparse ribbon fragments, rare clumps of troctolite xenoliths and sugary, pyroxene-bearing glass fragments. Section CC0802, several hundred meters to the NE of the cone, is interpreted to correlate with this lowermost unit (Collier-33D). The missing upper portions of this

section are interpreted to have eroded away. The middle unit (Collier-33C) consists of multiple packets (roughly equal in thickness), each with an upper layer (~2–3 cm) of tan lapilli underlain by dark ash (~10–11 cm). The entire deposit becomes noticeably more crystal-rich (predominantly olivine) in the upper packets of this middle unit. The uppermost unit (Collier-33A) consists of at least 13 alternating layers of ash and lapilli, each approximately 1.5–3 cm thick. The depositional characteristics of the Collier tephra section suggest an explosive eruption characterized initially by Strombolian-style activity (basal unit) transitioning into more energetic Violent Strombolian activity (upper units) (Pioli et al., 2008; Valentine & Gregg, 2008). The modest eruption volume and lack of identifiable internal unconformities, disturbed units, or other evidence for reworking suggests that this eruption was also relatively short-lived (weeks to months).

2.2.1.3. Sand Mountain

The Sand Mountain chain of cinder cones represents the largest of the studied eruptions and either represents a single, long-lived (year to decadal scale) event or a series of discrete events spaced within a few hundred years. Recent work constrains the age of the basaltic lava flows associated with the cones at ~2800–2900 yrs. b.p. (N. Deligne, personal communication, 2010). The associated tephra blanket is substantially more extensive (~ 1 km^3) than either the Four-in-One or Collier deposits, perhaps because of enhanced fragmentation through interaction with snow or ice similar to the March-May 2010 eruption at Eyjafjallajökull, Iceland (Figure 1a) (McKay & Cashman, 2010). The deposit is unusually fine-grained (average clast size: 0.06–0.5 mm) and consists predominantly of interbedded layers of laminated and massive, crystal-rich (olivine) ash beds (Figure 2). Lack of obvious internal erosion within the preserved tephra beds suggests a single phase of explosive activity.

Table 1. Stratigraphic descriptions.

Collier-33 (151 cm)		CC0802 (200 cm)		Fo0803 (245 cm)		SM10-1 (180 cm)	
A	13 alternating layers (1.5-3 cm thick) of fine ash and coarser (avg ~ 4 mm) lapilli. Overlain by reworked Collier tephra.	A	Well-sorted layer of tan lapilli approximately 5 cm beneath reworked surface deposits.	A	Reworked, coarse (2-6 cm) lapilli set within a slightly finer-grained matrix.	A	Weathered dark brown ash-rich tephra and abundant grass roots in upper 23 cm grading down to red brown tephra with 2-3 cm lenses of fine ash.
B	Light brown, ash-rich layer. This layer contains larger vesicular lapilli at locations closer to vent.	B	Similar to layer D below.	B	Predominantly fine-grained ash layer containing rare larger (3 cm) lapilli. Modern day roots present.	B	Mostly laminated, fine ash with laterally continuous layers of coarser ash at 70-78 cm and 94-96 cm depth. Local lenses of oxidized ash surround root clumps, but tephra is not reworked.
C	3 packets of roughly equal thicknesses, each consisting of a ~2 cm thick upper layer of tan lapilli underlain by a finer-grained darker layer of black, crystal-rich (ol+plag) ash. Top packet is particularly crystal-rich.	C	Finer-grained, well-sorted layer of tan lapilli.	C	Clast-supported unit of 2-6 cm tan, vesicular lapilli. Local erosional surfaces at base indicate fluvial incision into unit D.	C	Coarse ash containing larger lapilli (up to 3-4 mm). Both tan and black components are present along with abundant olivine and lesser plagioclase crystals.
D	Massive clast-supported unit of coarse (0.7-3 cm diameter), vesicular lapilli. Black & tan tephra components both present.	D	Massive clast-supported unit of coarse (2-4 cm) lapilli consisting of both tan, vesicular and black, denser components. Broken ribbon fragments protrude from wall. Scarce, frothy/sugary light-colored glass containing pyroxenes and troctolite clumps are present.	D	Massive clast-supported unit of tan, vesicular clasts (2-4 cm) with little to no fine material present. Larger (>10 cm) dark, glassy clasts are interspersed throughout the unit but become more concentrated towards base.	D	Mostly laminated fine ash with lenses of coarser ash. A coarse layer of ash appears laterally continuous at ~132-133 cm depth. Lower section consists of interbedded layers of VERY fine and coarse ash. Basal coarse ash layer in contact with underyling paleosol.
Base	Oxidized, ash-rich layer (Yapoah?) overlying poorly sorted glacial deposits. Upper 2 cm of glacial deposits contain discontinuous lenses of fine, white ash interpreted to be Devil's Hill/Rock Mesa eruption.	Base	Not reached.	Base	Fluvial deposits of modern stream channel cutting through deposit. In other localities, an orange paleosol containing lenses of white ash (Devil's Hill/Rock Mesa) underlies a crystal-rich, oxidized ash layer (Yapoah?).	Base	Undulatory surface (paleo-topography) on charcoal-rich paleosol. Glacial erratics.

2.3. Sample Preparation and Analytical Techniques

Loose olivine crystals were hand picked from stratigraphically controlled tephra samples spanning the full range of explosive activity during the eruptions of Collier Cone (Collier-33 and CC0802), Four-in-One (Fo0803), and Sand Mountain (SM10-1) (Figure 1, Figure 2; Table 1). Additional olivine crystals from Collier Cone were picked from a sample of loose material (CC0801-2) from the summit of the cone (Figure 1). Olivines were treated in HBF_4 to remove attached matrix glass and allow inclusion inspection under refractive index oil (n=1.678). Crystals containing fully enclosed melt inclusions were ground and polished into wafers containing doubly intersected glass inclusions. Inclusion-bearing wafers were analyzed for H_2O and CO_2 using a Thermo-Nicolet Nexus 670 FT-IR spectrometer interfaced with a Continuum IR microscope. Wafers were subsequently mounted in Araldite 502 resin for host crystal and glass analyses using a Cameca SX-100 electron microprobe (EMPA). All analyses were performed at the University of Oregon.

Hydrous glass compositions were determined using multiple beam conditions during a single spot analysis (15 kV, 10 μm beam diameter, and 10 or 50 nA; see Ruscitto et al. 2010a, b for detailed analytical procedures). Individual analyses reported in Appendix A are averages of 3–5 analyzed spots. BIR-1G and VG2-1 glasses were analyzed to monitor accuracy, and element concentrations are within 5% of accepted values (most elements are within 2%; S is within 6%). Host olivine compositions were determined by averaging 3–5 spot analyses >100 μm away from inclusions and crystal edges for each wafer and are reported as forsterite content (%Fo = 100*MgO/ [MgO+FeO]; oxides in molar proportions) in Table 2 and Appendix A.

H_2O and CO_2 concentrations were calculated from IR peak absorbances using the Beer-Lambert law. Wafer thicknesses were first determined with a digital micrometer and then checked using the interference fringe method of Wysoczanski & Tani (2006). H_2O concentrations were determined using the 3550 cm^{-1} peak, 4520 + 5200 cm^{-1} peaks, or 4520+1630 cm^{-1} peaks. CO_2 concentrations were determined using the CO_3^{2-} doublet at 1515–1430 cm^{-1}. Absorption coefficients (with the exception of ε_{3550}) are compositionally dependent and were calculated using average glass compositions

determined by EMPA (Dixon & Pan, 1995; Mandeville et al. 2002). Glass densities were calculated using oxide molar volumes reported in Luhr (2001), and hydrous densities were determined by iteration. Average relative uncertainties for H_2O and CO_2 concentrations are ±10%.

Bulk tephra samples were analyzed for major and trace elements by XRF at the Washington State University GeoAnalytical Laboratory and are given in Table 3. The lava compositions shown in subsequent figures are from Schick (1994) and from unpublished whole rock analyses of lava flows associated with the cinder cones. These supplementary data were also analyzed at WSU (provided by Rick Conrey, Natalia Deligne, and Nick Deardorff).

2.4. Results

2.4.1. Melt Inclusion Compositions

The analyzed melt inclusions are predominantly within Fo_{82-85} host olivines, and most are out of equilibrium with their host crystals because of post-entrapment crystallization and Fe-loss associated with diffusive Fe-Mg re-equilibration (Figure 3; Danyushevsky et al., 2000; Gaetani & Watson, 2000). Therefore, inclusion compositions have been recalculated to inferred initial conditions following the method of Danyushevsky et al. (2000). Initial $FeO^{T(otal)}$ contents were estimated for each set of melt inclusions by using the maximum value in glasses within the least-evolved host crystals (i.e., highest forsterite contents). Estimated initial FeO^T contents within the restored inclusions are in agreement with FeO^T values in bulk tephra and lavas (shaded fields in Figure 3a). Rare sulfide droplets occur in both Collier and Four-in-One melt inclusions and constrain the oxidation state to NNO ±0.5 (Fe^{2+}/Fe^{Total} = 0.76–0.80) (Wallace & Carmichael, 1992; Mavrogenes & O'Neill, 1999). Many Sand Mountain melt inclusions have significantly higher dissolved S contents than either Collier or Four-in-One inclusions and do not contain sulfide globules. Therefore, these inclusions must reflect more oxidizing conditions (Wallace & Carmichael, 1992; Jugo, 2010). Oxidation states for Central Oregon magmas are highly variable and can be as high as NNO +1.5 (Rowe

Table 2. Restored melt inclusion compositions.

Sample	Collier: CC0801-2								Collier-33A			Collier-33B			
Long (W)	121° 47' 3.84"								121° 45' 25.62"			121° 45' 25.62"			
Lat (N)	44° 11' 15.12"								44° 12' 1.56"			44° 12' 1.56"			
Inclusion	h	c	i	a	b	f1	g	d	e	c	d	e1	e2	d	b
Host (%Fo)	84.5	84.5	84.6	84.7	84.7	84.8	84.8	85.0	84.2	84.4	84.5	84.9	84.9	84.9	85.0
Total	99.46	98.54	100.73	98.83	98.80	98.77	99.81	98.38	99.59	99.80	100.6	99.93	99.27	100.65	99.63
Restored Compositions: Oxides Normalized to 100 wt.% Volatile-Free															
Wt% Ol add.	1.3	1.2	0.8	2.2	1.0	3.3	0.9	0.4	0.5	-0.1	1.8	2.1	3.0	5.4	-0.2
SiO_2 (wt.%)	54.91	55.06	54.69	56.34	54.83	54.40	54.81	55.77	53.81	53.61	53.50	54.00	54.39	54.28	53.70
TiO_2	0.98	0.90	0.93	1.00	0.96	1.00	0.93	0.90	0.89	0.91	0.91	0.88	0.90	0.86	0.87
Al_2O_3	18.95	18.55	18.98	17.88	18.85	19.29	18.81	18.26	19.04	19.26	19.29	19.46	19.11	19.36	19.64
FeO^T	7.19	7.15	7.13	7.23	7.15	7.23	7.14	7.14	7.26	7.27	7.28	6.80	6.80	6.76	6.73
MnO	0.11	0.11	0.11	0.11	0.12	0.09	0.11	0.11	0.12	0.13	0.11	0.11	0.10	0.08	0.10
MgO	5.78	5.71	5.72	5.94	5.84	5.93	5.81	6.10	5.40	5.46	5.52	5.27	5.28	5.14	5.27
CaO	8.70	8.88	8.87	8.11	8.90	8.82	8.76	8.85	8.87	8.74	8.83	8.83	8.71	8.22	8.91
Na_2O	2.72	2.99	2.93	2.59	2.72	2.52	2.90	2.12	3.98	4.03	3.96	4.05	4.09	4.54	3.95
K_2O	0.54	0.52	0.51	0.65	0.50	0.58	0.56	0.64	0.52	0.50	0.49	0.52	0.53	0.65	0.64
P_2O_5	0.13	0.12	0.13	0.14	0.12	0.15	0.15	0.11	0.11	0.10	0.10	0.09	0.10	0.13	0.19
S	0.080	0.078	0.080	0.077	0.080	0.085	0.083	0.080	0.072	0.070	0.074	0.069	0.071	0.075	0.077
Cl	0.074	0.076	0.077	0.082	0.075	0.080	0.081	0.069	0.064	0.066	0.057	0.059	0.069	0.067	0.060
H_2O	2.88	2.50	3.44	2.74	2.69	2.67	2.85	3.33	3.16	3.15	3.79	3.46	2.38	3.40	2.91
±1s.d.	0.13	0.26	0.32	0.16	0.17	0.33	0.41	0.20	0.19	0.62	0.31	0.23	0.16	0.28	0.30
CO_2 ppm	976	657	802	658	792	614	911	448	964	663	1328	718	n.d.	994	975
±1s.d.	56	42	72	55	152	38	75	31	57	108	116	55		76	66
$T_{formation}$ (°C)	1029	1040	1013	1040	1036	1039	1033	1023	1020	1022	1007	1007	1038	1011	1019
P (MPa)	171	122	175	131	143	122	163	130	185	151	246	161	44	192	177
$^vX_{H2O}$	0.489	0.519	0.609	0.554	0.506	0.559	0.501	0.711	0.480	0.557	0.502	0.592	1.000	0.520	0.459
Open System															
DS	12.3	7.8	15.8	14.1	9.9	8.1	7.3	12.3	21.5	24.4	46.8	37.5	12.4	-	10.0
DCl	11.0	3.8	8.3	5.3	8.2	6.3	1.9	18.5	8.3	7.0	51.0	23.4	0.3	-	10.4
Closed															
DS	12.7	8.2	16.3	14.8	10.2	8.1	7.3	12.6	23.5	27.0	50.5	41.7	13.6	-	10.5
DCl	11.2	3.9	8.2	5.2	8.3	6.2	1.8	19.6	8.5	7.1	55.5	24.9	0.3	-	11.0
Closed +1%															
DS	7.2	4.6	6.7	8.8	5.8	4.8	3.8	5.0	10.8	12.9	14.3	15.0	8.1	-	5.1
DCl	6.3	2.0	3.1	2.9	4.7	3.5	0.7	8.1	3.6	3.0	15.7	8.7	-0.2	-	5.3

Table 2. Extended.

Sample	33B	Collier-33C								Collier-33D				
Long (W)		121° 45' 25.62"								121° 45' 25.62"				
Lat (N)		44° 12' 1.56"								44° 12' 1.56"				
Inclusion	a	lower-b	lower-e	lower-a	upper-b1	upper-b2	upper-a	upper-d	upper-e	a	d	e	b1	b3
Host (%Fo)	85.2	80.1	80.8	83.0	84.2	84.2	84.9	84.9	84.9	77.1	78.3	83.7	84.8	84.8
Total	98.16	100.6	99.77	99.44	98.84	98.98	99.65	100.7	99.93	101.1	100.1	99.19	99.71	99.14
Restored Compositions: Oxides Normalized to 100 wt.% Volatile-Free														
Wt% Ol add.	1.3	1.1	0.5	1.5	0.8	-0.1	4.1	0.5	5.2	1.1	0.9	0.5	4.5	4.1
SiO_2 (wt.%)	53.00	55.91	55.43	54.96	54.11	54.02	53.74	53.30	54.12	57.31	55.00	55.22	54.22	53.72
TiO_2	0.90	1.11	1.00	1.00	0.91	0.92	0.86	0.88	0.96	1.13	0.97	1.00	0.94	0.95
Al_2O_3	19.94	18.40	18.80	19.05	19.36	19.51	19.42	20.03	19.01	17.48	18.29	18.71	19.55	19.75
FeO^T	6.75	6.81	6.96	6.81	6.83	6.81	6.83	6.80	6.82	7.31	8.03	6.61	6.46	6.57
MnO	0.11	0.11	0.12	0.10	0.12	0.12	0.10	0.12	0.10	0.13	0.15	0.12	0.08	0.09
MgO	5.40	3.68	4.09	4.55	5.01	4.97	5.32	5.29	5.31	3.28	4.07	4.65	4.97	5.02
CaO	9.45	7.91	8.53	8.28	8.86	8.77	9.13	9.06	8.82	6.71	8.20	8.48	8.97	9.03
Na_2O	3.84	5.21	4.35	4.45	4.17	4.23	3.90	3.89	4.06	5.46	4.54	4.49	4.12	4.23
K_2O	0.46	0.71	0.62	0.66	0.53	0.55	0.56	0.50	0.64	0.97	0.65	0.61	0.56	0.52
P_2O_5	0.14	0.14	0.12	0.12	0.10	0.11	0.16	0.11	0.18	0.22	0.11	0.11	0.12	0.12
S	0.072	0.079	0.072	0.075	0.069	0.071	0.081	0.074	0.082	0.076	0.071	0.073	0.073	0.068
Cl	0.067	0.069	0.064	0.062	0.062	0.086	0.081	0.062	0.059	0.073	0.059	0.065	0.061	0.069
H_2O	2.65	4.22	3.72	3.31	2.96	2.66	3.06	3.88	3.51	4.14	3.92	3.40	3.36	2.50
(±1s.d.)	0.34	0.55	0.31	0.15	0.35	0.75	0.14	0.63	0.21	0.31	0.29	0.22	0.25	0.26
CO_2 ppm	760	974	792	1096	643	667	841	1240	1032	1039	689	648	1162	1015
(±1s.d.)	90	128	77	59	84	78	45	129	135	100	65	282	88	103
$T_{formation}$ (°C)	1030	934	955	987	1011	1017	1019	992	1010	927	957	988	998	1024
P (MPa)	136	227	186	210	141	135	168	246	206	241	190	157	230	188
$^vX_{H2O}$	0.464	0.613	0.592	0.475	0.530	0.477	0.488	0.527	0.509	0.559	0.611	0.540	0.431	0.329
Open System														
DS	14.1	40.3	36.8	22.3	21.6	16.0	-	73.0	16.6	40.0	54.7	26.5	25.4	18.0
DCl	3.8	28.3	23.5	18.4	11.6	-11.8	-	46.7	25.5	18.6	43.8	15.8	19.4	4.1
Closed														
DS	15.3	41.9	40.1	23.8	24.1	17.5	-	78.4	17.0	42.4	60.1	28.7	27.6	20.3
DCl	3.8	27.9	24.1	19.1	12.1	-10.4	-	48.7	27.2	17.7	46.7	16.1	20.4	4.0
Closed +1%														
DS	8.7	17.0	17.2	12.3	12.6	10.1	-	13.5	7.2	18.7	19.6	14.4	12.7	12.4
DCl	1.8	11.2	10.1	9.8	6.1	-6.6	-	8.1	11.8	7.6	15.1	7.9	9.3	2.2

Table 2. Extended

Sample	Collier: CC0802D-200									Four-in-One: FO0803-A					
Long (W)	121° 46' 29.16"									121° 48' 19.08"					
Lat (N)	44° 11' 32.40"									44° 12' 39.36"					
Inclusion	i1	i2	i3	g	d	e	f	b	a	e	f1	f2	d	b	g
Host (%Fo)	78.9	78.9	78.9	80.1	83.9	84.0	84.1	84.2	84.7	82.4	82.9	82.9	83.0	83.3	83.3
Total	99.34	98.32	98.93	99.36	99.40	98.34	98.13	99.65	98.89	100.1	98.72	99.15	98.26	99.18	99.42
Restored Compositions: Oxides Normalized to 100 wt.% Volatile-Free															
Wt% Ol add.	0.0	0.0	0.1	0.0	0.3	1.6	2.2	2.9	5.4	2.6	3.5	3.0	-0.1	4.0	0.2
SiO_2 (wt.%)	56.52	58.10	58.48	57.62	54.86	54.70	55.91	57.05	58.40	54.89	54.30	54.10	52.95	52.90	53.33
TiO_2	0.97	1.10	1.10	0.94	0.93	0.98	0.93	0.98	1.09	1.19	1.13	1.15	1.15	1.17	1.14
Al_2O_3	18.30	17.74	17.41	17.77	19.40	19.46	18.37	18.07	16.95	16.78	17.43	17.66	18.68	18.42	17.56
FeO^T	8.05	7.90	7.79	7.78	7.08	7.18	7.07	7.14	7.07	8.17	8.16	8.16	8.15	8.26	8.15
MnO	0.15	0.13	0.13	0.12	0.12	0.11	0.10	0.10	0.09	0.11	0.12	0.12	0.14	0.12	0.14
MgO	4.68	4.63	4.52	4.82	5.46	5.57	5.59	5.88	5.97	5.60	5.89	5.87	5.79	5.91	5.77
CaO	8.25	7.42	7.36	7.67	8.90	8.73	8.75	8.21	7.39	9.13	9.30	9.22	9.19	9.06	9.32
Na_2O	2.29	1.98	2.21	2.26	2.59	2.60	2.59	1.89	2.14	3.20	2.74	2.79	2.98	3.23	3.59
K_2O	0.62	0.84	0.85	0.87	0.55	0.54	0.55	0.54	0.75	0.67	0.67	0.67	0.70	0.68	0.75
P_2O_5	0.15	0.16	0.15	0.15	0.12	0.13	0.12	0.13	0.15	0.25	0.25	0.25	0.27	0.26	0.25
S	0.076	0.088	0.090	0.073	0.083	0.076	0.078	0.080	0.058	0.095	0.089	0.091	0.090	0.090	0.093
Cl	0.073	0.087	0.086	0.085	0.078	0.074	0.070	0.075	0.081	0.076	0.083	0.086	0.080	0.078	0.083
H_2O	3.85	3.83	3.29	3.31	3.46	2.90	2.62	3.91	2.84	3.13	2.82	2.35	2.29	2.74	1.78
(±1s.d.)	0.55	0.40	0.28	0.30	0.18	0.24	0.12	0.34	0.17	0.18	0.46	0.14	0.17	0.15	0.10
CO_2 ppm	745	702	702	516	575	472	589	853	591	791	806	651	753	904	788
(±1s.d.)	67	63	61	38	35	25	34	74	53	88	56	52	51	57	45
$T_{formation}$ (°C)	965	963	975	986	1000	1019	1029	997	1035	1027	1042	1055	1054	1049	1078
P (MPa)	192	186	163	142	153	121	123	205	132	175	164	130	143	174	132
$^vX_{H2O}$	0.668	0.676	0.609	0.674	0.668	0.641	0.550	0.647	0.583	0.510	0.454	0.418	0.384	0.421	0.288
Open System															
DS	37.5	18.7	11.7	23.5	12.6	15.4	10.0	32.5	31.7	27.2	19.5	7.6	8.9	17.0	2.5
DCl	27.3	10.5	8.0	-1.5	8.8	10.9	10.5	26.8	9.4	64.9	2.9	-1.8	6.6	17.7	0.8
Closed															
DS	39.9	18.4	11.4	25.4	12.8	16.3	10.5	33.6	39.0	26.8	19.9	7.7	9.1	17.3	2.5
DCl	28.0	9.9	7.5	-1.4	8.7	11.1	11.0	27.3	9.1	67.1	2.9	-1.7	6.7	18.0	0.8
Closed +1%															
DS	14.3	8.7	6.3	11.8	5.1	9.2	6.0	11.6	24.4	4.1	4.6	3.0	3.8	5.3	1.0
DCl	9.9	4.5	4.1	-1.2	3.4	6.1	6.3	9.3	5.5	11.4	0.1	-1.3	2.6	5.5	0.1

Table 2. Extended.

Sample	FO0803-A		Four-in-One: FO0803-D3										Sand Mtn: SM1001-B		
Long (W)			121° 48' 19.08"										121° 52' 1.26"		
Lat (N)			44° 12' 39.36"										44° 23' 3.42"		
Inclusion	a1	a2	Xb	c1	f	e	g	a	m	i	k	L	b	c	d
Host (%Fo)	83.6	83.6	80.8	82.0	82.2	83.0	83.1	83.1	83.4	83.5	83.5	83.6	79.7	82.9	83.3
Total	99.51	99.01	99.43	99.23	98.66	98.56	99.36	99.29	96.73	99.63	98.66	99.36	99.72	99.21	99.17
Restored Compositions: Oxides Normalized to 100 wt.% Volatile-Free															
Wt% Ol add.	1.0	2.4	0.1	0.1	5.2	1.5	1.0	1.3	0.0	2.1	1.0	2.0	-0.1	4.3	5.3
SiO_2 (wt.%)	53.47	53.57	54.85	53.84	54.09	53.13	53.66	53.21	53.82	53.84	53.06	53.69	50.60	52.32	49.85
TiO_2	1.13	1.15	0.99	1.12	1.10	1.18	1.14	1.16	1.10	1.24	1.13	1.10	1.22	1.37	1.26
Al_2O_3	17.73	17.75	17.23	17.91	17.66	17.63	17.12	18.08	16.83	17.08	17.47	17.35	17.55	16.73	18.86
FeO^T	8.15	8.15	8.62	8.39	8.41	8.39	8.40	8.38	8.39	8.40	8.41	8.40	11.02	9.31	9.20
MnO	0.14	0.13	0.15	0.16	0.11	0.13	0.12	0.13	0.14	0.12	0.14	0.12	0.17	0.13	0.11
MgO	6.02	5.98	5.36	5.65	5.68	5.81	5.95	6.00	6.11	6.16	6.14	6.22	5.53	5.54	5.55
CaO	9.37	9.03	8.68	9.12	8.79	9.16	9.35	9.11	9.47	8.91	9.49	9.15	8.71	8.63	9.51
Na_2O	3.14	3.23	3.19	2.90	3.21	3.62	3.35	3.00	3.27	3.22	3.28	3.09	4.05	4.43	4.29
K_2O	0.64	0.74	0.73	0.65	0.72	0.70	0.67	0.67	0.64	0.69	0.63	0.67	0.78	1.14	0.94
P_2O_5	0.24	0.26	0.21	0.23	0.24	0.25	0.24	0.25	0.23	0.35	0.25	0.23	0.38	0.41	0.42
S	0.092	0.098	0.080	0.087	0.094	0.087	0.095	0.094	0.089	0.091	0.093	0.091	0.139	0.077	0.177
Cl	0.078	0.080	0.107	0.086	0.080	0.085	0.084	0.083	0.081	0.076	0.081	0.076	0.099	0.136	0.137
H_2O	3.03	2.49	2.97	2.82	2.01	1.96	1.94	2.44	1.02	3.13	2.22	2.86	2.19	0.49	0.15
(±1s.d.)	0.28	0.21	0.48	0.23	0.22	0.23	0.13	0.25	0.11	0.48	0.15	0.51	0.52	0.04	0.03
CO_2 ppm	866	532	660	833	635	534	724	839	n.d.	968	766	841	321	40	259
(±1s.d.)	52	37	95	68	62	106	60	45	-	135	63	118	33	15	25
$T_{formation}$ (°C)	1042	1059	1064	1034	1066	1075	1078	1059	1113	1048	1075	1056	1070	1129	1134
P (MPa)	181	122	162	174	123	110	135	164	14	200	147	176	109	21	-
$^vX_{H2O}$	0.477	0.490	0.513	0.436	0.346	0.374	0.316	0.373	0.992	0.454	0.353	0.441	0.413	0.246	-
Open System															
DS	24.7	-0.5	-	26.8	-	10.4	1.0	5.4	-	40.2	3.8	-	-	32.9	0.3
DCl	39.1	8.8	-	-8.5	-	2.3	0.4	3.4	-	51.0	4.1	-	-	2.7	-0.7
Closed															
DS	24.8	-0.5	-	27.7	-	10.8	1.0	5.3	-	40.6	3.8	-	-	51.0	0.3
DCl	39.7	8.9	-	-8.2	-	2.3	0.4	3.4	-	52.6	4.1	-	-	2.6	-0.7
Closed +1%															
DS	2.4	-0.8	-	6.4	-	5.6	0.1	1.8	-	9.3	1.3	-	-	36.5	0.0
DCl	4.3	3.2	-	-2.8	-	0.8	-0.2	1.0	-	12.3	1.5	-	-	1.7	-0.7

Table 2. Extended.

Sample	Sand Mtn: SM1001-B			Sand Mountain: SM1001-C					Sand Mountain: SM1001-D3					
Long (W)				121° 52' 1.26"					121° 52' 1.26"					
Lat (N)				44° 23' 3.42"					44° 23' 3.42"					
Inclusion	Xa	Xe	Xe_r	b1	b2	a	Xd	e	e	b	a	d	c	Avg
Host (%Fo)	84.0	84.1	84.1	82.9	82.9	83.4	83.6	83.7	82.9	83.0	83.2	84.1	84.8	1 s.e.
Total	99.83	99.37	99.34	99.56	100.2	99.30	99.58	99.71	99.18	99.03	100.4	99.50	100.8	
Restored Compositions: Oxides Normalized to 100 wt.% Volatile-Free														
Wt% Ol add.	4.6	5.1	0.3	0.1	0.1	0.3	1.2	3.0	0.3	2.7	2.7	2.4	4.2	
SiO_2 (wt.%)	50.90	50.59	51.26	51.85	52.35	49.83	51.47	51.87	52.23	51.24	52.19	51.60	51.71	0.16
TiO_2	1.45	1.52	1.54	1.28	1.23	1.39	1.50	1.28	1.25	1.43	1.29	1.39	1.28	0.01
Al_2O_3	17.95	17.97	17.17	18.47	18.23	19.38	18.76	18.39	18.23	18.02	17.76	17.48	17.82	0.10
FeO^T	9.20	9.28	9.21	8.12	8.11	8.10	8.10	8.10	8.33	8.36	8.34	8.46	8.33	0.08
MnO	0.13	0.12	0.16	0.14	0.14	0.13	0.14	0.12	0.13	0.11	0.14	0.12	0.10	0.01
MgO	5.99	6.11	5.96	4.93	4.96	4.87	5.09	5.13	5.05	5.02	5.02	5.43	5.69	0.05
CaO	9.39	9.31	9.03	10.05	9.90	10.42	9.81	9.63	9.48	10.25	9.36	9.72	9.59	0.03
Na_2O	3.92	3.88	4.33	3.89	3.83	4.45	3.98	4.20	4.01	4.08	4.67	4.41	4.09	0.09
K_2O	0.72	0.78	0.98	0.89	0.87	1.00	0.78	0.91	0.91	1.08	0.86	1.02	0.98	0.01
P_2O_5	0.36	0.44	0.36	0.38	0.38	0.42	0.37	0.38	0.37	0.42	0.37	0.36	0.40	0.003
S	0.091	0.089	0.067	0.170	0.164	0.256	0.102	0.186	0.175	0.180	0.173	0.196	0.191	0.001
Cl	0.061	0.061	0.059	0.128	0.129	0.141	0.059	0.127	0.126	0.101	0.120	0.094	0.115	0.002
H_2O	2.12	1.40	0.77	2.48	2.89	0.83	2.26	2.20	2.42	0.31	3.18	2.33	2.56	0.27
(±1s.d.)	0.16	0.20	0.05	0.21	0.34	0.10	0.16	0.20	0.21	0.09	0.38	0.17	0.19	
CO_2 ppm	1084	904	108	413	271	594	673	508	738	0	721	176	597	75
(±1s.d.)	82	82	15	84	103	156	84	58	64	114	83	31	34	
$T_{formation}$ (°C)	1077	1107	113	1023	1012	1076	1033	1041	1031	1100	1014	1057	1054	
P (MPa)	217	186	43	113	91	103	142	119	167	8	183	76	151	
$^vX_{H2O}$	0.235	0.151	0.222	0.488	0.722	0.119	0.360	0.397	0.346	0.396	0.475	0.611	0.404	
Open System														
DS	-	-	-	8.9	26.4	-10.2	-	-2.6	2.3	4.0	62.1	0.6	-8.1	
DCl	-	-	-	7.9	7.6	1.9	-	6.6	8.0	13.6	144.5	40.3	24.9	
Closed														
DS	-	-	-	9.0	27.1	-8.4	-	-2.5	2.3	3.9	62.2	0.5	-7.7	
DCl	-	-	-	7.9	7.7	1.8	-	6.7	8.1	15.6	150.2	47.8	26.5	
Closed +1%														
DS	-	-	-	3.2	4.1	-6.1	-	-1.7	0.4	2.6	4.1	-0.1	-3.6	
DCl	-	-	-	2.8	0.6	1.0	-	2.8	2.9	11.2	11.2	23.9	9.8	

Table 3. Bulk tephra compositions.

Source	Collier										Four-in-One		
Sample	CC0901-C	CC0901-A	CC0902-Base	CC0802-D200	CC0802-D0	33D	33C-lower	33C-upper	33B	33A	Fo0803-D3	FO0308-A	Fo0810-1
Longitude (W 121°)	45.329’		45.925’	46.486’				45.427’			48.318’		47.657’
Latitude (N 44°)	11.786’		11.200’	11.540’				12.026’			12.656’		12.980’
Total Depth (cm)	120	120	130	250	250	148	148	148	148	148	236	236	28
Position (cm)	115	70	110	199	21	145	107	81	74	52	216	30	25
Rel. Strat. Height[a]	0.04	0.42	0.15	0.20	0.25[b]	0.02	0.28	0.45	0.50	0.65	0.08	0.87	0.11
SiO_2 (wt.%)	56.91	54.62	57.27	57.14	57.03	56.54	57.31	55.18	56.40	55.27	52.68	54.40	52.92
TiO_2	1.09	0.71	1.06	1.09	1.09	1.09	1.05	0.75	0.85	0.81	1.11	1.17	1.15
Al_2O_3	18.31	21.04	18.12	18.05	18.19	18.50	18.27	19.51	18.93	19.44	19.25	18.47	19.30
FeO^T	7.40	5.62	7.28	7.19	7.29	7.44	7.10	6.21	6.53	6.39	7.84	7.82	7.91
MnO	0.13	0.10	0.12	0.13	0.13	0.13	0.12	0.11	0.12	0.11	0.14	0.13	0.14
MgO	3.70	4.55	3.71	3.77	3.72	3.78	3.70	5.63	4.87	5.30	5.52	4.86	5.29
CaO	7.14	9.04	7.03	7.25	7.20	7.27	7.00	8.06	7.33	8.03	8.96	8.14	8.71
Na_2O	4.30	3.53	4.35	4.35	4.33	4.27	4.37	3.67	3.94	3.75	3.62	3.86	3.65
K_2O	0.87	0.71	0.91	0.88	0.89	0.84	0.93	0.78	0.89	0.78	0.64	0.86	0.69
P_2O_5	0.15	0.10	0.14	0.14	0.14	0.15	0.14	0.10	0.13	0.12	0.23	0.28	0.24

[a] Base located at 0.0; top at 1.0

[b] Modified to reflect correlation with Collier-33D

et al., 2009). We calculated total S saturation values by modifying the sulfide-saturation model of Wallace & Carmichael (1992) to include the temperature dependence of Mavrogenes & O'Neill (1999) and combining it with the S saturation model for oxidized magmas of Jugo (2010) (Figure 3c). Calculated solubility limits of S at NNO +1 are similar to those found in Sand Mountain melt inclusions at the temperatures of interest (1050–1100 ºC; see below). Therefore, all calculations for Sand Mountain melt inclusions were performed at NNO +1 ($Fe^{2+}/Fe^{Total} = 0.71$) and all calculations for Collier and Four-in-one inclusions were done at NNO. All restored compositions required less than 5 wt.% olivine addition (average ±1 s.d.: 1.8 ±0.7 wt.%) and less than 2 wt.% FeO^T addition (average ±1 s.d.: 0.8±0.2 wt.%). Both restored and unrestored melt inclusion compositions are reported in Table 2. Only restored inclusion compositions are shown in subsequent figures and considered in discussions.

Restored melt inclusion compositions (normalized on a volatile-free basis) are similar to those reported previously by Ruscitto et al. (2010a) for the same cones (where samples SM2 and EJYO2 correspond to Sand Mountain and Collier Cone, respectively). Inclusions from Collier Cone range from basaltic andesite to andesite in composition, with 53–59 wt.% SiO_2 and 3.3–6.1 wt.% MgO. Inclusions from Four-in-One and Sand Mountain have basaltic andesite (53–55 wt.% SiO_2, 5.5–6.2 wt.% MgO) and basalt (50–52 wt.% SiO_2, 4.9–6.1 wt.% MgO) compositions, respectively (Table 2). Melt inclusion compositions are similar to associated bulk tephra compositions (Figure 3a; Table 3). The melt inclusions display limited variability in ratios that are sensitive to boundary layer enrichment effects during formation (e.g., CaO/Al_2O_3, TiO_2/P_2O_5; Faure & Schiano, 2005; Kent, 2008; Johnson et al., 2010). The olivine-melt thermometer of Putirka et al. (2007) was used to calculate temperatures of melt inclusion formation and eruption from the restored and unrestored glass compositions, respectively. Average temperatures of eruption and formation are the same, within uncertainty of ~30–40 ºC, and are 1000 ±20 (1 s.d.), 1060 ±20, and 1070 ±30 ºC for Collier, Four-in-One, and Sand Mountain inclusions, respectively.

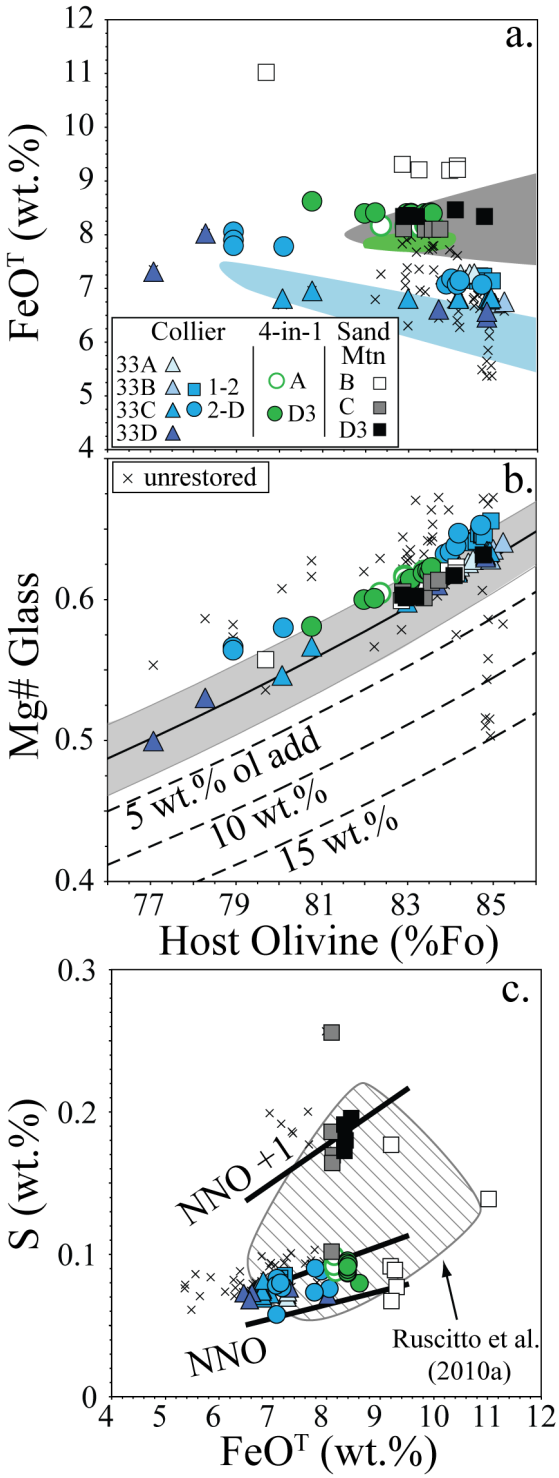

Figure 3. Olivine-hosted melt inclusion compositions from Collier, Four-in-One, and Sand Mountain tephra deposits reflect both Fe-loss resulting from Fe-Mg re-equilibration with host olivines (a) and post-entrapment crystallization of olivine during cooling (b) and have been restored to initial compositions following the method of Danyushevsky et al. (2000) (olivine-liquid Fe-Mg partitioning of Ford et al. 1983). Shaded fields in panel (a) encompass bulk tephra compositions (Collier: blue and Four-in-One: green) and bulk lava compositions (Sand Mountain: gray). Forsterite contents for the bulk samples were calculated at NNO and assuming a K_D=0.30. The solid line surrounded by the gray envelope in panel (b) is the calculated equilibrium line assuming Fe-Mg K_D=0.30 ±0.03 at NNO (Fe^{2+}/Fe^{Total} ~ 0.80). Dashed lines show approximate amounts of olivine crystallization required to bring inclusions back into equilibrium with host crystals and do not consider effects of Fe-loss by diffusive re-equilibration (see text). (c) Sulfur and FeO^T contents (both in wt.%) for restored and unrestored inclusions. Thick black lines show S solubility as a function of FeO^T at NNO, NNO +0.5 (not labeled), and NNO +1 calculated at 1050 °C using the models of Wallace & Carmichael (1992), Mavrogenes & O'Neill (1999), and Jugo (2010), as described in the text. Field with diagonal cross-hatching encompasses Central Oregon melt inclusions reported in Ruscitto et al. (2010a). 'X' symbols show unrestored inclusion compositions.

2.4.2. Volatile Contents in Melt Inclusions

Water contents in Collier Cone melt inclusions are the highest reported for the Central Oregon Cascades (up to 4.2 ±0.6 [1 s.d.] wt.% H_2O) (cf., Ruscitto et al., 2010a) and are similar to those found in high magnesian andesites and basaltic andesites from the Shasta region (Anderson, 1974; Ruscitto et al., 2010b). Maximum H_2O contents observed in Four-in-One and Sand Mountain melt inclusions are lower (3.1 ±0.2 and 3.2 ±0.4 wt.% H_2O, respectively). Maximum CO_2 values for all three cones range from ~1000–1300 ppm, with Collier Cone melt inclusions containing the highest values (Table 2, Figure 4). Dissolved sulfur and chlorine contents are similar to those found in other magmas from the Cascades and other arcs (Wallace, 2005; Ruscitto et al., 2010a).

Water and CO_2 in melt inclusions from Collier Cone and Four-in-One show limited variability, with only two inclusions that lack CO_2 (<50 ppm). Sand Mountain inclusions, however, display considerably more variability in both H_2O and CO_2, similar to patterns observed at Mexican cinder cones but lacking the range in H_2O at low CO_2 (Figure 4). Corresponding H_2O-CO_2 vapor saturation pressures were calculated using the Papale et al. (2006) algorithm. We prefer the Papale mixed H_2O-CO_2 solubility model over the commonly used VolatileCalc model (Newman & Lowenstern, 2002) because it is better suited for the high SiO_2 and CaO contents of the Central Oregon compositions (Moore, 2008). Trapping pressures calculated for the inclusions formed beneath Collier Cone (average ±1 s.d.: 172 ±39 MPa) and Four-in-One (147 ±37 MPa) are higher and more uniform than trapping pressures of 109 ±62 MPa calculated for Sand Mountain inclusions where pressures also extend to lower values (Table 2, Figure 4, Figure 5). Similar patterns are seen in dissolved S and Cl contents: Collier and Four-in-One inclusions show a restricted range in S and Cl contents while Sand Mountain inclusions show considerably more variability (Table 2, Figure 5).

Most of the melt inclusions studied here contain one or more vapor bubbles that likely formed by either differential thermal contraction between the melt and the host crystal during cooling or by inclusion rupture (and subsequent annealing, no cracks surrounding inclusions are evident). Therefore, reported dissolved CO_2 contents represent minima as much of the initial dissolved CO_2 has preferentially partitioned into the vapor bubbles (Anderson & Brown, 1993). Post-entrapment CO_2-losses are greatest in H_2O-

poor inclusions (see vapor isopleths in Figure 4) and these losses could result in the underestimation of vapor-saturation pressures by up to ~100 MPa (Johnson et al., 2010).

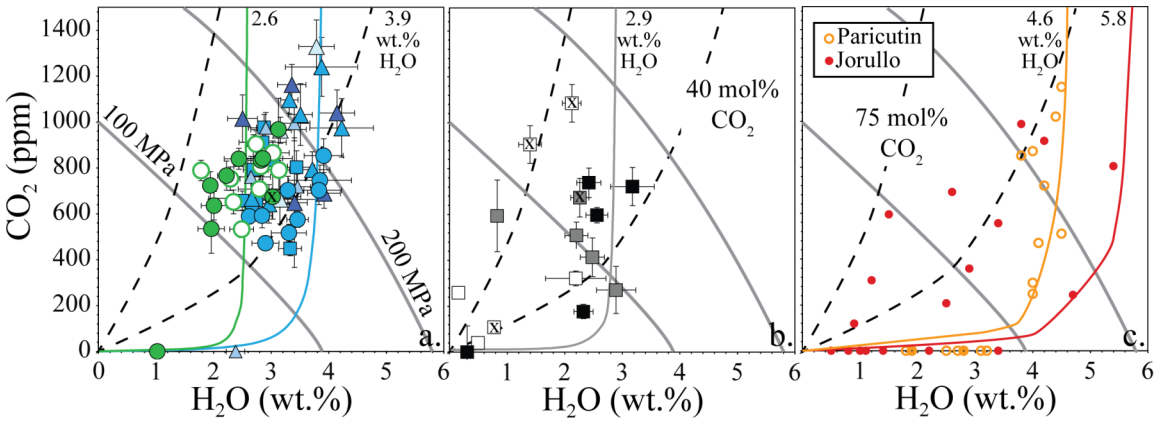

Figure 4. Restored H_2O and CO_2 contents of melt inclusions (1 s.d. error bars) from Central Oregon (a: Collier and Four-in-One, b: Sand Mountain). Central Mexico (c: Jorullo and Paricutin) data sets of Luhr (2001), Johnson et al., (2008) and Johnson et al., (2009) are shown for comparison. Symbols for Central Oregon inclusions are as in Figure 3. Solid gray and dashed black lines are isobars (100 and 200 MPa) and vapor isopleths (40 and 75 mol% CO_2), respectively, calculated for the average Central Oregon melt inclusion composition at 1050 °C using the model of Papale et al. (2006). Isothermal closed-system degassing paths (Papale model) are also shown with initial H_2O contents (all models start at 3000 ppm CO_2). Xenocrystic inclusions from Sand Mountain tephra are identified with an 'X'.

2.4.3. Relationships Between Composition and Stratigraphic Position

Melt inclusion compositions, together with associated bulk tephra compositions, are shown in stratigraphic order in Figure 5. The range in host olivine compositions for Collier Cone decreases up-section. Additionally, more evolved (lower %Fo hosts, higher K_2O) inclusions are found only in the lowest sections of the Collier Cone deposit. This transition is abrupt in the Collier Cone sequence and occurs at the boundary between inferred Strombolian and Violent Strombolian deposits (Section 2.2.1.2.; Figure 2). A reversed trend is observed in the Sand Mountain deposit, where variability in host olivine compositions and K_2O contents both increase up-section (Figure 5a,b). The Four-in-One olivine compositions and inclusion K_2O contents remain relatively constant throughout the tephra section. H_2O-CO_2 vapor saturation pressures are elevated and relatively constant (~100–250 MPa) throughout the stratigraphic sequences of both Collier Cone

and Four-in-One. Pressures calculated for Sand Mountain inclusions are more variable and show a decrease in the average pressure of inclusions closer to the top of the section (Figure 5c). As mentioned above, Collier Cone and Four-in-One inclusions display a restricted range in S contents, potentially reflecting sulfide-saturated conditions. Dissolved chlorine contents in melt inclusions from Collier Cone and Four-in-One also remain relatively constant throughout the stratigraphic sections. Sand Mountain inclusions, however, show increasing variability and slight decreases in average S and Cl contents (Figure 5d, e).

2.5. Discussion

2.5.1. Compositional Evolution of Explosive Eruption Products

Systematic variations in olivine compositions and incompatible element concentrations (e.g., K_2O, TiO_2, P_2O_5) in the tephra sections from Collier Cone and Four-in-One are not consistent with the fractional crystallization patterns observed at either Paricutin or Jorullo (Figure 5). Melt inclusions and bulk tephra from the Mexican deposits reflect increased fractional crystallization (increasing incompatible elements, decreasing %Fo) and extensive degassing as the eruptions progressed (Luhr, 2001; Johnson et al., 2008; Erlund et al., 2009). The inclusions and tephra deposits at Collier Cone and Four-in-One, however, record only limited fractional crystallization, with a maximum of ~22 wt.% and 11 wt.% for Collier Cone and Four-in-One, respectively (cf., ~40 wt.% at Jorullo and Paricutin). In addition, the most evolved tephra and melt inclusion compositions were erupted earliest in the eruption sequence at Collier Cone; this is in contrast to the Collier Cone lava flow, where the final erupted unit is a dacite (Schick, 1994). These observations suggest that little compositional evolution occurred over the course of explosive activity and that most of the fractional crystallization and crustal assimilation must have preceded each eruption. Compositional variations observed in Sand Mountain melt inclusions also reflect only modest amounts of crystallization (maximum ~11wt.%) when compared to Jorullo or Paricutin. However, unlike the Collier Cone and Four-in-One eruptions, the observed variations appear to

show that increasingly fractionated melt compositions were erupted as explosive activity progressed (Figure 5).

The restricted ranges in H_2O and CO_2 contents observed within melt inclusions from Collier Cone and Four-in-One olivines suggest that the inclusions formed at similar conditions and experienced only limited amounts of degassing prior to eruption. Alternatively, diffusive re-equilibration of H_2O contents between melt inclusions and the host magma may have homogenized an initially more varied population of inclusions if the system became stagnant in the upper crust prior to eruption (Massare et al., 2002; Portnyagin et al., 2008). Either scenario is compatible with the relatively constant S and Cl contents of the melt inclusions because these volatiles tend to exsolve more at lower pressures (<100–140 MPa; Spilliaert et al., 2006; Johnson et al., 2010). The melt inclusions record stalling in the upper crust in either scenario and we emphasize that measured H_2O contents are minimum estimates for the magmas. In contrast, H_2O and CO_2 variability in the Sand Mountain data reflects inclusion formation over a wide range of pressures (particularly at low pressures) and is more similar to patterns observed in cinder cones from Mexico (Figure 4b,c).. The H_2O-CO_2 systematics observed in inclusions from Paricutin and Jorullo are attributed to inclusion formation during ascent-driven degassing and simultaneous gas fluxing of CO_2-rich vapor from below (Rust et al., 2004; Johnson et al., 2008; 2010). The Sand Mountain data may also be consistent with such a process and would require fluxing with a ≥75 mol% CO_2 vapor. However, when identified xenocrysts are excluded (Section 2.5.2), a closed-system degassing path to ~100 MPa is able to account for the majority of Sand Mountain inclusion data (Figure 4b).

Compositional similarities between erupted and cumulate olivines in xenoliths suggest that a single stage of olivine crystallization at depth preceded each of the eruptions and that all of the erupted olivines and melt inclusions are sampled from these initial, relatively undegassed, populations. Limited amounts of fractional crystallization and degassing are also consistent with the relatively short duration of explosive activity inferred from the deposits at Collier Cone and Four-in-One compared to Paricutin (~9 years) and Jorullo (~15 years). At Sand Mountain, however, the observed variations indicate that increasingly degassed (and slightly more fractionated) melt compositions

were erupted as explosive activity progressed (Figure 5). These variations are consistent with olivine crystallization (and melt inclusion formation) over a range of pressures and suggest that eruption at Sand Mountain was more similar to (but probably shorter than) the eruptions observed in Mexico. Relationships between crystallization and degassing for the Central Oregon eruptions will be explored further below (Section 2.5.4)

2.5.2. Relationships Between Explosive and Effusive Products

Bulk lava compositions (shaded fields) are compared with restored Central Oregon melt inclusion compositions in Figure 6; eruption products from Jorullo and Paricutin are shown for comparison, as are the bulk compositions of xenoliths found in Collier and Four-in-One lavas (Schick, 1994). Bulk mixing lines link the average silicic xenolith composition and the average melt inclusion composition from Collier Cone (Figure 6a, b) and Sand Mountain (Figure 6c, d). The eruptions have been grouped on the basis of crustal assimilation histories for clarity: Collier Cone, Four-in-One, and Paricutin lavas show extensive interaction with silicic crust (Figure 6a, b) whereas Sand Mountain and Jorullo lavas are less influenced by silicic crust (Figure 6c, d). In all cases, melt inclusions (and tephras, although not shown for clarity; see Table 3) define the primitive end of the compositional spectrum (low SiO_2, low incompatible element abundances). The melt inclusions from Collier Cone and Four-in-One also show a considerably more restricted range in incompatible element ratios when compared with associated lavas.

Bulk lava compositions from Collier Cone and Four-in-One trend towards the average composition of silicic xenoliths, similar to the pattern observed at Paricutin. Melt inclusions from these eruptions show trends consistent with fractional crystallization and

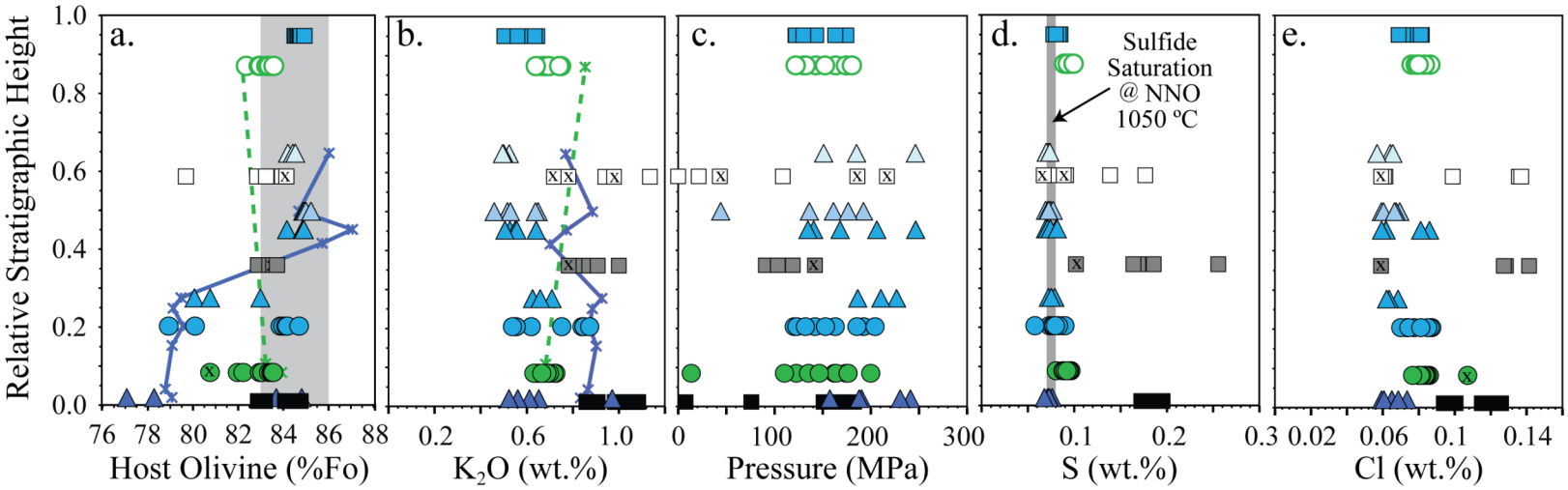

Figure 5. Variations of melt inclusion, bulk tephra, and host olivine compositions with relative stratigraphic height for the three studied eruptions from Central Oregon (symbols as in Figure 3). Asterisk symbols connected by solid (Collier) or dashed (Four-in-One) lines in panels (a) and (b) are bulk tephra compositions. Forsterite contents for the bulk samples were calculated at NNO and assuming a Fe-Mg K_D=0.30. Shaded region in panel (a) encompasses the compositional range of large (>1 mm) olivines in mafic xenoliths found in Collier lavas (Schick, 1994). Sulfide saturation line in panel (d) was calculated using the sulfide solubility model of Wallace & Carmichael (1992) modified to include the temperature dependence of Mavrogenes & O'Neill (1999).

trend directly away from the mafic xenoliths (Figure 6a). Several Collier Cone melt inclusions appear to follow the bulk lava trend. However, the crustal assimilation history recorded in Collier melt inclusions is much less extensive (<5%) than in the Paricutin inclusions (>15%) (Figure 6a,b; Erlund et al., 2009).

Bulk lavas from Sand Mountain and Jorullo are more similar to associated melt inclusion compositions (Figure 6c, d) and do not trend towards the silicic xenoliths. A potential fractional crystallization relationship (trending away from mafic cumulate compositions) is still observed, but large variations in TiO_2/K_2O ratios (i.e., >2 between 50 and 55 wt.% SiO_2) of the bulk lavas may indicate that additional processes such as magma mixing, xenocryst entrainment, and/or assimilation of older mafic crust may be responsible for observed variations. Indeed, three (out of 15) Sand Mountain melt inclusions appear to be derived from a separate batch of magma based on high TiO_2 (>1.45 wt.%) and TiO_2/K_2O (>1.90) values and considerably lower S and Cl contents. Additionally, an hourglass inclusion within one of the xenocrystic olivines appears to be partially hybridized with the lower TiO_2 entraining magma (i.e., the reentrant inclusion retains high TiO_2 contents but has lower overall TiO_2/K_2O values) (Figure 5, Figure 6; Table 2). An additional xenocrystic inclusion is identified from the base of the Four-in-One deposit (FO0803-D3-b in Table 2; Figure 5). This inclusion is hosted within a more evolved olivine (host %Fo = 80), but contains significantly lower TiO_2 and higher Cl (0.99 and 0.107 wt.%, respectively) than the other Four-in-One inclusions (>1.10 and <0.086 wt.%, respectively), precluding a fractional crystallization relationship (Section 2.5.4). Xenocrystic inclusions are shown in subsequent figures (marked by an 'X'), but are not included in discussions regarding conditions of formation (Section 2.5.3) or degassing (Section 2.5.4).

The silicic xenoliths found in Collier Cone and Four-in-One lavas are similar to the nearby Obsidian Cliffs and other recent rhyolitic eruption products surrounding Middle and South Sisters (Sherrod et al., 2004). At the other end of the compositional spectrum, melt inclusions from Four-in-One are nearly identical to the depleted, low-K_2O basaltic andesites erupted throughout the history of North Sister (~55–400+ ka; Schmidt & Grunder, 2009). The primitive melt inclusions from Collier Cone are even more depleted in K_2O and TiO_2 than North Sister lavas and represent either a less-fractionated

North Sister basaltic andesite or a distinct, more depleted magma batch. Neither set of melt inclusions appears related to the K_2O- and TiO_2-enriched lavas erupted at nearby Little Brother (50–150 ka) or the more recent Mathieu Lakes Fissure eruptions (14–75 ka) (Schmidt & Grunder, 2009). However, the Sand Mountain melt inclusions (cf., high-Sr basalts in Ruscitto et al., 2010a) appear similar to the high-K_2O lavas erupted at Little Brother.

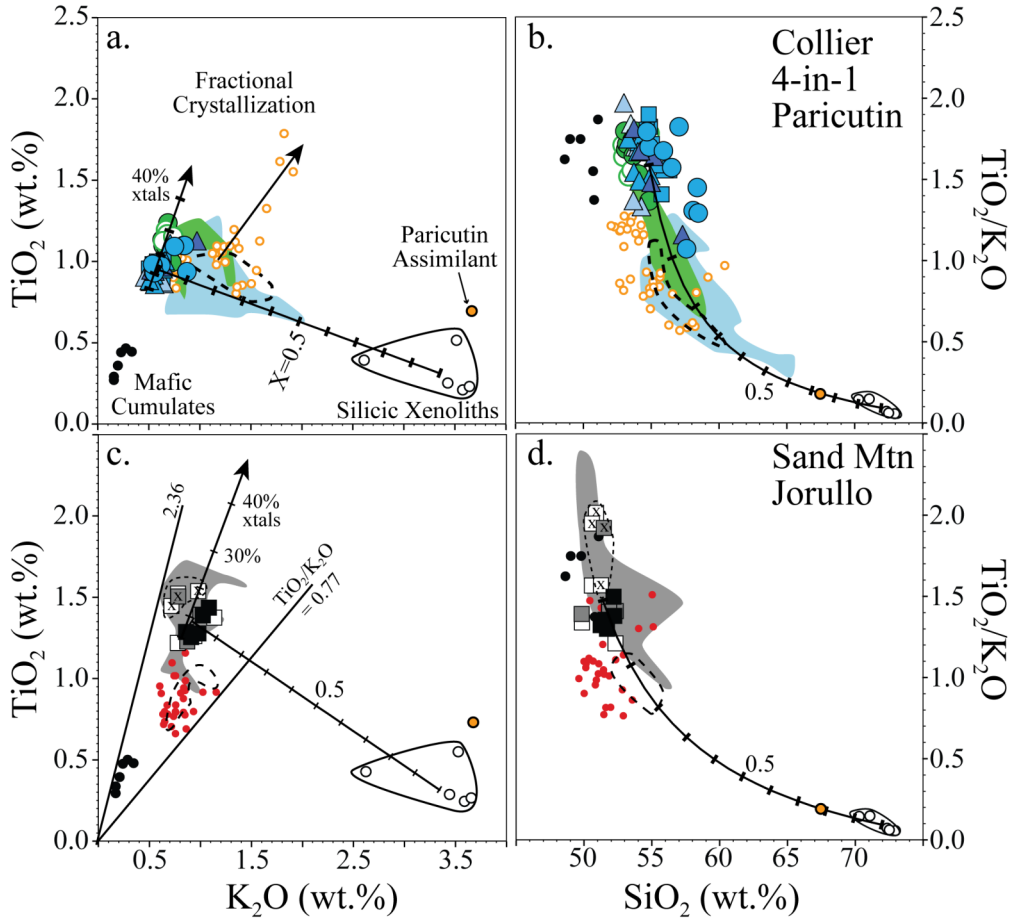

Figure 6. TiO_2, K_2O, and SiO_2 contents of restored melt inclusions (symbols as in Figure 3,Figure **4**), bulk lavas (shaded fields for Central Oregon, dashed fields for Paricutin and Jorullo), and bulk xenolith compositions from Collier Cone and Four-in-One lavas (Schick, 1994). The average composition of the basement surrounding Paricutin is also shown in each panel (McBirney et al., 1987). Lines with arrows show fractional crystallization paths (10 wt.% ticks, TiO_2 and K_2O assumed to be perfectly incompatible). Bulk mixing lines (10% ticks) are also shown linking the average melt inclusion compositions (Collier Cone in a, b; Sand Mountain in c, d) with the average silicic xenolith composition.

2.5.3. Inferred Pre-eruptive Conditions

Compositional variations in melt inclusions from the Collier Cone, Four-in-One, and Sand Mountain tephras suggest fractional crystallization was more important than crustal assimilation (Figure 6). Melt inclusion compositions and host olivines are too evolved to be considered primitive (e.g., MgO <6.5 wt.%; %Fo <87) and the magmas likely have experienced multiphase crystal fractionation prior to melt inclusion formation. Stable phases (other than olivine) at conditions of formation inferred from melt inclusions are shown in Figure 7. The melt inclusions constrain maximum H_2O contents to ~4 wt.%, probably in the presence of a mixed (H_2O+CO_2) vapor phase, and indicate that H_2O-saturated phase diagrams determined experimentally (e.g., Moore & Carmichael, 1998) are not appropriate at the pressures relevant to melt inclusion formation in our samples. The phase diagram in Figure 7 was constructed using MELTS (Ghiorso & Sack, 1995; Asimow & Ghiorso, 1998) and pMELTS (Ghiorso et al., 2002) for a basaltic andesite composition with 4 wt.% H_2O. At pressures below 100 MPa, the phase diagram presented in Figure 7 is similar to the H_2O-saturated phase equilibria for basaltic andesite experimentally determined by Moore & Carmichael (1998). At higher pressures, the magma becomes H_2O-undersaturated and the calculated liquidus shifts to higher temperatures compared to the experimentally determined H_2O-saturated liquidus, although stable phases appear in roughly the same order. Dashed gray lines demonstrate strong pressure (and weak temperature) dependence on H_2O solubility in a magma saturated with a 50 mol.% CO_2 vapor phase (cf., Figure 4). Hornblende is not stable at the conditions (pressure, temperature, or H_2O-contents) inferred from the Central Oregon melt inclusions (cf., Moore & Carmichael, 1998; Johnson et al., 2008) or even at higher pressure (~1.0–1.2 GPa) appropriate for the lower crust in this region (Mercer & Johnston, 2008). The calculated phase relations indicate that olivine + spinel ± clinopyroxene ± plagioclase were the primary crystallizing phases controlling compositional evolution during melt inclusion formation, consistent with the phases present in mafic xenoliths from the Collier lava flows (black circles in Figure 6; Schick, 1994).

2.5.4. Degassing and Crystallization

Volatile exsolution and crystallization are inherently related because of the strong liquidus temperature depression induced by the presence of dissolved H_2O. Ascending magmas begin to crystallize during decompression, as heat is lost to the surrounding country rock and as dissolved volatiles exsolve into a free vapor phase. At pressures below H_2O-saturation (or in mixed [e.g., $H_2O + CO_2$] vapor-saturated systems) degassing

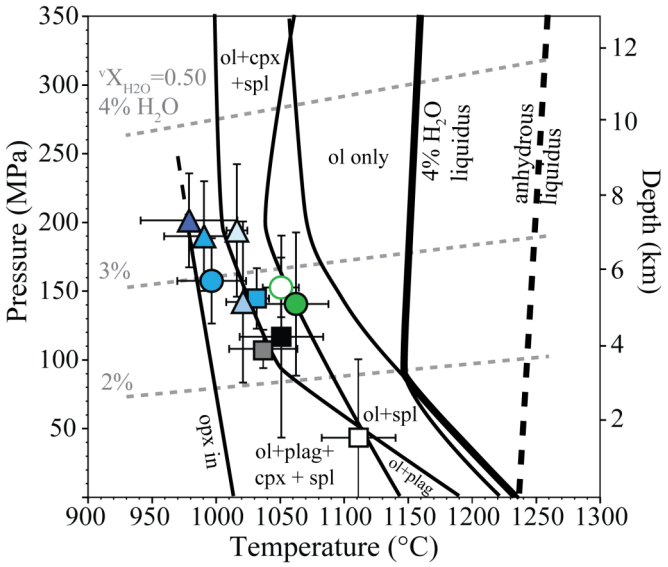

Figure 7. Calculated pressure-temperature conditions for the average melt inclusion composition (±1 s.d.) from each sample determined using the Papale et al. (2006) H_2O-CO_2 vapor saturation pressures and the Putirka et al. (2007) olivine-liquid temperatures. The phase diagram is for a primitive Cascades basaltic andesite with 4 wt.% H_2O and was constructed using MELTS (Ghiorso & Sack, 1995; Asimow & Ghiorso, 1998) and pMELTS (Ghiorso et al., 2002). Thick solid and dashed lines represent the wet and dry liquidi, respectively. Thin black lines indicate the appearance of solid phases. Gray dashed lines indicate H_2O saturation in the magma composition at given P-T conditions and was calculated assuming equilibrium with a vapor containing 50 mol.% H_2O. Depths along the right axis were calculated assuming a constant crustal density of 2800 kg/m^3.

of excess H_2O from the melt increases the liquidus temperature and induces crystallization (e.g., Sisson & Layne, 1993). Fluxing of magma with a CO_2-rich vapor, even at H_2O under-saturated conditions, further enhances crystallization as H_2O is removed from the melt and added to the vapor phase; this process can result in crystallization even in the absence of a temperature decrease (Spilliaert et al., 2006;

Johnson et al., 2008; 2010; Blundy et al., 2010). Many previous studies have established degassing patterns and calculated vapor-melt partition coefficients using observed relationships between indices of fractional crystallization and volatile concentrations (Sisson & Layne, 1993; Blundy & Cashman, 2005; 2008; Atlas et al., 2006; Wade et al., 2006; Benjamin et al., 2007; Spilliaert et al., 2006; Vigouroux et al., 2008; Johnson et al., 2008; 2010). In this section, we use a similar approach to examine degassing of H_2O, S and Cl as recorded in melt inclusions from Collier Cone, Four-in-One and Sand Mountain.

Melt components not incorporated into crystallizing minerals (i.e., $^{solid\text{-}melt}D \sim 0$) become increasingly concentrated in the residual melt as crystallization proceeds and are referred to as incompatible. K_2O is commonly used as an index of crystal fractionation in mafic melts because it is not incorporated into the most commonly crystallizing minerals in significant amounts (i.e., olivine, plagioclase, spinel, pyroxene). For the Central Oregon magmas, however, crustal assimilation involved a high K_2O contaminant (Figure 6), thus suggesting that K_2O cannot be used for simple fractionation calculations. Although many melt inclusions appear unaffected by contamination, the addition of small amounts of assimilant (< 5%) would increase K_2O contents by ~20%. For this reason, we use TiO_2 as an index of fractional crystallization for the Cascades magmas (5% assimilation would decrease TiO_2 contents by ~3%, only slightly above 2 s.e. analytical uncertainties). Additionally, bulk partition coefficients for TiO_2 are <0.06 in amphibole-free assemblages calculated from the experimental run products of Moore & Carmichael (1998).

Volatiles (H_2O, CO_2, S, and Cl) also tend to be incompatible in most mafic minerals, therefore volatile increases caused by crystallization can obscure or hide losses caused by degassing. To address this problem, we have normalized the volatile contents of the studied melt inclusions to TiO_2 (Figure 8) to emphasize degassing trends; we include the Jorullo and Paricutin datasets for comparison. Volatile-undersaturated crystallization would produce a horizontal trend (vector i in Figure 8a) as the volatile and TiO_2 both increase. Pure degassing would produce a vertical trend and no change in TiO_2 (vector ii in Figure 8a). Simultaneous degassing and crystallization would produce an intermediate path with a slope dependent on how strongly the volatile is partitioned into

the vapor phase. The volatile/TiO_2 ratios shown in Figure 8 indicate that the Collier Cone magma had degassed ~20-35%, 14-27%, and 10-27% of its initial H_2O, S, and Cl contents, respectively. Inclusions from Four-in-One indicate smaller extents of degassing (~30%, 6%, and 5% of initial H_2O, S, and Cl, respectively) while those from Sand Mountain, particularly in the latest erupted tephra, indicate greater extents of H_2O degassing (35-70%) but similar extents of S (3-27%) and Cl (5-21%) degassing to the Collier data. Both Paricutin and Jorullo display greater extents of degassing (~70–80% initial S and up to 53% initial Cl during crystallization) than any of the Central Oregon datasets (Johnson et al., 2010).

We use the melt inclusion data to model the vapor-melt partitioning of S and Cl during crystallization after the method outlined in Johnson et al. (2010) for three equilibrium degassing scenarios: (1) open-system degassing (i.e., Rayleigh fractionation), where the exsolved vapor immediately leaves the system, (2) closed system degassing with no initial vapor and all exsolved vapor remains in equilibrium with the degassing melt, and (3) closed system degassing in the presence of an initial vapor phase (1%) assumed to contain no S or Cl. This assumption is appropriate for deep (>100–140 MPa) conditions where CO_2 and H_2O are the primary degassing volatiles (Spilliaert et al., 2006; Johnson et al., 2010). Additionally, the equations describing the latter degassing scenario are appropriate for describing an open system fluxed with a fixed proportion of vapor (Johnson et al., 2010). Calculated vapor-melt D_S and D_{Cl} values for each model are listed in Table 2.

Vapor-melt D-values greater than one indicate preferential partitioning of the volatile into the vapor phase while D-values less than one indicate preferential partitioning into the melt phase. A D-value of zero would indicate that the volatile is not degassing (negative D-values indicate problems with the assumed initial volatile concentrations). For a given volatile, vapor-melt D-values are approximately the same for open (1) and closed (2) system degassing scenarios (Table 2). D-values are ~40–50% smaller for closed system degassing containing an initial 1% vapor because of the order of magnitude increase in vapor present (i.e., smaller D-values are required to add the same amount of S and Cl to larger proportions of vapor).

The H_2O-CO_2 systematics of the melt inclusion compositions from Collier Cone and Four-in-One do not support an open-system fluxing model. Rather they reflect limited degassing and crystallization at depth, potentially in the presence of a trapped CO_2-rich vapor. Sand Mountain melt inclusion compositions, however, show degassing and crystallization systematics more similar to those observed at Paricutin and Jorullo and are consistent with either a closed-system model or an open system, vapor fluxing model. Our preferred degassing model is the third scenario (closed system with 1% initial vapor) because: (1) the equations used are appropriate for both closed systems containing an exsolved $H_2O + CO_2$ vapor phase (i.e., Collier Cone and Four-in-One) and vapor-fluxed systems, (2) these values permit direct comparison to partition coefficients calculated for vapor-fluxed systems in Mexico (Johnson et al., 2010), and (3) calculated D_{Cl} values are similar to those experimentally determined by Aletti et al. (2009).

Figure 9 shows the vapor-melt partition coefficients for S and Cl calculated for the Central Oregon inclusions plotted against their H_2O-CO_2 vapor saturation pressures. Partition coefficients calculated from Jorullo and Paricutin melt inclusions are also shown and are generally in agreement with the values obtained from Central Oregon at similar pressures (Johnson et al., 2010). Central Oregon D_S values are in agreement with those calculated by Spilliaert et al. (2006) for high pressure inclusions from Mt. Etna (D_S = 0–60 with higher values at low (<100 MPa) pressures) and are also in agreement with those expected using the S solubility model of Scaillet & Pichavant (2005). Sulfur partition coefficients determined for Central Oregon and Mexico vents, however, are considerably lower than those determined for many large, long-lived volcanic centers (D_S Fuego: 34; Sisson & Layne, 1993; D_S Arenal and Irazu: 70–110; Wade et al. 2006; Benjamin et al. 2007). The D_{Cl} values calculated for the Central Oregon vents are also consistent with the experimental fluid-melt partitioning of Aletti et al. (2009) and the calculated D_{Cl} values from Fuego and Arenal (D_{Cl}=2.8–6; Sisson & Layne, 1993; Wade et al., 2006), but are generally higher than the Etna values (Etna D_{Cl} <1; Spilliaert et al., 2006).

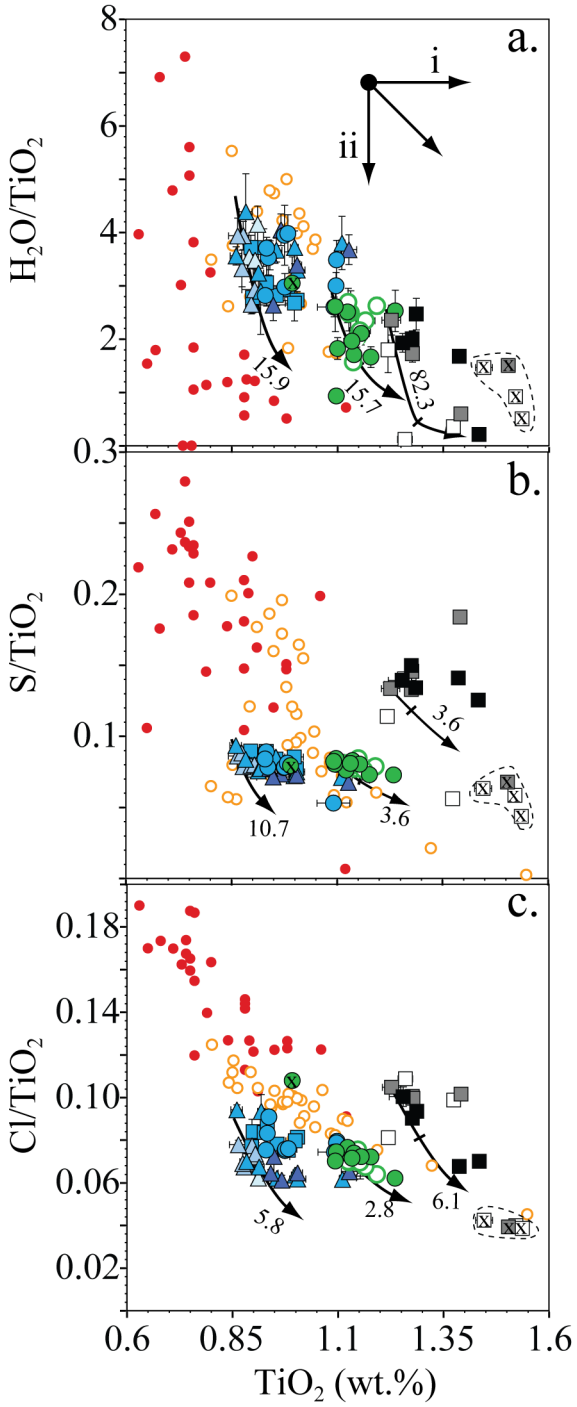

Figure 8. Volatile/TiO_2 vs. TiO_2 for restored melt inclusion compositions from Central Oregon with Mexican inclusions for comparison (symbols as in Figure 3, Figure **4**). Crystal fractionation paths (batch model showing 10–15 wt.% total crystallization, tick at 5 wt.%) are shown using the average vapor-melt partitioning values (shown) determined using the closed system + 1% initial vapor model (see text). Paths i and ii, illustrated in panel (a), show hypothetical vapor-undersaturated crystallization (no degassing) and degassing-only (no crystallization) curves, respectively.

A major discrepancy is apparent between high calculated D_S values for many of the large, long-lived volcanic centers (Arenal, Irazu, and Fuego) and the lower values for the cinder cone eruptions. This could be related to timescales of degassing resulting from differences in storage conditions or magma migration patterns (e.g., isolated magma batches versus well-mixed magma chambers). Slower magmatic diffusivities of S, Cl, and CO_2 compared to H_2O (e.g., Freda et al., 2005) may inhibit migration of these components into a vapor phase and lead to supersaturated, nonequilibrium volatile contents in the degassing magma (e.g., non-equilibrium degassing, Gonnermann & Manga, 2005). Non-equilibrium degassing recorded by melt inclusions could therefore lead to the lower apparent vapor-melt partition coefficients. Non-equilibrium conditions would prevail when the timescales of bubble growth are sufficiently fast compared to those of diffusion (Gonnermann & Mangan, 2005). Therefore, a well-mixed, long-lived magma system may be expected to achieve equilibrium vapor-melt partitioning while a short-lived isolated magma batch experiencing rapid ascent and a nucleation event may erupt too quickly to fully equilibrate with a vapor phase. The diffusivities of magmatic volatile components (particularly S and Cl), however, are not yet sufficiently constrained to model these scenarios and significantly more experimental and theoretical work needs to be conducted before such a hypothesis becomes testable.

2.5.5. Implications for Eruption Styles in Central Oregon

Melt inclusions are important geochemical tools used to constrain pre-eruptive magma storage conditions and evolution of the magma feeder system over the course of an eruption (e.g., Johnson et al., 2008; Pioli et al., 2008; Erlund et al., 2009). The eruption processes inferred from our melt inclusion data are illustrated schematically in Figure 10. The Sand Mountain eruption was a large (~1km^3), potentially long-lived event with olivine-hosted melt inclusions recording degassing over a range of pressures, particularly at shallow levels ≤ 4–5 km depth (Figure 10a).

The eruptions at Collier and Four-in-One were smaller volume (<<1 km^3) and shorter-lived events. The melt inclusions reflect deeper formation (~5–8 km) with limited extents of degassing and crystallization. The substantial crustal assimilation

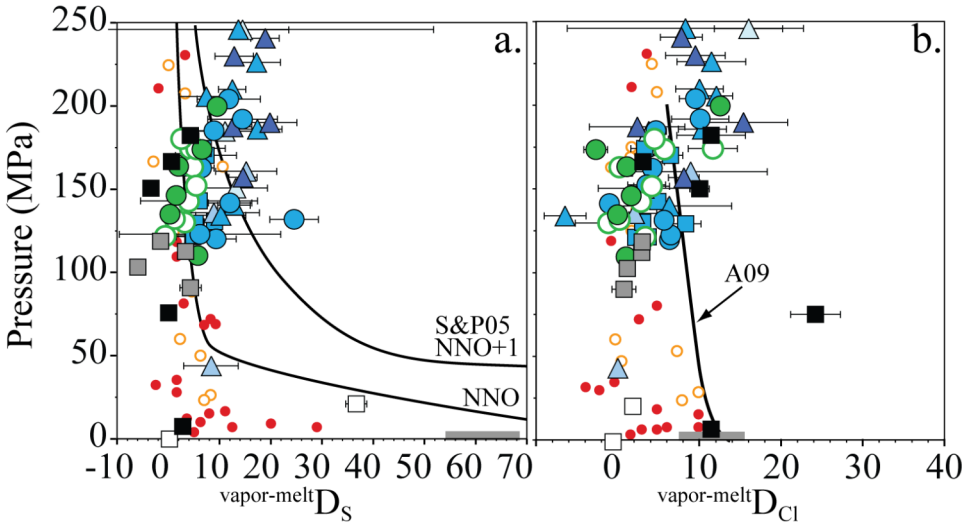

Figure 9. Calculated S (panel a) and Cl (panel b) vapor-melt partition coefficients for Central Oregon melt inclusions (closed system + 1% initial vapor; see text for details) plotted against H_2O–CO_2 vapor saturation pressures determined using the Papale et al. (2006) model. D-values (calculated using K_2O rather than TiO_2) from the Paricutin and Jorullo eruptions (Johnson et al., 2010) are shown for comparison (symbols as before. Curves in panel (a) illustrate the pressure dependence of S partitioning for a basaltic melt at NNO and NNO +1 and 1150 °C calculated from the model of Scaillet & Pichavant (2005). Curve in panel (b) is drawn through experimental vapor-melt partitioning data at NNO and 1200–1260 °C for Cl from Aletti et al. (2009).

recorded in the lava flows is not apparent in the melt inclusions and must have occurred after melt inclusion formation. We envision that all of these processes took place in a sill-like complex within the middle to upper crust prior to eruption (Figure 10b). While it is unclear why these magma batches stalled in the upper crust, Figure 10 presents two alternate scenarios illustrating potential eruption mechanisms. Both scenarios require a period of cooling, crystallization and degassing (to form the melt inclusions sampled at the surface) as magma closest to the intrusion margins assimilates nearby country rock. After some triggering event (e.g., extension-related faulting, input of new magma batch), the volatile-rich, less fractionated and less viscous magma erupts at the surface, carrying with it some entrained, more evolved components. This initial explosive activity primarily produces the cinder cone and associated tephra blanket along with some primitive lava flows. As the eruption proceeds, explosive activity wanes and more fractionated and degassed material is extruded as lava (cf., McBirney et al., 1987; Schick, 1994; Erlund et al., 2009). The very small (~0.005 km^3) fissure eruption at Four-in-One

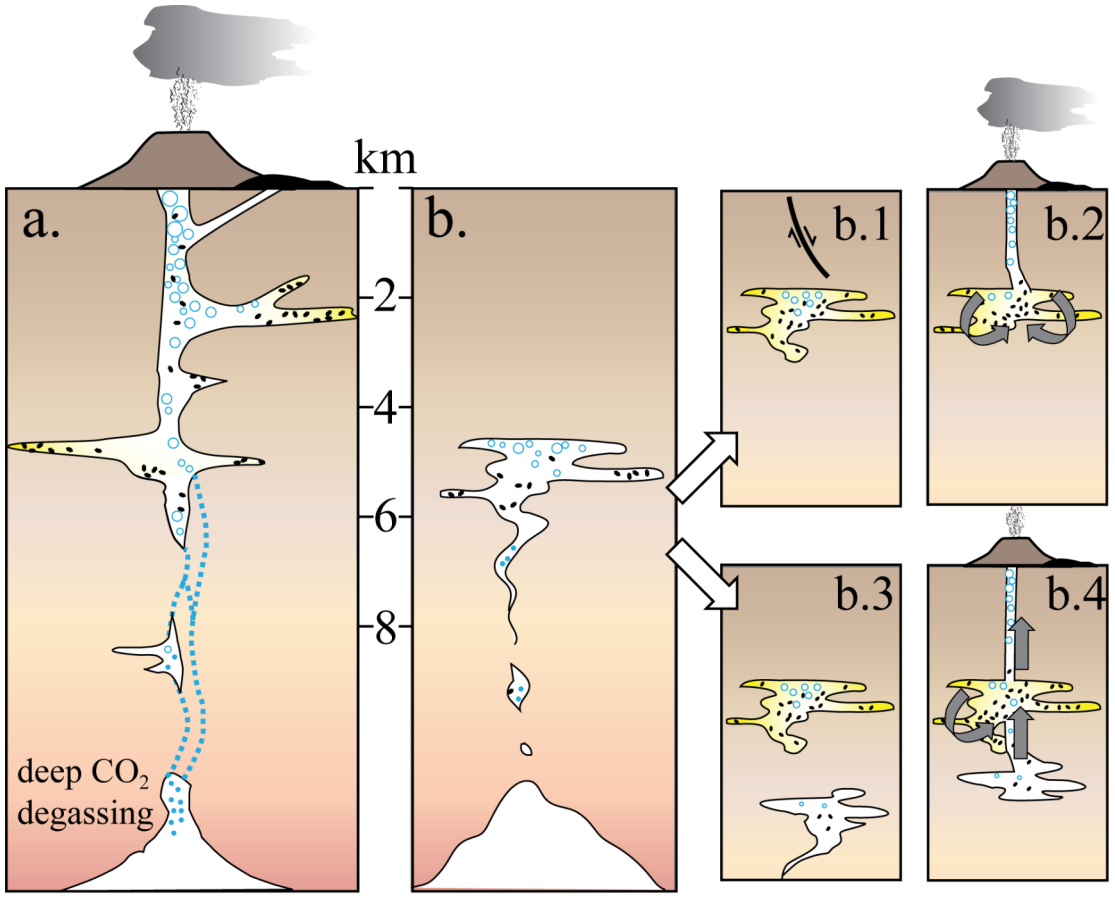

Figure 10. Schematic cartoons illustrating the inferred eruption processes for Sand Mountain (a) and Collier Cone/Four-in-One (b) as described in the text. In both panels (a) and (b), magma is injected from the mantle or lower crust. Panel (a) illustrates open-system fluxing of a shallow magma storage region by deeply derived CO_2-rich vapor (blue dashed lines); crystallization and melt inclusion formation occurs over a range of depths. Panel (b) illustrates a batch of magma stalling in the upper crust. The isolated batch of magma begins to cool, crystallize and degas as it assimilates surrounding wallrock (yellow shading). Panels (b.1 & b.2) and (b.3 & b.4) represent two eruption scenarios: an earthquake trigger (b.1) or a magma injection trigger (b.3). Depths are constrained by melt inclusion H_2O-CO_2 pressures assuming a constant density of 2800 kg/m^3.

may have been triggered by extension-related faulting facilitating the escape of magma from an over-pressurized sill (Figure 10b.1,b.2). Such a mechanism could have also triggered the larger eruption (~0.05 km^3) at Collier Cone. Alternatively, an ascending batch of more primitive magma may have burst through an older sill of degassing crystalline mush, entraining both silicic country rock xenoliths and mafic cumulates as it erupted at the surface (Figure 10b.3, b.4). Lack of low pressure inclusions at Collier Cone and Four-in-One suggests that the development of shallow storage reservoirs was not significant beneath these vents.

The shallower pressures recorded by Sand Mountain and the Mexican melt inclusions probably reflect the development of a multi-tiered magma supply system with a shallow magma storage region (e.g., Erlund et al., 2009). Development of such a system could be related to longer durations of explosive activity and/or larger erupted volumes inferred from Sand Mountain tephra deposits compared to the smaller, shorter-lived eruptions at Collier and Four-in-One. We note that the late-stage melt inclusions from Paricutin and Jorullo record considerably more low pressure crystallization than those from Sand Mountain and probably reflect either a more extensive shallow storage system and/or longer eruption durations (Figure 4b, c). Additionally, the H_2O-CO_2 systematics of Sand Mountain inclusions do not exhibit clear patterns interpreted to reflect extensive CO_2-rich vapor fluxing like those inferred from Paricutin and Jorullo melt inclusions (Figure 10a). This could potentially reflect a difference in magma supply to the lower crust from the mantle source (i.e., more magma supply beneath Mexico and more abundant to degassing in the lower crust).

Eruptions at Collier Cone and Four-in-One were influenced by their proximity to a large stratovolcano (North Sister). Melt inclusion compositions from the Collier Cone and Four-in-One eruptions are similar to or more primitive than the basaltic andesite lavas that had erupted from the (now extinct) North Sister edifice up to ~50 ka (Schmidt & Grunder, 2009). Therefore, the magmas are not simply remobilized remnants of a cooling pluton (as they would be more fractionated) and must be derived from the same source in the lower crust or mantle (Conrey et al., 1997; Ruscitto et al., 2010a). In addition, genetically distinct magmas were also erupted both during (i.e., Little Brother, Mathieu Lakes East Fissure) and after the period of active volcanism at North Sister (i.e.

Mathieu Lakes Central and West Fissures ~3–20 ka) (Schmidt & Grunder, 2009). The presence of these other magmas indicates (1) batches of distinct magma could bypass the main North Sister magma source without homogenizing, and (2) small batches of magma are still being supplied from the mantle or lower crust, although the North Sister edifice is now extinct.

2.6. Summary and Conclusions

We have examined and mapped three tephra blankets produced during the explosive phases of recent mafic cinder cone eruptions in the Central Oregon High Cascades. Inferred explosive activity ranges from Strombolian for the Four-in-One eruption to Violent Strombolian for the Collier and Sand Mountain eruptions. Olivine-hosted melt inclusions from stratigraphically-controlled tephra samples have been evaluated for post-entrapment modification and restored to initial compositions using the method of Danyushevsky et al. (2000). Restored inclusions are volatile-rich (maximum 3–4 wt.% H_2O, 1000–1300 ppm max CO_2, 700–1900 ppm S, and 850–1400 ppm Cl) and represent the most primitive compositions associated with each eruption, relatively unaffected by crustal assimilation processes. Maximum volatile contents for the Central Oregon eruptions are similar to (or less than) volatile contents from the historic mafic eruptions of Jorullo and Paricutin, Mexico (Luhr, 2001; Erlund et al., 2009; Johnson et al., 2008; 2009; 2010). Degassing patterns and inferred melt inclusion formation pressures from Sand Mountain are consistent with either closed system degassing model or a gas-fluxing model, where a shallow magma system was flushed by a CO_2-rich vapor derived from deeper in the system. Collier and Four-in-One inclusions, however, reflect limited amounts of degassing and suggest formation in isolated middle to upper crustal magma chambers/sills prior to eruption. Differences in magma migration and storage patterns between Collier and Four-in-One versus Sand Mountain and the Mexican cones may be related to magma volumes and eruption durations or proximity to a larger, well-established volcanic edifice. Despite the major differences in magma migration and storage processes, tephra deposits suggest phases of Violent Strombolian activity in the Central Oregon Cascades. This style of volcanism has previously gone unrecognized in

the Cascades and must be considered in future hazard assessments to mitigate dangers to surrounding communities.

2.7. Bridge Between Chapter II and Chapter III

In the preceding chapter (II), the eruption styles of three recent cinder cones in Central Oregon were inferred from tephra deposits and volatile contents within olivine-hosted melt inclusions. The next chapter (III) uses the volatile contents and geochemical variations of olivine-hosted melt inclusions from seven additional cinder cones in Central Oregon to investigate magma generation processes and mantle conditions beneath the Central Cascades.

CHAPTER III

VOLATILE CONTENTS OF MAFIC MAGMAS FROM CINDER CONES IN THE CENTRAL OREGON HIGH CASCADES: IMPLICATIONS FOR MAGMA FORMATION AND MANTLE CONDITIONS IN A HOT ARC

This work was published in volume 298 of the journal *Earth and Planetary Science Letters* in August, 2010. Coauthors Paul Wallace and Emily Johnson assisted in the field. Adam Kent assisted with LA-ICP-MS analyses and Ilya Bindeman assisted with oxygen isotope analyses. Emily Johnson provided the Blue Lake dataset. All coauthors assisted in the editorial process. I performed all laboratory work and was the primary author.

3.1. Introduction

Volatiles influence all aspects of subduction-related volcanic processes from mantle melting to eruption explosivity. Near- continuous dehydration reactions within the subducting slab release H_2O and mobile elements into the overlying mantle (e.g., Schmidt and Poli, 1998), which depress the mantle solidus and induce melting (e.g., Grove et al., 2002). The Cascades volcanic arc is the global end member, warm-slab subduction zone ($\Phi/100$ ~1.5–2.2 km; where Φ is the slab thermal parameter; e.g., Wada and Wang, 2009) resulting from the slow subduction (~3.5 cm/a) of the young Juan de Fuca plate (~6–9 Ma at the trench) beneath Western North America (Wilson, 2002). Kinematic models predict slab-mantle interface temperatures as much as 300 °C hotter than those calculated for older subducting lithosphere (Peacock, 2003). Higher temperatures should result in eclogite formation and significant slab dehydration beneath the Central Oregon forearc (<45 km depth), consistent with geophysical and geochemical observations (e.g., Leeman et al., 1990, 2005; Brocher et al., 2003; Hurwitz, et al., 2005; Rondenay et al., 2008). Loss of most volatiles beneath the forearc should result in reduced slab contributions to the mantle wedge below the arc as has been inferred in

Southern Washington and Northern Oregon (e.g., Leeman et al., 2005). In contrast, significantly higher volatile contents than expected are found in magmas from the southern part of the arc (e.g., Mt. Shasta; Anderson, 1974; Baker et al., 1994).

We measured pre-eruptive volatile (H_2O, CO_2, S, and Cl) contents in olivine-hosted melt inclusions from tephra deposits in the Central Oregon Cascades to examine the effects of a young subducting slab on magma generation in arcs. Volatile contents of three geochemically distinct mafic magma types are presented and compared with other arcs encompassing a wide range of slab thermal conditions. We also estimate the compositions of primary, mantle-derived magmas and mantle sources to infer how slab surface temperatures and degrees of mantle melting relate to H_2O flux into the mantle wedge.

3.1.1. Geologic setting and sample context

Intra-arc extension has promoted mafic volcanism in Central Oregon over the past ~5 Ma in the form of shield volcanoes and smaller monogenetic cones (Hildreth, 2007). The latter provides evidence for at least five distinct types of primitive magma (Hughes and Taylor, 1986; Bacon et al., 1997; Conrey et al., 1997). Low-K tholeiites (LKT; synonymous with MORB-like, high-Al olivine tholeiites, HAOT) and ocean–island-like basalts (OIB; also EIB or HFSE-enriched) are thought to represent decompression melts of depleted and enriched mantle domains, respectively (e.g., Hughes, 1990; Leeman et al., 1990; Conrey et al., 1997). Primitive calc-alkaline basalts (CAB) and rare, alkali-rich basalts (absarokites and shoshonites) represent melts generated from the addition of slab-derived fluids to the overlying mantle wedge (Leeman et al., 1990; Sisson and Layne, 1993; Bacon et al., 1997; Conrey et al., 1997; Rowe et al., 2009). Despite having elevated FeO^T/MgO, sub-alkaline basalts in the Cascades have enrichments in Sr, K, and Ba, and depletions in Nb and Ta and have been classified as calc-alkaline by multiple authors on the basis of trace element ratios (e.g., Ba/Nb >20; $(Sr/P)_{PM}$ >1.8; Leeman et al., 2005; Rowe et al., 2009). The timing of fluid addition and whether CABs are derived from lithospheric or asthenospheric mantle, however, are the subjects of debate (Leeman et al., 2005; Hildreth, 2007). Calc-alkaline basaltic andesites (BA) are also common and result from differentiation of basaltic parents or melting of highly depleted (harzburgitic)

mantle fluxed by slab-derived fluids (Hughes and Taylor, 1986; Hughes, 1990; Conrey et al., 1997).

3.1.2. Sample descriptions and analytical methods

Samples studied here are from tephra deposits (mostly Holocene; Sherrod et al., 2004) erupted from monogenetic vents in the Santiam–McKenzie Pass area, Central Oregon Cascades (Figure 11). We focused on calc-alkaline basalt and basaltic andesite samples to determine their relationships to subduction processes. Most of the tephras contain phenocrysts of olivine + plagioclase (and rarely pyroxene). Spinels occur as mineral inclusions inside most olivines. Tephra from Garrison Butte (GB072) contains only olivine (+spinel inclusions). The tephra sample from the Island Fissure (PT05) was from a subglacial eruption and, despite strong palagonitization, contains unaltered olivine phenocrysts with glassy inclusions.

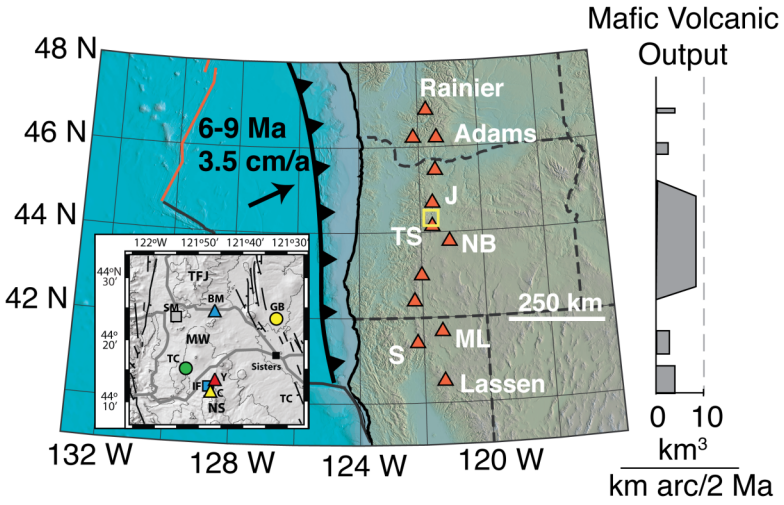

Figure 11. Southern portion of the Cascadia subduction zone after Haugerud (2004). The Cascades volcanic arc is defined by the major peaks shown as labeled, red triangles (J: Mt. Jefferson; TS: Three Sisters; NB: Newberry volcano; S: Mt. Shasta; ML: Medicine Lake volcano). A yellow box between Mt. Jefferson and the Three Sisters volcanoes marks the study area shown as an inset. Cumulative mafic volcanic output along the arc over the past 2 Ma is shown in the histogram to the right (Sherrod and Smith, 1990). Inset is a shaded relief map of the Santiam–McKenzie Pass (study area) in Central Oregon with vent locations shown (symbols as in Figure 12; TC: Twin Craters, GB: Garrison Butte, SM: Sand Mountain, IF: Island Fissure, Y: Yapoah, C: Collier, BM: Blue Lake Maar). Prominent volcanic peaks are labeled: TFJ (Three-Fingered Jack), MW (Mount Washington), and NS (North Sister). Graben-bounding faults (black), major highways (dark gray), and the town of Sisters (black square) are also highlighted.

Loose olivine crystals were picked from tephra samples. Olivines were treated in HBF_4 to remove attached matrix and allow inspection under refractive index oil. Fully enclosed glassy inclusions were selected and host crystals were ground and polished into wafers. Melt inclusions were analyzed for H_2O and CO_2 using a Thermo-Nicolet Nexus 670 FTIR spectrometer interfaced with a Continuum IR microscope and subsequently mounted in epoxy for electron microprobe and laser ablation ICP–MS analyses.

H_2O and CO_2 concentrations were calculated from IR peak absorbances using the Beer-Lambert law and appropriate absorption coefficients. Electron microprobe analyses were performed using a Cameca SX-100 at the University of Oregon. Hydrous glass compositions were measured with a 10 nA, 10 μm diameter beam and 15 kV accelerating voltage (see details in Appendix B). Individual inclusion analyses are averages of 3–5 spots and are reported in Appendix C. Host olivine compositions were determined using a 15 kV accelerating voltage and a 50 nA, 2 μm diameter beam. Three to five point analyses of olivine (>100 μm away from inclusions and crystal edges) were averaged for each crystal to obtain a representative olivine composition. Trace elements in melt inclusion glasses were analyzed at Oregon State University with a VG PQ ExCell quadrupole ICP–MS equipped with a NewWave DUV 193 nm ArF Excimer laser system using a 70 μm spot size and a 4 Hz pulse rate. Measured trace element concentrations were determined by reference to BCR-2G glass as a calibration standard and using ^{43}Ca as an internal standard (see Kent et al., 2004 for details). BHVO-2G glass was analyzed to monitor accuracy and precision, and the analyzed values were within 10% of accepted values. Oxygen isotopes in olivine from several tephra samples were measured at the University of Oregon using CO_2 -laser fluorination and an MAT 253 mass spectrometer. Major and trace elements for bulk tephra and bomb samples (Appendix C) were determined by XRF and ICP–MS analyses at the Washington State University GeoAnalytical lab.

3.2. Results

3.2.1. Major and trace element chemistry

Olivine host crystals are mostly $Fo_{82–84}$ and have oxygen isotope values within the range of and slightly heavier than values for mantle-derived basalts (Eiler, 2001; Table 4). The melt inclusions are medium-K calc-alkaline basalt and basaltic andesite in composition (Group II in Leeman et al., 2005). Inclusions from a given tephra sample have variable FeO^T contents at similar MgO and are out of Fe-Mg equilibrium with host crystals. Therefore, melt inclusions have been numerically restored back to equilibrium with their host crystals using the method of Danyushevsky et al. (2000), which accounts for both olivine post-entrapment crystallization and diffusive Fe-Mg exchange. The maximum FeO^T observed for each set of melt inclusions was assumed to be representative of the initial composition. A constant f_{O2} of NNO +0.25 was assumed based on the average S-FeO^T relationship in Appendix D. Melt inclusions required an average of 2.8 wt.% (maximum 7.9 wt.%) olivine addition to be restored to equilibrium with host olivines (Appendix E).

Major and trace element compositions of the melt inclusions are similar to whole-rock compositions of basalts and basaltic andesites in Oregon (Conrey et al., 1997; Rowe et al., 2009). Calc-alkaline melt inclusions are subdivided into three groups based on composition: (1) basalts from Twin Craters (TC063A) and Garrison Butte (GB072), (2) Sr-rich basalts from the Island Fissure (PT05) and Sand Mountain (SM2), and (3) basaltic andesites (technically North Sister-type; Hughes and Taylor, 1986) from Yapoah (Yo061E and Yo065D), Collier (EJYo2) and Blue Lake maar (BL1 and BL3) (Figure 12). Restored inclusions contain 4.5–7.6 wt.% MgO and 48.2–55.5 wt.% SiO_2 (Appendix E). Basalt and Sr-rich basalt compositions have similar major and high-field strength element (HFSE) abundances. Sr-rich basalts are distinguished from the basalts by higher alkali and large ion lithophile element (LILE) concentrations (Figure 12). In addition to higher SiO_2 (>52 wt.%) and lower MgO (<5.5 wt.%), basaltic andesites are distinguished from the two types of basalts by lower incompatible element abundances, especially the HFSE and heavy rare earth elements (HREE). LILE abundances, however, are similar for

both the basalts and the basaltic andesites. Basaltic andesites, on average, have more pronounced Nb-Ta depletions than either of the two basalt groups.

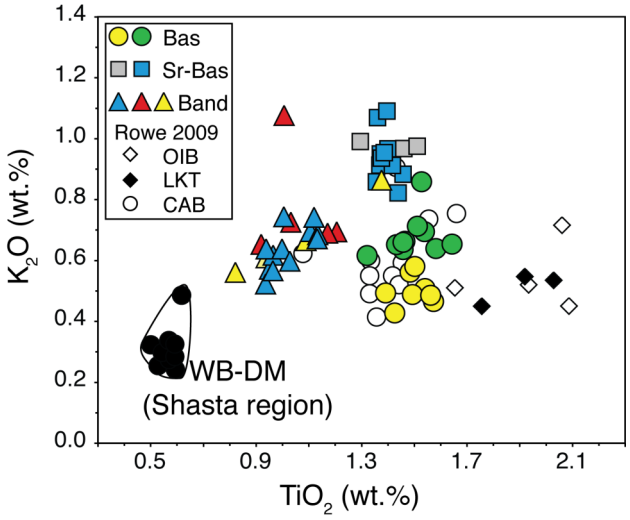

Figure 12. K_2O and TiO_2 contents of restored melt inclusions illustrating compositional differences between three types of mafic magmas studied (basalts [Twin Craters and Garrison Butte] as circles ['Bas'], Sr-rich basalts [Island Fissure and Sand Mountain] as squares ['Sr-Bas'], and basaltic andesites [Yapoah, Collier and Blue Lake Maar] as triangles ['Band']). Shown for comparison are high-Mg andesite melt inclusions from the Whaleback–Deer Mountain (WB–DM) cinder cone near Mt. Shasta (black circles in white field; Ruscitto and Wallace, 2008) and average melt inclusion compositions from Rowe et al. (2009) (OIB=ocean-island-like basalt, LKT=low-K tholeiite, and CAB=calc-alkaline basalt).

3.2.2. Magmatic volatile contents

Dissolved H_2O contents are higher in the basaltic andesites (3.6 wt.% H_2O_{max}) than in either of the basalt types (1.8 [basalts] and 2.7 wt.% H_2O_{max} [Sr-rich basalts]). CO_2 contents range from below detection (≤50 ppm) to 1400 ppm, with the highest concentrations in the basalts (Figure 13). Maximum S contents are 1500 (basalts), 2100 (Sr-rich basalts), and 1800 ppm (basaltic andesites). An increase in maximum Cl is observed from the basalts (900 ppm) and Sr-rich basalts (1000 ppm) to the basaltic andesites (1300 ppm) (Figure 13). High dissolved S contents in many samples require more oxidizing conditions (fo_2 ≥NNO; Figure 13c) than those inferred by Rowe et al. (2009) (NNO-1 to NNO). Basaltic andesite inclusions from Yapoah and Collier have the

lowest FeO^T and S. Olivines from some Collier samples contain ≤50 μm diameter sulfide globules, demonstrating sulfide-saturation.

Primary H_2O–CO_2 variability in melt inclusions results from either degassing or gas fluxing prior to melt inclusion formation (e.g., Metrich and Wallace, 2008; Johnson et al., 2009). Additional variations in H_2O and CO_2 may be attributed to post-entrapment diffusive loss of H_2O through the host crystal (e.g., Portnyagin et al., 2008) and CO_2 partitioning into shrinkage bubbles (e.g., Anderson and Brown, 1993). To constrain pre-eruptive volatile contents in each sample suite, only melt inclusions trapped above 100 MPa (Appendix E) were considered, and of these inclusions, the maximum H_2O, S, and Cl contents identified in each suite were taken to represent the minimum pre-eruptive concentration for these mafic magmas (cf., Johnson et al., 2009).

3.3. Discussion

3.3.1. Comparison of volatile contents in the Cascades with other arcs

Magmatic volatile contents in Central Oregon are elevated compared to MORB and overlap with values for many other arcs, including Kamchatka and the Marianas, which have considerably older subducting slabs (Φ/100=47.8 [Kamchatka] and 36.7 km [Marianas]; Wada and Wang, 2009) (Figure 13). Despite these overlaps, the maximum magmatic H_2O contents in Central Oregon are not as high as maxima in other arcs. H_2O and CO_2 in the Central Oregon basaltic andesite inclusions overlap those in Mt. Shasta high-Mg andesites determined by FTIR (≤3.4 wt.%; Ruscitto and Wallace, 2008), but H_2O contents are considerable lower than those inferred by Anderson (1974) using the H_2O-by-difference method (≤6 wt.%). We note that the data from Shasta come from inclusions hosted in Fo_{94} olivines and are therefore not directly comparable to the Central Oregon melt inclusions until further corrections for fractionation are made (see below). Central Oregon magmatic volatiles are most similar to those in behind the volcanic front magmas from Guatemala and are intermediate between those for oceanic back-arc basin lavas and mafic magmas from other arcs (Figure 13a and b). As in many other arcs, H_2O and Cl contents in Central Oregon are well explained by mixing between a mantle source

Table 4. Average primitive compositions

Source	TWIN CRATER		GARRISON BUTTE		ISLAND FISSURE		SAND MTN		YAPOAH		COLLIER		BLUE LAKE MAAR	
Long (121ºW)	52.808’		32.315’		47.731’		55.370’		46.603’		n.d.		46.448’	
Lat (44º N)	15.283’		23.242’		12.543’		23.651’		13.155’		n.d.		24.514’	
	Average	1s.e.												
wt%	n=10		8		11		3		4		5		12	
SiO_2	50.01	0.19	48.03	0.17	50.36	0.06	49.73	0.05	52.19	0.51	52.18	0.49	51.66	0.16
TiO_2	1.31	0.02	1.29	0.02	1.20	0.01	1.27	0.06	0.86	0.03	0.96	0.08	0.85	0.02
Al_2O_3	15.58	0.17	14.89	0.17	15.30	0.08	15.59	0.09	15.72	0.32	16.46	0.40	14.72	0.17
FeO^T	9.24	0.02	10.75	0.02	9.50	0.01	9.12	0.05	8.23	0.10	7.75	0.02	8.99	0.02
MnO	0.12	0.01	0.13	0.01	0.13	0.01	0.11	0.01	0.11	0.02	0.09	0.01	0.10	0.00
MgO	11.04	0.04	12.89	0.03	11.37	0.03	10.89	0.08	11.24	0.15	10.51	0.06	12.44	0.06
CaO	8.72	0.08	8.51	0.04	7.63	0.05	8.89	0.08	7.18	0.35	7.67	0.13	6.98	0.08
Na_2O	3.10	0.11	2.75	0.04	3.33	0.05	3.21	0.01	3.62	0.06	3.58	0.05	3.58	0.03
K_2O	0.60	0.02	0.43	0.02	0.81	0.02	0.87	0.00	0.67	0.08	0.59	0.04	0.53	0.02
P_2O_5	0.28	0.01	0.34	0.01	0.37	0.01	0.33	0.01	0.18	0.02	0.20	0.04	0.15	0.01
S_{max} (ppm)	1340	20	1200	10	1310	10	1890	30	960	10	1010	30	1490	70
Cl_{max} (ppm)	440	20	770	160	440	40	850	10	980	60	700	20	880	30
H_2O_{max}	1.59	0.12	1.45	0.20	2.28	0.15	2.26	0.20	2.60	0.21	2.33	0.16	2.96	0.21
CO_{2max}(ppm)	1234	74	823	75	938	63	943	71	738	58	718	27	694	50
$T_{formation}$ (ºC)[a]	1243	40	1282	40	1250	40	1229	40	1233	40	1222	40	1254	40
Mg# Ol	90		90		90		90		91		91		91	
% Ol add.	13.8	0.2	16.4	0.5	15.8	0.3	12.2	0.5	16.9	0.8	14.9	0.4	19.9	0.6
Lee Temp (ºC)	1273	38	1331	40	1266	38	1260	38	1239	38	1227	38	1269	38
Lee Press (GPa)	1.19	0.2	1.59	0.2	1.25	0.2	1.28	0.2	1.05	0.2	1.11	0.2	1.25	0.2
	n=5		3		4		4		3		1		3	
$\delta^{18}O$ ol(‰)	5.236	0.040	5.324	0.075	5.704	0.056	5.345	0.030	5.435	0.085	5.568	-	5.201	0.017

Table 4. Continued.

Source	TWIN CRATER		GARRISON BUTTE		ISLAND FISSURE		SAND MTN		YAPOAH		COLLIER		BLUE LAKE MAAR	
ppm	n=7		4		7		2		4		4		6	
Sc	24.2	1.7	25.1	0.5	19.8	0.8	24.8	0.1	21.3	0.5	21.9	1.2	20.3	1.2
V	210	5	183	5	189	4	169	3	170	5	163	7	184	8
Cr	96	21	90	11	77	2	260	145	101	20	69	9	58	4
Rb	6.4	0.3	4.9	1.0	13.0	0.5	8.4	0.7	8.0	1.7	7.9	0.5	7.8	0.6
Sr	514	9	454	12	616	16	903	2	501	29	444	20	505	4
Y	21.4	0.5	20.7	0.6	19.1	0.5	21.4	0.6	14.4	0.6	14.3	2.2	12.1	0.9
Zr	111	2.5	120	8.5	119	3.3	135	2.3	83	5.4	79	11.2	62	5.4
Nb	6.3	0.2	8.3	0.2	12.2	0.3	12.0	1.5	5.7	0.7	6.9	1.4	4.6	0.4
Ba	318	8	189	4	413	14	347	1	230	16	201	12	210	12
La	11.5	0.5	10.5	0.4	14.9	0.2	17.8	0.2	8.5	0.4	8.0	1.1	6.7	0.6
Ce	32.7	1.1	28.1	0.7	39.5	1.0	41.9	0.2	21.3	0.9	19.0	1.9	17.4	1.2
Pr	4.4	0.1	3.8	0.1	4.7	0.2	5.5	0.0	2.6	0.2	2.6	0.3	2.3	0.1
Nd	17.7	0.5	15.4	0.4	20.5	0.7	22.2	0.1	11.0	0.7	10.9	1.3	9.7	0.6
Sm	4.3	0.5	3.6	0.2	3.7	0.1	4.8	0.3	2.4	0.2	2.5	0.3	2.0	0.1
Eu	1.4	0.1	1.3	0.1	1.6	0.1	1.4	0.0	0.9	0.1	1.0	0.1	0.8	0.0
Gd	4.1	0.5	3.6	0.2	3.6	0.2	4.1	0.4	2.4	0.2	2.7	0.3	2.2	0.3
Dy	4.5	0.4	3.7	0.1	3.0	0.2	4.2	0.1	2.7	0.2	2.6	0.34	1.7	0.1
Er	2.2	0.1	2.2	0.1	2.0	0.1	2.1	0.0	1.4	0.1	1.3	0.2	1.1	0.1
Yb	1.9	0.1	1.8	0.0	1.7	0.2	1.8	0.0	1.3	0.1	1.2	0.1	1.1	0.1
Ta	0.35	0.05	0.45	0.02	0.61	0.05	0.77	0.18	0.28	0.06	0.40	0.09	0.26	0.05
Pb	2.9	0.1	2.8	0.3	5.4	1.0	3.7	0.4	3.1	0.3	2.6	0.1	2.8	0.2
Th	1.02	0.06	0.62	0.04	1.15	0.05	1.28	0.05	0.80	0.13	0.77	0.05	0.61	0.06
U	0.38	0.02	0.26	0.03	0.62	0.04	0.40	0.02	0.32	0.06	0.33	0.02	0.36	0.05

[a] Temperature calculated after Sugawara (2000).

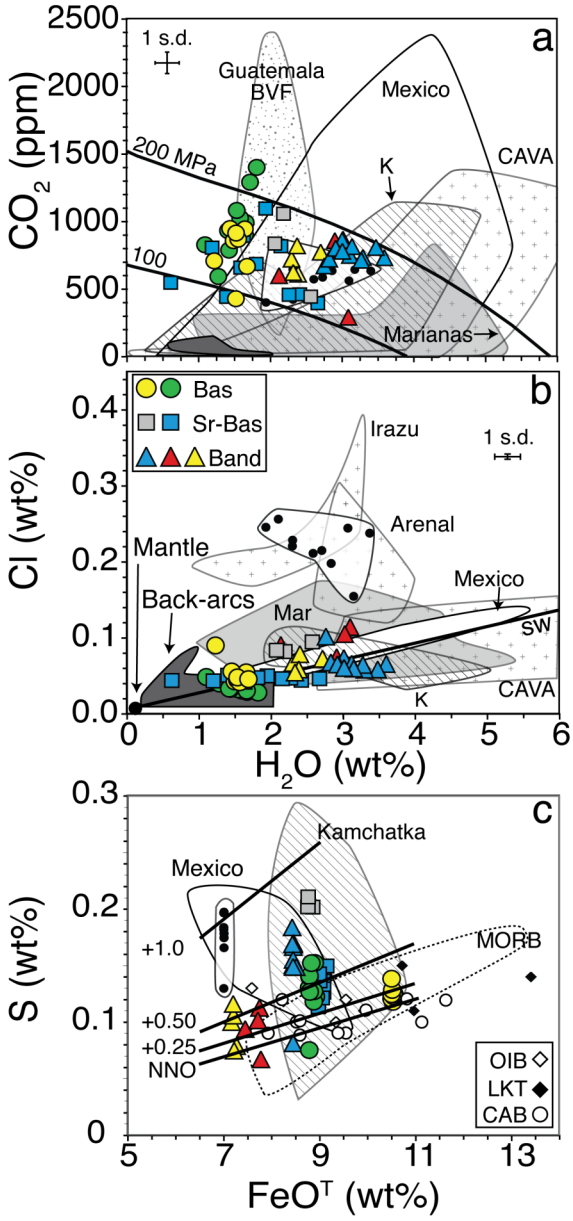

Figure 13. Dissolved volatile contents in restored olivine-hosted melt inclusions. (a) H_2O and CO_2 contents from this study (symbols as in Figure 12). Thick black lines are vapor saturation isobars (Papale et al., 2006). Fields enclose melt inclusion compositions from the following sources: CAVA (Central American Volcanic Arc) — Roggensack et al. (1997), Wade et al. (2006), Benjamin et al. (2007), Sadofsky et al. (2008); Mexico — Johnson et al. (2009); Guatemala BVF (behind the volcanic front) — Walker et al. (2003); K (Kamchatka) — Portnyagin et al. (2007), Auer et al. (2009); Marianas — Shaw et al. (2008); back-arcs — Shaw et al. (2004). Back-arc glass compositions are also shown (Stolper and Newman, 1994; Kelley et al., 2006; Bezos et al., 2009). (b) H_2O and Cl, with the line labeled SW illustrating a mixing trajectory between a MORB mantle source and sea water (3.5 wt.% NaCl) after Kent et al. (1999) and Kent and Elliot (2002). Data sources as in (a) with the Central American field separated into: Irazu and Arenal, Costa Rica, and CAVA = Guatemala, El Salvador, Nicaragua. (c) S vs. FeOT, with the addition of MORB field (data from PetDB) and sulfide-saturation curves at NNO after Wallace and Carmichael (1992) modified using the temperature dependence from Mavrogenes & O'Neill (1999). Estimates of the total dissolved sulfur for NNO +0.25, +0.50, and +1.0 were calculated by combining S_{Total} calculated at NNO while assuming S^{6+}/S^{Total} ~0.21 (at NNO) and using equation (7) from Jugo (2009) (All calculations at T = 1100 °C). Mexico and Kamchatka fields are shown for comparison; fields for other arcs are omitted for clarity but largely overlap with those shown.

and small amounts of fluid with Cl/ H_2O similar to seawater (Figure 13b; Kent et al., 1999; Wallace, 2005; Johnson et al., 2009). Sulfur contents are similar to those in melts from other arcs and back-arc basins (Figure 13c).

3.3.2. Magmatic differentiation, mixing and crustal interaction

The mafic samples studied are not primitive and have evolved from parental magmas during transit through the crust. Dissolved volatile contents, therefore, cannot be related back to parent magmas or source compositions until differentiation processes are assessed. Minimum melt inclusion trapping pressures are 100–200 MPa (~4–8 km depth; Papale et al., 2006) and constrain melt evolution to the mid- and lower-crust prior to melt inclusion formation (Moho ~40–44 km; Trehu et al., 1994; Brocher et al., 2003; Hildreth, 2007). The extent to which the basalt and basaltic andesite magmas have interacted with the crust and/or mixed with one another is difficult to constrain. The diversity in primitive mafic magma types erupted at cinder cones throughout Oregon and Southern Washington suggests that homogenization by magma mixing and crustal assimilation are not dominant processes for small volume mafic eruptions, though they might be more important beneath larger, long-lived stratocones (Leeman et al., 2005; Hildreth, 2007; Mercer and Johnston, 2008). Evolved magmas in the Cascades could be heavily influenced by lower crustal melting (Hildreth and Moorbath, 1988; Conrey et al., 2001; Hildreth, 2007). However, studies of exposed island arc crustal sections (e.g., Kohistan and Talkeetna) demonstrate that intrusion induced melting is subordinate to fractional crystallization processes (Kelemen et al., 2003; Greene et al., 2006; Jagoutz et al., 2009). U-series and Os isotope ratios of basalts from the Mt. Adams region also indicate that lower crustal interaction is relatively minor (<5 wt.%; Jicha et al., 2009). From these lines of evidence, we assume that the compositional evolution of basalts and basaltic andesites in Central Oregon is dominated by fractional crystallization.

It is important to consider the possible effects of crustal interaction on magmatic volatile contents, even if the extent of such interaction was minor. One possibility is a contribution from amphibole in lower crustal rocks. Minor assimilation (<10 wt.%) of bulk amphibolite (~50% modal amph; bulk rock 1 wt.% H_2O) would contribute <0.1 wt. % H_2O. Mixing between low- H_2O mantle-derived magmas and dacitic partial melts of amphibolite (~6 wt.% H_2O; Rapp and Watson, 1995) could potentially result in hybrid compositions similar to those of the basaltic andesite melt inclusions. However, high-pressure experiments on basaltic andesite compositions from the region imply last

equilibration near the base of the crust between hydrous (~3.5 wt.% H_2O) mafic melt and anhydrous gabbro (Mercer and Johnston, 2008). Therefore, any lower crustal interaction must have involved gabbro rather than amphibolite or dacitic partial melt. Low trace element abundances in the basaltic andesites have been interpreted to result from extensive interaction of mantle-derived LKT magma with gabbroic lower crust (Schmidt, 2005). LKT magmas, however, are interpreted to be volatile-poor (e.g., Sisson and Layne, 1993; Rowe et al., 2009), and gabbroic assimilation is unlikely to contribute significant H_2O, CO_2, or Cl to the melt. Therefore, whatever the role of lower crustal input is, we conclude that the volatile contents in all three magma types are primarily controlled by mantle source variations.

3.3.3. Mantle-derived parental melt compositions

Melt inclusions were restored to primary, mantle-derived compositions through incremental addition (0.1 wt.%) of equilibrium olivine until the composition was in equilibrium with mantle olivine (Table 4). Primary basalt and Sr-rich basalt samples were assumed to have equilibrated with Fo_{90} olivine. Basaltic andesite compositions were assumed to be from more refractory mantle (Fo_{91} olivine) based on lower incompatible element abundances and higher SiO_2 compared to the basalts (Figure 12). Mantle equilibration required an average addition of 16 wt.% olivine. This approach may not fully account for effects of fractional crystallization on incompatible elements because some of the magmas were likely saturated in both olivine and Ca-rich pyroxene and potentially plagioclase (e.g., Sisson and Grove, 1993). However, hydrous, isobaric pMELTS simulations suggest that olivine is the dominant crystallizing phase until ~6 wt.% MgO (~13 wt.% crystallization) in the compositions of interest, and therefore the method of simulating olivine-only crystallization can approximate total extents of multi-phase crystal fractionation (Appendix D). We emphasize that the MgO contents of the calculated primary melts are not as robust as the incompatible element concentrations.

Primary melt compositions (denoted by °) from Central Oregon have 1.5–3.0 wt.% $H_2O°$, 1000–1500 ppm S°, and 450–1000 ppm Cl° (Table 4). The highest pre-eruptive $H_2O°$ and Cl° contents are in HFSE depleted primary melts (parents of basaltic andesites), whereas the basalts contain the lowest $H_2O°$. S° contents do not vary

systematically between the compositions. Primary melt CO_2° contents cannot be inferred from the melt inclusions because of pre-entrapment degassing but could be ~0.6 wt.% (Wallace, 2005).

Correlations between H_2O°, major elements, and indices of slab component addition are shown in Figure 14. H_2O° is positively correlated with SiO_2°, Na_2O°, Pb/Ce, and Ba/Zr and negatively correlated with TiO_2°, CaO°, P_2O_5°, and HFSE°. Average primary (Fo_{90}) melt compositions from Northern California are consistent with the Central Oregon trend (Sisson and Layne, 1993). We note that the low H_2O ° concentration (~0.3 wt.%) of the Black Crater sample (Sisson and Layne, 1993) is close to the solubility of H_2O at 0.1 MPa and may reflect pre-entrapment degassing or post-entrapment diffusive loss. The high-Mg melt composition from the Mt. Shasta region extends the Central Oregon trend to higher SiO_2° and H_2O° and lower TiO_2° (Figure 14a and b). In contrast, estimated H_2O° contents (see Appendix F) of Central Oregon melt compositions from Rowe et al. (2009) plot at the opposite end of the trend. Less significant positive correlations are observed between H_2O° and indices of slab addition (i.e., Pb/Ce and Ba/Zr) (Figure 14c and d). Positive correlations observed between H_2O°, Pb/Ce, and Ba/Zr appear consistent with a flux-melting model (Stolper and Newman, 1994; Kelley et al., 2006) and suggest that small additions of a slab-derived hydrous component into the mantle wedge are responsible for the observed volatile contents (Figure 14). However, melt compositions require that either low (< 1 wt.%) TiO_2° melts are generated from high extents of melting (F > 0.15) of a single source or that the large variations in TiO_2° result from distinct mantle sources (e.g., the high-Mg composition from Mt. Shasta region is in equilibrium with harzburgite rather than lherzolite; Baker et al., 1994; Ruscitto and Wallace, 2008). We investigate these competing models in more detail below.

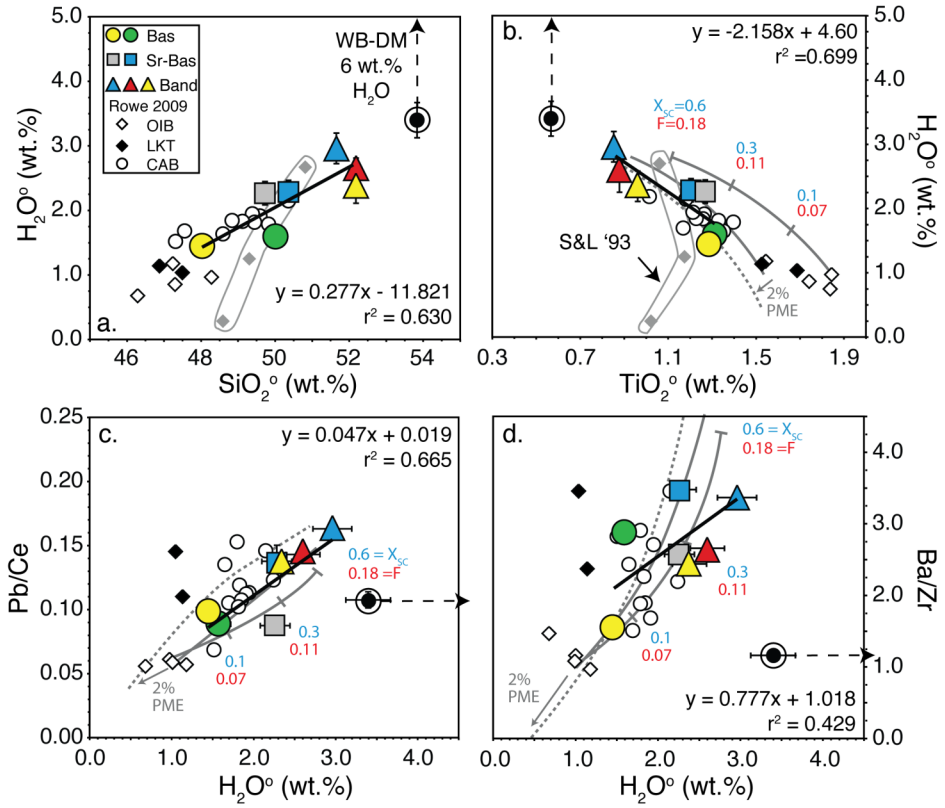

Figure 14. Primary (mantle-derived) magma compositions (e.g., SiO_2°) calculated from melt inclusions in Central Oregon (major and trace elements are averages of restored, undegassed compositions; maximum H_2O from each suite; see Table **4**). Symbols as in Figure 12, with the addition of Sisson and Layne (1993) data (averaged and restored to Fo_{90} equilibrium values as gray diamonds). (a, b) Linear correlations between H_2O° and major elements (central OR samples from current study only with r^2 values shown) can be used to calculate H_2O° in the magma compositions of Rowe et al. (2009). Values shown for Rowe et al. samples are H_2O° contents determined from averaging equations shown for SiO_2° and TiO_2°. OIB and LKT H_2O° contents are extrapolated. (c, d) Correlations between H_2O° and some common trace element proxies for water. H_2O° shown for the Shasta High-Mg composition is based on the observed maximum concentration in olivine-hosted (Fo94) melt inclusions (6%, Anderson, 1974; 3.4%, Ruscitto and Wallace, 2008). Experiments suggest that H_2O° in Shasta magmas may be as high as ~10 wt.% (e.g., Baker et al., 1994; Grove et al., 2003). Low H_2O° value (~0.3 wt.%) from Sisson and Layne may represent a degassed sample. The two solid gray lines in panels (b), (c), and (d) represent flux-melting models of distinct enriched mantle sources using the relationship between amount of subduction component added to source (X_{SC} in wt.%) and degree of melting (F as mass fraction) for back-arc basin basalts
Figure 14. (continued) described in Kelley et al. (2006) (i.e., dF/dX_{SC}=0.48). The dashed gray line represents a flux melting model of mantle that had undergone 2% previous melt extraction (PME; effect of PME on the mantle source is indicated by gray arrows). All three melting models begin at X_{SC}=0 wt.%, F=0.05 and end at X_{SC}=0.6 wt.%, F=0.18.

3.3.4. Mantle sources and melting conditions

Figure 15 shows calculated pressures and temperatures of last equilibration between the primary melts and the mantle (Table 4; Lee et al., 2009). Most compositions have equilibrated near the base of the crust (~1.3 GPa), within the spinel stability field. LKT and OIB compositions (along with Garrison Butte) appear to have equilibrated slightly deeper (~1.6 GPa), and these results are consistent with Elkins-Tanton et al. (2001) and Leeman et al. (2005), though we note that pressure uncertainties are ±0.2 GPa (Lee et al., 2009).

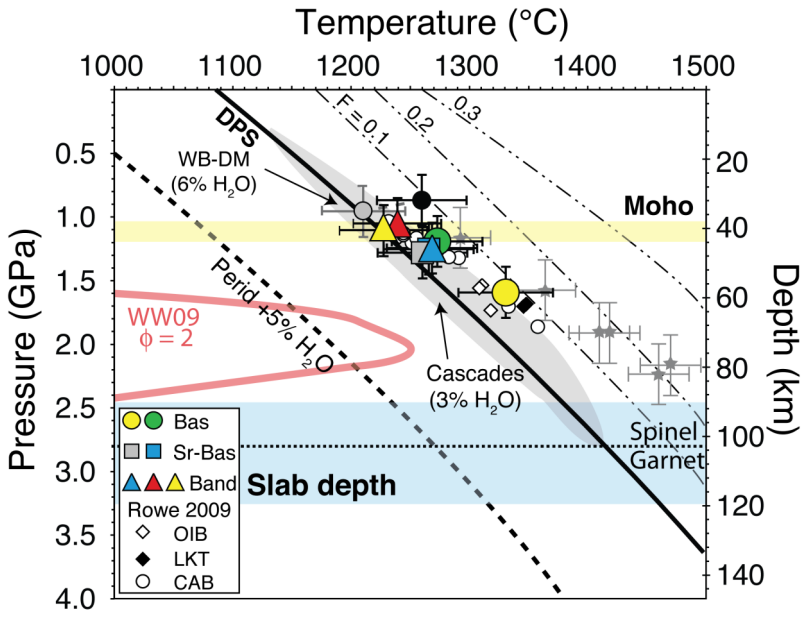

Figure 15. Pressures and temperatures at which calculated primary magma compositions for Central Oregon (and WB–DM) are in equilibrium with lherzolite or harzburgite using the thermometer and barometer of Lee et al. (2009). Symbols as in Figure 12, with the exception of the 6 wt.% H_2O WB–DM magma (gray circle connected to black [3% H_2O] with dashed line). Error bars on symbols are ±0.2 GPa and ±3% for calculated pressures and temperatures, respectively. Also shown are the P–T estimates of primitive melts in Northern California from Elkins-Tanton et al. (2001) (gray stars with error bars; note that the lowest pressure point from Elkins-Tanton et al., which represents a Shasta region high-Mg andesite, is within error of black circle WB–DM from Ruscitto and Wallace (2008). Light gray field represents Cascades whole-rock data (assuming 3 wt.% H_2O) from Lee et al. (2009). Approximate depths to the Moho (yellow) and slab (blue) are also shown, depth axis was calculated assuming constant ρ=2.8 g/cm^3. Thick black line is the dry peridotite solidus (DPS) taken from Lee et al. (2009). Thick dashed lines represent hydrous peridotite solidi. Thin dot–dot–dash lines approximate melt fraction isopleths. Pressure of the Spinel (spl)- garnet (gt) transition (horizontal dashed line) is labeled at 2.8 GPa. Thick red line (WW09 represents the geotherm calculated for Northern Cascadia in Wada and Wang (2009).

The diverse primitive magma types in the Cascades have been attributed to mantle heterogeneities that include an enriched OIB-like source, a depleted MORB-like source (with or without overprinting by a subduction component), and a less common ultra-depleted (harzburgite) source (Hughes and Taylor, 1986; Hughes, 1990; Conrey et al., 1997; Schmidt et al., 2008; Rowe et al., 2009). A range in mantle compositions is expected given the complex tectonic history of this region (Hildreth, 2007). However, unlike other segments of the arc, isotopic constraints (Sr and Nd) permit Central Oregon magmas (except for shoshonites) to be derived from a single mantle source (Schmidt et al., 2008). Previous studies have demonstrated that fluid flux-melting models can reproduce the OIB, LKT, and CAB compositions using a single, enriched mantle source in which increasing amounts of slab-fluid addition drive increasing degrees of melting (Reiners et al., 2000; Rowe et al., 2009). We adopted a similar approach and calculated potential enriched mantle sources by assuming that primitive OIB compositions represent small (5%) degree melts (Conrey et al., 1997; Johnson et al., 2009). The inferred Central Oregon subarc mantle compositions have elevated Dy/Yb ~2, similar to the OIB mantle source of Sun and McDonough (1989). All melting calculations assumed modal batch melting as an approximation of pooled melts formed by polybaric fractional melting (Kelley et al., 2006; Portnyagin et al., 2007). Bulk mantle–melt partition coefficients were calculated from mineral–melt coefficients reported in Johnson et al. (2009). Mantle source compositions, modal mineralogy, and bulk partition coefficients are listed in Appendix G.

We evaluate potential mantle sources (Figure 16) using the approach of Portnyagin et al. (2007). Large variations in Nb/Y suggest that the Cascades subarc mantle is heterogeneous. OIB-type sources could produce the range of melts inferred from the melt inclusions, but more depleted sources (e.g., E-DMM; Workman and Hart, 2005) appear required to produce the range of primary melts inferred from the larger database of whole-rock compositions. Extents of mantle melting were calculated from the primary melt compositions by assuming that HFSE (Nb, Ti, and Zr), HREE (Dy, Er, and Yb) and Y are derived solely from the mantle wedge (Kelley et al., 2006; Portnyagin et al., 2007). These elements have relatively low fluid solubilities under most conditions relevant to slab dehydration (Kessel et al., 2005). The melting models suggest that the

basalts and Sr-rich basalts represent melt fractions of ~10–15%. The more depleted primary melts (parents of basaltic andesites) require either higher extents of melting (~18–20%) than the basalts and Sr-rich basalts or similar extents of melting of a more depleted mantle source (dashed curve in Figure 16a) (cf., Hughes and Taylor, 1986; Conrey et al., 1997). Interestingly, the depleted basaltic andesite trace element compositions are similar to high-Mg andesites from the Mt. Shasta region that are interpreted to represent 15–20% melting (Grove et al., 2002). The Shasta high-Mg andesites, basaltic andesites of Central Oregon, and rare depleted basaltic andesites from the Western Cascades of Oregon may all represent melts that have equilibrated with refractory mantle (Conrey et al., 1997; Grove et al., 2003).

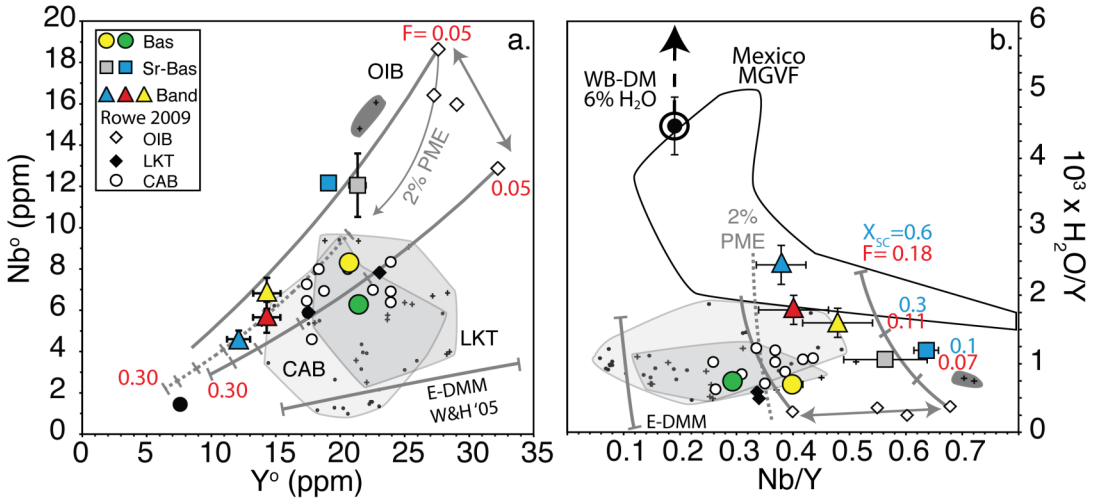

Figure 16. (a) Primary melt Nb and Y contents (denoted by °) for Central Oregon magmas, symbols as in Figure 12. Gray fields enclosing small symbols are whole-rock compositions. Solid gray curves show batch modal melting models (from F=0.05 to 0.30; increments of 0.05 are shown on lower curves; Nb and Y concentrations in the subduction component are assumed to be 0) for a spinel lherzolite source (see text). The double-headed arrow illustrates the range in mantle variability implied by the compositional variations of OIB samples. The dashed gray curve represents melting of a previously depleted source (2% PME). (b) H_2O/Y vs. Nb/Y of Central Oregon magmas illustrating the effects of trace element enrichment from slab component addition (resulting in elevated H_2O/Y) and the effects of previous melting and source depletion (resulting in decreased Nb/Y). Model curves are the same flux-melting models shown in Figure 14. As in (a), the double-headed arrow illustrates mantle variability based on OIB samples and the dashed curve represents melting of a previously depleted mantle (2% PME from high Nb/Y source). Curves extend from X_{SC}=0 wt.%, F=0.05 to X_{SC}=0.6 wt.%, F=0.18. Field for Mexico MGVF (Michoachan Guanajuato Volcanic Field) from Johnson et al. (2009).

Given the similar P–T conditions inferred for all three magma types (Figure 15) and the likelihood of mantle heterogeneities beneath the Central Oregon Cascades, we suggest a melting scenario that has resulted in similar overall extents of melting for each type. The primitive basaltic and Sr-rich basaltic magmas can be generated by 9–11% partial melting of an enriched mantle source (0.13–0.24 wt.% source H_2O) with final equilibration temperatures of 1260–1330 °C at 1.2–1.6 GPa (Figure 15 and Figure 17;Table 4). Depleted basaltic andesite parent magmas can be generated by 12–16% partial melting of a more refractory mantle source (0.40–0.56 wt.% source H_2O) with final temperatures of 1240–1270 °C at 1.1–1.3 GPa. Based on these models, conditions beneath Central Oregon appear similar to or slightly warmer than other well-studied arcs but cooler and wetter than backarc basins (Figure 17). Melting conditions for the primitive LKTs appear hotter than for the calc-alkaline melts, consistent with deeper equilibration pressures (cf., Leeman et al., 2005) and plot within the field defined for back-arc basin magmas. Higher degrees (>20%) of hydrous melting (>0.7 wt.% source H_2O) are required to produce the high-Mg melt from the Shasta region, consistent with interpretations of previous workers (Baker et al., 1994; Grove et al., 2002; Ruscitto et al., 2008).

We conclude that LKT and OIB magmas form by decompression melting of variably enriched mantle domains. An apparent continuum exists between the calc-alkaline basalts and Sr-rich basalts, depleted basaltic andesites, and high-Mg andesites, representing melts derived from subduction component addition to increasingly refractory mantle sources. Because of the tectonic complexity beneath the region, this continuum may not imply a simple genetic relationship between the enriched and refractory mantle sources, though we note that radiogenic isotope data are consistent with such a relationship.

Inferred mantle temperatures and pressures are similar to those calculated for basalts and basaltic andesites in Northern California and SW Washington (Elkins-Tanton et al., 2001; Leeman et al., 2005; Lee et al., 2009) and inferred maximum temperatures of 1250–1260 °C predicted by geodynamic models (Currie et al., 2004; Wada and Wang, 2009) (Figure 15 and Figure 17). The apparent high mantle temperatures just beneath the crust cannot represent steady-state values as this would result in widespread melting of

the lower crust (Elkins-Tanton et al., 2001). Such transient high temperatures could result from advection of heat by melts as they ascend from the hot core of the wedge.

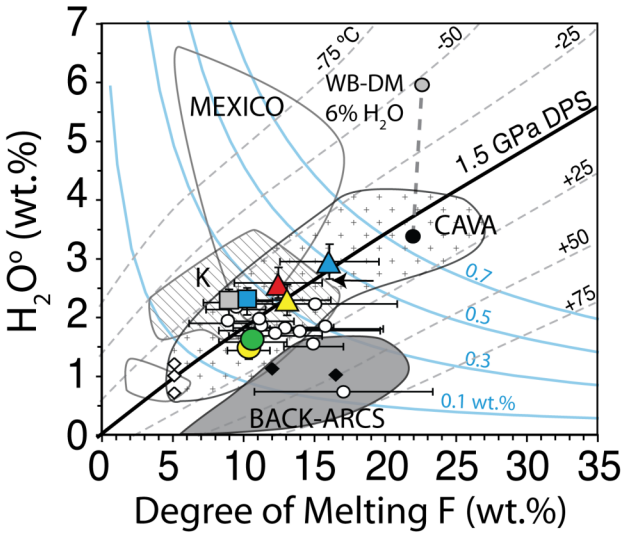

Figure 17. Primary melt H_2O and calculated degree of partial mantle melting (F) in wt.%. Central Oregon magmas (symbols as in Figure 12), and fields encompass data from sources mentioned previously. Thick black line is the 1.5 GPa dry peridotite solidus and gray dashed lines represent equal temperature deviations from the solidus (Portnyagin et al., 2007). Blue lines contour equal wt.% H_2O concentrations in mantle sources. H_2O° contents were calculated using crystallization estimates derived from models, and degrees of melting were calculated as described in the text. Degrees of melting were calculated for basaltic andesites using mantle sources that were affected by 2% PME. Dashed gray line connects estimates for the WB–DM sample (Shasta region high-Mg composition) based on the observed maximum concentration in olivine-hosted (Fo_{94}) melt inclusions (6%, Anderson, 1974; 3.4%, Ruscitto and Wallace, 2008).

Moderate input of slab-derived H_2O into the mantle wedge beneath Central Oregon is consistent with modest subduction-related geochemical signatures compared to other arcs (Leeman et al., 1990, 2005), geophysical evidence for shallow slab dehydration (Rondenay et al., 2008), and halogen outputs from spring waters (Hurwitz et al., 2005). Ratios reflecting volatile addition from a slab component (H_2O/ Ce ~490–1700; S/Nb ~110–310; and Cl/Nb ~37–190) are low compared to those from the southern Cascades (Shasta) and other arcs (Mexico, Central America, and Kamchatka).

We calculated slab component compositions using the inferred mantle sources and average primary melt compositions (Appendix H). H_2O /Ce and H_2O/K_2O of the slab components are shown in Figure 18. Slab surface temperatures can be estimated using

these ratios calibrated with fluid–rock partitioning experiments (e.g., Kessel et al., 2005; Plank et al., 2009). As expected for an arc with a young slab, inferred slab temperatures are high (850–950 °C) and at the high temperature end of the global range for arcs. Partitioning experiments indicate that Nb may preferentially partition into the slab component at elevated temperatures (>900 °C; Kessel et al., 2005), possibly undermining an assumption in our melting model. We emphasize, however, that our melting calculations used a combination of HFSE, HREE, and Y and that calculated melt fractions do not significantly change if Nb is excluded.

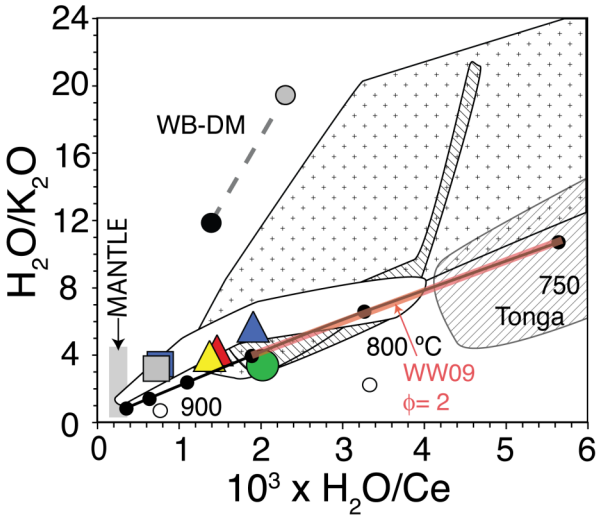

Figure 18. H_2O/Ce and H_2O/K_2O ratios of the slab-derived fluid components calculated for the Central Oregon magmas (calculated using methods described in Portnyagin et al., 2007). Other arcs are shown for comparison, and symbols and fields are the same in Figure 17. Field for Tonga is from Plank et al. (2009). H_2O/Ce and H_2O/K_2O ratios are also shown (gray box) for the mantle sources calculated by assuming that OIB compositions represent 5 wt.% partial melts (see text). Black line illustrates slab surface temperature concordance between the geothermometers of Plank et al. (2009). Very low Ce contents were calculated for the slab component in Garrison Butte and many of the Rowe et al. compositions and are not included in the diagram because of large uncertainties in H_2O/Ce. Note that the fluid composition from WB–DM falls off of the geothermometer concordance line. This could indicate formation of phlogopite or another significant K_2O-bearing phase in the mantle (Plank et al., 2009). The thick line (WW09) represents the range of slab surface temperatures at subarc depths calculated for Northern Cascadia in Wada andWang (2009).

Based on geochemical data and inferred depths of magma generation, it has been proposed that CAB magmas in the Southern Washington and Northern Oregon Cascades

form by remobilization of a 'stored' subduction component in the lithospheric mantle by ascending decompression-derived melts (LKT and OIB) from the asthenosphere (Leeman et al., 2005). This lithospheric component may be derived from the early stages of Cascadia subduction (~40 Ma) when subduction rates were faster. Our data do not permit us to address this issue in detail, but we note that the low volatile/HFSE ratios and high inferred slab surface temperatures for Central Oregon (Figure 18) are consistent with an active but diminished role for volatile fluxing, as would be expected from a young oceanic plate.

3.4. Conclusions

Water contents of Central Oregon magmas are generally lower than those found in other arcs, but elevated compared to oceanic back-arc magmas. Sulfur, Cl, and CO_2 contents are comparable to those found in other arcs. The melt inclusions studied represent the differentiation products of mantle-derived melts that underwent ~16 wt.% fractional crystallization involving mostly olivine. Primitive basalt and Sr-rich basaltic melts were generated by 9–11% partial melting of an enriched mantle source. Primitive depleted melts were likely generated by slightly higher degrees of melting (12–16%) of a more refractory source. Calculated mantle equilibration temperatures are comparable to the hottest temperatures observed in geodynamic models. Calculated mantle equilibration pressures (~1.2 GPa), however, indicate shallow mantle equilibration near the Moho. Inferred mantle melting conditions beneath Central Oregon are similar to other arcs despite the modest subduction-related geochemical signatures expected from a hot slab. Concordance between slab surface geothermometers suggests high temperatures (850–950 °C) for the slab component compared to arcs with older subducting slabs, consistent with geodynamic calculations.

3.5. Bridge Between Chapter III and Chapter IV

The previous chapter (III) explored the role of volatiles on magma generation in Central Oregon. The following chapter (IV) presents a detailed textural and geochemical study of olivine-hosted melt inclusions from a tephra locality near Mt. Shasta, CA. It

includes a detailed discussion of melt inclusion formation and post-entrapment processes that must be considered before interpreting chemical compositions. This chapter will also largely outline the analytical methods used throughout the rest of the dissertation. New data presented in this chapter is also synthesized with existing work in order to provide insight into magma generation processes beneath Northern California.

CHAPTER IV

REVISITING THE COMPOSITIONS AND VOLATILE CONTENTS OF OLIVINE-HOSTED MELT INCLUSIONS FROM THE MOUNT SHASTA REGION: IMPLICATIONS FOR THE FORMATION OF HIGH-MG ANDESITES

This work is currently "in press" in the journal *Contributions to Mineralogy and Petrology*. It was published online under doi: 10.1007/s00410-010-0587-y in November 2010. Coauthors Paul Wallace and Adam Kent assisted in the editorial process. Adam Kent also assisted with LA-ICP-MS analyses. I performed all laboratory work and was the primary author.

Introduction

High-Mg andesites (HMA) are potentially important in the formation of continental crust (Kelemen 1995; Kelemen et al. 2004). Unusually primitive chemical characteristics at elevated SiO_2 contents (Mg# >0.6 with >54 wt.% SiO_2; molar Mg# = MgO/[MgO + FeO]) have raised interest in these compositions because they appear to have (or nearly) equilibrated with a mantle peridotite assemblage and are similar to the bulk continental crust (Rudnick and Fountain 1995). Modern HMAs are found in ''hot'' subduction zone settings characterized by young subducting oceanic crust, ridge subduction, or slab tearing and formation of slab ''windows'' (Kay 1978; Crawford et al. 1989; Defant and Drummond 1990; Yogodzinski et al. 2001; Shimoda et al. 1998; Grove et al. 2003; Kelemen et al. 2004; Pallares et al. 2008). Previous workers have suggested that primary, mantle-derived HMA melts may form by either shallow, wet partial melting of the mantle (e.g., Crawford et al. 1989; Grove et al. 2003) or re-equilibration of slab melts migrating through the wedge (e.g., Kelemen 1995). Distinctions between the origins of HMAs are generally based on trace element ratios and concentrations (i.e., adakites and boninites are subsets of HMAs with elevated Sr/Y (>50) and low TiO2 (<0.5 wt.%), respectively) (Defant and Drummond 1990; Le Bas 2000). Despite previous

studies, important questions remain regarding the origin of HMAs and whether they reflect actual melt compositions formed in equilibrium with mantle peridotite.

HMA magmas have been a topic of recent debate because petrographic evidence for magma mixing calls into question whether HMA melts have a mantle origin (Streck et al. 2007a). The core of this disagreement is a well characterized example from a young (Holocene) cinder cone ~20 km NNE of Mt. Shasta, CA (Anderson 1974; Baker et al. 1994). Anderson (1974) studied olivine-hosted glass inclusions in mafic tephra from this locality. He documented petrographic evidence for magma mixing and concluded that a volatile-rich, primitive melt (with up to ~24 wt.% MgO) existed beneath the Shasta region. Subsequent studies suggested that high-Mg andesite lavas in this region were formed in equilibrium with a depleted harzburgite and may represent near-primary, subduction related melts (Baker et al. 1994; Grove et al. 2002, 2003). Streck et al. (2007a) questioned this interpretation on the basis of complex petrographic textures and proposed a mixing model in which ascending dacitic melts entrained ultramafic country rock (from the Trinity ultramafic complex, a Paleozoic accreted oceanic terrane underlying the Shasta region; Quick 1981) and subsequently mixed with primitive basaltic melt prior to eruption. They concluded that mixing resulted in a late-stage hybrid magma of HMA composition with decoupled primitive and adakitic signatures (high Mg# from ultramafic contaminants and high Sr/Y from the dacite component), and the mixture contained both ultramafic xenoliths and late-stage, lower Mg# magmatic phenocrysts.

Barr et al. (2007) pointed out that spinel inclusions within Fo_{90-94} olivines are significantly more Cr-rich than those found in the Trinity ophiolite. They also argued that the mixing models proposed by Streck et al. (2007a) do not adequately reproduce the trace element and isotopic characteristics of the HMA melts in question. Kelemen and Yogodzinski (2007) also disagreed with the proposed mixing model and argued that Mt. Shasta HMA are similar to those found in the Aleutians and require a primitive, adakitic parental melt. Streck et al. (2007b,c) reasserted their interpretations that (1) disequilibrium textures require a xenocrystic origin for Mg-rich olivines, (2) mixing scenarios are plausible but highly dependent on the choice of dacitic endmember, and (3) Aleutian HMA compositions are not directly comparable to those at Mt. Shasta. To

contribute additional evidence to this ongoing debate, we have re-examined naturally quenched, glassy, olivine-hosted ($Fo_{87–94}$) melt inclusions from Anderson's S17 locality to investigate the compositions and pre-eruptive volatile contents of magmas beneath the beneath Mt. Shasta region.

Samples and methods

Mafic tephra from The Whaleback Mountain (S17 cinder cone) contains approximately 15–20 vol.% crystals based on visual estimates (Anderson 1974; Streck et al. 2007a; Streck, personal communication 2010), higher than the modal analysis (~6 vol.%) reported by Baker et al. (1994) for lava from the same locality. Disequilibrium conditions resulting from magma mixing prior to eruption are indicated by the presence of (1) euhedral, reversely zoned clino and orthopyroxenes (Mg# core: 0.65–0.72; rim: 0.85–0.92) containing dacitic glass inclusions, (2) anhedral, high-Mg# (0.85–0.88) orthopyroxene crystals (opx) (<100 μm to >1000 μm) occasionally rimmed by lower-Mg rims, (3) unzoned, high-Mg ($Fo_{90–94}$) olivine megacrysts rimmed by thin (generally <10 μm) opx or lower-Mg (Fo_{87}) olivine that is similar in composition to skeletal microphenocrysts, and (4) rare, partially resorbed plagioclase megacrysts (Anderson 1974; Baker et al. 1994; Streck et al. 2007a; Streck, personal communication 2010). Additionally, skeletal olivines (Mg# ~0.87) do not exhibit disequilibrium textures and likely crystallized from the hybrid magma shortly before eruption (Streck et al. 2007a). The textural relationships clearly demonstrate that a mixed magma was erupted from the S17 cinder cone.

Only fully enclosed, glassy inclusions from euhedral to subhedral olivines ($Fo_{87–94}$) were targeted in this study to minimize uncertainties associated with melt inclusion formation and evolution. Previously published (and unpublished) melt inclusion data provided by A.T. Anderson augment this data set to permit more robust conclusions about pre-eruptive melt compositions. Loose olivine crystals were picked from three tephra samples: MS-1304 and MS-1404 from Streck et al. (2007a) and the original S173 of Anderson (1974). Olivines were treated with HBF4 to remove attached matrix glass and allow inclusion inspection under refractive index oil (n = 1.678). Melt inclusion and vapor bubble dimensions were measured (Table 5), and selected crystals were ground and

polished into wafers containing doubly intersected glass inclusions. Wafers were analyzed for H_2O and CO_2 using a Thermo-Nicolet Nexus 670 FT-IR spectrometer interfaced with a Continuum IR microscope at the University of Oregon and subsequently mounted in Araldite 502 resin for host crystal and glass analyses by electron microprobe.

All electron microprobe analyses (EPMA) were done using the Cameca SX-100 at the University of Oregon. Hydrous glass compositions were determined using multiple beam conditions during a single spot analysis (15 kV, 10 μm beam diameter, and 10 or 50 nA; see footnote in Table 6). Individual analyses reported in Table 6 are averages of 3–5 analyzed spots. BIR-1G glass was analyzed to monitor accuracy, and element concentrations are within 5% of accepted values. Five representative inclusions were selected to measure SKa peak positions to constrain fo_2 conditions of the glasses (Wallace and Carmichael 1994). Wavelength scans were run at 15 kV using a 5-μm, 50-nA beam for 142 min using anhydrite and pyrrhotite standards to characterize the full wavelength shift ($\Delta\lambda$ SKα = 32.68 ±0.71 x 103 Å).

Trace elements in melt inclusion glasses were analyzed in the W. M. Keck Collaboratory for Plasma Mass Spectrometry at Oregon State University with a VG PQ ExCell quadrupole ICP-MS fitted with a NewWave DUV 193 nm ArF Excimer laser system and using a 70-μm spot size and a 4-Hz pulse rate. Measured trace element concentrations were determined by reference to BCR-2G glass as a calibration standard and using ^{43}Ca as an internal standard. BHVO-2G glass was analyzed to monitor accuracy and precision. In general, measured trace element abundances in BHVO-2G are within 12% of accepted values. Additional analytical details can be found in Kent et al. (2004).

Table 5. Physical descriptions of olivine-hosted melt inclusions.

Inclusion	Host %Fo	Shape	Size (μm)	Bubble[a] (μm)	Vapor Bubble (vol% ±2σ)	Texture/Color	Crystals[b]	Notes
2S173-g	87.4	Triangular	–	None	–	Glassy, lt. brown	–	Skeletal growth
2S173-f	87.5	Triangular	–	None	–	Glassy, lt. brown	–	Skeletal growth
S173-a	87.8	Triangularc	65 x 36 x 36	18	6.9 ±2.3	Glassy, very lt. brown	–	Skeletal?
S173-e	87.8	Wormyc	43 x 31 x 31	20	19.4 ±6.1	Glassy, lt. brown	–	Bubble volume overestimated
S173-c	88.0	Amorphc	35 x 24 x 24	10	5.0 ±3.0	Glassy, lt. brown	–	
2S173-a	93.1	Prolate	210 x 110 x 80	65	14.9 ±1.5	Glassy, lt. brown, wrinkled/faceted	Few v. small spls	‘‘Dusty’’ halo around outer rim
2MS-1304c	93.3	Prolatec	140 x 100 x 100	60	15.4 ±1.6	Glassy, v. dark brown (almost opaque)	–	Center of crystal
S173-f	93.3	Prolatec	60 x 56 x 56	20	4.3 ±1.3	Glassy, lt. brown	–	
2S173-c2	93.3	Oblate	85 x 50 x 70	25	5.3 ±1.3	Glassy, v. lt. brown	Small spl acts as nucleation site	
2S173-e1	93.4	Prolate	90 x 75 x75	40	12.6 ±2.0	Glassy, lt. brown, wrinkled	V. small, acicular radiate from bubble	Many other inclusions present
2S173-e2	93.4	Prolatec	65 9 50 9 50	28	13.5 ± 3.0	Glassy, lt. brown, wrinkled	–	
2S173-d2	93.4	Sphered	D = 120	?	–	Glassy, lt. brown	–	
2MS-1404b	93.5	Prolate	140 x 60 x 60	40	12.7 ±2.0	Glassy, very lt. brown, wrinkled	Single, small spl	Many other inclusions present
2S173-d	93.5	Oblate	85 x 75 x60	35	11.2 ±2.0	Glassy, lt. brown, wrinkled	–	Many other inclusions present
2MS-1404d	93.5	Prolate	180 x 55 x 55	32	6.0 ±1.2	Glassy, brown, wrinkled	Single, v. small px or plag	Many other inclusions present
2MS-1404d3	93.5	Prolatec	80 x 50 x 50	30	13.5 ±2.8	Glassy, lt. brown	2, small, red spls embedded in wall	
2MS-1404a	93.6	Sphere	D = 115	55	10.9 ±1.2	Glassy, wrinkled, lt. brown	~μ40 lm spl	
MS-1404j	93.6	Prolatec	60 x 40 x 40	20	8.3 ±2.6	Glassy, lt. brown, faceted	V. small, scarce spls	Relict grain boundary
2MS-1304a	93.7	Prolate	65 x 45 x 40	26	15.0 ±3.6	Glassy, lt. brown	Single, small spl	
2MS-1404c	93.7	Prolate	65 x 55 x 55	25	7.9 ±2.0	Glassy, lt. brown	Single, small spl	Plag-rich melt attached to host

[a] diameters reported [b] mineral inclusion size descriptions: small (5-10 μm diameter), v. small (5 μm diameter); spl = spinel, px = pyroxene, plag = plagioclase [c] dimensions described after intersection or dimensions approximated as prolate spheroid [d] assumed spherical shape, dimensions described after intersection

H_2O and CO_2 concentrations were calculated from IR peak absorbances determined by FTIR and using the Beer- Lambert law. Wafer thicknesses were first determined with a digital micrometer and then checked using the interference fringe method of Wyszocanski and Tani (2006); thicknesses determined by both methods agree to within 2 μm and were confirmed by optical inspection for several wafers. H_2O concentrations were determined using the 3550 cm^{-1} peak, 4520 + 5200 cm^{-1} peaks, or 4520 + 1630 cm^{-1} peaks. CO_2 concentrations were determined using the CO_3^{2-} doublet at 1515-1430 cm^{-1}. Absorption coefficients (with the exception of ε_{3550}) are compositionally dependent and were calculated using average glass compositions determined by EMPA and equations from Dixon and Pan (1995) and Mandeville et al. (2002). Glass densities were calculated using oxide molar volumes reported in Luhr (2001), and hydrous densities were determined by iteration between the density and Beer–Lambert calculations. Comparison of uncertainties determined by formal error propagation and Monte Carlo simulations are in agreement and suggest average 1r relative uncertainties of 13 and 19% for H_2O and CO_2 concentrations, respectively

Host olivine compositions were determined by averaging 4-5 point analyses of olivine (>100 μm away from inclusions and crystal edges) for each crystal. Olivine compositional profiles, extending up to 200 μm away from inclusions, were also measured for six samples. The profiles show elevated FeO contents that decrease until far-field olivine FeO contents are reached (≤35 μm away from glass inclusion-olivine host interfaces; cf., Anderson 1974). Observed melt inclusion and host olivine compositions (%Fo) are reported in Table 6.

Table 6. Melt inclusion compositions. Dashed line separates low-CaO glasses (left) from high-CaO glasses (right).

Inclusion	2S173 -g	2S173 -f	S173 -a	S173 -e	S173 -c	2S173 -a	2MS 1304c	S173 -f	2S173 -c2	2S173 -e1	2S173 -e2	2S173 -d2	2MS 1404b	2S173 -d
SiO_2	57.9	57.6	56.7	56.4	57.0	54.7	55.2	55.3	54.3	54.2	53.8	54.0	54.1	54.4
TiO_2	0.72	0.73	0.65	0.69	0.69	0.71	0.60	0.59	0.72	0.68	0.68	0.69	0.75	0.65
Al_2O_3	16.0	15.2	16.8	17.8	17.8	15.6	14.7	15.5	16.1	14.6	15.0	15.2	17.1	14.1
FeO^{Total}	5.56	5.88	5.06	5.15	5.11	4.29	4.48	3.73	3.78	4.10	3.91	4.61	4.33	4.07
MnO	0.10	0.11	0.08	0.10	0.08	0.10	0.09	0.07	0.08	0.07	0.07	0.08	0.08	0.08
MgO	4.54	4.41	4.08	4.32	4.69	6.38	7.51	6.49	5.80	5.84	7.01	6.95	5.18	7.17
CaO	7.90	8.40	8.30	9.50	9.20	12.3	11.6	12.5	13.2	12.6	12.3	9.52	13.4	11.8
Na_2O	2.45	2.73	2.22	3.08	3.73	2.52	0.98	2.42	3.04	1.56	2.02	2.00	2.76	1.94
K_2O	1.05	1.00	0.79	0.84	0.86	0.43	0.29	0.38	0.44	0.35	0.37	0.55	0.38	0.38
P_2O_5	0.29	0.31	0.14	0.16	0.16	0.35	0.31	0.18	0.40	0.35	0.34	0.30	0.37	0.32
S[a]	0.02	0.02	0.08	0.07	0.07	0.15	0.22	0.15	0.14	0.21	0.20	0.22	0.19	0.19
Cl	0.16	0.14	0.13	0.15	0.14	0.26	0.22	0.18	0.27	0.27	0.26	0.29	0.28	0.24
H_2O	1.70	1.22	3.45	1.47	0.78	1.58	3.34	3.79	0.90	4.09	2.75	2.45	1.51	3.23
(± 1s.d.)	(0.18)	(0.16)	(0.23)	(0.20)	(0.46)	(0.23)	(0.53)	(0.59)	(0.06)	(0.34)	(0.49)	(0.30)	(0.12)	(0.38)
CO_2 ppm (± 1s.d.)	b.d.	b.d.	516 (114)	b.d.	b.d.	320 (25)	726[b] (122)	753 (109)	b.d.	749 (48)	485 (55)	959 (59)	b.d.	678 (90)
Total	98.3	97.7	98.6	99.7	100.3	99.4	99.5	101.4	99.2	99.0	98.9	97.0	100.4	98.8
%Fo Host	87.4	87.5	87.8	87.8	88.0	93.1	93.3	93.3	93.3	93.4	93.4	93.4	93.5	93.5
S^{6+}/S^{Tot} (± 1s.e.)	-	-	-	-	0.972 (0.027)	-	0.686 (0.015)	-	-	-	0.935 (0.021	-	-	0.904[c] (0.020)
T_{erupt} (ºC)[d]	1015	1028	944	1007	1048	1076	1048	1012	1076	983	1059	1076	1028	1053
SiO_2	59.6	59.0	59.1	57.3	57.0	53.32	54.72	53.72	52.45	53.98	53.36	54.61	51.96	54.19
TiO_2	0.72	0.73	0.66	0.69	0.69	0.61	0.53	0.50	0.61	0.58	0.59	0.62	0.61	0.57
Al_2O_3	16.2	15.2	17.1	17.8	17.8	13.41	12.92	13.17	13.53	12.57	13.10	13.56	14.02	12.34
FeO^{Total}	5.92	6.39	5.59	5.38	5.18	7.02	7.02	7.02	7.02	7.02	7.02	7.02	7.02	7.02
MnO	0.11	0.11	0.08	0.10	0.08	0.08	0.08	0.06	0.07	0.07	0.06	0.08	0.06	0.08
MgO	5.65	6.23	5.70	5.21	4.93	12.13	13.19	12.40	12.01	13.03	12.76	13.06	12.46	13.11
CaO	8.00	8.35	8.49	9.49	9.18	10.58	10.16	10.60	11.07	10.80	10.72	8.50	10.99	10.37
Na_2O	2.48	2.72	2.26	3.08	3.74	2.17	0.86	2.05	2.54	1.35	1.76	1.80	2.26	1.70
K_2O	1.06	1.00	0.80	0.84	0.86	0.38	0.26	0.32	0.37	0.30	0.32	0.49	0.31	0.33
P_2O_5	0.30	0.31	0.15	0.16	0.16	0.30	0.27	0.16	0.34	0.30	0.30	0.27	0.30	0.28
S	0.02	0.02	0.08	0.07	0.07	0.13	0.20	0.13	0.12	0.18	0.18	0.20	0.16	0.17
Cl	0.16	0.14	0.13	0.15	0.14	0.23	0.20	0.16	0.23	0.24	0.23	0.26	0.23	0.22
H_2O	1.67	1.17	3.34	1.45	0.78	1.35	2.86	3.17	0.75	3.40	2.32	2.12	1.26	2.73
(± 1s.d.)	(0.18)	(0.15)	(0.23)	(0.20)	(0.46)	(0.19)	(0.45)	(0.50)	(0.05)	(0.28)	(0.41)	(0.26)	(0.10)	(0.32)
CO_2 ppm (± 1s.d.)	-	-	498 (110)	-	-	273 (18)	622 (104)	631 (91)	-	622 (40)	409 (47)	823 (51)	-	573 (76)
Oladd wt%	2.3	4.1	3.4	1.9	0.5	18.2	17.7	19.5	20.3	22.0	18.6	18.1	22.4	18.8
T_{trap} (ºC)[d]	1055	1098	1001	1043	1058	1260	1204	1191	1289	1188	1229	1248	1273	1221

Table 6. Extended.

Inclusion	2MS 1404d	2MS 1404d3	2MS 1404a	MS 1404j	2MS 1304a	2MS14 04c	1s.e. (%)
SiO_2	55.9	54.7	54.1	53.0	53.0	53.9	0.4
TiO_2	0.65	0.66	0.65	0.73	0.77	0.74	1.8
Al_2O_3	13.3	14.5	14.3	16.5	17.0	16.2	0.9
FeO^{Total}	3.94	3.74	4.45	3.89	3.55	4.16	1.7
MnO	0.07	0.07	0.08	0.08	0.07	0.08	8.9
MgO	7.52	7.44	7.13	4.87	4.69	4.21	2.7
CaO	11.9	12.2	11.9	13.9	14.1	14.2	0.7
Na_2O	2.05	2.01	1.64	2.95	2.88	2.32	2.7
K_2O	0.35	0.33	0.30	0.36	0.34	0.31	2.2
P_2O_5	0.32	0.33	0.33	0.16	0.40	0.38	1.5
S^a	0.20	0.21	0.22	0.19	0.19	0.21	2.0
Cl	0.24	0.25	0.27	0.24	0.31	0.30	1.2
H_2O (± 1s.d.)	3.10 (0.34)	2.77 (0.18)	3.65 (0.51)	0.87 (0.05)	1.27 (0.07)	2.42 (0.36)	13.3
CO_2 ppm (± 1s.d.)	666 (63)	756 (56)	647 (140)	425 (100)	292 (197)	481 (118)	18.7
Total	99.7	99.2	99.0	97.9	98.6	99.5	-
%Fo Host	93.5	93.5	93.6	93.6	93.7	93.7	-
S^{6+}/S^{Tot} (± 1s.e.)	-	-	0.912 (0.020)	-	-	-	-
T_{erupt} (ºC)[d]	1066	1071	1037	1039	1015	961	-
SiO_2	54.89	53.89	54.04	51.73	51.39	52.22	
TiO_2	0.56	0.56	0.57	0.60	0.62	0.60	
Al_2O_3	11.54	12.50	12.49	13.68	13.75	13.10	
FeO^{Total}	7.02	7.02	7.02	7.02	7.02	7.02	
MnO	0.06	0.06	0.07	0.06	0.06	0.06	
MgO	13.30	13.15	13.45	12.51	12.78	13.14	
CaO	10.28	10.53	10.38	11.52	11.46	11.44	
Na_2O	1.78	1.73	1.44	2.44	2.33	1.88	
K_2O	0.31	0.28	0.26	0.30	0.27	0.25	
P_2O_5	0.28	0.28	0.29	0.14	0.32	0.30	
S	0.17	0.18	0.20	0.16	0.16	0.17	
Cl	0.21	0.22	0.25	0.21	0.26	0.25	
H_2O (± 1s.d.)	2.61 (0.28)	2.32 (0.15)	3.09 (0.43)	0.71 (0.04)	1.02 (0.06)	1.94 (0.29)	
CO_2 ppm (± 1s.d.)	560 (53)	633 (46)	548 (119)	349 (82)	235 (158)	387 (95)	
Oladd wt%	18.9	19.0	19.3	23.7	25.7	27.1	
T_{trap} (ºC)[d]	1232	1238	1209	1301	1292	1253	-

Table 6. Continued

Inclusion	2S173 -g	2S173 -f	S173 -a	S173 -e	S173 -c	2S173 -a	2MS 1304c	S173 -f	2S173 -c2	2S173 -e1	2S173 -e2	2S173- d2	2MS 1404b	2S173 -d
Li	18.4	11.9	18.1	11.9	25.2	14.6	5.2	4.3	3.7	5.3	4.9	5.0	6.1	4.3
Sc	30.2	20.8	23.0	28.8	39.1	49.3	27.8	28.8	27.4	29.6	36.7	21.4	27.7	24.9
V	196	216	185	212	233	329	190	198	210	212	245	234	233	214
Cr[e]	343	90	270	344	760	1775	192	394	189	387	4170	154	226	373
Rb	19.3	23.1	18.7	19.3	22.2	10.2	3.9	7.2	4.9	4.0	4.4	7.8	4.9	4.7
Sr	805	897	846	943	842	1029	1178	860	1042	1043	1071	1073	1048	988
Y	12.9	10.5	9.9	11.0	11.2	11.6	7.1	7.5	8.4	8.3	9.2	7.2	6.8	6.8
Zr	102.1	89.7	82.8	96.5	101.7	81.3	62.7	59.9	72.4	71.5	77.6	68.3	64.3	57.7
Nb	3.1	3.2	3.0	3.1	3.1	2.0	1.4	1.2	1.7	1.4	1.6	1.8	1.4	1.5
Ba	257	274	234	248	269	126	74	91	82	73	80	102	85	84
La	11.4	12.7	10.3	12.0	10.8	10.2	9.3	9.2	10.3	10.2	10.1	10.5	9.6	9.0
Ce	30.8	34.4	31.1	34.7	35.7	34.9	23.2	27.3	26.3	25.8	28.6	30.1	29.3	27.2
Pr	3.4	3.8	3.2	4.0	3.7	4.0	2.9	3.1	3.4	3.4	3.4	3.3	3.6	2.9
Nd	16.8	14.4	12.4	12.8	12.6	13.1	12.3	11.9	14.2	12.5	14.0	13.1	12.7	11.3
Sm	3.2	2.7	2.5	2.8	2.1	3.2	2.4	1.6	2.6	1.8	2.1	2.6	2.1	2.2
Eu	0.9	1.1	0.9	1.0	0.9	1.1	0.8	0.8	0.7	0.7	0.7	0.8	0.7	0.7
Gd	2.9	2.4	1.3	2.1	1.7	2.9	1.6	1.7	1.7	2.0	2.1	1.6	1.9	1.9
Dy	2.1	2.0	1.6	2.0	2.3	1.4	1.2	1.1	1.4	1.4	1.2	1.5	1.3	1.3
Er	0.8	1.0	0.7	1.4	1.0	1.5	0.4	0.6	0.7	1.2	1.0	1.0	0.8	0.7
Yb	1.0	1.0	1.0	1.5	1.6	1.2	0.9	0.6	0.5	0.8	1.1	0.8	0.7	0.7
Hf	3.1	2.8	2.2	3.2	2.6	2.4	1.8	1.5	2.4	1.9	1.5	1.9	1.3	1.6
Ta	0.2	0.2	0.1	0.2	n.d.	n.d.	0.06	0.08	0.10	0.08	0.12	0.04	0.09	0.11
Pb	6.0	7.6	5.9	5.8	6.8	5.0	2.8	3.3	2.5	2.9	2.6	3.8	3.0	3.0
Th	1.9	2.1	1.6	2.3	2.0	1.7	1.0	1.1	1.1	1.0	0.9	1.1	1.0	0.9
U	1.0	0.9	1.0	0.9	0.8	0.6	0.3	0.4	0.4	0.3	0.4	0.4	0.4	0.4

Specific procedures for electron probe microanalyses: Hydrous glass compositions were determined using multiple beam conditions during a single spot analysis (15 kV, 10 μm beam diameter) with the following counting times: 30 (Mn), 60 (Si, Mg), 80 (K, Ca, Al), 100 (S, Cl, Ti, P), 120 (Na), and 180 s (Fe). Na, Si, K, Al, Fe, Mg, Ca, and Mn were analyzed under a 10 nA beam current. The beam current was then increased to 50 nA, during the same analysis, to measure S, Cl, P, and Ti. Linear off-peak background corrections were applied to K, Mn, S, Cl, Ti, and P intensities. The MAN background continuum absorption intensity correction was applied to Na, Si, Al, Mg, Fe and Ca (Donovan and Tingle 1996). Interference corrections were applied to Fe for interference by Mn (Donovan et al. 1993). Effects of element migration were corrected by performing linear regressions to time zero on Na, K, Al, and Si counts (Hanson et al. 1996; Morgan and London 1996). Host olivine compositions (Si, Mg, Fe, Ca, Ni, Mn) were determined at 15 kV and 50 nA with a 2 μm beam diameter. On-peak counting times were: 40 s (Si), 80 s (Ca), 90 s (Mg, Ni, Mn), and 135 s (Fe). Linear off-peak background corrections were applied to Ni

and Mn and the MAN background continuum absorption intensity correction was applied to Si, Mg, Fe, and Ca (Donovan and Tingle 1996). Interference corrections were applied to Fe for interference by Mn (Donovan et al. 1993).

Table 6. Extended continued.

Inclusion	2MS 1404d	2MS 1404d3	2MS 1404a	MS 1404j	2MS 1304a	2MS 1404c	1 std err (%)
Li	4.1	3.5	2.4	4.7	3.8	6.9	14
Sc	29.0	29.7	29.1	35.3	31.1	31.6	7
V	194	203	193	229	261	301	5
Cr[e]	225	237	243	599	848	506	20
Rb	4.2	3.6	2.8	3.8	3.3	3.6	5
Sr	995	1040	1029	1073	1122	1087	2
Y	7.7	7.5	7.1	8.4	6.7	7.5	10
Zr	66.8	72.2	66.3	72.3	65.9	61.7	9
Nb	1.5	1.4	1.3	1.5	1.4	1.4	10
Ba	75	67	54	76	68	74	3
La	9.2	9.8	9.4	10.3	9.7	9.6	3
Ce	24.9	24.8	24.5	31.1	33.0	32.6	3
Pr	3.2	3.3	3.4	3.5	3.3	3.6	7
Nd	11.5	13.3	11.5	13.0	12.8	13.2	5
Sm	1.7	2.4	1.9	2.9	1.6	2.2	11
Eu	0.8	0.8	0.8	1.0	0.8	0.9	9
Gd	1.9	1.6	1.4	1.8	0.8	1.2	15
Dy	1.4	1.6	1.1	1.9	1.6	1.5	11
Er	0.8	0.9	0.8	0.8	0.8	0.6	13
Yb	0.6	0.8	0.7	0.5	0.4	0.6	19
Hf	1.5	1.6	1.8	2.1	1.9	1.7	13
Ta	0.08	0.09	0.06	0.07	n.d.	n.d.	29
Pb	2.4	2.6	2.4	2.8	2.8	3.2	13
Th	0.9	0.9	0.9	1.0	0.9	1.0	10
U	0.3	0.3	0.3	0.4	0.3	0.4	12

[a] S contents are minima and were measured prior to S Kα wavescans. Initial glass analyses use a S-peak set to a position 1/3 of the way from pyrite toward anhydrite (~NNO).
[b] Both CO_2 (molecular) and CO_3^{2-} peaks present in spectra.
[c] S Kα on nearby inclusion
[d] Temperatures calculated after Putrirka et al. (2007) using equations 2 and 3; see text for explanations of $T_{trapping}$ and $T_{eruption}$
[e] High Cr contents reflect analyses including Cr-rich spinels. Mass balance calculations indicate no more than ~3 wt% spinel contamination in analyses

Results

Major elements and volatiles

Olivine crystals in the S17 tephra span a wide range in composition from Fo_{86} to Fo_{94}. Samples from this study exhibit a distinct bimodal distribution between lower Fo (%Fo = 87–89) and higher Fo (%Fo = 93–94) core compositions. Additional data from Anderson (1974) and Baker et al. (1994), however, display a more continuous variation in olivine core compositions from high to low Fo contents (Figure 19a). The strong bimodality observed in this study is likely due to the strict selection criteria used here (i.e., only inclusions observed to be fully enclosed within loose crystals as opposed to analyzing exposed inclusions from mounted olivines). Higher Fo olivines are large (0.5–2 mm diameters) and have broad, homogenous, high-Fo cores enclosed in thin (generally <10 μm) rims of Fe-rich orthopyroxene or Fo_{87} olivine (cf., Anderson 1974; Streck et al. 2007a). The Mg-rich cores contain ellipsoidal (major axis >65 μm) glassy inclusions with large vapor bubbles (>5 vol.%). Lower Fo olivines tend to be smaller, exhibit skeletal growth morphologies and contain either small ellipsoidal (major axis <50 μm) glassy inclusions with vapor bubbles up to ~7 vol.% (maximum) or symmetrically distributed inclusions (with respect to crystal center in 010-plane; cf., Faure and Schiano 2005) with or without vapor bubbles. The majority of melt inclusions that we selected and analyzed were in ~Fo_{93}, euhedral to subhedral olivines. In many cases, a small (<10 μm), red-brown Cr-spinel (Cr# ~0.7–0.8; Cr# = $[Cr/(Cr + Al)]_{molar}$; Baker et al. 1994) is embedded within the wall of the inclusion and likely acted as the initiation site for inclusion formation during olivine growth. Spinel inclusions are primarily found in high-Fo olivines (Table 5). Statistically significant differences (p-value ≤ 0.05) in CaO, TiO_2, and Cl concentrations are observed between spinel-bearing and spinel-free inclusions within the high-Fo olivines (average CaO, TiO_2, and Cl compositions are 1.0, 0.08, and 0.04 wt.% higher, respectively, in spinel-bearing inclusions).

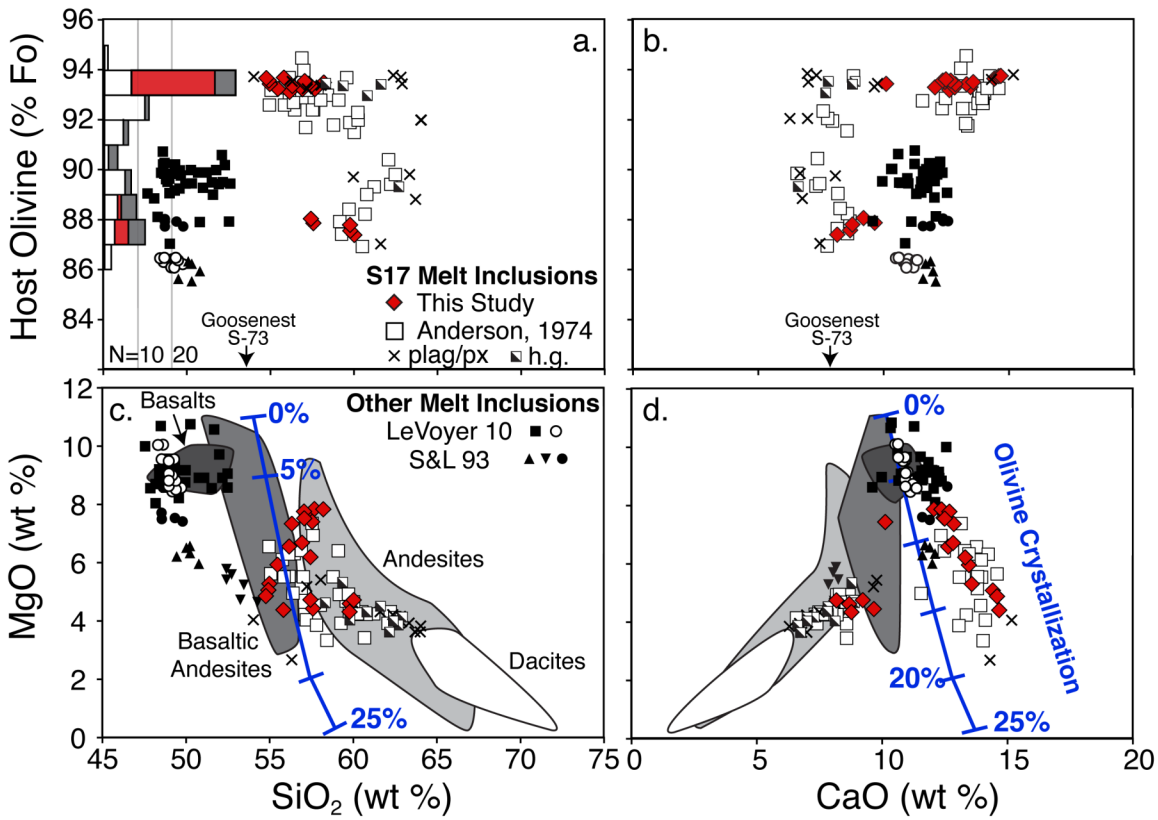

Figure 19. (a–d) Fully enclosed S17 melt inclusion compositions (uncorrected for post-entrapment effects) from this study (red diamonds) and Anderson (1974) (open squares) compared with other melt inclusions (Sisson and Layne 1993 and Le Voyer et al. 2010; symbol key shown in Fig. 3) and bulk lava compositions (labeled fields) from the Shasta region (whole-rock data from Smith and Carmichael 1968; Anderson 1974; Baker et al. 1994; Bacon et al. 1997; Grove et al. 2002; Elkins-Tanton et al. 2001; Grove et al. 2005; Magna et al. 2006; Streck et al. 2007a). Shown for comparison are S17 melt inclusions (from this study and Anderson) with hourglass morphologies (half-filled square) and inclusions containing plagioclase or pyroxene crystals (crosses). All compositions are normalized to 100% on a volatile-free basis. Blue lines in panels (c) and (d) show fractional crystallization path for melt undergoing olivine-only crystallization (i.e., post-entrapment crystallization within melt inclusions). Histogram of host olivine compositions (from this study and Anderson 1974) and olivines from S17 lava (85-41) by Baker et al. (1994) (gray bars) is shown on the left side of panel (a).

Melt inclusion compositions (normalized on a volatile-free basis) range from 55 to 62 wt.% SiO_2 and 3–8 wt.% MgO (Figure 19; Table 6). Glass compositions measured in this study are comparable to those determined by Anderson (1974) and more SiO_2- and CaO-rich than other inclusions from the region (Sisson and Layne 1993; Le Voyer et al. 2010) (Figure 19). Fully enclosed inclusions are divided into two chemically distinct

groups: high-CaO (>10 wt.%) glasses found only within high-Fo (%Fo >91) olivines and lower-CaO (<10 wt.%) glasses in olivines ranging from $Fo_{93.7}$ to $Fo_{86.9}$. Additionally, hourglass inclusions (i.e., not fully enclosed; Anderson 1991) and inclusions in contact with a large, silicate mineral inclusion or daughter crystals (plagioclase and/or pyroxene) are shown for comparison with the unrestored (see below), fully enclosed inclusion compositions in Figure 19, Figure 20, and Figure 21. The inclusions containing plagioclase and/or pyroxene crystals are not considered further because of the difficulty of accounting for post-entrapment effects. Additionally, we ignore possible effects of spinel on post-entrapment crystallization in the fully enclosed inclusions because the compositional differences between high-CaO inclusions with and without spinels are small.

The melt inclusions are similar to whole-rock basaltic andesite and andesite lava compositions from the Shasta region with respect to all major oxides except CaO and FeO^T. High-CaO inclusions trend away from the bulk lavas and follow an olivine crystallization path toward higher CaO (~15 wt.%), whereas low-CaO melts follow the bulk lava trend (Figure 19). High-CaO inclusions also have lower FeO^T than bulk lavas at similar MgO values. Hourglass inclusions plot toward the evolved end of the fractionation trend (Figure 19b, c), suggesting that those found in lower Fo olivines may represent arrested formation of late-stage inclusions (e.g., Streck et al. 2007a, b, c). Many inclusions (both high-CaO and low-CaO) appear out of equilibrium with host crystal compositions (Figure 20). Additionally, thin shells (<35 μm) of Fe-rich olivine are observed adjacent to the inclusion glass–host crystal interface in olivines with %Fo>91 (cf., Anderson 1974). Fe-rich olivine shells are not observed surrounding low-CaO inclusions in low-Fo olivines. These observations suggest that post-entrapment modification processes have affected many of the melt inclusion compositions, and these effects need to be addressed before interpretations can be made.

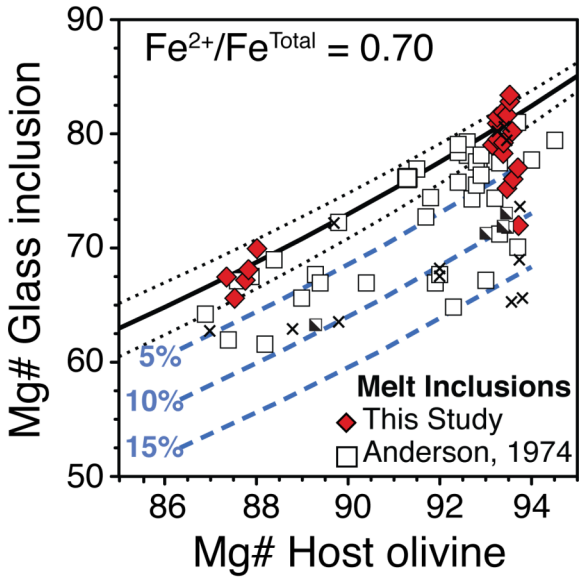

Figure 20. Glass inclusion compositions plotted against host olivine compositions (where Mg# = [100xMg/(Mg + Fe^{2+})]molar). Symbols as in Figure 19. Thick dark line (and short-dashed lines above and below) shows equilibrium between a melt and olivine at ~NNO + 1.5 (Fe^{2+}/Fe^{Total} = 0.70; K_D = 0.30 ± 0.03; Roeder and Emslie 1970; Toplis 2005). Blue long-dashed lines labeled 5, 10, and 15% approximately show the amount of post-entrapment olivine crystallization (in wt.%) experienced by melt inclusions.

Measured dissolved volatile contents for melt inclusions are shown in Figure 21 and compared to inclusions from other regions. H_2O contents of inclusions studied here vary from 0.8 to 4.1 wt.%. These values agree with H_2O contents determined by Anderson (1974) using the electron probe H_2O-by-difference technique (0–6.4 wt.%). The H_2O data extend to higher values than those at several nearby volcanic centers analyzed by Sisson and Layne (1993) and LeVoyer et al. (2010) using an ion microprobe (0.4–3.3 wt.%) (Figure 21a). CO_2 contents vary from below detection (<50 ppm) up to 750 ppm. The elevated H_2O and CO_2 contents found in both low-CaO and high-CaO melt compositions are comparable to values found in other subduction zone magmas (e.g., Marianas and Central America). Maximum H_2O contents dissolved in high-CaO inclusions are 4–6 wt.% and are higher than mafic magmas from Central Oregon (Ruscitto et al. 2010). Vapor saturation pressures (which represent minimum pressures of inclusion formation due to the presence of a vapor bubble in each inclusion) are ~150 MPa for low-CaO inclusions and ~200 MPa for high-CaO inclusions (calculated after Papale et al. 2006). Average dissolved S and Cl contents are greater in high-CaO

inclusions (2160 ±470 (1 s.d.) ppm S; 2420 ±430 ppm Cl) than in low-CaO inclusions (470 ±250 ppm S; 1250 ±230 ppm Cl). Sulfur contents in Shasta S17 melt inclusions are comparable to those from Central Oregon and many other arcs, but Cl contents in high-CaO melt inclusions are higher than those typically found at other locations. S^{6+}/S_{Total} ratios suggest oxidizing conditions (≥NNO +1) for both high- and low-CaO inclusions (Table 6). Hourglass inclusions have lower H_2O, CO_2, and S than many of the fully enclosed inclusions, but comparable amounts of dissolved Cl (Figure 21).

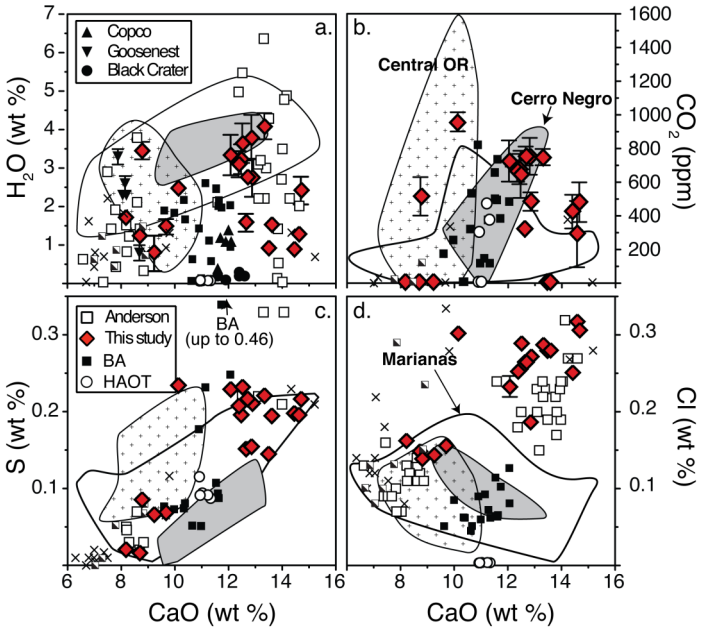

Figure 21. Dissolved volatiles and CaO contents of S17 melt inclusions (unrestored; symbols as in Figure 19). (a, b) H_2O and CO_2 concentrations for melt inclusions were determined by FTIR in this study compared to H_2O contents determined using the H_2O-by-difference electron microprobe technique of Anderson (1974). Black triangles (Copco and Goosenest along volcanic front) and circles (Black Crater in back arc) shown in panel a are from Sisson and Layne (1993). Black squares (basaltic andesite [BA] samples 85-1a, 85-47, 95-15) and open circles (high alumina olivine tholeiite [HAOT] 85-38) are rehomogenized melt inclusions from Le Voyer et al. (2010). Maximum H_2O and CO_2 contents in S17 inclusions (determined by FTIR) are 4.1 wt.% and 760 ppm, respectively. (c, d) Average S and Cl contents are greater in high-CaO (2160 ppm S; 2420 ppm Cl) inclusions than in low-CaO inclusions (470 ppm S; 1250 ppm Cl). Maximum observed volatile contents are interpreted as minimum pre-eruptive magmatic concentrations. Volatile comparisons with melt inclusions from other studies (uncorrected for PEC) are shown: Cerro Negro(gray field) from Roggensack et al. (1997); Marianas (white field) from Kent and Elliot (2002); Shaw et al. (2008); Central Oregon (stippled field) from Ruscitto et al. (2010).

Post-entrapment modification of olivine-hosted melt inclusions

Caution is warranted when making chemical comparisons between raw (unrestored) melt inclusion data and genetically related bulk rocks because melt inclusions commonly have experienced post-entrapment modification effects (e.g., olivine crystallization; Danyushevsky et al. 2002a). Figure 20 illustrates that many of the analyzed melt inclusion compositions are not in Fe–Mg equilibrium with their host olivine crystals. Therefore, the melt inclusion compositions must be restored before more meaningful comparisons with bulk lavas can be made. Restored melt inclusions yield information about parental magma compositions provided that they did not sample unrepresentative boundary layers at their time of formation (Watson et al. 1982; Bacon 1989; Kent 2008). Inclusions (fully enclosed low-CaO and high- CaO, as well as hourglass and crystal-bearing inclusions) show limited variability in CaO/Al_2O_3 over a large (~4wt.%) range in Al_2O_3, suggesting that melt inclusions studied did not experience significant boundary layer effects during trapping (Faure and Schiano 2005), consistent with result in most natural sample suites (Kent 2008).

Post-entrapment modification (PEM) results from the crystallization of olivine along the interior walls of the inclusion during cooling and diffusive re-equilibration of the newly formed olivine with the host crystal (Lowenstern 1995; Danyushevsky et al. 2000, 2002a; Gaetani and Watson 2000, 2002; Schiano 2003; Kent 2008). Effects of PEM are evident in Figure 22 (FeO^T vs. MgO), in which melts in equilibrium with a particular olivine composition fall on a line with constant slope. A trapped melt inclusion is assumed to initially be in equilibrium with its host crystal. Instantaneous cooling-induced crystallization of olivine would cause the melt inclusion composition to evolve toward lower MgO contents through the preferential depletion of the forsterite over fayalite component from the melt (gray line in Figure 22b). In reality, cooling and crystallization are not instantaneous and precipitation of increasingly Fe-rich olivine produces a compositional gradient between the host crystal and the newly formed olivine layer. Diffusive Fe–Mg re-equilibration between the newly formed Fe-rich olivine, the comparatively high Fe/Mg melt inclusion and the Fe-poor olivine host results in a net decrease in Fe from the inclusion (Danyushevsky et al. 2000, 2002b; Gaetani and Watson 2000, 2002; concave upward lines in Figure 22b).

FeO^T contents in high-CaO inclusions are low (~4–5 wt.%) compared to whole-rock samples (~6–8 wt.%) at equivalent MgO contents (see higher MgO inclusions in Figure 22a). Additionally, Fe-enriched olivine shells are only observed surrounding high-CaO inclusions within high Fo olivines, suggesting that these inclusions have undergone diffusive Fe–Mg exchange with the host crystal (Figure 22c). These profiles indicate incomplete melt inclusion-host olivine re-equilibration.

We assessed PEM in the high-CaO inclusions using a combination of forward and reverse modeling to determine whether inferred primary melt inclusion compositions are able to evolve to observed inclusion compositions over geologically reasonable timescales and cooling intervals. We then compared modeling results with observed vapor bubble volumes in the inclusions and those expected to form over estimated cooling intervals in order to evaluate whether extents of crystallization inferred from the modeling are consistent with physical observations.

Danyushevsky method: equilibrium olivine and FeO^T addition

The most commonly used method to restore melt inclusions back to their initial trapped compositions is through incremental addition of equilibrium olivine into the glass composition until Fe–Mg equilibrium is established with the host crystal (e.g., Sobolev and Chaussidon 1996; Danyushevsky et al. 2000). This correction method, however, requires that either diffusive loss of FeO^T out of the inclusion is negligible or forces an assumption to be made about initial FeO^T contents and oxidation states. Erroneously low estimates of olivine post-entrapment crystallization (PEC) result if diffusive Fe-loss is not negligible and is ignored or if initial FeO^T contents are underestimated (Danyushevsky et al. 2000). Oxidation state of the melt is another important consideration when applying PEC corrections. Highly oxidizing melt conditions result in equilibrium with Mg-rich olivines. As a result, estimated amounts of olivine PEC decrease by ~5 wt.% for a 0.1 reduction in melt Fe^{2+}/Fe^T. All olivine PEC corrections have been calculated assuming a constant f_{O2} of ~NNO +1.5, equivalent to $Fe^{2+}/Fe^T = 0.70$ (Table 6). This f_{O2} value is reasonable based on measured SKα peak shifts and is more oxidizing than the experimentally determined estimate for Shasta magmas (NNO +1) by Grove et al. (2005).

FeO^T contents of primitive (MgO >8 wt.%) whole-rock compositions and re-homogenized melt inclusions from the Shasta region are ~6 wt.% for HMA lavas (which may themselves represent mixtures) and ~7–8 wt.% for basaltic andesites and other high-CaO (>10 wt.%) compositions. Comparison between these S17 inclusions and primitive compositions suggests loss of ~2–4 wt.% FeO^T (absolute) (Figure 22a). We assume that high-CaO glass inclusion compositions initially contained ~7 wt.% to be consistent with the whole-rock data and FeO^T contents of other HMA compositions (e.g., Wood and Turner 2009). Restored melt inclusion compositions were calculated following the procedures described in Danyushevsky et al. (2000) at constant f_{O2} (NNO +1.5). Low-CaO inclusions (from this study) are not surrounded by Fe-enriched olivine shells, and FeO^T was not added back into these compositions during olivine PEC corrections. Restored compositions (Table 6) suggest that high-CaO inclusions underwent ~18–27 wt.% post-entrapment olivine crystallization. In contrast, calculated extents of crystallization are significantly lower for low-CaO inclusions (<5 wt.%).

Gaetani and Watson method: forward cooling models

Large extents of PEM for the high-CaO inclusions result in significant compositional corrections. Therefore, we used a finite difference model developed by E. B. Watson and described in Gaetani and Watson (2000, 2002), modified to include the olivine-melt partitioning equations of Putrirka et al. (2007) (incorporating the effects of H_2O), to simulate cooling of the restored high-CaO melt inclusion compositions. In this model, olivine crystallization and Fe-diffusion were assumed to occur only during the pre-eruptive cooling interval ($T_{trapping}$ to $T_{eruption}$). Upon eruption and ejection from the vent, quenching was assumed to be too rapid for significant amounts of olivine crystallization or diffusive re-equilibration to continue ($T_{eruption}$ to $T_{glass\ transition}$). Pre-eruptive cooling intervals were estimated using the olivine-melt partitioning equations (eq. 2 and 3) developed in Putrirka et al. (2007) (Table 6). $T_{trapping}$ (temperature of melt inclusion formation) was calculated using the PEM-corrected melt inclusion compositions. $T_{eruption}$ (temperature of eruption) was calculated using the analyzed (unrestored) inclusion compositions (both temperatures were calculated at 100 MPa since pressure effects over several hundred MPa are negligible). Using these constraints, pre-

eruptive cooling intervals ($T_{trapping}$ - $T_{eruption}$) are estimated to be 200–250 ºC. To maintain consistency with observations, we further subdivide the pre-eruptive cooling interval into an initial period of slower cooling, representing olivine growth and melt inclusion formation, and a later period of rapid cooling representing a magma mixing event, as required by phenocryst and textural data.

Figure 22b and c illustrates model results for one of the six modeled inclusions (2MS-1304c). Models that best reproduce both the observed (unrestored) glass compositions and host olivine Fe–Mg profiles are those combining an initial 75–100 ºC cooling interval over 3–6 months (0.017–0.046 ºC/h) with a subsequent 150–175 ºC cooling interval over 1–8 weeks (0.104–1.042 ºC/h). Estimated amounts of olivine PEC are ~19–21 wt.% (~6% olivine PEC in the initial slow cooling phenocryst growth phase) and are in excellent agreement with extents of crystallization determined using the Danyushevsky approach (Table 7).

Table 7. Estimated extents (wt.%) of post-entrapment olivine crystallization.

Sample	Danyushevsky Approach (7 wt% initial FeO^T)	Gaetani-Watson Diffusion Models	Bubble Volume Estimate[a]
S17-3-a	3.4	-	7 (6)
S17-3-c	0.5	-	6 (12)
2-S17-3-a	18.2		25 (5)
2-MS-13-04-c	17.7	19-21	22 (5)
S17-3-f	19.5	-	-3 (5)
2-S17-3-c2	203	-	3 (5)
2-S17-3-e1	22	-	15 (5)
2-S17-3-e2	18.6	19-21	19 (8)
2-S17-3-d2	18.1	21	-
2-MS-14-04-b	22.4	-	21 (6)
2-S17-3-d	18.8	21	14 (5)
2-MS-14-04-d	18.9	-	-2 (4)
2-MS-14-04-d3	19.0	21	19 (7)
2-MS-14-04-a	19.3	19	13 (4)
MS-14-04-j	23.7	-	12 (8)
2-MS-13-04-a	25.7	-	27 (9)
2-MS-14-04-c	27.1	-	8 (6)
Low CaO (Avg ±1s)[b]	4.7 (1.4)[b]	-	6 (9)
High CaO (Avg ±1s)[b]	20.8 (2.9)[b]	~20	14 (6)

[a] Errors (parentheses) are estimated from vapor bubble and temperature uncertainties. Negative values likely reflect overestimates of cooling intervals.[b] Values includes all available data (i.e., Anderson, 1974). Standard deviations are reported in parentheses.

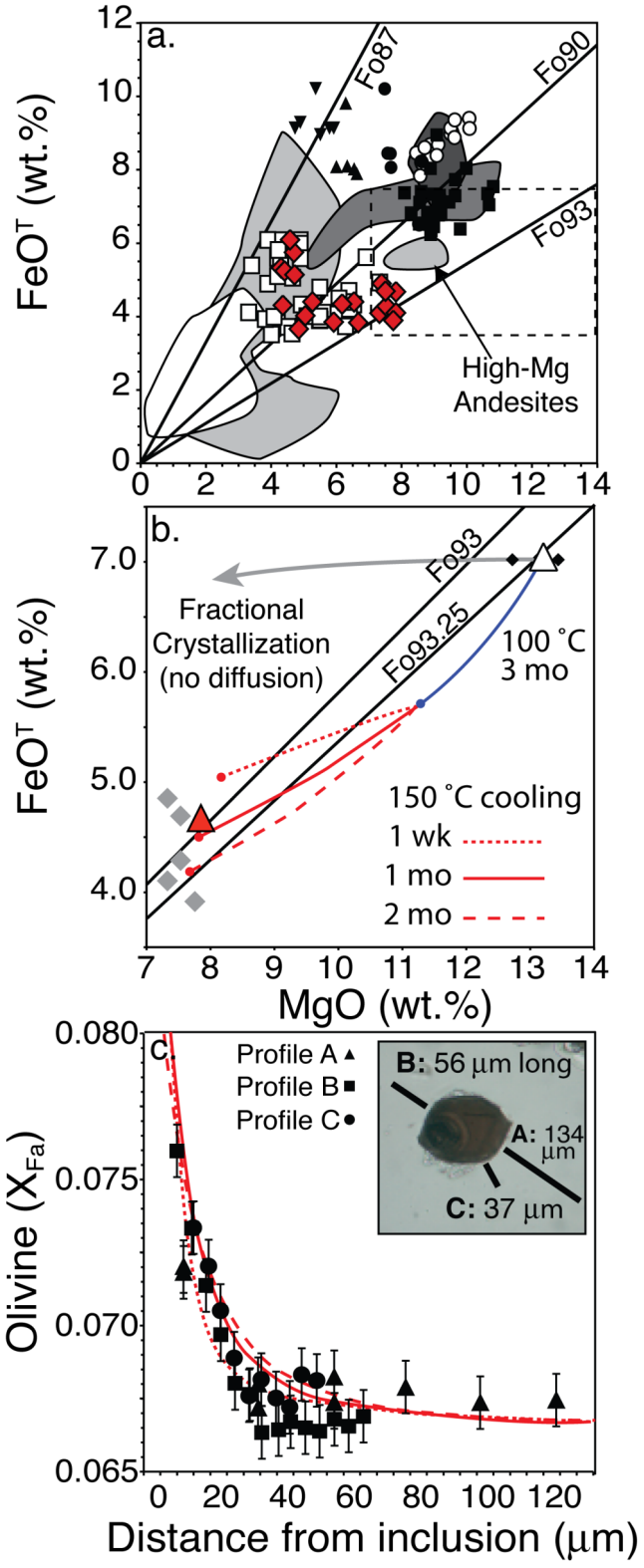

Figure 22. (a, b) FeO^T vs. MgO for fully enclosed olivine-hosted melt inclusions (symbols and fields as in Figure 19). Dark lines represent melt compositions in equilibrium with a particular olivine composition (Fo_{87}, Fo_{90}, or Fo_{93}). Panel (b) is an enlarged version of the dashed rectangle in (a). The large red triangle (sample 2MS-1304c) and gray diamonds are measured glass compositions from inclusions where host olivine profiles were also measured. The white triangle and black diamonds (7 wt.% FeO^T) are inferred initial melt inclusion compositions (white triangle corresponds to restored 2MS-1304c) modeled using the method of Danyushevsky et al. (2000). Labeled blue line shows melt inclusion evolution during an initial cooling stage of 100 ºC over 3 months. Red lines show melt inclusion evolution modeled over a second cooling interval of 150 ºC. (c) Example host olivine composition profile for sample 2MS-1304c along with calculated diffusion gradients from the three models (red lines) shown in panel (b). Inset diagram shows locations of the profiles with respect to the melt inclusion.

Our preferred models suggest that total extents of pre-eruptive cooling were <8 months from the time of melt inclusion formation to magma mixing and eruption. The timescale of the initial, slow cooling interval is difficult to constrain but observations require that (1) the composition of the host olivine core remains forsterite-rich and (2) the host olivine remains relatively homogeneous over hundreds of microns. Model timescales were determined by considering a wide range of conditions (e.g., lower initial FeO^T contents, single- and multi-stage cooling simulations); however, we acknowledge that these results are non-unique and other cooling scenarios may be able to reproduce observations.

The estimated total magma residences times are shorter than those required to establish rare earth element (REE) equilibration between a melt inclusion and host magma (3+ years; Spandler et al. 2007; Cherniak 2010), but long enough for large (>2 mm diameter) olivines to develop based on published estimates of crystal growth rates (e.g., Zieg and Lofgren 2006; Chen and Zhang 2009). The second, rapid cooling event is shorter than the timescales required to establish major element chemical communication between melt inclusions and the external melt by diffusion through the host crystal (Gaetani and Watson 2002). This suggests that irreversible post-entrapment diffusive communication through the host olivines between the melt inclusions and the surrounding host magma did not occur after magma mixing. Experiments suggest that complete diffusive exchange of H_2O between a melt inclusion and an external melt through the host olivine (~1 mm diameter) may occur within 2 days (Portnyagin et al. 2008; Gaetani and Hauri 2008). Therefore, observed H_2O contents within the high-Fo olivines may not be primary. The presence of high CO_2, S, and Cl (volatiles that will not diffuse through olivine), however, indicate that the high-CaO melt inclusions within high-Fo olivines were initially volatile-rich (Figure 21).

Vapor bubble growth during cooling

Vapor bubbles inside melt inclusions can be either a primary gas phase trapped along with the melt during inclusion formation or a shrinkage bubble resulting from differential thermal contraction between the melt and host coupled with melt crystallization during cooling (Lowenstern 1995; Schiano 2003). Vapor bubbles larger

than 5 vol.% are commonly interpreted to be primary (Lowenstern 1995), but larger bubbles could potentially form by contraction and crystallization of hydrous melt over a large post-entrapment temperature interval. Large vapor bubbles (>5 vol.%) are ubiquitous within the S17 melt inclusions (even in multiple inclusions within a single olivine; see 2S173-e1, -e2; Table 5), and it seems unlikely that a single primary vapor bubble was trapped in each inclusion. Therefore, we used a second approach to estimate extents of PEC that assumes vapor bubbles nucleated and grew after inclusion formation to determine whether extents of PEC determined above are reasonable (Anderson 1974).

We assess the amount of post-entrapment olivine crystallization experienced by first estimating the total cooling interval ($T_{trapping}$ to T_{glass} transition; where $T_{trapping}$ is defined above and T_{glass} transition = 550 ±50 ºC after Giordano et al. 2005). Average total cooling intervals are estimated to be 479 ±60 and 691 ±60 ºC for low-CaO and high- CaO inclusions, respectively. Changes in the molar volume of the melt due to thermal contraction were calculated using the formulation of Lange (1994) and the molar volume of H_2O from Ochs and Lange (1997). Expected amounts of host olivine contraction were calculated ($\alpha = 10^{-5}$ K^{-1}; Lange and Carmichael 1987) and combined with the expected melt volume contraction to estimate vapor bubble volume for a given temperature interval. Predicted bubble volumes were subtracted from the observed bubble volumes and excess was attributed to olivine PEC (Figure 23). Diffusive loss of chemical components from the melt inclusions could potentially modify bubble sizes. However, lack of correlations between observed bubble volumes and inclusion compositions (particularly H_2O or FeO^T) suggests that this effect is negligible. These PEC estimates are not entirely independent from those made above because the restored inclusion compositions were used to estimate trapping temperatures. Calculated uncertainties are estimated from uncertainties in vapor bubble volumes and cooling intervals. Negative amounts of olivine crystallization result for several inclusions and likely reflect overestimates in cooling intervals. We emphasize that this approach may be complicated by a number of factors including (1) trapping of primary vapor bubbles during inclusion formation, (2) diffusive loss of H_2O into or out of the melt, and (3) errors in calculated temperature intervals. Average extents of olivine PEC estimated from vapor bubble volumes are 14 ±6 (1 S.D.) wt.% for high-CaO inclusions and 7 ±9 wt.% for low-CaO

inclusions. PEC estimates based on observed vapor bubble sizes are comparable to those estimated above (Table 7).

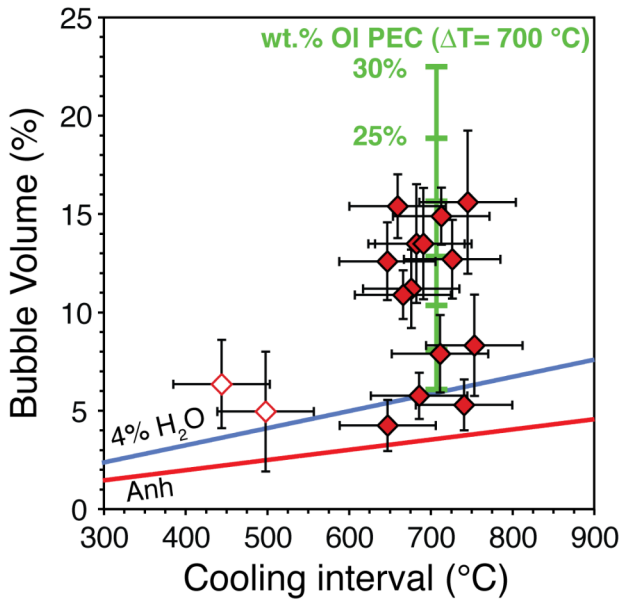

Figure 23. Vapor bubble sizes compared with calculated cooling intervals for high-CaO (filled, red diamonds) and low-CaO (open, red diamonds) melt inclusions. Lines labeled 'Anh' and '4% H_2O' (red and blue, respectively) show expected amounts of melt contraction over a given temperature interval for anhydrous and hydrous melts of average high-CaO composition (calculated at 100 MPa, $Fe^{2+}/Fe^{T} = 0.70$ after Lange 1994; Ochs and Lange 1997). Calculations include host olivine contraction (after Lange and Carmichael 1987). Vertical green line represents growth of a bubble attributed to melt volume loss during post-entrapment olivine crystallization. Tick marks denote 5 wt.% increments of Fo_{90} olivine crystallization from a melt with 4% H_2O over a cooling interval of 700 ºC.

Restored melt inclusion compositions

Restored melt compositions from samples analyzed here are reported in Table 6. All restored compositions shown in subsequent figures have been calculated using the procedure of Danyushevsky et al. (2000) and constant $Fe^{2+}/Fe^{Total} = 0.70$ (NNO +1.5). High-CaO inclusions have been restored assuming 7.0 wt.% initial FeO^{T}. The melt inclusion data of Anderson (1974) have been restored using the same method to augment our new data (restored compositions reported in Appendix I). In addition, though we lack evidence for Fe-enriched olivine profiles surrounding fully enclosed low-CaO inclusions within high-Fo olivines (unpublished data provided by A.T. Anderson), these inclusions display anomalously low FeO^{T} contents compared to low-CaO inclusions within more

Fe-rich host olivines (highlighted gray symbols in Fig. 6a). These inclusions also have major element compositions similar to the bulk rock HMA composition (85–41b) of Grove et al. (2002). Therefore, this subset of low-CaO inclusions was restored back to equilibrium with host olivines ($Fo_{>90}$) assuming 5.75 wt.% initial FeO^T (Figure 24).

All chemical components other than MgO, FeO^T, and SiO_2 are diluted during the restoration calculation. Average extents of olivine PEC for the combined data set are 6.0 ±3.6 (1 s.d.) and 20.1 ±4.0 wt.% olivine for low- and high-CaO inclusions, respectively. We emphasize that knowledge of the exact initial FeO^T content of the high- CaO inclusions remains a fundamental uncertainty to interpreting these melt inclusions and that the MgO contents of the restored inclusions are the least robust of the major elements. However, agreement between extents of olivine PEC determined by forward and reverse models and consistency with observed vapor bubble sizes provide confidence for our restored melt inclusion compositions.

Restored low-CaO melt inclusions are high-Mg andesites (HMA) with 4.9–10.9 wt.% MgO, 5.2–6.6 wt.% FeO^T, and 57–61 wt.% SiO_2. They are volatile-rich, with maximum values of 3.5 wt.% H_2O, 500 ppm CO_2, 830 ppm S, and 1590 ppm Cl (Figure 24, Figure 25, and Figure 26). Restored low-CaO inclusions in $Fo_{87–88}$ olivines (inferred to have formed at ~150 MPa and 1050 ±35 ºC; see Table 6) are intermediate between the HMA bulk lava compositions (85–41b,c) of Baker et al. (1994) (and Grove et al. 2002) and the 1040 ºC, 200 MPa fractional crystallization experiment (85–41c#5) of Grove et al. (2003) (Figure 24). Restored low-CaO inclusions in $Fo_{>90}$ host olivines are generally similar to the bulk rock composition (85–41b), though with slightly lower CaO, and we take the average of these inclusions to represent the most primitive low-CaO liquid composition (designated iHMA to distinguish it from bulk rock HMA compositions; see Table 8). Some of the compositional variation in the low-CaO suite of inclusions can be explained by fractional crystallization (9 wt.% olivine ± 10 wt.% clinopyroxene using the model proportions and Fe–Mg K_D's of Grove et al. 2003), but additional process(es) must be involved given the extent of the scatter in the data (Figure 24, Figure 25).

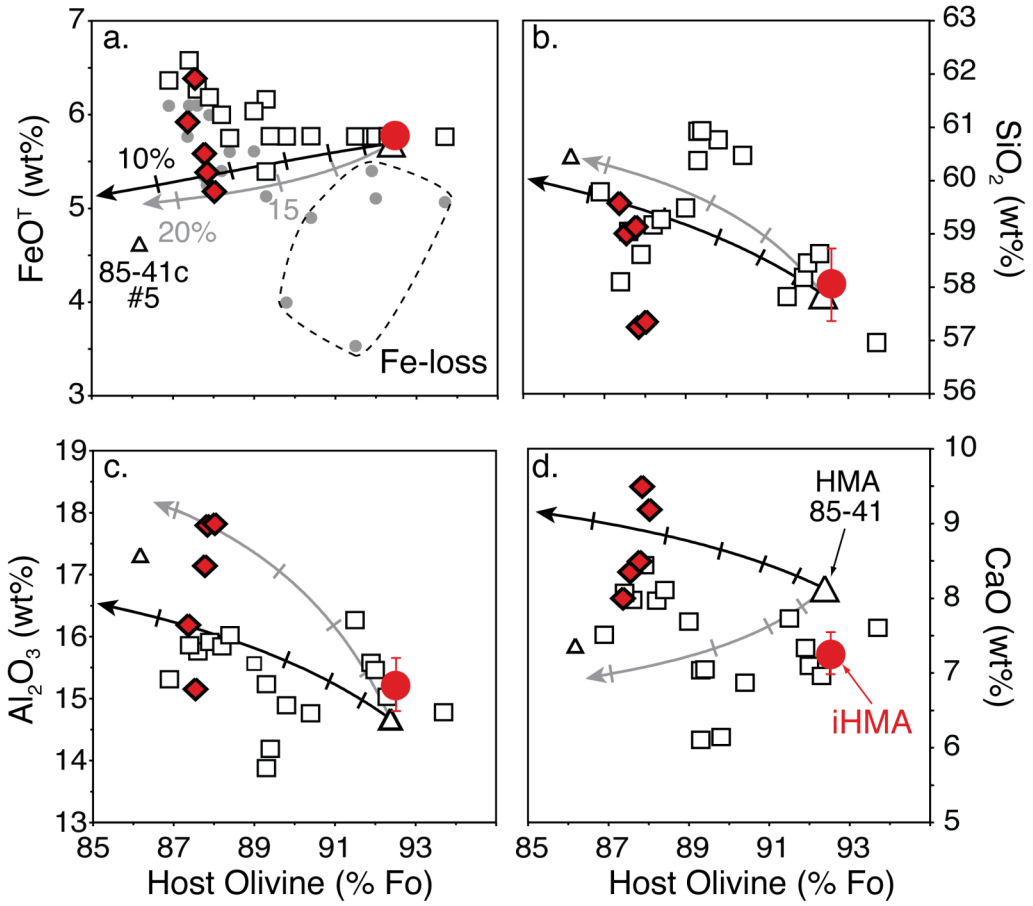

Figure 24. (a–d) Restored low-CaO (HMA) inclusion compositions from this study (red diamonds) and Anderson (open squares) plotted against olivine hosts. Large white triangle is the bulk rock HMA sample 85-41c used as a starting composition in fractional crystallization experiments by Grove et al. (2003). Small triangle labeled 85- 41c#5 is a run product from the same set of water-saturated crystal fractionation experiments (200 MPa, 1040 ºC, 18 wt.% olivine + clinopyroxene crystals). Black and gray lines with tick marks are calculated olivine-only and olivine + clinopyroxene (using constant modal proportions and Fe–Mg KD's of 85-41c#5) fractional crystallization paths. Olivine ticks are shown at 2 wt.% increments. Olivine + clinopyroxene ticks are shown at 5 wt.% increments. Small gray dots in panel a are unrestored melt inclusion compositions demonstrating Fe-loss (labeled) in the inclusions within higher Fo hosts. Red circle (with 1 s.d.) is the average composition of restored low-CaO inclusions in host olivines (%Fo > 92).

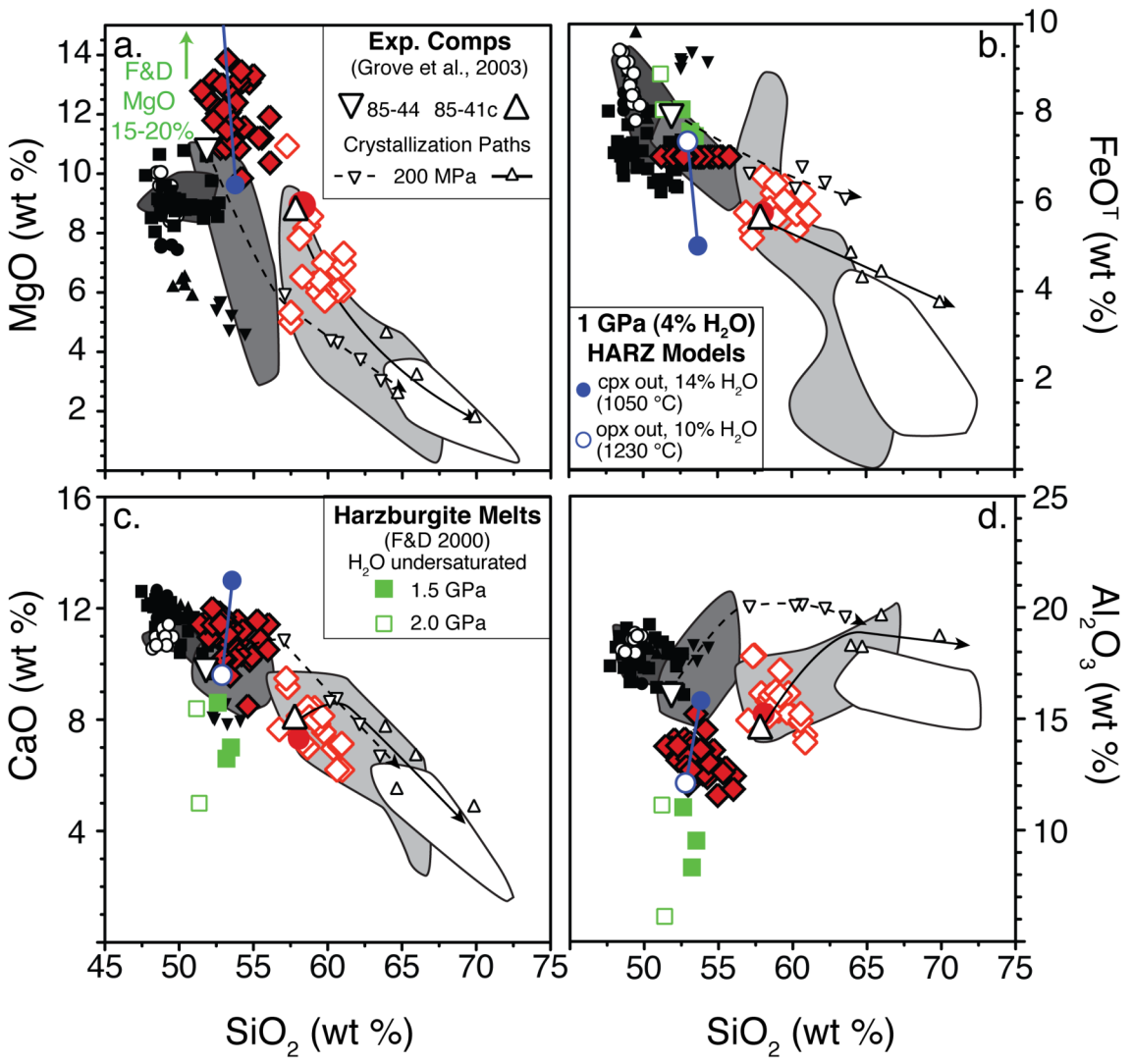

Figure 25. (a-d) Selected major element compositions of restored melt inclusions (filled, red diamonds: high-CaO, high-Fo (PBA); open red diamonds: low-CaO, low-Fo (HMA); filled red circle: iHMA) compared with other melt inclusions and bulk lavas (symbols and fields as in Figure 19). The melt inclusion data sets of this study and Anderson (1974) have been combined and compositions have been restored to equilibrium with host crystals as described in the text. High-Mg starting compositions and fractional crystallization experiment results from Grove et al. (2003) (open triangles) and experimentally produced, high pressure hydrous melts in equilibrium with a harzburgitic assemblage from Falloon and Danyushevsky (2000) (green squares) are also shown. Hydrous melt compositions calculated from the HARZ model of Parman and Grove (2004) for two bulk compositions at 1 GPa are shown as blue lines (filled circle denotes the earliest melts in equilibrium with both olivine and orthopyroxene; open circle denotes final composition of melt before orthopyroxene is exhausted during melting).

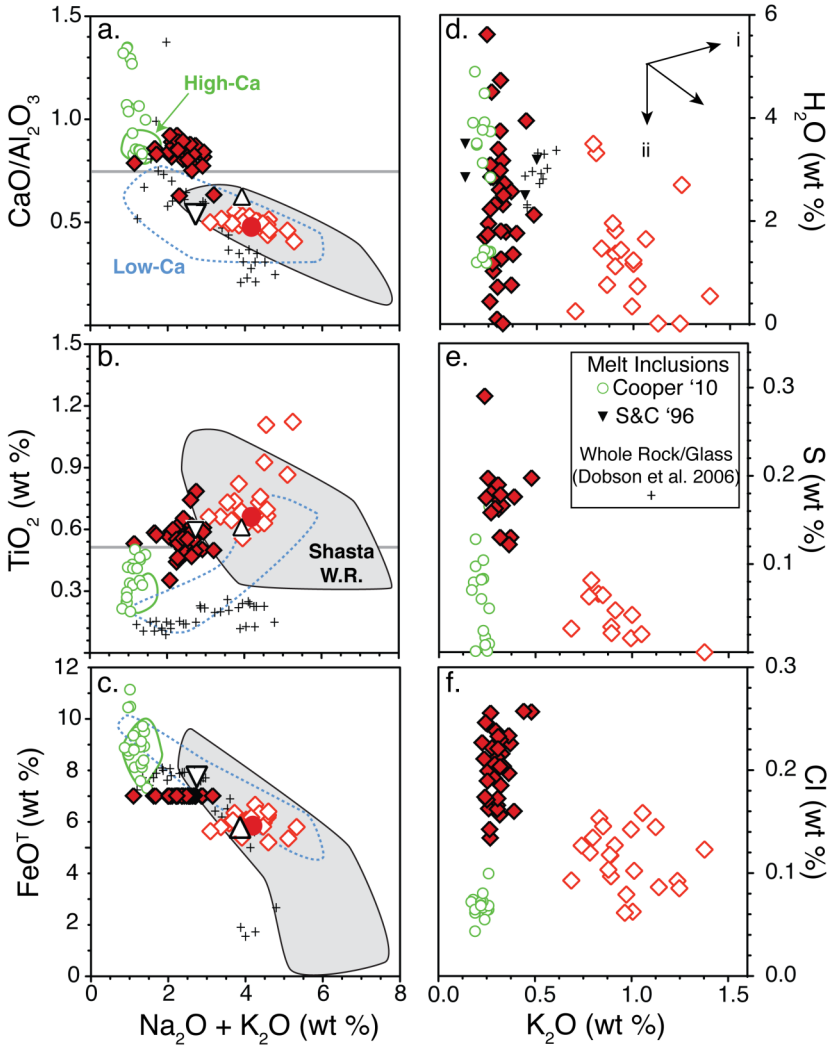

Figure 26. (a–c) Restored S17 melt inclusion compositions (symbols as in Figure 25) and Shasta whole-rock lavas (single gray field for clarity) in plots emphasizing differences between high- and low-Ca boninites. Boninite fields (high-Ca: green; low-Ca: blue, dashed) are from Crawford et al. (1989). High-Ca boninite melt inclusions from the Tonga arc are also shown (open green circles; Cooper et al. 2010) along with whole-rock and glass analyses of boninite series rocks from Chichi-Jima, Bonin Islands, Japan (Dobson and O'Neil 1987; Dobson et al. 2006). Horizontal gray line in (a) at CaO/Al_2O_3 = 0.75 separates high-Ca (>0.75) from low-Ca (<0.75) boninites (Crawford et al. 1989). True boninites are defined to have TiO_2 < 0.5 wt.% (gray line in (b); Le Bas 2000). (d, e) Volatile (H_2O, S, and Cl) contents vs. K_2O for restored S17 melt inclusions, Tongan high-Ca boninite inclusions, and additional inclusions (upside-down black triangles in panel (d) from Tonga, Izu-Bonin and Kamchatka arcs (Sobolev and Chaussidon 1996). Arrows in panel (d) illustrate idealized degassing and crystallization trajectories. Trend (i) illustrates vapor-undersaturated crystallization, where both volatile and K_2O contents behave incompatibly in the crystallizing assemblage. Trend (ii) shows degassing with no accompanying crystallization. Any trend between (i) and (ii) (slope < 1) illustrates simultaneous degassing and crystallization.

Table 8. Comparisons between mixing model, calculated iHMA, average inclusion compositions and whole rock sample.

wt %	Dacite 82-92[a] (bulk)	Average PBA (inclusion)[b]	Mixing Model HMA[c]	85-41b HMA[d] (bulk)	Mixing Model iHMA[c]	Average iHMA[e] (inclusion)	Average HMA (inclusion)[b]
SiO_2	67.0	53.47 ±0.40	58.94 ±0.84	57.86	60.25 ±0.70	58.06 ±1.19	59.69 ±0.64
TiO_2	0.45	0.56 ±0.03	0.52 ±0.05	0.60	0.51 ±0.04	0.67±0.08	0.74 ±0.08
Al_2O_3	16.52	13.14 ±0.27	14.51 ±0.48	14.67	14.84 ±0.42	15.21±0.59	15.58 ±0.62
FeO^T	3.62	7.00	5.63 ±0.13	5.69	5.31 ±0.11	5.77	5.84 ±0.32
MnO	0.06	0.070 ±0.003	0.063 ±0.005	0.11	0.063 ±0.004	0.06±0.03	0.090 ±0.010
MgO	1.91	12.19 ±0.38	8.03 ±0.78	8.88	7.04 ±0.67	8.89±2.13	6.12 ±0.38
CaO	4.22	10.88 ±0.25	8.18 ±0.48	8.13	7.54 ±0.43	7.25±0.45	7.67 ±0.45
Na_2O	4.14	2.06 ±0.14	2.90 ±0.25	3.18	3.10 ±0.22	3.24±0.40	3.26 ±0.22
K_2O	1.96	0.31 ±0.02	0.98 ±0.07	0.72	1.14 ±0.06	0.91±0.22	1.01 ±0.09
P_2O_5	0.13	0.27 ±0.02	0.21 ±0.04	0.16	0.20 ±0.03	0.30±0.03	0.21 ±0.04
ppm							
Rb	31.1	4.9 ±1.1	15.5 ±0.6	16	18 ±0.8	18 ±2.2	20.5 ±2.5
Sr	556	1045 ±39	847 ±45	779	800 ±39	764 ±59	867 ±67
Y	13.0	7.9 ±0.7	9.9 ±0.8	12	10.4 ±0.7	9.9 ±1.2	11.1 ±1.4
Zr	115	68 ±4	87 ±4	83	91 ±4	84 ±9	95 ±10
Nb	4.6	1.5 ±0.1	2.7 ±0.2	3.6	3.0 ±0.1	2.7 ±0.9	3.1 ±0.1
Ba	369	81 ±9	197 ±14	182	225 ±11	225 ±18	256 ±20
La	11.4	9.8 ±0.3	10.4 ±0.3	10.7	10.6 ±0.2	10.2 ±1.1	11.5 ±1.2
Ce	25.8	28.2 ±2.0	27.2 ±2.1	24.2	27.0 ±1.8	29.4 ±2.5	33.3 ±2.8
Sr/Y	43	136 ±5	85 ±9	68	77 ±7	78 ±10	79 ±10
Proportions			41 / 59 ±4		48 / 52 ±3		

[a] Dacite sample 82-92A of Grove et al. (2005). In equilibrium with Mg# 77-81 pyroxenes using experimentally determined Fe-Mg K_D values (85-41c#9, Grove et al., 2005)
[b] Average of all (those from this study and Anderson) restored PBA and HMA inclusions (with 95% confidence interval)
[c] Best-fit HMA or iHMA composition created by mixing Dacite 82-92 and the average PBA composition. Uncertainties constrained by Monte Carlo simulations.(N=425)
[d] Target HMA whole rock composition (85-41b) (Baker et al., 1994;Grove et al., 2002).
[e] Major elements are the average of restored low CaO compositions (%Fo Host > 92) of Anderson (1974) (with 95% confidence interval). MnO and P_2O_5 contents are the average of HMA inclusions from this study (%Fo Host ~88). Trace elements are from HMA inclusions of this study and are back-corrected for crystal fractionation (14 wt.% olivine + clinopyroxene). Mineral-melt partition coefficients used are from Grove et al. (2005) (Step 1).

Restored high-CaO melt inclusions are high-magnesian basaltic andesites with 9.8–15.1 wt.% MgO and 51.3–55.9 wt.% SiO_2 (Figure 25). They are also volatile rich, with maximum values of 3.4 (FTIR)-5.6 (EMPA) wt.% H_2O, 820 ppm CO_2, 2900 ppm S and 2580 ppm Cl (Figure 26). These have compositional similarities to primitive basaltic andesites (BA) from the Shasta region (Baker et al. 1994; Grove et al. 2005) but with some notable differences (melt inclusions have higher MgO and CaO/Al_2O_3) (Figure 24, Figure 25). We emphasize that the restored high-CaO melt inclusions are distinct from

the BA composition, particularly in CaO/Al_2O_3 and trace element characteristics, and we will refer to this new melt inclusion composition as a primitive basaltic andesite (PBA). These data clearly demonstrate that volatile-rich PBA and HMA melts both exist beneath the Mt. Shasta region and that HMA melts have major element similarities to bulk rock samples despite clear petrographic evidence for mixing and entrainment of crystal debris in the latter (cf., Grove et al. 2005; Streck et al. 2007a).

Figure 27 shows trace element abundances relative to NMORB (Sun and McDonough 1989) for average primitive melt inclusion compositions (PBA and iHMA) and bulk lavas (HMA: 85–41b and BA: 85–44). Trace elements were not analyzed in the inclusions used to calculate the iHMA composition (Anderson data), so trace element contents for iHMA were estimated by back-correcting the average trace element composition of the HMA inclusions ($Fo_{87–88}$) for 14 ±5% crystallization (using mineral-melt partition coefficients of Grove et al. 2005; we assumed mineral-melt D = 0 for unreported elements). Elevated large ion lithophile element (LILE) abundances, high field strength and heavy rare earth element (HFSE and HREE) depletions, and distinct negative Nb–Ta anomalies are common signatures in arc magmas (Perfit et al. 1980; Gill 1981; Sun and McDonough 1989; Elliot 2003). Trace element abundances are similar between iHMA and the bulk HMA lava, although the inclusions show a distinct enrichment in Pb. In contrast, the BA lava composition has distinctly lower LREE and higher HFSE contents than either HMA (inclusions and lava) or PBA, and we emphasize that high LILE/HFSE ratios distinguish the PBA melt inclusion compositions found here from BA bulk lavas (Figure 27 inset). Both groups of melt inclusions (HMA and PBA) have adakitic trace element characteristics, with PBA inclusions showing more extreme values than HMA inclusions or primitive bulk lavas (Sr/Y = 136 ±23 [1 s.d.] inPBAvs. 78 ±9 in HMA; La/Yb = 13.4 ±4.2 vs. 9.6 ±2.6; Y ppm = 7.9 ±1.2 vs. 11.1 ±1.1; Yb ppm = 0.7 ±0.2 vs. 1.2 ±0.3; Defant and Drummond 1990) (Figure 27, Figure 28; Table 6). Both types of restored melt inclusion compositions presented in Table 6 are considered low-SiO_2 adakites based on the classification scheme of Martin et al. (2005).

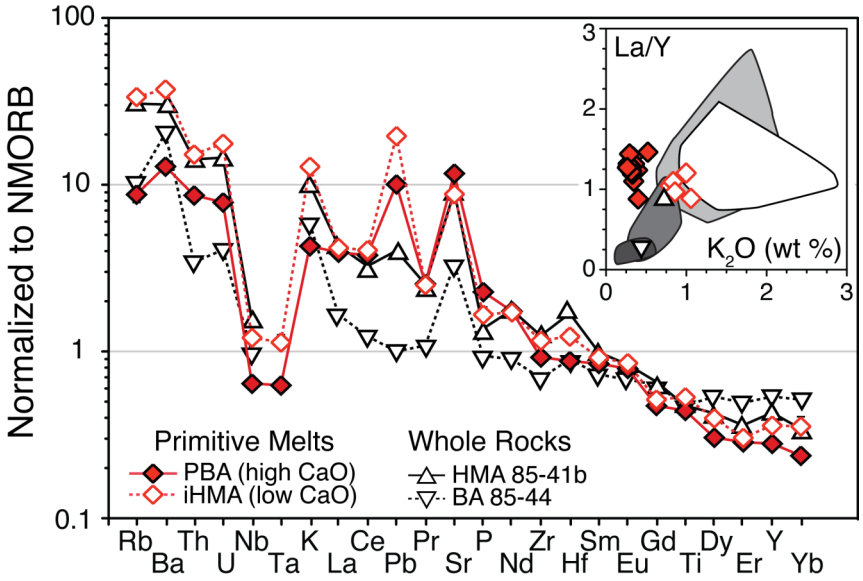

Figure 27. Trace element abundances in average restored melt inclusions (PBA and iHMA) compared to bulk lava compositions (fields in inset as in Figure 19) and inferred mantle-derived compositions of Grove et al. (2003) used in experiments (downward triangle: 85-44 basaltic andesite; upward triangle: 85-41b high-Mg andesite). All compositions are normalized to NMORB (Sun and McDonough 1989). Symbols shown are larger than 1 standard error of the mean for melt inclusion averages.

Discussion

Grove et al. (2005) used experimental phase equilibria combined with evidence from phenocryst compositions to argue that both primitive HMA (referred to as PMA by Grove and coworkers for primitive high-Mg andesite) and BA compositions are volatile-rich, mantle-derived melts, initially in equilibrium with a harzburgitic residue. These melts are inferred to enter the lower crust and experience variable extents of polybaric crystallization involving olivine, amphibole, pyroxenes, plagioclase, and spinel. Magma mixing textures have long been recognized in these lavas/tephras (e.g., Anderson 1974; Baker et al. 1994) and have been interpreted to reflect mixing between evolved derivative liquids and more primitive melts. Fractionation and mixing are proposed to occur throughout the entire crustal section (Moho depth of 33–38 km) in a complex transport network beneath the Shasta region (Grove et al. 2005). Primitive magma (i.e., HMA or BA) erupts occasionally at satellite vents, whereas more evolved compositions are erupted from Mt. Shasta itself. Grove et al. (2005) interpreted this system to be fed predominantly by the HMA composition with a limited role for the BA composition.

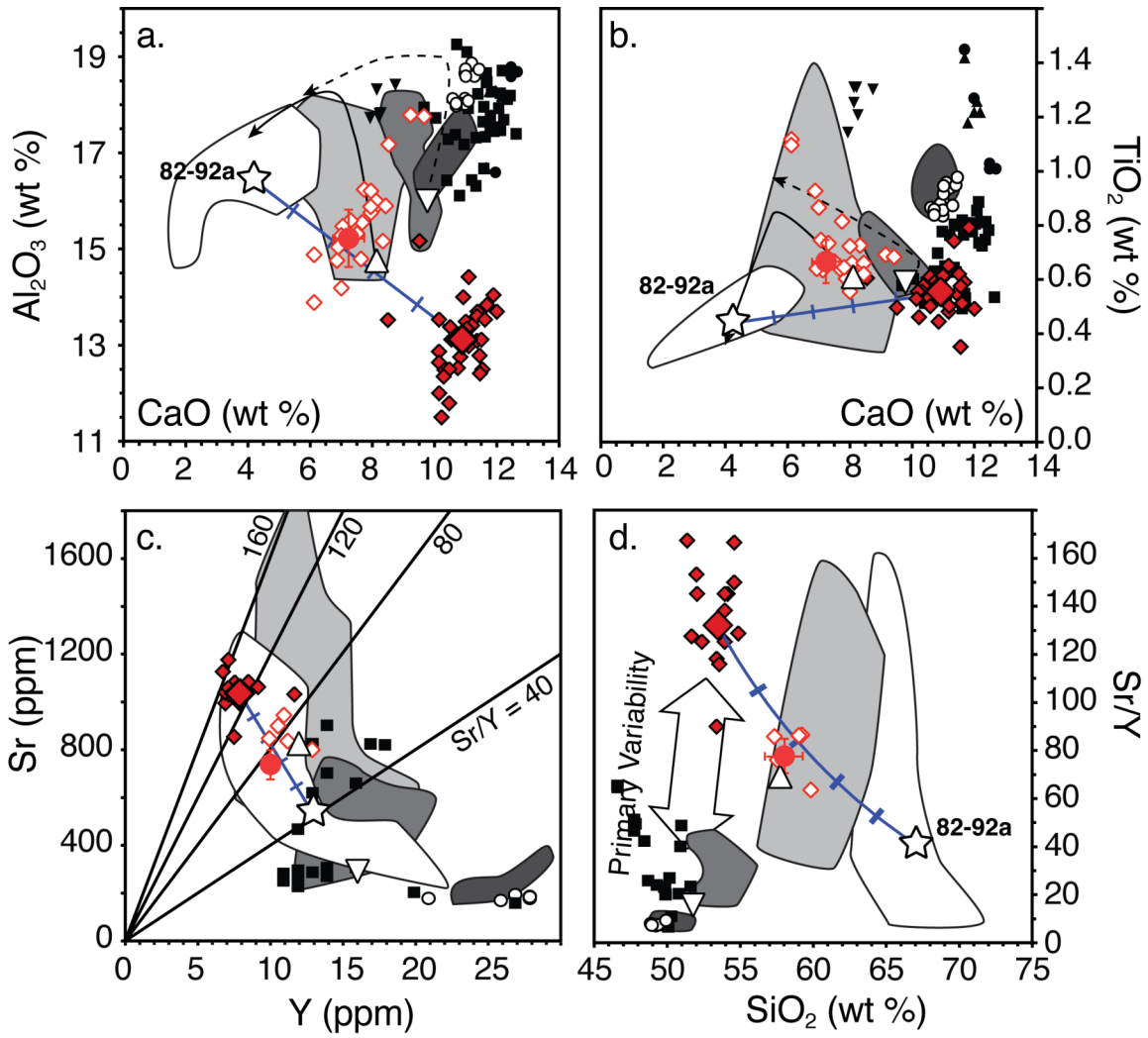

Figure 28. (a–d) Average (large symbols; averages in Table 8) and individual (small symbols) melt inclusion and whole-rock compositions (symbols and fields as in Figure 25; open star is dacite composition 82–92a used in mixing model and given in Table 8). The two-component mixing model (blue line with 0.2 increment ticks) is also shown. Double-headed arrow in (d) represents the potential variability in mantle-derived melts necessary to produce primitive magma compositions (PBA, iHMA, BA).

Alternatively, Streck et al. (2007a) proposed a model in which a crustally derived dacitic melt entrains harzburgitic debris from the Trinity peridotite and mixes with a primitive basaltic melt prior to eruption. They conclude that this process creates hybridized HMA bulk rock compositions in which primitive and 'adakitic' signatures are decoupled (i.e., high Mg# from harzburgitic contamination and primitive basalt, high Sr/Y and SiO_2 from dacite).

Variations in volatile contents within the HMA and PBA melt inclusions could be caused by degassing and/or vapor fluxing of melts prior to inclusion formation (e.g., Johnson et al. 2008; Vigouroux et al. 2008; Metrich and Wallace 2008). Dissolved S and Cl contents are less sensitive to degassing than H_2O and CO_2 at depth. However, the low S contents in HMA almost certainly reflect degassing, whereas observed variations in Cl probably result from variations between the two magma types (Figure 21, Figure 25; Kent et al. 2002; Wallace 2005; Spilliaert et al. 2006). Rapid diffusion of H^+ or H_2O through host olivine crystals (on timescale of days) can modify H_2O concentrations in melt inclusions (Massare et al. 2002; Portnyagin et al. 2008). Regardless of the possible effects of diffusion on H_2O in the melt inclusions in $Fo_{93–94}$ olivines, high S and Cl concentrations in the PBA inclusions are comparable to other subduction-related magmas (Wallace 2005; Wade et al. 2006; Benjamin et al. 2007; Johnson et al. 2008, 2009; Vigouroux et al. 2008; Roberge et al. 2009; Ruscitto et al. 2010). These comparisons also provide evidence that these are magmatic phenocrysts that crystallized from primitive, volatile-rich, subduction-related melts and are not related to the Trinity ophiolite.

In the following sections, we compare the PBA composition to experimentally produced hydrous melts in equilibrium with a harzburgite assemblage. We explore potential genetic relationships between the PBA and HMA through fractional crystallization and/or magma mixing and evaluate whether the PBA composition is compatible with the model presented in Grove et al. (2005). We also note similarities between the restored Shasta compositions and lavas and melt inclusions from the Bonin Islands and the Tonga arc, and we speculate upon the origins of high-Mg compositions beneath the Shasta region.

Comparison with high pressure, hydrous experimental and theoretical compositions

Baker et al. (1994) initially showed that Shasta BA and HMA resemble hydrous (3–5 and 6 wt.% H_2O, respectively) melts in equilibrium with a depleted harzburgite residue, as opposed to near anhydrous melts of a more fertile mantle source represented by high-Al olivine tholeiites (HAOT) in the region (cf., Figure 21, Figure 26). The restored melt inclusion compositions are compared to experimental high pressure (~1.5–2.0 GPa), hydrous melts in equilibrium with refractory harzburgite in Figure 26. The

numerical model (HARZ) of Parman and Grove (2004) predicts 1 GPa olivine-orthopyroxene-saturated liquid compositions with 10–14 wt.% H_2O (T = 1050–1230 ºC with melt fraction [F] = 0.33–0.37; starting bulk mantle H_2O content of 4 wt.%) and major elements similar to the restored PBA inclusions. Extents of melting for the PBA composition estimated using the HARZ model, however, are significantly higher than the average extent of mantle melting (F = 0.19 ±0.06; source H_2O ~0.7–1.1 wt.%) calculated using the method of Portnyagin et al. (2007) (mineral-melt D's from Johnson et al. 2009) and the depleted source from Grove et al. (2002). High H_2O contents required by the HARZ model also suggest that PBA inclusions have lost 6–8 wt.% H_2O, either before inclusion formation or by diffusive loss. Such extreme H_2O-loss from a melt (or melt inclusion) would induce considerable amounts of multiphase crystallization that is not observed. Therefore, we assume a conservative 4 wt.% H_2O (FTIR measurement) in the initial PBA magma and calculate a mantle equilibration temperature and pressure of 1237 ±37 ºC ($T_{Putirka}$ =1205 ±30ºC) and 0.9 ±0.2 GPa using the thermobarometer of Lee et al. (2009). Calculated pressures and similarities between the PBA melt inclusions and hydrous, high-pressure partial melts equilibrated with harzburgite suggest that PBA melts are primary, mantle-derived magma compositions derived from a refractory source.

Relationship between PBA and HMA melts

Volatile contents (H_2O, S, and Cl) plotted against indices of fractionation (e.g., K_2O) suggest a relationship between degassing and crystallization both within each magma type and potentially between PBA and HMA melts. Fractional crystallization from a PBA parent toward HMA is permitted by LREE/HREE ratios (e.g., La/Y ~1.0) (Figure 26, Figure 27). Assuming that K_2O is perfectly incompatible, a fractional crystallization model indicates that >70 wt.% crystallization of the PBA is required to reproduce K_2O contents of the HMA. In contrast, the heavy rare earth element concentrations for the two compositions roughly overlap, and the average amount of crystallization required to reproduce iHMA Y concentrations from the PBA composition is ~20 wt.% (assuming $D_Y = 0$) (Figure 27). We conclude that the HMA composition cannot be produced by fractional crystallization of a more primitive PBA parent melt. We did not find any melt inclusions comparable to the whole-rock BA composition (cf., Le

Voyer et al. 2010), and we emphasize that this composition, like the HMA, cannot be derived from PBA solely through fractional crystallization.

Generation of primitive HMA bulk rocks and observed mixing textures

Obvious mixing textures found in S17 HMA whole-rock samples and other Shasta lavas suggest that magma mixing may be an important process involved in the formation of HMA compositions. Experimental and trace element arguments suggest that the primitive PBA and BA end members cannot be related through fractional crystallization and are primary, mantle-derived melts. HMA melt inclusions within $Fo_{87–88}$ skeletal olivines in the S17 tephra likely formed by fractional crystallization from a primitive HMA parent (iHMA) that has many similarities to but a few key differences (e.g., lower CaO, MnO, and Y, higher P_2O_5, Ba, and Ce) from the primitive HMA lava sample (85–41b). While this suggests the existence of a distinct primitive HMA parent melt, there remains the possibility that some HMA bulk rock and tephra samples (such as 85–41b) formed by mixing between the newly identified PBA melt and a more silicic composition given that the bulk samples contain both $Fo_{93–94}$ olivines and dacitic phenocrysts.

Grove et al. (2005) identified two evolved end members in the Shasta lava suite on the basis of phenocryst compositions: a rhyodacite (McKenzie Butte samples 75–22 and 85–43) and a dacite similar to the lowest temperature (940 ºC), 200 MPa fractionation experiment (85–41c#9) of Grove et al. (2003). Reversely zoned orthopyroxenes in the S17 tephra and lava (Mg# core: 0.65–0.72; rim: 0.85–0.92) contain dacitic melt inclusions, indicating that magma mixing beneath the S17 cinder cone involved a dacitic component (Streck et al. 2007a). We approximate the dacitic end member using sample 82–92a (Sargents Ridge phase) from Grove et al. (2005) (Table 8). We note that this composition is actually in equilibrium with Mg# 0.77–0.81 pyroxenes (using K_D's from Grove et al. 2003). The actual evolved end member responsible for producing the low Mg# pyroxenes in the S17 magma must be slightly more fractionated than this composition (82–92a) but less evolved than the rhyodacite end member. We also note that unlike the Streck et al. (2007a) model, our evolved end member requires low Sr/Y values.

We evaluated a two-component mixing model between the dacite and the average PBA melt inclusion composition to determine whether mixing could reproduce the primitive HMA bulk rock composition (85–41b) of Grove et al. (2002). Best-fit mixing proportions were determined using only trace elements in order to minimize uncertainties caused by variations in end member major element compositions resulting from crystal fractionation. The two component mixing model reproduces a composition with similar major and trace element characteristics of the primitive HMA bulk rock; however, it underpredicts concentrations for TiO_2, MnO, Na_2O, Y, and Nb and overpredicts SiO_2, K_2O, P_2O_5, Sr, Ce, and Sr/Y (Figure 28,Table 8). This mixing model better reproduces the iHMA composition; however, it underestimates TiO_2, FeO^T and P_2O_5 (Figure 28, Table 8). We emphasize that our model is highly sensitive to the choice of end members, so there may exist other possible dacite end members that would provide better fits. We conclude that although the two component mixing model is able to produce a primitive HMA-like composition, it does not reproduce all aspects of sample 85–41b or the iHMA composition to within 95% confidence limits.

Considerable compositional and magmatic temperature differences between the two end members might inhibit the efficient magma mixing required to produce a hybrid HMA composition. Therefore, we also tested whether a two component mixing scenario is physically feasible by adapting the thermomechanical model of Sparks and Marshall (1986) (see Appendix J for detailed explanation). Figure 29 shows the calculated viscosities of the end member compositions following magma mixing and thermal equilibration between varying proportions of mafic and silicic magmas (eq. 3 in Sparks and Marshall 1986). The model assumes that the mafic end member crystallizes as the equilibration temperature decreases during addition of the silicic component. The silicic magma correspondingly increases in temperature and dissolves crystals. An isobaric (200 MPa) pMELTS calculation (Ghiorso et al. 2002) was used to establish the relationships between crystal content and mafic liquid composition with temperature. Liquid viscosities for each end member at the corresponding equilibration temperature were calculated following Hui and Zhang (2007). Bulk viscosities were calculated using the Roscoe-Einstein equation (Sparks and Marshall 1986). Magma mixing and hybridization are possible for all mixing proportions of these two end members (Figure 29). Using the

proportion of PBA constrained by trace elements (X_{mafic} = 0.59 ±0.04 for Model HMA and 0.52 ±0.03 for Model iHMA), the corresponding equilibration temperatures should be ~1090–1120 ºC with ~11–13% crystals or 1075–1095 ºC with ~13–15% crystals, respectively. These temperatures are consistent with liquidus temperatures of 1097 ±30 and 1119 ±30 ºC calculated for the primitive HMA bulk rock and iHMA compositions (with 6 wt.% H_2O), respectively. The mixture equilibration temperatures are slightly higher than the average of calculated HMA temperature of inclusion formation (HMA $T_{trapping}$ = 1051 ±35 (1 s.d.) ºC) and so are consistent with the interpretation that the HMA melt inclusions were trapped in rapidly grown skeletal olivines after mixing (Figure 29). These results demonstrate that it is both chemically and physically possible to form a primitive HMA composition by magma mixing, even if our mixing models do not exactly reproduce the 85–41b whole rock and iHMA compositions.

Complications arise with the mixing scenario because the required dacite end member may itself be a product of low pressure (200 MPa) fractional crystallization from a primitive HMA parent (cf., Grove et al. 2003, 2005). A mixing origin for primitive HMA as outlined earlier would therefore involve derivative liquids that require previous mixing events. This type of scenario would not be unexpected beneath a long-lived stratovolcano, but it does result in a ‘‘chicken or the egg’’-type conundrum. Additionally, the existence of other primitive HMA compositions in the Lassen region to the south (Clynne and Borg 1997) and elsewhere at the Whaleback-Deer Mountain locality (Grove, personal communication 2010) with no obvious magma mixing textures argue against a crustal mixing scenario as a general explanation for formation of primitive HMA in the northern California Cascades.

For these reasons, we consider an alternative interpretation in which the 85–41b lava and S17 tephra samples form through entrainment of dacitic and PBA xenocrysts into an ascending primitive HMA magma. Martin et al. (2010) point out that large olivines (the high-Fo group) from S17 have distinctly lower $\delta^{18}O$ values compared to the majority of smaller olivines and orthopyroxenes, and they therefore interpret the large olivines as xenocrysts. We also note that the most magnesian olivines present in comparable primitive HMA from the Lassen region (Clynne and Borg 1997) have lower forsterite contents (%Fo < 92) than the crystals in S17 that contain PBA melt inclusions,

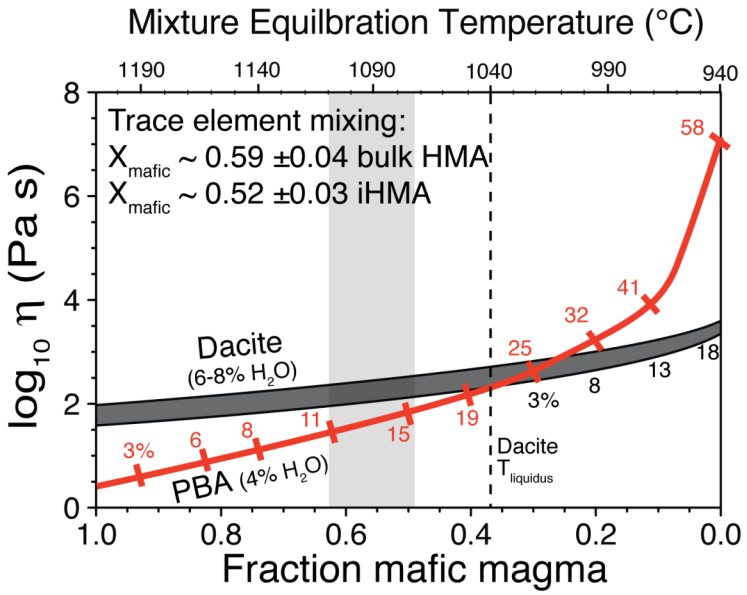

Figure 29. End member bulk viscosities as a function of mixing proportions calculated assuming complete thermal equilibration of the magma mixture following the method of Sparks and Marshall (1986) and using the liquid viscosity model of Hui and Zhang (2007). The red line represents the PBA end member (initially at 1210 ºC with 4 wt.% H_2O). Tick marks and red numbers denote approximate crystallinity of the mafic end member. The thick dark gray field represents the dacite end member with either 6 or 8 wt.% H_2O, respectively, and both initially at ~940 ºC with 18 wt.% crystals. The dashed line shows the dacite liquidus temperature and black numbers below the dark gray field denote approximate crystallinity of the dacite end member. The relationship between crystal content and temperature for the mafic end member was determined using pMELTS (Ghiorso et al. 2002). Least-squares trace element calculations (Table 8) indicate that hybrid HMA magmas can be produced by two-component mixing between 49 and 63% PBA magma and a dacitic liquid (vertical gray bar).

and this observation also supports the interpretation that most of the extremely forsteritic olivines (%Fo ~ 93–94) are xenocrystic. In this scenario, the HMA melt inclusions were formed during and/or after xenocryst entrainment, and the xenocrysts became rimmed as they tried to equilibrate with the entraining and fractionating HMA magma. Melt compositions in the HMA magma were not greatly affected by the xenocryst entrainment process, but some of the compositional scatter in the HMA inclusions in lower Fo olivines (Figure 24) could be related to incomplete blending.

The range in primitive melt compositions with distinctive trace element ratios (e.g., Sr/Y), suggests the existence of a spectrum of volatile-rich primitive magma compositions (PBA, primitive HMA, BA) that formed in equilibrium with variably

refractory mantle beneath the Shasta region (Figure 26, Figure 27). The HMA melt inclusions studied here represent a fractionated derivative of a primitive HMA parent (iHMA). The volumetric proportions or the importance of the different primitive magma types are not constrained by our results, but the newly identified PBA composition could be an important parental magma type beneath the Shasta region that has been unrecognized due to its rarity at the surface. We note that fractional crystallization of a PBA parent melt can explain the high Sr/Y of some Shasta andesites and dacites (Figure 28c,d), but testing whether PBA could be a common parent magma in this region requires new experimental phase equilibria (cf., Grove et al. 2003) and further analysis of melt inclusions and quenched mafic enclaves from additional samples.

Comparison with boninites

Boninites are a rare subset of high-Mg magma compositions that occur mostly in island arcs (forearc and trench slope) and ophiolites (Crawford et al. 1989). These compositions represent an important endmember magma type that is derived from highly refractory mantle metasomatized by subduction-derived components, and they may require anomalously hot mantle (1400–1550 ºC) (Crawford et al. 1989; Sobolev and Danyushevsky 1994; Falloon and Danyushevsky 2000; Cooper et al. 2010). Primitive, SiO_2-rich compositions and phenocryst assemblages with high-Mg olivine (up to Fo_{94}), clino and orthopyroxenes (Umino 1986; Crawford et al. 1989) make boninites a natural comparison with high-Mg compositions from Mt.Shasta. Figure 26 illustrates the compositional characteristics of Shasta melt inclusions (PBA and HMA) along with boninite lavas and olivine-hosted melt inclusions (Sobolev and Chaussidon 1996; Dobson et al. 2006; Cooper et al. 2010). Boninites are subdivided into high-Ca ($CaO/Al_2O_3>0.75$) and low-Ca ($CaO/Al_2O_3<0.75$) groups, reflecting the amount of modal clinopyroxene in the initial mantle source (i.e., melting of clinopyroxene-poor lherzolite generates high-Ca boninites whereas melting of harzburgite produces low-Ca boninites) (Figure 26a-c; Crawford et al., 1989). PBA melt inclusions have high CaO/Al_2O_3 (>0.75) ratios similar to high-Ca boninites but with higher TiO_2 and alkali contents. Volatile contents in Shasta melt inclusions are similar to or greater than those reported in boninite melt inclusions from around the Pacific (Tonga, Izu-Bonin, Kamchatka) (Figure 26d–f).

Shasta HMA inclusion compositions are nearly identical to low-Ca boninites (specifically Type II; Crawford et al. 1989). Similarities between boninites and Shasta PBA melts may indicate similar magma generation processes (shallow, wet mantle melting), but the distinctly lower TiO_2 contents of boninites seem to require either higher degrees of melting and/ or an initially more depleted source. Additionally, we note that inferred mantle equilibration temperatures for Shasta PBA melts are significantly lower (<1300 ºC) than those inferred for many boninites. A possible explanation for the higher TiO_2 contents and lower equilibration temperatures in Shasta magmas is that they may be melts of lherzolite formed in the hottest part of the wedge that re-equilibrated extensively with harzburgite at lower pressures in the uppermost part of the mantle during ascent (e.g., Grove et al. 2003).

Origin of refractory mantle beneath Shasta

The southern region of the modern Cascades is built upon accreted island arc terranes, and the western continental margin of North America has experienced arc-related magmatism since at least the Late Cretaceous (Dickinson 2004). Therefore, it is reasonable to expect that parts of the lithospheric mantle root, decoupled from deeper asthenospheric flow (e.g., Silver and Holt 2002), might become highly refractory over time. This region of refractory lithospheric mantle may exist between the base of the crust (33–38 km; Grove et al. 2005 and references therein) and lithosphere-asthenosphere boundary at ~70 km (Li et al. 2007; Levander et al. 2008; Miller et al. 2008). Depths in this range are consistent with pressures obtained from mantle-melt equilibration experiments (~1.0–1.2 GPa; Baker et al. 1994; Muntener et al. 2001) and estimates using the Lee et al. (2009) thermobarometer.

The PBA composition identified here is a low-SiO_2 adakitic melt. Martin et al. (2005) interpret these magmas to form by flux melting of a peridotite mantle wedge that had previously been metasomatized by felsic slab melts. Grove et al. (2002) identified at least two distinct fluid-rich subduction components beneath the Shasta region that dominate the magmatic trace element budget. They concluded that these components represent small degree melts or supercritical hydrous fluids derived from oceanic crust and sediment (see also Le Voyer et al. 2010). We conclude that volatile-rich high-Mg at

Shasta melts originate from flux melting of a metasomatized mantle wedge induced by the active dehydration (and possible melting) of the young, subducting Gorda plate, aided by toroidal flow of deep asthenosphere around the southern slab edge (Zandt and Humphreys, 2008). Final mantle equilibration is with a refractory lithospheric root at shallow depths and high temperatures. Such a scenario can also explain the generation of high-Mg andesites with correlated radiogenic Os and slab signatures in the forearc around Lassen to the south of Shasta (Clynne and Borg 1997; Borg et al. 2000).

Summary

High-Mg olivines ($Fo_{87–94}$) in S17 tephra are magmatic phenocrysts that have crystallized from volatile-rich melts. We have assessed the effects of post-entrapment modification on glass inclusions hosted within the olivines and have identified two distinct high-Mg melt compositions: HMA and PBA. HMA melts have 4.9–10.9 wt.% MgO and 57–61 wt.% SiO_2. Some of the compositional variability in the HMA melt inclusions can be explained by fractionation of olivine ± clinopyroxene from a more primitive HMA parent melt (iHMA) that is similar in composition to the whole-rock primitive HMA sample (85-41) studied by Grove et al. (2005). The HMA melt inclusions within $Fo_{87–88}$ olivines must have formed shortly prior to eruption based on host olivine morphology and limited post-entrapment modification. PBA melt inclusions are found inside larger olivines (%Fo >91) that are xenocrystic based on the major and trace element differences between PBA inclusions and the HMA bulk rock sample. These inclusions are considerably more primitive (9.8–15.1 wt.% MgO), with distinct, elevated Sr/Y ratios (up to ~180) compared to the primitive HMA bulk rock or iHMA composition. Our data show that both PBA and HMA melts were initially volatile-rich (Figure 21, Figure 26). The PBA composition is similar to hydrous mantle melts formed in equilibrium with a harzburgite residue (Parman and Grove 2004).

Melt generation and migration beneath the Shasta region is complex and involves some combination of magma mixing coupled with differentiation over a wide range of pressures (Grove et al. 2005). Neither HMA nor BA compositions can be reproduced through fractional crystallization of the PBA composition. Mixing between PBA and a

more evolved melt (dacite) is able to produce a primitive HMA composition, but the predicted mixture shows some small major and trace element discrepancies from published whole-rock analyses. Alternatively, the bulk rock 85-41b composition and mixing textures could have resulted from entrainment of crystalline debris (derived from both PBA and dacite) into a primitive HMA magma. Our results are consistent with the crustal fractionation, magma recharge, and magma mixing model presented in Grove et al. (2005), but they do require the addition of a distinct PBA component with relatively high Sr/Y that may be parental to many Shasta andesites and dacites. Primitive, volatile-rich magmas from the Shasta region are compositionally similar to boninites, but have higher TiO_2 contents and lower apparent mantle equilibration temperatures, suggesting that they may form initially as melts of lherzolite followed by shallow equilibration with harzburgite. Accretion of island arcs to the western margin of North America and the persistence of arc magmatism in this region since at least the Cretaceous suggest a high likelihood of refractory mantle present in the lithospheric root directly beneath the lower crust.

Bridge Between Chapter IV and Chapter V

The previous chapter (IV) discussed the pre-eruptive volatile contents and geochemistry of high-Mg compositions from the Mt. Shasta region of Northern California and demonstrated that these compositions are likely mantle-derived. The next chapter (V) will combine all of the Cascades data (from Chapters II, III, and IV) with a global data compilation from the literature in order to put the Cascades arc into a global context.

CHAPTER V
GLOBAL VARIATIONS IN ARC-RELATED MAGMATIC VOLATILE CONTENTS

This chapter includes co-authored material with Dr. P.J. Wallace, who provided editorial assistance. All analyses and writing was done entirely by me.

5.1. Introduction

Arc volcanism ultimately occurs along most destructive plate margins because hydrous fluids, derived from the dehydrating subducting slab, lower the solidus of the overlying mantle wedge and induce melting. As a result, primitive arc magmas reflect contributions from both the down-going plate (subducted sediment and oceanic crust) and the overlying mantle wedge (e.g., Plank & Langmuir, 1993; 1998; Elliot, 2003). No single reaction is responsible for slab dehydration, rather a complex series of continuous dehydration reactions occurs in response to increasing pressure and temperature of the subducting plate (Schmidt & Poli, 1998). Previous studies have related global variations in arc volcanics to the compositions of incoming sediments and observed that arc outputs generally reflect subduction inputs (e.g., Plank & Langmuir, 1988; 1993; 1998). Arc outputs should be expected to reflect other subduction input parameters as well (e.g., age of incoming plate, dip angle). Another important subduction parameter (Φ) corresponds to expected slab temperature conditions at depth:

$$\Phi = V_{\perp} \cdot A = A \cdot V_C \cdot \sin\alpha \qquad (1)$$

where A is the age of the incoming oceanic crust and $V_{\perp}$ is the vertical descent rate (equal to the product of the convergence velocity [V_C] and the sine of the dip angle [α]; Figure 30; Kirby et al., 1996; Gorbatov & Kostoglodov, 1997). Equation (1) approximates the thermal structure of the downgoing plate and is proportional to the maximum depth reached by an isotherm (i.e., fast subducting, old slabs [high Φ] should be cooler than slowly subducting, young slabs [low Φ] at equivalent depths). Results

from recent geodynamic models appear to confirm this relationship (Syracuse et al., 2010).

Other recent studies have predicted relationships between physical subduction zone parameters (i.e., Φ) and volatile recycling efficiencies inferred from theoretical and experimental phase-equilibria (Figure 31; Peacock, 2003; Hacker, 2008; van Keken et al., 2011). Slabs characterized by low-Φ (higher temperatures) are expected to undergo dehydration reactions at lower pressures (shallower depths) than those characterized by higher-Φ values (Figure 31). We have tested this predicted relationship by constructing a global dataset of primitive magma compositions (i.e., in equilibrium with Fo_{90-91} olivine) for over 70 volcanic centers encompassing the global range in slab thermal parameter (Figure 30, Table 9).

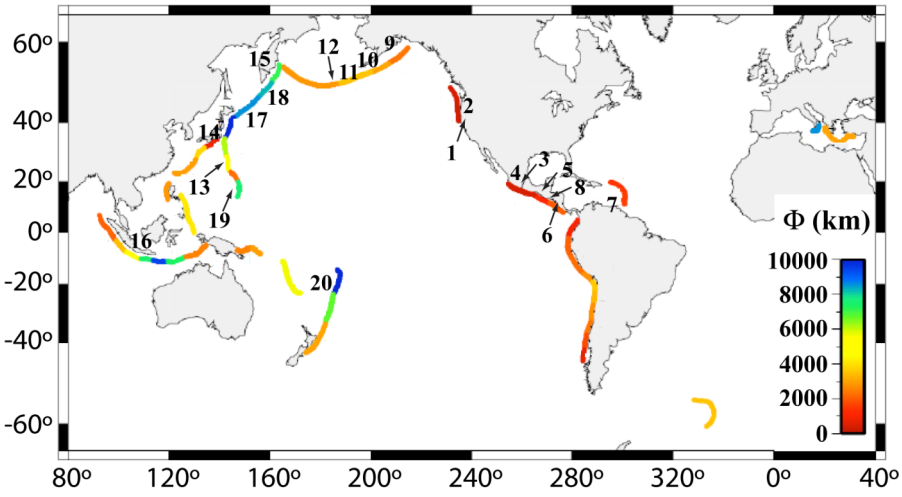

Figure 30. Location map after van Keken et al. (2011) showing subduction zone trenches color-coded by slab thermal parameter (Φ). Arc segments are labeled as follows: (1) Southern Cascades, (2) Central Cascades, (3) Chichinautzin Volcanic Field, (4) Michoacan-Guanajuato Volcanic Field, (5) Guatemala and El Salvador, (6) Costa Rica, (7) Southern Lesser Antilles, (8) Nicaragua, (9) Alaska, (10) Alaskan Peninsula, (11) Eastern Aleutians, (12) Central Aleutians, (13) Bonin Islands, (14) Izu Peninsula, (15) Kamchatka, (16) Java, (17) Southern Kurile Islands, (18) Northern Kurile Islands, (19) Marianas, (20) Tonga.

Ratios of large ion lithophile (LILE) and high-field strength (HFSE) elements (e.g., Ba/La, Pb/Ce, U/Th) have long been used as proxies for slab contributions to arc magmas because LILEs preferentially partition into the fluid phase during dehydration

and preferentially into the melt phase during mantle melting (e.g., Kay, 1978; Gill, 1981; Leeman et al., 1990; Stolper & Newman, 1994; Winter, 2001; McBirney, 2007). Arc magmas show elevated LILE contents and negative Nb-Ta anomalies (ascribed to residual rutile in the slab; Elliot et al., 1997) compared to primitive magmas from other settings (i.e., mid-ocean ridges, ocean islands) (Sun & McDonough, 1989; Elliot, 2003). However, the nature of the slab-derived component is considerably more complex than a single fluid and ranges in character from solute-rich aqueous fluids (>90% H_2O) at subsolidus temperatures to hydrous partial melts (<30% H_2O) of sediment and oceanic crust at higher temperatures (Kessel et al., 2005; Hermann & Spandler, 2008). At sufficiently high pressures, above the second critical endpoint, these end-member slab components form a miscible compositional continuum, becoming indistinguishable from one another and complicating traditional slab tracer ratios by mobilizing HFSEs and other elements traditionally considered fluid 'immobile' (Manning et al., 2004; Kessel et al., 2005; Hermann et al., 2006).

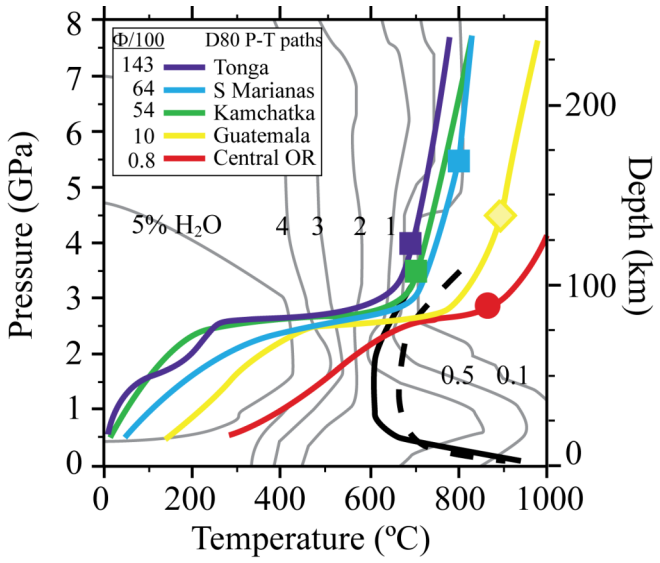

Figure 31. Pressure-temperature paths of model slab surfaces for five arc segments spanning the global range in slab thermal parameters (paths correspond to D80 models of Syracuse et al., 2010). Average depth to the slab surface beneath each volcanic front is indicated by the symbol on the P-T path. Light gray lines show contours of maximum bound H_2O (wt.%) in hydrated MORB from Hacker (2008). The thick solid and dashed lines show the H_2O-saturated MORB and oceanic sediment solidi (Vielzeuf & Schmidt, 2001; Schmidt et al., 2004). Figure modified after Syracuse et al. (2010).

Measurements of dissolved volatiles (H_2O, S, Cl, CO_2) within melt inclusions permit direct comparison of magmatic volatile contents with trace element proxies (e.g., Cervantes & Wallace, 2003). Importantly, volatile/trace element ratios constrained by experimental work suggest a provisional slab-fluid geothermometer (see Section 5.4) that permits robust comparisons among subduction zones characterized by different thermal regimes (Plank et al., 2009). We use our global dataset to examine the relationships between volatiles, slab tracers, and average subduction components and variations in the subarc thermal structure. We note that many studies have inferred multiple slab contributions to arc magmas derived from varying proportions of the subducting sediment and altered oceanic crust (Elliot et al., 1997; Eiler et al., 2005), in addition to both modern and ancient subduction components (Borg et al., 2002; Auer et al., 2009). The slab components discussed in this work, however, represent the average 'non-mantle wedge' contribution to the magmas and do not distinguish between various sources. We assume, however, that most of the subduction component signature is derived from modern inputs and use only recent volcanic samples from active arcs.

5.2. Data and Methods

Primitive magma compositions (i.e., in equilibrium with Fo_{90-91} olivine) were determined from olivine-hosted melt inclusion and whole rock data for over 70 volcanic centers comprising 20 arc segments encompassing the global range in slab thermal parameters (Figure 30, Table 9). Preferred primitive magma compositions were used if specified (e.g., Portnyagin et al., 2007; Johnson et al., 2009), otherwise compositions were constructed using available data. Complete compositional datasets (major, volatile, and trace analyses) for olivine-hosted melt inclusions are not available for all volcanoes and were augmented with whole rock data and glass analyses of similar composition from the same vent. All melt inclusion compositions were restored to equilibrium with host olivines based on the preferred methods described in their sources. Major and trace elements for parent magma compositions from each volcano were determined by averaging the least evolved samples (i.e., highest MgO contents) and then incrementally (0.1 wt.%) adding equilibrium olivine until the melt composition was equilibrated with

the mantle (e.g., Fo_{90}). All calculations were performed under the conditions (f_{O2}, Fe–Mg K_D, mantle Fo content) specified by the authors. If no conditions were specified, compositions were restored to equilibrium with Fo_{90} olivine at NNO using K_D=0.30. All melt components, other than MgO, FeO and SiO_2, were diluted during the restoration process (i.e., $^{solid\text{-}melt}D$ =0). Initial volatile contents (denoted by *) were determined by taking the maximum H_2O and average S and Cl contents from the least degassed inclusions. Average S and Cl contents were used, rather than maxima, because these components tend to degas at shallower pressures than H_2O (Spilliaert et al., 2006; Johnson et al., 2010). Volatile contents were then diluted by the appropriate amount of olivine addition required for mantle equilibration. Parental melt H_2O*, S*, Cl*, and selected trace elements for each volcano are tabulated in Table 9.

All correlations are tested using the robust Kendall-Theil line in order to reduce the influence of outliers (i.e., Tonga; Table 9) (Helsel & Hirsch, 2003). The slope of each trend is computed by choosing the median slope ($\tilde{m}$) of all (i.e., $n(n-1)/2$ for n data points) data pairs (X,Y). The intercept ($\tilde{b}$) is calculated as $\tilde{b} = \tilde{y} - \tilde{m}\tilde{x}$, where $\tilde{x}$ and $\tilde{y}$ are the medians of X and Y, respectively. The significance of this method is reflected in the confidence interval of the slope (rather than an r^2 value traditionally reported in linear regression analyses). The confidence interval of the slope is determined by ordering all slopes from smallest to largest and taking the I^{th} and J^{th} values such that $P(m_I < \tilde{m} < m_J) \geq 1-\alpha$. The 95% confidence interval ($\alpha = 0.05$) is reported for all slopes shown in subsequent figures.

5.3 Results

The vast majority of dissolved volatiles in mafic arc magmas are derived from fluids originating during dehydration of the subducting oceanic plate. The considerable variability in estimated magmatic volatile contents from the global arc dataset is illustrated in Figure 32. Some of this variability may be attributed to poor sampling (e.g., degassed samples, diffusive loss), but most of it is probably primary. In general, a broad decrease in magmatic volatiles is observed in magmas erupted farther from the volcanic

front (VF) (or distance from the trench), however, most back-arc magmas still have elevated values compared to MORB (Figure 32).

Magmas from the Trans-Mexican Volcanic Belt that currently are influenced (CVF), or previously were influenced (MGVF), by flat slab subduction complicate this trend (Johnson et al., 2009). Magmatic volatile contents at the VF are not uniformly higher than those in back-arc regions, where contributions from the slab should be diminished (e.g., Schmidt & Poli, 1998; Kelley et al., 2006; Bezos, 2009). Instead VF magmas display considerable scatter but extend to higher average values.

Interestingly, absolute volatile concentrations are similar for basaltic magmas from arcs with drastically different slab thermal parameters (e.g., H_2O^* in Mexico [$\Phi/100$=6.4 km] and Tonga [$\Phi/100$=143 km] is ~4 wt.%; Figure 32a). Almost all of the arc-related magmas contain higher Cl* contents than typically found in MORB (~100 ppm; Wallace, 2005). Most H_2O^*/Cl^* ratios (not shown) are consistent with mixing between the mantle and seawater (3.5 wt.% NaCl equivalent; Kent et al., 1999; Ruscitto et al., 2010a). A subset of volcanoes (e.g., Shasta, Stromboli, Irazu, Augustine, and Granada), however, appear to require mixing with a more concentrated brine as reflected in high (>2000 ppm) Cl* contents (Figure 32b). Magmatic S* contents are generally higher than MORB (at equivalent FeO^T contents), but there is considerable overlap which may reflect complications related to sulfide saturation in the mantle wedge beneath some arcs (Figure 32c). Magmas in the well-characterized Central Oregon segment ($\Phi/100$= 0.8 km) of the Cascades show uniformly lower volatile concentrations than found in many other arcs, however, the pattern of increased variability at the arc front is still observed. Low H_2O^* contents in Galunggung (Java) magma are shown in Figure 32a for completeness, but will not be considered in further discussions. This magma was interpreted to reflect decompression-related melting (rather than fluid flux melting) by Sisson & Bronto (1998), however the low values could potentially reflect diffusive H_2O-loss (note that S* and Cl* contents are relatively high, similar to other arc magmas; Figure 32b,c; Table 9) (Massare et al., 2002; Portnyagin et al., 2008). Only magmas situated within ~60 km of the volcanic front (to the left of the gray lines in Figure 32) are considered in subsequent discussions to avoid potential complications arising from the increasing influence of adiabatic melting in the backarc (e.g., Walker et al., 2003).

Table 9. Primitive magma compositions and arc segment parameters.

Arc Segment	Volcano	Φ /100 (km)	SST 120km (ºC)[a]	H_2O* (wt.%)	S*	Cl*	Nb (ppm)	Ba	La	Ce	H_2O*/Ce	Cl*/Nb	Ba/La
1. Southern Cascades		0.4	955 ±25	2.83	0.14	0.21	2.29	168	10.6	30.8	1209	1129	15.3
	Goosenest[1]			2.71	n.d.	n.d.	n.d.	n.d.	n.d.	n.d.	n.d.	n.d.	n.d.
	Copco[1]			1.27	n.d.	n.d.	n.d.	n.d.	n.d.	n.d.	n.d.	n.d.	n.d.
	Shasta PBA[2]			4.00	0.20	0.26	1.49	81	9.8	28.2	1417	1740	8.3
	Shasta HMA[2]			3.34	0.08	0.16	3.10	256	11.5	33.3	1002	517	22.4
	Black Crater[1]			*0.28*	*n.d.*	*n.d.*	*n.d.*	*n.d.*	*n.d.*	*n.d.*	*n.d.*	*n.d.*	*n.d.*
2. Central Cascades		0.8	955 ±25	2.47	0.11	0.06	8.03	274	11.2	28.7	997	82	25.2
	Sand Mountain[unpub]			2.88	0.15	0.09	12.35	356	18.3	43.0	670	74	19.5
	Twin Craters[3]			1.59	0.11	0.03	6.27	318	11.5	32.7	487	49	27.7
	Island Fissure[3]			2.28	0.11	0.04	12.16	413	14.9	39.5	578	34	27.7
	Four-in-One[unpub]			2.61	0.08	0.07	n.d.	n.d.	n.d.	n.d.	n.d.	n.d.	n.d.
	Collier[3,unpub]			3.39	0.07	0.06	6.82	199	7.9	18.7	1807	88	25.0
	Yapoah[3]			2.60	0.08	0.08	5.69	230	8.5	21.3	1223	146	27.1
	Blue Lake[3]			2.96	0.13	0.06	4.60	210	6.7	17.4	1701	124	31.3
	Garrison Butte[3]			1.45	0.11	0.05	8.30	189	10.5	28.1	515	56	18.0
2. Central Cascades (Rowe)[3,4]		0.8	955 ±25	2.02[b]	0.09	0.04	7.06	214	8.6	23.0	898	51	25.0
3. Mexico: Chichinautzin		4	984 ±12	3.96	0.24	0.13	6.96	525	25.7	60.1	904	282	18.4
	Jumiltepec[5]			2.96	0.15	0.19	3.95	438	20.7	45.4	652	490	21.1
	Las Tetillas[5]			3.51	0.11	0.08	2.93	165	9.8	24.4	1440	267	16.9
	Tepetlapa[5]			3.12	0.17	0.10	16.56	320	22.4	54.1	577	62	14.3
	Xitle[5]			*1.21*	*0.09*	*0.07*	*26.90*	*341*	*25.0*	*56.6*	*213*	*25*	*13.6*
	Tuxtepec[5]			5.20	0.60	0.19	4.00	1453	59.0	143.0	364	475	24.6
	Popocatepetl[6]			5.00	0.19	0.08	7.37	248	16.7	33.6	1488	114	14.8
4. Mexico: Michoacan		6.4	700±50[c]	4.07	0.17	0.10	5.30	226	8.5	20.8	2233	308	26.8
	San Juan[7]			2.45	0.11	0.07	12.83	296	12.2	31.4	780	56	24.3
	Hungaro[7]			3.83	0.14	0.10	4.60	267	9.7	22.5	1698	215	27.4
	Jorullo[7]			5.75	0.21	0.13	2.02	183	6.6	14.6	3933	663	27.8

Table 9. Continued.

Arc Segment / Volcano	Φ /100 (km)	SST 120km (ºC) [a]	H_2O* (wt.%)	S*	Cl*	Nb (ppm)	Ba	La	Ce	H2O/Ce	Cl/Nb	Ba/La
4. Mexico: Michoacan	6.4	700±50[c]	4.07	0.17	0.10	5.30	226	8.5	20.8	2233	308	26.8
Astillero[7]			3.83	0.20	0.11	2.93	170	6.1	15.4	2480	388	27.6
Paricutin[7]			4.52	0.18	0.09	4.14	213	7.9	19.9	2273	221	27.0
San Miguel[7]			*3.71*	*0.20*	*0.09*	*3.97*	*173*	*7.1*	*19.8*	*1874*	*228*	*24.3*
El Pelon[7]			*3.57*	*0.19*	*0.09*	*7.54*	*292*	*13.9*	*34.6*	*1031*	*121*	*21.1*
La Loma[7]			*4.58*	*0.18*	*0.10*	*3.06*	*132*	*5.1*	*12.9*	*3561*	*335*	*25.8*
Hoya Alvarez[7]			*0.72*	*0.06*	*0.03*	*23.74*	*144*	*15.7*	*30.6*	*235*	*11*	*9.2*
5. Central American Arc: Guatemal/El Salvador	9.8	768±101	2.92	0.18	0.08	2.55	303	8.8	16.5	1921	330	41.8
Atitlan[8]			3.10	0.36	0.08	3.00	358	8.0	18.5	1674	267	44.8
Santa Maria[8]			3.70	0.26	0.08	2.70	318	7.0	15.1	2446	296	45.4
Fuego[1,8]			5.01	0.13	0.09	1.90	330	6.3	13.7	3654	487	52.4
Agua[8]			2.90	0.20	0.07	2.60	342	7.5	12.3	2363	269	45.6
La Providencia[9]			0.90	0.05	0.05	n.d.	157	n.d.	17.6	510	n.d.	n.d.
Cerro Mongoy[9]			1.94	0.09	0.08	n.d.	315	15.1	22.0	879	n.d.	20.8
Cerro Ovejero[9]			*2.13*	*0.13*	*0.05*	*n.d.*	*274*	*13.2*	*20.9*	*1019*	*n.d.*	*20.7*
C. Las Ruedas[9]			*2.16*	*0.10*	*0.03*	*n.d.*	*50*	*8.0*	*19.5*	*1108*	*n.d.*	*6.2*
6. Central American Arc: Costa Rica	10.2	811 ±5	4.42	0.27	0.13	8.84	523	22.4	46.2	1148	248	29.0
Irazu[8,10]			5.50	0.25	0.14	14.61	626	34.2	70.4	781	96	18.3
Arenal[8,11]			3.33	0.30	0.12	3.06	420	10.6	22.0	1515	400	39.6
7. Southern Lesser Antilles	10.5	760±10	4.82	0.17	0.17	6.51	155	7.0	15.6	3061	320	22.5
Granada[12]			6.01	0.23	0.22	10.12	166	8.1	18.6	3230	213	20.4
St. Vincent[13]			3.63	0.12	0.12	2.90	145	5.9	12.6	2892	428	24.6
8. Central American Arc: Nicaragua	11	651±201	3.83	0.18	0.06	2.73	152	3.2	6.9	6436	319	51.2
Nejapa[8]			3.00	0.18	0.04	4.10	88	3.1	8.3	3609	98	28.4
Cerro Negro[8,14,15]			5.40	0.19	0.07	1.20	190	2.3	4.2	12851	548	82.6
Granada (low Nb)[8]			4.20	0.22	0.08	1.50	272	3.5	7.0	5996	533	77.7
Granada (High Nb)[8]			2.70	0.12	0.04	4.10	59	3.7	8.2	3287	98	15.9

Table 9. Continued.

Arc Segment / Volcano	Φ /100 (km)	SST 120km (ºC) [a]	H_2O* (wt.%)	S*	Cl*	Nb (ppm)	Ba	La	Ce	H2O/Ce	Cl/Nb	Ba/La
9. Aleutians: Alaska: Augustine Volcano[16]	15.44	834 ±9	6.17	0.40	0.32	1.69	129	6.6	15.5	3979	1920	19.7
10. Aleutians: Alaskan Peninsula	21.8	796 ±11	2.13	0.12	0.06	3.21	222	8.6	19.8	1245	234	27.1
Emmons[16,18]			2.36	0.15	0.06	2.01	188	6.0	13.4	1768	322	31.4
Shishaldin[16,19]			1.89	0.08	0.06	4.41	257	11.3	26.3	722	146	22.7
11. Aleutians: East	25.4	788 ±10	2.91	0.14	0.08	2.34	228	6.3	14.9	2004	404	36.5
Akutan[16,20]			3.10	0.10	0.07	2.77	274	7.6	18.7	1659	262	35.9
Unalaska[16,21,22]			2.62	0.28	0.13	1.61	221	6.1	13.8	1893	780	36.2
Okmok[16,23,24]			3.01	0.04	0.04	2.64	188	5.0	12.2	2460	170	37.3
12. Aleutians: Central	28.6	793 ±7	3.78	0.22	0.09	3.42	233	4.9	11.3	3856	431	48.6
Seguam[16,19]			3.50	0.07	0.05	0.78	152	3.0	6.8	5135	648	50.3
Korovin[16,25,26]			4.05	0.37	0.13	6.07	313	6.7	15.7	2576	213	46.9
13. Bonin: Knolls Dredge[27,28]	40.8	680±132	2.16	0.11	0.05	n.d.	n.d.	n.d.	n.d.	n.d.	n.d.	n.d.
14. Izu: Miyakejima[29]	44.5	679±111	2.66	0.15	0.06	n.d.	n.d.	n.d.	n.d.	n.d.	n.d.	n.d.
15. Kamchatka Arc	54	725 ±25	3.11	0.15	0.07	1.39	176	4.6	11.9	2966	671	37.2
Ksudach[30]			2.71	0.08	0.07	0.52	51	1.9	5.9	4593	1304	26.8
Karymsky[30]			2.75	0.11	0.07	1.73	179	5.3	13.5	2037	405	33.8
Klyuchevskoy[30,31]			4.17	0.16	0.07	1.40	225	4.5	11.8	3519	492	50.3
Tolbachik[30]			2.81	0.23	0.09	1.89	249	6.6	16.4	1713	483	37.7
Farafonova Pad[30]			*2.61*	*0.27*	*0.11*	*1.76*	*148*	*5.6*	*15.8*	*1652*	*616*	*26.4*
16. Java: Galunggung[32]	54	544±238	0.34[d]	0.14	0.11	2.23	152	5.7	13.9	245	491	26.5
17. South Kurile: Kudryavy[33]	60.8	717 ±31	n.d.	0.09	0.12	n.d.	n.d.	n.d.	n.d.	n.d.	n.d.	n.d.
18. N. Kurile:Chikurachki[30,34]	63.7	728 ±24	2.91	0.11	0.07	1.05	156	5.0	12.4	2337	700	31.5
19. Marianas Arc	63.5	566±231	4.01	0.11	0.08	0.68	103	4.0	9.0	4862	1221	29.0
Asuncion[35]			3.70	0.11	0.10	n.d.	n.d.	n.d.	n.d.	n.d.	n.d.	n.d.
Alamagan[35]			3.95	0.12	0.10	n.d.	n.d.	n.d.	n.d.	n.d.	n.d.	n.d.
Guguan[35,36,37]			3.62	0.08	0.09	0.57	94	2.5	6.1	5945	1501	38.0
Pagan[35,36]			2.87	0.09	0.04	n.d.	n.d.	n.d.	n.d.	n.d.	n.d.	n.d.
Sarigan[35,36]			5.42	0.15	0.06	n.d.	n.d.	n.d.	n.d.	n.d.	n.d.	n.d.

Table 9. Continued.

Arc Segment / Volcano	Φ /100 (km)	SST 120km (ºC)[a]	H_2O* (wt.%)	S*	Cl*	Nb (ppm)	Ba	La	Ce	H2O/Ce	Cl/Nb	Ba/La
19. Marianas Arc (cont.)												
Agrigan[35,36,37,38]			4.48	0.10	0.07	0.78	112	5.6	11.9	3778	942	19.9
20: Tonga Arc: Volcano A[39]	143	659 ±51[e]	4.39	0.08	0.07	0.09	76	0.5	1.3	34186	6951	152.7

[a] average (±1 s.d.) slab surface temperature (SST) of D80, X25, W1300, T550 models of Syracuse et al. (2010) at 120 km.
[b] H_2O* interpolated from correlations with high-field strength elements after Ruscitto et al. (2010a).
[c] SST from Johnson et al. (2009).
[d] value likely reflects diffusive H_2O-loss.
[e] average SST excludes T550 model after Syracuse et al. (2010).
Magmas >60 km away from the VF were not included in arc segment averages and are italicized.
Refs: 1. Sisson & Layne (1993); 2. Ruscitto et al. (2010b); 3. Ruscitto et al. (2010a); 4. Rowe et al. (2009); 5. Cervantes & Wallace (2003); 6. Roberge et al. (2009); 7. Johnson et al. (2009); 8. Sadofsky et al. (2008); 9. Walker et al. (2003); 10. Benjamin et al. (2007); 11. Wade et al. (2006); 12. Bouvier et al. (2008); 13. Bouvier et al. (2010); 14. Roggensack et al. (1997); 15. Roggensack (2001); 16. Zimmer et al. (2010); 17. Johnson et al. (1996); 18. Mangan et al. (2009); 19. Jicha et al. (2004); 20. Romick et al. (1990); 21. Singer et al. (2007); 22. George et al. (2003); 23. Miller et al. (1992); 24. Nye & Reid (1986); 25. Myers et al. (2002); 26. Marsh (1982); 27. Rowe et al. (2007); 28. Hamada & Fujii (2007); 29. Saito et al. (2010); 30. Portnyagin et al. (2007); 31. Auer et al. (2009); 32. Sisson & Bronto (1998); 33. Tolstykh et al. (2003); 34. Gurenko et al. (2005); 35. Shaw et al. (2008); 36. Kelley et al. (2010); 37. Kent & Elliot (2002); 38. Newman et al. (2000); 39. Cooper et al. (2010).

Ratios of volatiles and trace elements of similar mineral-melt compatibility in the mantle (e.g., H_2O/Ce; Dixon et al., 2002; Hauri et al., 2006) are positively correlated with traditional fluid-mobile/immobile slab tracers (e.g., Ba/La; Elliot et al., 2003) and elevated above both MORB and OIB-like magmas (Figure 33). Importantly, a second trend is embedded within these correlations indicating that magmas originating in high-Φ subduction zones (e.g., Marianas, Nicaragua, Tonga) tend to have higher ratios than magmas from low-Φ settings (e.g., Central Oregon, Chichinautzin Volcanic Field) (Figure 33). Back-arc magmas from the Eastern Lau Spreading Center and the Marianas Trough are also consistent with patterns observed for magmas at the volcanic front.

5.4. Discussion

Important recent work by Plank et al. (2009) combined experimental studies on fluids and melts liberated from subducting oceanic crust and sediments with accessory phase solubility determinations and has yielded a provisional slab-fluid geothermometer:

$$H_2O/Ce = 2 \times 10^7 e^{-0.0109T} \quad (2)$$

The thermometer takes advantage of the large-scale (~3–4 orders of magnitude) variation in H_2O/Ce (Ce as a proxy for light rare earth element concentrations) contents in allanite/monazite-saturated liquids at high pressure (3.5–4.0 GPa) over a modest (several hundred degree) temperature shift from ~600 to 950 °C. Application of the geothermometer requires that the subduction component be saturated with a residual LREE-bearing accessory mineral (e.g., allanite or monazite) in order for the LREE contents of fluid phase to reflect the calibrated relationship to temperature (Plank et al., 2009).

This assumption is likely valid given the wide stability field for allanite and monazite (Klimm et al., 2008) and therefore measured H_2O/Ce ratios of primitive arc magmas potentially reflect the temperature of fluids/melts exiting the slab surface. Slab surface temperatures calculated using equation (1) are shown along the top axis in Figure 33 and imply that magmas generated in low-Φ arcs are influenced by hotter fluids with more muted subduction-related signatures compared to those generated in high-Φ arcs. We test this observation further in Figure 34 and find a statistically significant negative

correlation between average H_2O*/Ce ratios (for a given arc segment defined by Syracuse et al., 2010; Table 9) and average slab surface temperatures predicted by geodynamic models at 120 km depth (Syracuse et al., 2010). Calculated slab-fluid temperatures (equation 2) do not exhibit a one-to-one relationship with predicted temperatures from the

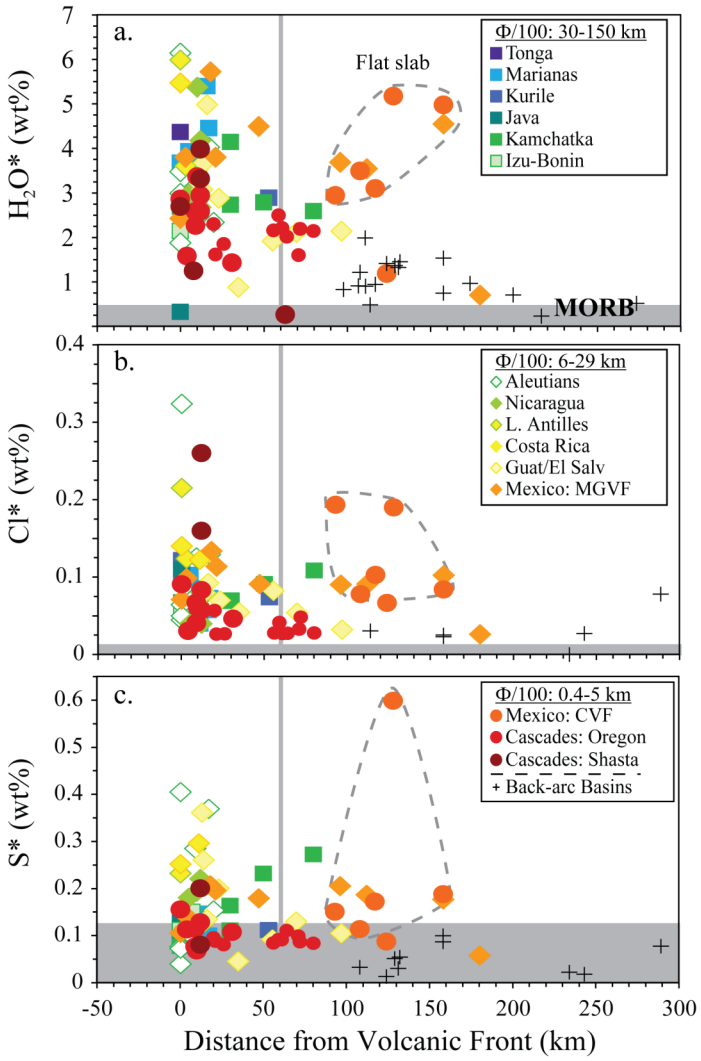

Figure 32. Initial (undegassed) volatile contents (* denotes back-corrected to equilibrium with mantle olivine) of parental magmas for individual volcanoes plotted against relative distance to the volcanic front. Small red circles (Central Oregon) are from rehomogenized melt inclusions from Rowe et al. (2009). Samples denoted as Back-arc Basin Basalts (BABB; +) are basaltic glasses from the Marianas Trough, East Scotia Ridge, Lau Basin, Manus Basin, Ngatoro Basin, and Havre Trough (Hawkins et al. 1990; Stolper & Newman et al. 1994; Gribble et al. 1996; Newman et al. 2000; Haase et al., 2002; Kelley et al., 2006; Wysoczanski et al., 2006; Bezos et al., 2009). The shaded field in each panel represents the range in primitive MORB (Wallace et al., 2005). Vertical lines at 60 km in each panel show the cut-off for samples averaged in volcanic front arc segments. Legend is broken up into three panels for clarity.

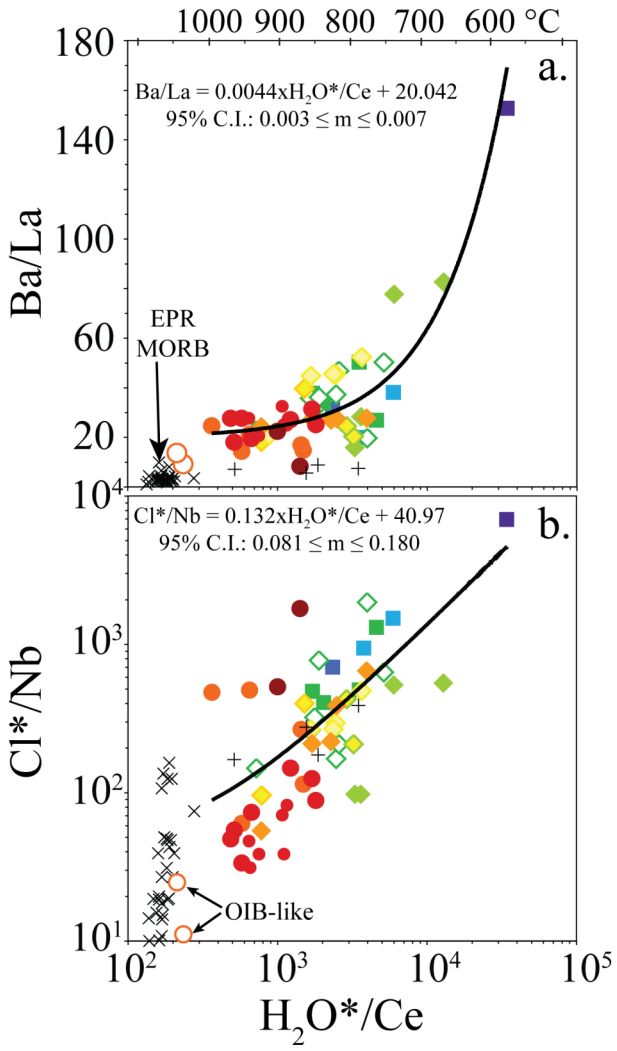

Figure 33. H_2O^*/Ce versus Ba/La (a) and Cl*/Nb for primitive magma compositions (symbols as in Figure 32). MORB glasses 'X' from the East Pacific Rise and OIB-like magmas from Mexico are also shown (Cervantes & Wallace, 2003; Le Roux et al., 2006; Johnson et al., 2009). Thick lines through data are calculated using the robust Kendall-Thiel line (Helsel & Hirsch, 2003) through arc front magmas only (equations with confidence intervals of slopes, m, are shown in each panel). Top axis corresponds to temperatures of slab fluids calculated from the provisional H_2O/Ce slab fluid geothermometer of Plank et al. (2009).

geodynamic models. The H_2O^*/Ce ratios of the magmas likely reflect the average temperature of the fluids released over a range of depths rather than at single location along the descending slab. Additionally, uncertainties regarding the position of the slab-mantle coupling depth (i.e., between 51-80 km for the Central Cascades, depending on the model) cause considerable variability in calculated slab surface temperatures because

of the sharp increase in calculated dP/dT slopes associated with full slab-mantle coupling (Syracuse et al., 2010).

Alternatively, we note that the provisional slab-fluid thermometer yields finite temperatures of ~1020–1120 °C for mantle H_2O^*/Ce ratios (200 ±100; Dixon et al., 2002), which suggests that the apparent trends in Figure 33 and Figure 34 may reflect variable mixing between a MORB-source and a high-H_2O/Ce slab-derived component. This alternative scenario may not be important in high-Φ arcs where H_2O/Ce of the subduction components are expected to swamp out any mantle signature, but may be important in low-Φ arc environments, where slab contributions to the mantle wedge may be diminished because of shallow dehydration (e.g., Central Oregon, Mexico; Figure 30, Figure 31, Figure 33, Figure 34). Therefore, the H_2O/Ce ratios of the fluids, rather than those from the magmas, must be examined to distinguish between these two competing hypotheses.

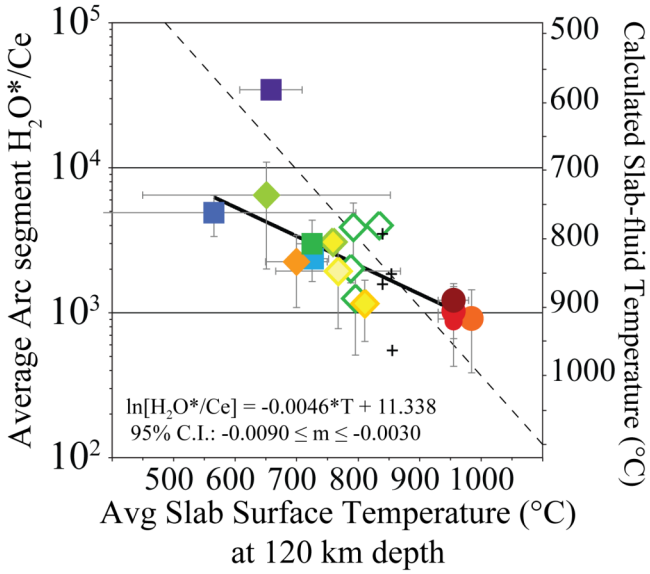

Figure 34. Average H_2O^*/Ce ratios of VF magmas versus predicted slab surface temperatures at 120 km depth (Syracuse et al., 2010) for each arc segment listed in Table 9; symbols are as in Figure 32. Right axis corresponds to temperatures of slab fluids calculated from the provisional H_2O/Ce slab fluid geothermometer of Plank et al. (2009) and dashed line shows 1:1 correspondence with the abscissa. Thick line is the robust Kendall-Thiel line (Helsel & Hirsch, 2003) through the arc front magmas (equation with confidence interval of slope, m, is shown). BABB data are averages of high and low Nb/Zr basalts from the Lau Basin (Bezos et al., 2009) and basalts from the Marianas Trough (Hawkins et al. ,1990; Stolper & Newman et al., 1994; Gribble et al., 1996;

Newman et al., 2000) and are plotted at slab surface temperatures corresponding to 240 km depth.

We calculated subduction fluid compositions for primitive magmas from Central Oregon and Mt. Shasta using an approach similar to that outlined by Portnyagin et al. (2007). Following the rationale presented in Ruscitto et al. (2010a), we use an enriched mantle source to infer degrees of melting constrained by elements that are not significantly mobilized in high pressure slab-derived fluids and melts (e.g., TiO_2, Dy, Er, Gd, Yb, Y; Kessel et al., 2005). Calculated subduction fluid compositions are presented in Table 10. Errors (2σ) for slab component compositions were determined using Monte Carlo methods (N=300) and allowing primitive magma compositions to vary within uncertainty. Ba/La and H_2O/Ce ratios of the calculated slab components (along with slab components from the literature) are shown in Figure 35. Slab components were not calculated for all primitive magmas listed in Table 9 because of uncertainties regarding mantle sources. The similarities between ratios of the magmas and the slab components support the hypothesis that magmas formed in low-Φ arc environments are influenced by hotter slab-derived fluids than arcs characterized by higher-Φ values. Additionally, fractional melting models of sediment (GLOSS; Plank & Langmuir, 1998) and altered oceanic crust ('Super'-AOC; Kelley et al., 2003), using the fluid-solid partition coefficients of Kessel et al. (2005) at 4 GPa, are able to reproduce the thermo-chemical trends defined by the magma and fluid compositions (Figure 35). Whether or not sediment-derived fluids/melts are actually more important than AOC-fluids/melts to magma generation in lower-Φ arcs, as implied in Figure 6, is not well-constrained by this study.

A MORB-normalized spidergram of calculated subduction components demonstrates the similarities and differences between slab-derived fluids in arcs characterized by different thermal parameters (Figure 36). While all of the slab components display LILE-enrichments over light-rare earth elements and negative Nb anomalies, fluid compositions in lower-Φ arcs tend to be more solute-rich while those in higher-Φ arcs are more dilute. This observation is consistent with the expected transition of high-pressure slab-derived components from solute-rich aqueous fluids to H_2O-rich slab melts with increasing temperature (Kessel et al., 2005; Hermann & Spandler, 2008).

Figure 36 also indicates that the subduction component calculated by Stolper & Newman, 1994 represents a good global average composition.

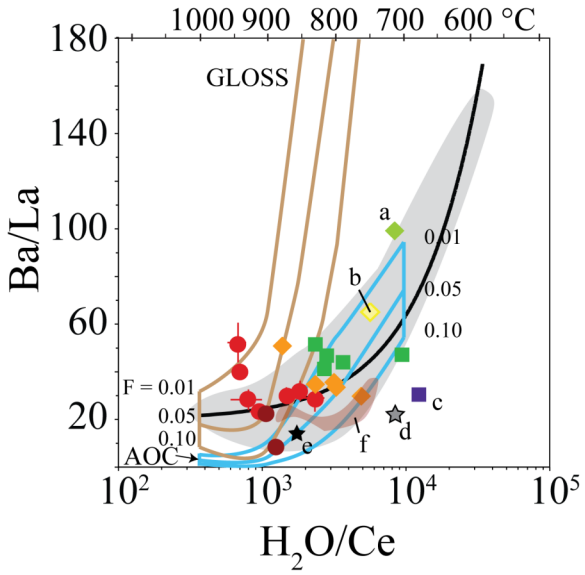

Figure 35. H_2O/Ce versus Ba/La ratios of calculated subduction fluids for the Central Cascades and Southern Cascades (this study), MGVF (Johnson et al., 2009), and Kamchatka (Portnyagin et al., 2007) (symbols as before). H_2O/Ce temperatures calculated from the H_2O/Ce slab fluid thermometer are shown across the top axis. Also shown are estimated fluid compositions from Central America from Eiler et al. (2005) (a: Nicaragua = low $\delta^{18}O$ fluid, b: Guatemala = high $\delta^{18}O$ fluid), the Tonga arc (c: 'Wet' component) and Lau basin (d: 'Damp' component) from Bezos et al. (2009), the Marianas Trough (e) from Stolper & Newman (1994), and the Shasta region (field labeled f) from Grove et al. (2002). Magmatic ratios (gray field) and Kendall-Thiel line (black line) from Figure 33a are shown for reference. Fractional melting models, calculated using experimental fluid-melt partition coefficients at 4 GPa from Kessel et al. (2005), are shown for the altered oceanic crust ("Super" AOC; Kelley et al., 2003) and average global subducting sediment (GLOSS; Plank & Langmuir, 1998) at F values of 0.01, 0.05, and 0.10.

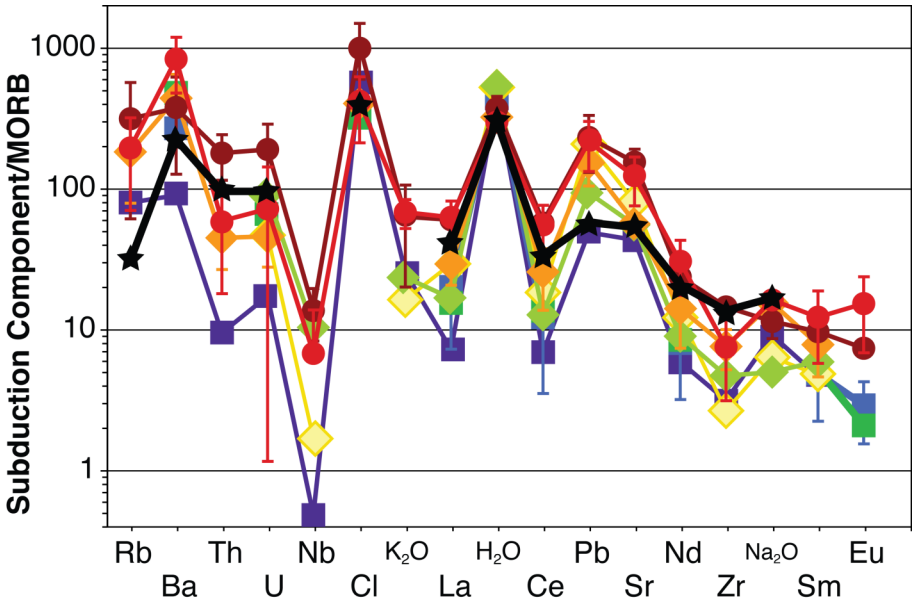

Figure 36. Spiderplot of calculated average (±1 s.d.) subduction components (shown in Figure 35) normalized to N-MORB (Sun & McDonough, 1989; McDonough & Sun, 1995).

5.5. Conclusions

We have compiled a dataset of primitive magma compositions for over 70 volcanic centers comprising 20 arc segments encompassing the global range in slab thermal parameters. We demonstrated that magmatic volatile contents (H2O*, S*, Cl*) are more variable and extend to greater values in magmas generated closer to the trench and that most arc-related magmas have volatile contents elevated above MORB values (Figure 32). These data provide clear evidence that magmatic volatiles are ultimately derived from the dehydrating subducting slab. We also demonstrated significant positive correlations between H2O*/Ce and Cl*/Nb and traditional slab tracers like Ba/La (Figure 33). Average H2O*/Ce ratios for a given arc segment are negatively correlated with slab surface temperatures predicted by geodynamic models at 120 km depth (Figure 34). Observed correlations do not result from mixing between MORB source and a volatile-rich fluid component. Rather, our data reflect genuine changes in the nature of the slab-derived fluid(s), which becomes increasingly solute-rich at higher temperatures (Figure 35, Figure 36). We emphasize that the importance of the correlation and close temperature agreement seen in Figure 34 cannot be overstated because it represents the convergence of two independent (geochemical and geophysical) methods of inquiry.

Table 10. Calculated slab component compositions**.**

	Twin Craters[a]	Garrison Butte	Island Fissure	Sand Mtn	Yapoah	Collier	Blue Lake	Shasta HMA	Shasta PBA
Rb[b]	57.5 ±46.1	21.0 ±60.9	234.9 ±26.8	68.6 ±25.0	143.2 ±27.8	127.9 ±12.0	112.6 ±11.1	277.2 ±14.8	76.1 ±8.3
Ba	8484 ±927	5210 ±1008	8222 ±543	4993 ±479	3746 ±342	3284 ±268	3021 ±226	3466 ±154	1258 ±84
Th	1.23 ±5.04	0.00	9.98 ±4.10	5.80 ±2.63	12.42 ±2.16	11.76 ±1.17	8.74 ±1.00	26.96 ±1.87	16.11 ±1.08
U	0.0	0.0	8.1 ±2.2	0.0	5.2 ±1.1	5.3 ±0.7	5.2 ±1.0	12.2 ±1.7	5.7 ±0.8
Nb	0.0	0.0	35.2 ±18.9	0.0	15.6 ±15.3	37.0 ±25.2	23.0 ±9.5	41.9 ±1.7	23.3 ±1.2
Cl wt.%	1.16 ±0.14	2.28 ±0.84	0.91 ±0.06	1.80 ±0.23	1.38 ±0.14	0.45 ±0.04	0.84 ±0.07	2.20 ±0.09	4.11 ±0.18
K_2O wt.%	11.15 ±1.82	7.52 ±2.20	13.81 ±1.23	10.09 ±1.13	10.80 ±1.27	8.11 ±0.83	7.68 ±0.41	13.60 ±0.74	4.74 ±0.26
La	162 ±26	184 ±30	209 ±14	215 ±17	122 ±8	113 ±20	95 ±10	153 ±8	150 ±7
H_2O wt.%	38.22 ±3.78	43.75 ±6.16	41.44 ±2.46	47.52 ±3.79	42.22 ±2.36	55.99 ±2.67	44.22 ±1.97	47.37 ±2.06	64.53 ±1.56
Ce	561 ±57	541 ±66	574 ±35	493 ±37	281 ±23	238 ±34	238 ±21	442 ±22	433 ±22
Pb	72.2 ±7.9	90.6 ±20.8	106.1 ±23.6	53.8 ±9.9	50.1 ±4.8	41.9 ±2.8	41.7 ±2.8	91.1 ±5.6	48.3 ±3.4
Sr	13811 ±1296	14846 ±1984	11379 ±674	16496 ±1242	7244 ±578	6262 ±483	7069 ±246	11645 ±520	16267 ±700
Nd	315 ±31	303 ±41	296 ±21	269 ±20	124 ±14	122 ±24	122 ±12	166 ±12	181 ±8
Zr	145 ±162	1114 ±569	745 ±123	727 ±132	472 ±162	411 ±225	299 ±117	1180 ±65	970 ±48
Na_2O wt.%	47.11 ±3.91	44.21 ±4.89	41.66 ±1.79	38.26 ±3.06	44.37 ±2.25	34.38 ±2.33	46.16 ±1.76	35.08 ±1.77	24.68 ±1.31
Sm	59.7 ±25.3	42.3 ±14.7	30.9 ±5.1	44.9 ±8.2	14.8 ±4.8	16.4 ±5.0	17.8 ±3.0	25.3 ±2.9	25.7 ±2.2
Eu	23.7 ±6.3	27.2 ±5.3	22.7 ±2.3	12.9 ±1.2	6.9 ±1.6	8.0 ±1.7	8.0 ±1.1	7.3 ±0.8	7.9 ±0.6
H_2O/Ce	681 ±102	809 ±197	722 ±76	964 ±137	1505 ±177	2353 ±389	1861 ±244	1072 ±86	1265 ±97
Ba/La	52.3 ±8.3	28.4 ±4.4	39.3 ±2.5	23.2 ±1.2	30.7 ±2.9	29.1 ±5.7	32.0 ±4.3	22.7 ±1.1	8.4±0.5
Parameters from best-fits (after Portnyagin et al. 2007)									
Sum. Resid.[c]	0.38 ±0.13	0.14 ±0.07	0.35 ±0.11	0.50 ±0.09	0.67 ±0.58	0.80 ±0.27	0.96 ±0.41	0.92 ±0.41	1.03 ±0.13
PME[d]	0.00	0.00	0.00	0.00	0.02 ±0.01	0.02 ±0.00	0.03 ±0.01	0.06	0.06
F[d]	0.082 ±0.004	0.087 ±0.003	0.101 ±0.005	0.082 ±0.006	0.129 ±0.023	0.132 ±0.019	0.113 ±0.033	0.140 ±0.016	0.196 ±0.011
X_SC[e] wt.%	0.22 ±0.03	0.008 ±0.003	0.017 ±0.004	0.019 ±0.005	0.043 ±0.025	0.045 ±0.015	0.052 ±0.024	1.03 ±0.13	1.24 ±0.08
$H2O^0$ wt.%	0.15 ±0.01	0.18 ±0.03	0.46 ±0.03	0.43 ±0.05	0.79 ±0.15	0.81 ±0.14	0.78 ±0.20	0.49 ±0.06	0.81 ±0.06

[a] Uncertainty determined from 300 Monte Carlo simulations allowing each element to vary within 1 standard error of the mean. [b] All units in ppm unless noted. [c] Sum of the residual differences for TiO_2, Dy, Er, Gd, Yb, and Y between the model composition and sample. [d] Previous melt extraction of mantle source (PME) and degree of melting required to produce sample (F). [e] wt.% subduction component added to mantle source with H_2O^0 of mantle reported below.

CHAPTER VI
CONCLUSIONS

This dissertation synthesizes research on magma formation and evolution, cinder cone eruption styles, and subduction zone volatile recycling in the modern High Cascades, with an emphasis on the pre-eruptive volatile (H_2O, CO_2, S, and Cl) contents of mafic magmas. I have pursued this line of inquiry because volatiles influence all aspects of volcanic activity from magma formation and mineral stability to eruption explosivity and climate forcing. Therefore, understanding the volatile components is critical for both mitigating volcanic hazards and attaining a deeper understanding of large-scale geodynamic processes and geochemical cycles. I have used a combination of geochemical techniques coupled with field-based observations and thermodynamic principles to infer pre-eruptive volatile contents and eruption histories recorded in olivine-hosted melt inclusions from recent mafic tephra deposits.

The first two studies characterized pre-eruptive volatile contents from Central Oregon. Chapter II detailed the eruptive histories and degassing styles of three recent (≤ 3000 yrs b.p.) cinder cones in Central Oregon and related them to well-studied historical eruptions from Mexico. Inferred explosive activity ranged from Strombolian for the Four-in-One eruption to Violent Strombolian for the Collier Cone and Sand Mountain eruptions. Olivine-hosted melt inclusions from the deposits are volatile-rich and represent the most primitive compositions associated with each eruption, relatively unaffected by crustal assimilation processes. Degassing patterns and inferred melt inclusion trapping pressures from Sand Mountain are consistent with either a closed system model or a gas-fluxing model, where a CO_2-rich vapor from the lower crust was fluxing the overlying shallow magma system. Collier and Four-in-One melt inclusions reflect limited amounts of degassing, suggesting formation in isolated middle to upper crustal magma reservoirs (probably sills) prior to eruption. Differences in magma migration and storage patterns between Collier and Four-in-One versus Sand Mountain and the Mexican cinder cones

may be related to differences in magma volumes and eruption durations and/or proximity to a larger, well-established volcanic edifice (i.e., North Sister).

The Central Oregon dataset was expanded in Chapter III to include seven more cinder cones Conditions of formation were inferred for several types of mafic arc magmas: calc-alkaline basalt, Sr-rich basalt, and depleted basaltic andesite. H_2O contents of the Central Oregon magmas are generally lower than those found in other arcs, but elevated compared to oceanic back-arc magmas. Sulfur, Cl, and CO_2 contents are comparable to those found in other arcs. Calc-alkaline basalt and Sr-rich basalt melts can be generated by partial melting of spinel lherzolite. H_2O-rich basaltic andesite melts are highly depleted in incompatible elements and were probably generated from a more depleted mantle source. Subarc mantle temperatures inferred from H_2O and trace elements are similar to or slightly warmer than temperatures in other arcs. Additionally, concordance between slab surface geothermometers (based on H_2O/Ce and H_2O/K_2O) suggests high temperatures (850–950 °C) for calculated slab components compared to arcs with older subducting slabs.

Chapter IV re-examined a well studied example of high-Mg andesite (HMA) was re-examined from near Mt. Shasta, CA. Petrographic evidence for magma mixing in this locality has stimulated a recent debate over whether HMA magmas have a mantle origin. Two types of volatile-rich primitive magmas were identified in the olivine-hosted melt inclusions (HMAs and primitive basaltic andesites; PBAs); each with distinct trace element characteristics. PBA melts are comparable to experimental hydrous melts in equilibrium with harzburgite. A two-component bulk mixing model between PBA and a dacitic magma was able to produce a primitive HMA composition, but the predicted mixture shows some small but significant major and trace element discrepancies from published whole-rock analyses from the Shasta locality. An alternative model involves incorporation of xenocrysts (high-Mg olivine from PBA and pyroxenes from dacite) into a primary (mantle-derived) HMA magma and may explain the phenocryst and melt inclusion compositions. However, this model is difficult to evaluate quantitatively because of the complex crystal populations. The results suggest that a spectrum of mantle-derived melts, including both PBA and HMA, may be produced beneath the Shasta region. Additionally, compositional similarities between Shasta parental melts and

boninites from intraoceanic arcs imply similar magma generation processes related to the presence of refractory harzburgite in the shallow mantle.

The final study, Chapter V, compared the volatile contents of primitive magmas inferred from Central Oregon and Northern California melt inclusion data to those from other arcs. The nature of the slab-derived component added to the mantle wedge beneath the Cascades was also examined by putting the Cascades into a global context. Primitive magma compositions for over 70 volcanic centers comprising 20 arc segments were compiled into a global dataset encompassing the global range in slab thermal parameters. Magmatic volatile contents (H_2O, Cl, S) were demonstrated to be both more variable and extend to higher values in magmas generated closer to the trench compared to those from the back-arc. Significant positive correlations between H_2O/Ce, Cl/Nb, and Ba/La and a negative correlation between H_2O/Ce and predicted slab surface temperatures from geodynamic models provide evidence for a change in the nature of the slab-derived component with increasing slab temperature. The observations do not result from mixing between a MORB source mantle and a volatile-rich fluid and instead are consistent with the expected transition of high-pressure slab-derived components from solute-rich aqueous fluids to H_2O-rich slab melts as temperature increases (Kessel et al., 2005; Hermann & Spandler, 2008).

This work successfully investigates two interrelated aspects of volcanology and igneous petrology: (1) relationships between pre-eruptive magmatic volatile contents and eruption activity in explosive monogenetic cinder cone eruptions, and (2) the role of volatiles in magma generation in a 'warm-slab' subduction environment. I hope that these works highlight the need for additional investigations into these complex, fundamental, and potentially hazardous earth processes.

APPENDIX A

ANALYZED MELT INCLUSION COMPOSITIONS

Inclusion	Fo Host	(wt%) SiO_2	TiO_2	Al_2O_3	FeO^T	MnO	MgO	CaO	Na_2O	K_2O	P_2O_5	S	Cl	H_2O	1s.d.	(ppm) CO_2	1s.d.	Total
CC0801-2																		
h	84.51	53.12	0.96	18.48	6.54	0.10	5.31	8.49	2.65	0.53	0.13	0.08	0.07	2.91	0.13	988	57	99.46
c	84.53	53.03	0.88	18.08	6.54	0.11	4.96	8.65	2.92	0.51	0.12	0.08	0.08	2.53	0.26	665	42	98.54
i	84.61	53.21	0.91	18.56	6.66	0.11	5.42	8.67	2.87	0.50	0.12	0.08	0.08	3.47	0.32	809	73	100.73
a	84.66	54.48	0.99	17.60	6.35	0.11	4.96	7.98	2.55	0.64	0.14	0.08	0.08	2.80	0.16	672	56	98.83
b	84.73	52.79	0.93	18.35	6.62	0.12	5.12	8.66	2.65	0.49	0.12	0.08	0.08	2.72	0.17	799	154	98.80
f1	84.75	52.85	1.00	19.36	6.12	0.09	4.23	8.85	2.53	0.58	0.15	0.09	0.08	2.76	0.34	635	39	98.77
g	84.79	53.16	0.91	18.35	6.62	0.11	5.46	8.55	2.83	0.55	0.15	0.08	0.08	2.88	0.41	919	76	99.81
d	84.95	53.06	0.86	17.53	6.76	0.10	5.30	8.49	2.03	0.61	0.11	0.08	0.07	3.34	0.20	450	31	98.38
Collier-33A																		
e	84.21	51.78	0.86	18.31	6.82	0.11	5.35	8.52	3.83	0.50	0.10	0.07	0.06	3.17	0.19	969	58	99.59
c	84.42	51.57	0.86	18.36	7.00	0.12	5.79	8.34	3.84	0.48	0.10	0.07	0.07	3.15	0.62	663	108	99.80
d	84.53	51.91	0.89	18.89	6.44	0.11	5.17	8.64	3.88	0.48	0.10	0.07	0.06	3.86	0.31	1352	118	100.64
Collier-33B																		
e1	84.88	52.48	0.87	19.40	6.05	0.11	3.84	8.81	4.03	0.51	0.09	0.07	0.06	3.53	0.23	733	56	99.93
e2	84.88	53.35	0.91	19.42	5.91	0.10	3.35	8.85	4.15	0.54	0.10	0.07	0.07	2.45	0.17	n.d.	-	99.27
d	84.94	53.81	0.91	20.27	5.20	0.08	2.36	8.61	4.75	0.68	0.13	0.08	0.07	3.59	0.29	1048	81	100.65
b	85.00	51.58	0.83	18.57	6.50	0.10	5.98	8.42	3.74	0.60	0.18	0.08	0.06	2.90	0.30	973	66	99.63
a	85.23	50.86	0.89	19.58	6.27	0.11	3.92	9.28	3.78	0.45	0.13	0.07	0.07	2.68	0.34	770	91	98.16
Collier-33C																		
lower-b	80.07	53.51	1.05	17.37	6.43	0.10	4.47	7.46	4.92	0.67	0.13	0.08	0.07	4.27	0.56	985	129	100.64
lower-e	80.76	52.78	0.93	17.57	6.67	0.11	5.04	7.97	4.06	0.58	0.11	0.07	0.06	3.73	0.31	797	78	99.77
lower-a	82.99	52.78	0.96	18.29	6.04	0.10	4.67	7.95	4.28	0.63	0.12	0.08	0.06	3.36	0.15	1112	60	99.44
upper-b1	84.16	51.90	0.88	18.66	6.29	0.11	4.65	8.54	4.02	0.51	0.09	0.07	0.06	2.98	0.36	648	84	98.84
upper-b2	84.16	51.82	0.88	18.61	6.54	0.11	5.12	8.36	4.03	0.52	0.10	0.07	0.09	2.66	0.75	666	78	98.98
upper-a	84.85	52.64	0.88	19.89	5.62	0.10	3.00	9.35	3.99	0.57	0.16	0.08	0.08	3.19	0.15	876	47	99.65
upper-d	84.88	51.39	0.84	19.14	6.36	0.11	5.74	8.66	3.72	0.48	0.11	0.07	0.06	3.89	0.63	1246	129	100.72
upper-e	84.92	53.14	0.99	19.69	5.34	0.10	2.55	9.13	4.21	0.66	0.18	0.09	0.06	3.69	0.22	1086	142	99.93

Appendix A. Continued.

Inclusion	Fo Host	(wt%) SiO_2	TiO_2	Al_2O_3	FeO^T	MnO	MgO	CaO	Na_2O	K_2O	P_2O_5	S	Cl	H_2O	1s.d.	(ppm) CO_2	1s. d.	Total
Collier-33D																		
a	77.07	55.14	1.07	16.61	7.11	0.13	3.95	6.38	5.19	0.92	0.21	0.08	0.07	4.19	0.31	1050	102	101.1
d	78.28	52.50	0.91	17.17	7.70	0.14	4.90	7.70	4.26	0.61	0.10	0.07	0.06	3.95	0.29	695	66	100.1
e	83.7	52.90	0.97	18.02	6.16	0.11	4.19	8.17	4.33	0.59	0.11	0.07	0.07	3.42	0.22	651	284	99.19
b1	84.82	53.07	0.96	20.07	5.15	0.09	2.46	9.21	4.23	0.58	0.13	0.08	0.06	3.51	0.26	1215	92	99.71
b3	84.82	52.68	0.97	20.28	5.44	0.09	2.54	9.28	4.35	0.54	0.12	0.07	0.07	2.60	0.27	1056	107	99.14
CC0802D-200																		
i1	78.93	53.73	0.92	17.30	7.68	0.14	4.80	7.80	2.17	0.59	0.14	0.08	0.07	3.85	0.55	745	67	99.34
i2	78.93	54.73	1.03	16.70	7.44	0.13	4.43	6.98	1.87	0.79	0.15	0.09	0.09	3.83	0.40	703	63	98.32
i3	78.93	55.72	1.04	16.55	7.43	0.12	4.48	7.00	2.10	0.81	0.14	0.09	0.09	3.29	0.28	703	61	98.93
g	80.1	55.21	0.90	17.01	7.46	0.12	4.67	7.34	2.16	0.84	0.15	0.07	0.09	3.31	0.30	516	38	99.36
d	83.88	52.66	0.90	18.77	6.75	0.11	4.75	8.61	2.50	0.53	0.12	0.08	0.08	3.47	0.18	577	35	99.40
e	84	52.39	0.95	18.88	6.39	0.10	4.83	8.47	2.52	0.53	0.13	0.08	0.08	2.95	0.24	479	25	98.34
f	84.13	53.73	0.91	17.95	6.09	0.10	4.71	8.55	2.54	0.54	0.12	0.08	0.07	2.68	0.12	602	35	98.13
b	84.19	55.05	0.97	17.79	5.98	0.10	4.88	8.08	1.86	0.53	0.12	0.08	0.08	4.03	0.35	878	76	99.65
a	84.71	57.12	1.11	17.17	5.25	0.09	4.38	7.48	2.17	0.76	0.15	0.06	0.09	2.99	0.18	623	56	98.89
FO0803-A																		
e	82.36	53.43	1.17	16.50	7.02	0.11	5.34	8.98	3.15	0.66	0.25	0.10	0.08	3.22	0.19	812	90	100.1
f1	82.93	52.60	1.13	17.36	6.74	0.12	4.70	9.26	2.73	0.66	0.25	0.09	0.09	2.92	0.48	835	58	98.72
f2	82.93	52.80	1.15	17.63	6.96	0.12	4.91	9.20	2.79	0.67	0.25	0.09	0.09	2.42	0.15	671	53	99.15
d	83	50.60	1.09	17.73	7.80	0.13	5.91	8.72	2.83	0.66	0.26	0.09	0.08	2.29	0.17	752	51	98.26
b	83.27	51.51	1.16	18.41	6.69	0.12	4.96	9.05	3.23	0.68	0.26	0.09	0.08	2.85	0.16	940	59	99.18
g	83.28	51.95	1.11	17.10	7.86	0.13	5.68	9.08	3.50	0.73	0.24	0.09	0.08	1.79	0.10	790	45	99.42
c	83.39	52.00	1.11	17.06	6.58	0.11	5.08	9.12	3.01	0.68	0.23	0.09	0.08	2.90	0.38	735	74	98.13
a1	83.59	51.49	1.08	17.04	7.50	0.13	6.09	9.01	3.01	0.62	0.23	0.09	0.08	3.06	0.29	874	53	99.51
a2	83.59	51.81	1.12	17.25	7.06	0.13	5.97	8.78	3.14	0.72	0.25	0.10	0.08	2.55	0.21	545	38	99.01
FO0803-D3																		
b	80.76	52.48	0.94	16.25	8.30	0.14	5.98	8.18	3.00	0.68	0.19	0.08	0.11	3.03	0.49	674	97	99.43
c1	81.98	51.66	1.07	17.06	8.04	0.15	5.88	8.69	2.77	0.62	0.22	0.09	0.09	2.82	0.23	833	68	99.23
f	82.23	53.21	1.13	18.15	6.54	0.12	3.84	9.03	3.30	0.74	0.25	0.10	0.08	2.11	0.23	668	65	98.66
e	82.96	51.34	1.14	17.08	7.61	0.13	5.73	8.88	3.51	0.68	0.24	0.09	0.09	1.99	0.23	542	108	98.56
g	83.06	52.22	1.11	16.67	7.81	0.12	5.95	9.11	3.26	0.66	0.24	0.10	0.08	1.96	0.13	731	61	99.36
a	83.07	51.50	1.12	17.50	7.68	0.13	6.00	8.82	2.91	0.65	0.25	0.10	0.08	2.47	0.25	850	46	99.29
m	83.37	51.37	1.04	16.02	8.01	0.13	5.99	9.02	3.11	0.61	0.22	0.09	0.08	1.02	0.11	n.d.	-	96.73
i	83.47	52.05	1.20	16.62	7.41	0.12	5.96	8.67	3.13	0.67	0.34	0.09	0.08	3.19	0.49	988	138	99.63
k	83.52	51.23	1.11	17.03	7.81	0.13	5.55	9.25	3.20	0.62	0.24	0.09	0.08	2.25	0.15	774	64	98.66
L	83.56	51.91	1.07	16.90	7.44	0.12	5.97	8.91	3.01	0.65	0.22	0.09	0.08	2.91	0.52	858	121	99.36

Appendix A. Continued

Inclusion	Fo Host	(wt%) SiO_2	TiO_2	Al_2O_3	FeO^T	MnO	MgO	CaO	Na_2O	K_2O	P_2O_5	S	Cl	H_2O	1 s.d.	(ppm) CO_2	1s.d.	Total
SM1001-B																		
b	79.69	49.34	1.20	17.28	10.67	0.17	4.91	8.57	3.99	0.77	0.37	0.14	0.10	2.19	0.52	321	33	99.72
c	82.86	52.42	1.43	17.39	7.71	0.13	4.21	8.97	4.60	1.18	0.42	0.08	0.14	0.51	0.05	42	15	99.21
d	83.25	50.03	1.32	19.69	7.26	0.11	4.43	9.93	4.47	0.98	0.44	0.19	0.14	0.16	0.04	273	26	99.17
a	83.96	50.07	1.44	17.92	7.51	0.13	5.90	9.37	3.92	0.72	0.36	0.10	0.06	2.22	0.17	1134	86	99.83
e	84.14	50.17	1.56	18.41	7.43	0.12	5.20	9.53	3.98	0.80	0.45	0.09	0.06	1.47	0.21	950	86	99.37
e_reent	84.14	50.70	1.55	17.31	9.03	0.16	4.87	9.10	4.37	0.99	0.37	0.07	0.06	0.78	0.05	108	15	99.34
SM1001-C																		
b1	82.89	50.17	1.24	17.89	7.83	0.14	4.73	9.74	3.77	0.86	0.37	0.17	0.13	2.48	0.21	414	84	99.56
b2	82.89	50.70	1.18	17.57	7.82	0.13	5.12	9.54	3.69	0.84	0.37	0.16	0.13	2.90	0.34	271	103	100.2
a	83.39	48.87	1.37	19.01	7.84	0.13	4.81	10.22	4.37	0.98	0.41	0.26	0.14	0.83	0.10	595	157	99.30
d	83.56	49.84	1.44	17.90	7.55	0.13	5.93	9.37	3.80	0.75	0.35	0.10	0.06	2.29	0.16	681	85	99.58
e	83.73	50.52	1.24	17.87	6.95	0.11	5.68	9.36	4.08	0.88	0.37	0.19	0.13	2.27	0.21	524	60	99.71
SM1001-D3																		
e	82.89	50.12	1.18	17.21	8.02	0.12	5.79	8.95	3.78	0.86	0.35	0.18	0.13	2.43	0.21	740	64	99.18
b	82.97	50.92	1.46	18.28	7.27	0.11	4.33	10.40	4.13	1.10	0.42	0.18	0.10	0.31	0.09	0	114	99.03
a	83.19	50.44	1.23	16.93	7.42	0.13	6.01	8.93	4.45	0.82	0.35	0.18	0.12	3.26	0.39	740	85	100.4
d	84.09	50.31	1.37	17.27	7.41	0.12	4.99	9.61	4.36	1.01	0.36	0.20	0.10	2.38	0.17	181	32	99.50
c	84.77	51.05	1.28	17.87	6.78	0.10	5.52	9.62	4.10	0.98	0.40	0.20	0.12	2.67	0.20	621	35	100.8
Average 1 s.e.		0.16	0.01	0.10	0.08	0.01	0.05	0.03	0.09	0.01	0.00	0.00	0.00		0.27		75	

APPENDIX B

SUPPLEMENTARY ANALYTICAL METHODS

FTIR

Melt inclusions were analyzed for H_2O and CO_2 using a Thermo-Nicolet Nexus 670 FT-IR spectrometer interfaced with a Continuum IR microscope. H_2O and CO_2 concentrations were calculated from IR peak absorbances using the Beer-Lambert law. Wafer thicknesses were determined with both a digital micrometer and using the interference fringe method of Wyszocanski et al. (2006) and both methods agree to within ±2 μm. H_2O concentrations were determined using the 3550 cm^{-1} peak, 4520 cm^{-1} + 5200 cm^{-1} peaks, or 4520 cm^{-1} + 1630 cm^{-1} peaks. CO_2 concentrations were determined using the CO_3^{2-} doublet at 1515–1430 cm^{-1} determined from a least-squares minimization routine by Sally Newman. Absorption coefficients (with the exception of ε_{3550}) are compositionally dependent and were calculated using average glass compositions determined by EMPA and equations from Dixon & Pan (1995) and Mandeville et al. (2002). Hydrous densities were determined by iteration between calculated glass densities (Luhr, 2001) and Beer-Lambert calculations. Comparison of uncertainties determined by formal error propagation and Monte Carlo simulations are in agreement and suggest relative uncertainties of 9% and 11% for H_2O and CO_2 concentrations, respectively.

EMPA

All electron microprobe analyses (EMPA) were done using a Cameca SX-100 equipped with five wavelength dispersive spectrometers in the CAMCOR facility at the University of Oregon. Hydrous glass compositions were measured using a 10 μm diameter, 10 nA beam with a 15 kV accelerating voltage. Samples TC063A, Yo061E, and PT05 were analyzed with the following counting times: 20 s (Mn), 40 s (K, Al, Ti, Si, Fe, P), 60 s (Ca, Mg), 96 s (S), 100 s (Cl), and 160 s (Na). Samples SM2, EJYo2, Yo065D, and GB072 were run using a slightly different set-up: 20 s (Mn), 40 s (K, Si, Ca), 60 s (Mg, P, Al), 80 s (Ti), 96 s (S), 120 s (Fe), 150 s (Cl), and 160 s (Na). Linear off-peak background corrections were applied to S, Cl, Ti, Mn, K, and P intensities. Off-peak counting times were: 20 s (Mn, K, P), 40 s (Ti,), 50 s (Cl), and 96 s

(S). The MAN background continuum absorption intensity correction was used for Na, Si, Al, Mg, Fe and Ca (Donovan & Tingle, 1996). Effects of element migration were corrected by performing linear regressions to time zero on Na, K, Al, and Si counts (Hanson et al., 1996; Morgan & London, 1996; 2005). Individual inclusion analyses are averages of 3–5 analyzed spots. Both analytical set-ups resulted in similar standard errors (Table 1) and volatile detection limits (e.g., 0.006 wt.% S, 0.008 wt.% Cl).

Host olivine compositions (Si, Mg, Fe, Ca, Ni, Mn) were determined using a 15 kV accelerating voltage and a 50 nA beam with a 2 μm diameter. On-peak counting times were: 20 s (Mn), 40 s (Si), 54 s (Ni, Ca) and 120 s (Mg, Fe). Linear off-peak background corrections were applied to Ni, Mn, and Ca with off peak counting times of 20 s, 54 s, and 54 s, respectively. The MAN background continuum absorption intensity correction was applied to Si, Mg, and Fe (Donovan & Tingle, 1996). Three to five point analyses of olivine (>100 μm away from inclusions and crystal edges) were averaged for each crystal to obtain a representative host olivine composition.

Oxygen Isotopes

Oxygen isotopes in olivine from several tephra samples were measured at the University of Oregon stable isotope lab using CO_2-laser fluorination and an MAT 253 mass spectrometer (Auer et al., 2009). San Carlos olivine ($\delta^{18}O = 5.35‰$) and Gore Mountain garnet ($\delta^{18}O = 5.75‰$) were used as standards to assess instrument variability and analyzed together with unknown olivine samples. Standard $\delta^{18}O$ values were 0.10‰ lighter than reference values and were taken into account in calculating the $\delta^{18}O$ values reported in Table 1. Average analytical precision was better than 0.05‰.

Supplemental References Cited

Auer, S., Bindeman, I., Wallace, P., Ponomareva, V., Portnyagin, M., 2009. The origin of hydrous, high-$\delta^{18}O$ voluminous volcanism: diverse oxygen isotope values and high magmatic water contents within the volcanic record of Klyuchevsky volcano, Kamchatka, Russia. Contrib. Mineral. Petrol. 157, 209–230.

Dixon, J.E., Pan, V., 1995. Determination of the molar absorptivity of dissolved carbonate in basanitic glass. Am. Mineral. 80, 1339–1342.

Donovan, J.J., Tingle, T.N., 1996. An improved mean atomic number correction for quantitative microanalysis. J. Microscop. Microanal. 2(1), 1–7.

Hanson, B., Delano, J.W., Lindstrom, D.J., 1996. High-precision analysis of hydrous rhyolitic glass inclusions in quartz phenocrysts using the electron microprobe and INAA. Am. Mineral. 81, 1249–1262.

Luhr, J.F., 2001. Glass inclusions and melt volatile contents at Paricutin Volcano, Mexico. Contrib. Mineral. Petrol.142, 261–283.

Mandeville, C.W., Webster, J.D., Rutherford, M.J., Taylor, B.E., Timbal, A., Faure, K., 2002. Determination of molar absorptivities for infrared absorption bands of H_2O in andesitic glasses. Am. Mineral. 87, 813–821.

Morgan, G.B., London, D., 1996. Optimizing the electron microprobe analysis of hydrous alkali aluminosilicate glasses. Am. Mineral. 81, 1176–1185.

Morgan, G.B., London, D., 2005. Effect of current density on the electron microprobe analysis of alkali aluminosilicate glasses. Am. Mineral. 90, 1131–1138.

Wysoczanski, R., Tani, K., 2006. Spectroscopic FTIR imaging of water species in silicic volcanic glasses and melt inclusions: An example from the Izu-Bonin arc. J. Volcanol. Geotherm. Res. 156, 302–314.

APPENDIX C

ANALYZED MELT INCLUSION COMPOSITIONS

Sample	%Fo Host	(wt%) SiO_2	TiO_2	Al_2O_3	FeO^T	MnO	MgO	CaO	Na_2O	K_2O	P_2O_5	S	Cl	H_2O	1 s.d.	(ppm) CO_2	1 s.d.	Sum	(°C) T_{Sug}[a]
TWIN CRATERS																			
TC063Abottom																			
Bulk Tephra		54.50	1.23	15.90	9.03	0.15	7.17	7.54	3.09	1.13	0.26								
1-d1	82.69	50.47	1.55	18.07	7.91	0.14	4.80	10.09	3.72	0.70	0.32	0.13	0.03	1.76	0.21	1325	237	99.83	1107
1-f	82.72	51.49	1.48	17.52	8.08	0.12	5.03	9.78	3.75	0.67	0.34	0.16	0.03	1.70	0.17	1017	103	100.24	1113
1-c	82.77	51.82	1.55	17.92	8.07	0.13	4.84	9.78	3.79	0.73	0.30	0.13	0.03	1.63	0.08	1057	79	100.82	1110
1-e	83.10	50.54	1.61	18.24	7.77	0.12	4.83	10.36	3.51	0.65	0.35	0.15	0.03	1.58	0.17	1118	126	99.85	1110
1-g2	83.70	50.63	1.49	18.27	7.92	0.14	5.10	10.16	3.83	0.65	0.32	0.12	0.03	1.87	0.15	1446	87	100.68	1111
1-g3	83.70	51.17	1.55	18.14	8.66	0.18	5.05	9.64	3.32	0.87	0.33	0.08	0.05	1.11	0.08	848	181	100.24	1125
1-i	83.95	52.49	1.35	16.58	8.03	0.16	5.17	9.91	4.01	0.63	0.32	0.15	0.03	1.70	0.08	930	47	100.62	1115
TC063Atop																			
1-e	82.73	49.64	1.43	18.37	8.04	0.14	5.17	10.22	3.59	0.65	0.31	0.13	0.04	1.30	0.10	602	35	99.09	1124
1-f1	83.48	50.28	1.48	18.19	7.46	0.14	5.19	10.34	3.72	0.67	0.33	0.16	0.04	1.47	0.09	813	48	99.54	1120
1-f2	83.48	49.93	1.66	18.61	7.83	0.13	4.82	10.36	2.51	0.66	0.33	0.13	0.04	1.46	0.09	969	58	98.57	1112
SAND MOUNTAIN CHAIN																			
SM2																			
Bulk		51.15	1.36	17.38	8.58	0.15	7.83	9.19	3.12	0.86	0.37							100.00	
1-g	83.74	49.78	1.36	17.25	8.52	0.15	4.84	9.97	4.14	1.08	0.39	0.18	0.10	1.10	0.15	115	42	98.88	1121
1-h	83.89	49.46	1.42	17.98	7.85	0.12	4.98	10.00	3.68	1.03	0.37	0.21	0.09	1.65	0.08	115	108	98.85	1114
1-c1	84.02	48.69	1.27	17.28	7.80	0.13	5.01	9.73	3.56	0.97	0.35	0.21	0.10	2.64	0.23	457	47	97.78	1099
1-c3	84.02	50.48	1.39	17.75	8.36	0.15	4.88	10.23	3.94	1.13	0.39	0.17	0.10	2.13	0.09	n.d.		101.09	1102
1-i	84.50	49.75	1.45	17.52	7.36	0.14	6.24	9.84	3.54	0.96	0.40	0.21	0.08	2.21	0.15	1074	81	99.81	1131
1-f	84.78	49.89	1.55	17.66	6.85	0.09	4.80	10.33	3.69	1.00	0.37	0.22	0.09	2.18	0.34	885	126	98.81	1099
PALAGONITIZED TUFF (ISLAND FISSURE)																			
PT05																			
2-h1	80.74	50.68	1.40	17.82	8.32	0.11	5.49	8.74	3.83	0.80	0.40	0.11	0.05	1.38	0.17	438	86	99.18	1134
1-b1	81.49	49.88	1.33	16.94	7.52	0.11	5.34	8.08	3.95	0.99	0.43	0.11	0.05	1.59	0.10	367	32	96.36	1130
2-b	81.74	51.42	1.42	18.04	7.39	0.16	5.05	9.12	4.01	0.98	0.47	0.15	0.05	1.99	0.14	1124	75	100.36	1112
P1-1	82.17	51.04	1.35	17.58	7.81	0.18	5.34	8.43	3.98	1.06	0.45	0.13	0.05	2.45	0.18	466	32	99.89	1113
P1-2	82.17	51.05	1.37	16.80	8.73	0.15	5.24	8.47	4.09	1.07	0.43	0.14	0.05	2.27	0.14	459	411	99.90	1113
1-h1	82.20	51.20	1.47	18.05	7.45	0.13	5.38	9.15	3.48	0.89	0.41	0.13	0.05	1.85	0.27	703	57	99.71	1121
1-h2	82.20	50.79	1.43	17.56	7.38	0.08	5.20	9.25	3.44	0.87	0.41	0.14	0.05	1.51	0.09	429	259	98.16	1123
1-g2	82.23	51.06	1.36	17.77	8.32	0.15	5.26	8.61	3.69	0.94	0.41	0.13	0.05	2.69	0.17	399	40	100.48	1106

Appendix C. Extended.

Sample	(ppm) Sc	V	Cr	Rb	Sr	Y	Zr	Nb	Ba	La	Ce	Pr	Nd	Sm	Eu	Gd	Dy	Er	Yb	Ta	Pb	Th	U
TWIN CRATERS																							
TC063Abottom																							
Bulk	21.6	171	237	20.3	459	22.9	134	5.2	415	14.3	32.8	4.6	19.6	4.6	1.5	4.6	4.7	2.6	2.3	0.42	4.0	2.4	0.9
1-d1	-	-	-	-	-	-	-	-	-	-	-	-	-	-	-	-	-	-	-	-	-	-	-
1-f	31.7	267	216	8.4	645	24.7	135	6.4	427	16.1	45.8	5.3	19.7	8.2	1.3	3.6	4.8	2.3	1.8	0.24	4.2	1.4	0.5
1-c	-	-	-	-	-	-	-	-	-	-	-	-	-	-	-	-	-	-	-	-	-	-	-
1-e	23.0	237	87	7.1	614	23.6	125	6.8	372	12.8	38.4	5.0	20.9	4.0	1.8	5.2	5.6	2.3	2.7	0.33	3.3	1.2	0.5
1-g2	25.2	256	92	7.9	573	23.8	124	7.4	359	11.9	37.3	5.3	18.9	3.8	1.7	3.8	4.9	2.4	2.6	0.36	3.3	0.9	0.5
1-g3	-	-	-	-	-	-	-	-	-	-	-	-	-	-	-	-	-	-	-	-	-	-	-
1-i	26.7	244	141	8.2	568	23.5	120	7.2	354	12.0	37.1	5.0	19.2	4.9	1.4	4.1	4.7	2.2	2.3	0.29	3.4	1.1	0.4
TC063Atop																							
1-e	27.0	235	134	7.1	624	25.9	135	7.6	370	13.5	38.1	5.4	22.9	5.3	1.9	5.6	4.5	2.9	2.1	0.46	3.3	1.2	0.4
1-f1	38.9	261		8.0	575	27.8	133	8.2	381	14.1	37.6	4.4	22.3	4.0	1.2	3.0	7.9	3.2	2.1	0.58	3.5	1.4	0.5
1-f2	26.4	223	120	6.2	625	26.8	143	8.0	353	14.1	34.5	5.4	21.9	5.2	2.3	8.1	4.7	2.6	2.4	0.61	2.8	1.1	0.4
SAND MOUNTAIN CHAIN																							
SM2																							
Bulk	26.0	185	233	7.9	1010	22.8	146	10.1	381	20.4	46.5	6.3	26.4	5.6	1.8	5.0	4.8	2.5	2.2	0.68	4.3	1.5	0.5
1-g	-	-	-	-	-	-	-	-	-	-	-	-	-	-	-	-	-	-	-	-	-	-	-
1-h	24.7	214	101	10.6	1075	21.7	138	13.4	421	19.8	51.7	6.3	25.0	5.2	1.7	4.2	4.2	2.1	1.9	0.67	5.6	1.5	0.5
1-c1	28.9	194		9.0	1056	25.7	155	12.3	406	20.6	48.7	6.4	25.8	6.0	1.7	4.3	4.8	2.4	2.0	0.69	4.8	1.4	0.5
1-c3	24.9	172	69	9.0	997	23.0	144	12.3	403	19.4	46.1	6.2	25.5	4.9	1.9	4.5	4.3	1.9	2.3	0.60	4.7	1.2	0.4
1-i	-	-	-	-	-	-	-	-	-	-	-	-	-	-	-	-	-	-	-	-	-	-	-
1-f	29.5	204	136	10.8	1065	24.5	162	16.1	408	21.2	49.7	6.4	26.4	5.4	1.7	5.3	5.0	2.5	2.1	1.12	3.8	1.6	0.5
PALAGONITIZED TUFF (ISLAND FISSURE)																							
PT05																							
2-h1	-	-	-	-	-	-	-	-	-	-	-	-	-	-	-	-	-	-	-	-	-	-	-
1-b1	21.1	205	102	16.3	633	23.2	152	14.0	468	15.9	46.3	5.4	24.7	4.8	1.5	4.3	4.5	2.4	1.8	0.86	6.5	1.5	0.8
2-b	20.0	213	84	15.5	767	22.2	142	15.9	500	18.4	49.7	6.0	26.3	4.1	1.7	4.3	3.7	1.9	2.5	0.60	5.3	1.4	0.6
P1-1	-	-	-	-	-	-	-	-	-	-	-	-	-	-	-	-	-	-	-	-	-	-	-
P1-2	26.1	236	95	17.7	678	21.6	140	15.0	506	18.6	48.4	6.4	22.0	5.2	2.2	4.1	4.3	2.4	2.4	0.66	5.8	1.5	0.8
1-h1	22.6	210	96	13.6	689	26.3	160	13.6	436	17.7	42.6	5.2	24.6	4.1	2.1	4.3	4.1	3.0	2.1	0.77	5.2	1.4	0.9
1-h2	31.6	216	276	16.0	688	29.1	149	13.9	432	15.9	46.2	5.8	23.1	4.2	2.0	4.3	5.6	2.0	2.3	0.63	6.2	1.4	0.9
1-g2	-	-	-	-	-	-	-	-	-	-	-	-	-	-	-	-	-	-	-	-	-	-	-

Appendix C. Continued.

Sample	%Fo Host	(wt%) SiO_2	TiO_2	Al_2O_3	FeO^T	MnO	MgO	CaO	Na_2O	K_2O	P_2O_5	S	Cl	H_2O	1 s.d.	(ppm) CO_2	1 s.d.	Sum	(°C) T_{Sug}
PT05																			
P-5A	82.61	51.56	1.38	17.38	7.47	0.17	5.46	8.95	3.82	0.92	0.39	0.13	0.05	1.62	0.12	675	41	99.4	1127
2-d	82.75	51.27	1.43	17.89	7.36	0.12	5.57	9.02	3.85	0.92	0.42	0.14	0.04	1.66	0.13	916	91	99.8	1129
2-c1	82.84	51.18	1.41	18.16	7.22	0.10	5.08	9.10	3.96	0.96	0.45	0.16	0.05	0.63	0.10	569	75	98.5	1137
2-f	82.84	51.19	1.38	17.31	7.83	0.17	5.63	8.77	3.90	0.95	0.43	0.14	0.05	2.18	0.43	828	92	100.	1122
2-a1	83.24	50.63	1.36	17.92	7.36	0.16	5.63	8.83	3.74	0.86	0.43	0.12	0.05	1.22	0.29	827	190	98.4	1139
YAPOAH																			
Yo061E																			
Bulk		53.81	0.82	20.00	6.85	0.12	5.88	8.29	3.37	0.72	0.15								
1E-h	83.88	53.52	0.90	17.83	6.76	0.09	5.45	8.39	4.03	0.64	0.16	0.09	0.09	2.12	0.12	598	44	100.	1118
1E-I	84.05	51.58	0.94	18.59	7.24	0.10	5.10	8.87	4.04	0.63	0.16	0.09	0.09	1.91	0.12	1	220	99.3	1115
Yo065D																			
Bulk		54.91	0.89	19.39	6.69	0.12	4.94	8.34	3.72	0.83	0.18								
5D-b1	82.34	53.57	0.84	18.77	6.29	0.05	4.31	8.13	4.55	0.77	0.16	0.08	0.10	2.34	0.55	-	-	100.	1045
5D-b2	82.34	54.10	0.99	17.34	6.84	0.15	4.37	7.16	4.42	1.06	0.19	0.07	0.12	3.13	0.26	296	54	100.	1083
5D-e	82.60	52.32	1.13	20.04	6.17	0.10	2.83	9.24	4.26	0.69	0.27	0.12	0.11	3.20	0.24	924	73	101	1043
5D-a	83.28	51.83	0.98	17.44	7.50	0.16	6.09	8.37	4.02	0.69	0.23	0.10	0.07	2.82	0.19	837	64	100.	1122
COLLIER																			
EJYo2 (Surface grab sample)																			
Bulk		55.43	0.98	18.65	7.08	0.13	5.07	7.68	3.94	0.84	0.18								
EJ-c1	82.51	50.64	1.18	20.28	6.33	0.16	4.56	8.96	4.22	0.68	0.28	0.10	0.07	2.30	0.20	723	58	99.8	1098
EJ-c2	82.51	47.64	1.06	19.77	6.48	0.13	4.10	8.86	3.63	0.72	0.26	0.09	0.13	1.93	0.28	527	43	94.9	1096
EJ-i	82.91	52.61	1.12	17.30	6.96	0.09	5.23	8.84	3.85	0.66	0.26	0.10	0.07	2.66	0.17	762	47	99.8	1104
EJ-a	83.24	51.95	1.32	17.58	6.93	0.12	4.76	8.51	4.00	0.83	0.31	0.12	0.08	2.38	0.46	608	134	98.9	1100
EJ-g1	84.32	53.76	0.94	18.59	6.10	0.08	4.38	8.34	3.97	0.61	0.14	0.08	0.06	2.44	0.17	845	51	99.6	1090
EJ-g2	84.61	53.10	0.82	18.85	6.19	0.08	4.29	8.48	4.09	0.56	0.11	0.08	0.06	2.39	0.14	640	63	99.2	1089
GARRISON BUTTE CHAIN																			
GB072																			
Bulk		49.71	1.33	16.42	10.30	0.18	9.09	9.33	2.80	0.54	0.29								
1-g	82.05	49.42	1.48	16.63	10.22	0.18	5.38	9.89	3.42	0.64	0.34	0.13	0.07	1.19	0.08	273	41	99.0	1131
1-i	82.26	48.43	1.59	17.90	8.92	0.15	6.32	10.27	3.33	0.47	0.40	0.13	0.04	1.59	0.16	891	99	99.6	1143
1-a	82.67	48.70	1.48	17.43	9.64	0.18	6.45	9.73	3.22	0.56	0.34	0.13	0.05	1.55	0.10	930	55	99.6	1148
1-b	83.59	49.61	1.41	16.65	10.00	0.20	6.22	9.66	3.55	0.63	0.33	0.13	0.08	1.21	0.25	238	47	99.7	1148
1-h	83.99	49.33	1.50	16.10	9.87	0.16	6.84	9.67	3.33	0.58	0.34	0.14	0.05	1.70	0.24	679	109	99.7	1153
1-f	82.42	49.40	1.58	17.71	8.12	0.13	6.40	10.23	3.15	0.52	0.43	0.13	0.09	1.26	0.17	736	150	99.2	1150
1-k1	83.29	48.75	1.47	18.15	8.52	0.17	6.18	10.24	3.12	0.44	0.42	0.12	0.05	1.56	0.08	899	56	99.3	1141
1-k2	83.29	48.81	1.54	18.25	8.51	0.13	6.26	10.23	3.34	0.50	0.44	0.13	0.05	1.60	0.08	0	0	99.8	1142

Appendix C. Continued Extended.

	Sc	V	Cr	Rb	Sr	Y	Zr	Nb	Ba	La	Ce	Pr	Nd	Sm	Eu	Gd	Dy	Er	Yb	Ta	Pb	Th	U
PT05																							
P-5A	27	221	84	13.9	711	23	148	15	461	18	43	5	23	4.7	2	5.3	3.9	2.2	2.4	0.7	5.7	1.4	0.5
2-d	22	229	84	15.4	703	22	131	14	465	17	46	5	22	4.1	2	3.7	2.9	2.1	1.3	0.6	4.8	1.0	0.8
2-c1	23	241	95	16.9	830	22	138	14	569	17	50	6	28	4.8	2	4.6	3.0	2.4	1.5	1.0	14	1.5	0.8
2-f	23	217	98	14.6	731	21	126	14	489	18	48	5	25	4.1	2	3.7	3.3	2.7	1.5	0.8	4.9	1.3	0.8
2-a1	-	-	-	-	-	-	-	-	-	-	-	-	-	-	-	-	-	-	-	-	-	-	-
YAPOAH																							
Yo061E																							
Bulk	18	149	92	10.9	606	14	89	3	242	9	20	3	12	2.8	1	2.8	2.8	1.5	1.4	0.3	3.1	1.3	0.5
1E-h	23	210	80	8.5	674	16	82	6	256	9	23	3	11	2.3	1	2.8	2.6	1.2	1.3	0.2	3.7	0.6	0.3
1E-I	21	216	76	8.9	705	15	84	6	280	9	23	3	11	2.1	1	2.2	3.0	1.2	1.0	0.4	3.7	1.0	0.5
Yo065D																							
Bulk	19	157	76	13.0	626	15	97	5	273	11	23	3	13	3.2	1	3.2	3.2	1.7	1.5	0.4	3.3	1.5	0.6
b1	-	-	-	-	-	-	-	-	-	-	-	-	-	-	-	-	-	-	-	-	-	-	-
b2	27	198	108	16.6	549	19	117	7	333	11	28	4	14	3.3	1	2.4	3.6	2.0	1.6	0.5	4.6	1.4	0.6
e	27	212	200	7.4	610	16	99	6	251	10	25	3	14	2.5	1	3.4	3.4	1.9	1.4	0.3	3.5	0.9	0.3
a	24	183	98	9.2	542	17	96	9	250	10	25	3	14	3.1	1	2.9	3.2	1.8	1.9	0.4	3.1	0.9	0.4
COLLIER																							
EJYo2 (Surface grab sample)																							
Bulk	19	165	79	13.6	615	16	93	4	301	10	22	3	12	3.0	1	3.0	3.1	1.6	1.5	0.4	4.5	1.5	0.6
c1	26	182	79	7.7	551	19	106	9	222	10	22	3	14	3.1	1	3.4	3.5	1.8	1.6	0.6	2.9	1.0	0.4
c2	-	-	-	-	-	-	-	-	-	-	-	-	-	-	-	-	-	-	-	-	-	-	-
i	24	193	71	8.4	541	15	84	9	233	9	23	3	13	2.6	1	2.8	3.1	1.4	1.5	0.4	2.8	0.8	0.4
a	29	204	61	9.9	499	21	116	11	267	12	27	4	16	3.5	1	3.8	3.6	1.9	1.6	0.7	3.1	1.0	0.4
g1	22	174	109	10.4	461	10	59	4	208	6	17	2	9	2.1	1	2.5	1.8	0.8	0.9	0.2	3.3	0.8	0.4
g2	-	-	-	-	-	-	-	-	-	-	-	-	-	-	-	-	-	-	-	-	-	-	-
GARRISON BUTTE CHAIN																							
GB072																							
Bulk	30	193	287	7.9	507	23	123	6	207	12	29	4	18	4.4	2	4.5	4.7	2.7	2.4	0.5	11	1.1	0.4
1-g	37	252	206	10.5	519	26	138	10	256	13	39	5	21	5.2	2	4.5	4.7	2.8	2.6	0.5	4.8	1.1	0.4
1-i	30	227	107	3.9	592	27	176	11	225	14	36	5	20	5.1	2	4.9	4.6	3.1	2.2	0.6	2.9	0.7	0.3
1-a	31	207	119	6.6	516	25	136	9	222	12	32	4	17	3.7	2	4.4	4.7	2.4	2.4	0.5	3.3	0.9	0.3
1-b	35	201	107	8.7	488	28	139	9	227	13	32	5	20	4.1	1	4.2	4.7	2.7	2.4	0.4	3.8	1.1	0.3
1-h	31	231	133	8.7	519	23	126	10	238	12	33	5	18	4.1	2	3.5	4.1	2.3	2.1	0.5	4.3	0.8	0.4
1-f	-	-	-	-	-	-	-	-	-	-	-	-	-	-	-	-	-	-	-	-	-	-	-
1-k1	-	-	-	-	-	-	-	-	-	-	-	-	-	-	-	-	-	-	-	-	-	-	-
1-k2	36	200	206	3.4	604	30	177	12	229	15	37	5	23	4.5	2	6.6	5.9	3.2	2.8	0.6	2.6	0.7	0.3

Appendix C. Continued.

Sample	%Fo Host	(wt%) SiO_2	TiO_2	Al_2O_3	FeO^T	MnO	MgO	CaO	Na_2O	K_2O	P_2O_5	S	Cl	H_2O	1 s.d.	(ppm) CO_2	1 s.d.	Sum	(°C) T_{Sug}
GB072																			
1-c	83.78	48.51	1.53	17.88	8.86	0.17	6.24	10.04	3.25	0.50	0.39	0.13	0.05	1.59	0.14	447	33	99.18	1142
1-L	83.84	48.65	1.61	17.54	8.44	0.14	6.36	10.24	3.31	0.50	0.42	0.13	0.06	1.73	0.13	992	58	99.23	1141
1-d	83.95	47.63	1.44	18.61	8.26	0.14	6.09	10.32	3.34	0.51	0.48	0.13	0.06	1.52	0.13	1004	91	98.63	1141
BLUE LAKE MAAR																			
Bulk B1		54.10	0.93	19.59	6.69	0.12	5.00	9.00	3.77	0.64	0.16							100.00	
Bulk B5		54.07	0.93	19.61	6.69	0.12	4.98	9.08	3.71	0.65	0.16							100.00	
BulkB21		54.11	0.94	19.50	6.74	0.12	5.00	8.99	3.77	0.66	0.17							100.00	
BL1																			
1-4	79.68	53.46	1.08	17.01	8.24	0.14	4.48	8.26	4.24	0.68	0.21	0.18	0.07	2.99	0.15	858	103	101.13	1064
1-5	81.93	52.62	0.95	17.88	7.49	0.11	4.49	8.74	4.30	0.57	0.15	0.15	0.07	2.99	0.07	809	97	100.58	1067
1-6_1	82.06	54.03	1.19	18.45	6.16	0.11	3.03	8.44	4.51	0.72	0.20	0.18	0.07	3.86	0.28	789	95	101.03	1040
1-6_2	83.06	54.18	1.18	17.93	6.47	0.13	3.13	8.51	4.32	0.70	0.19	0.18	0.07	3.33	0.07	802	96	100.40	1054
1-3_1	83.21	53.25	1.00	18.35	6.47	0.12	3.72	8.67	4.29	0.64	0.15	0.16	0.06	3.70	0.04	861	103	100.68	1053
1-3_2	84.21	52.49	1.01	18.79	6.41	0.11	3.16	8.89	4.60	0.61	0.15	0.15	0.07	3.81	0.12			100.26	1055
1-2	83.90	52.94	0.94	19.52	7.35	0.12	5.15	8.84	4.41	0.52	0.21	n.d.	n.d.	2.81	0.05	685	82		1080
BL3																			
3-3	81.87	53.05	1.10	16.88	7.28	0.14	4.88	7.98	4.21	0.73	0.20	0.17	0.07	2.86	0.20	732	88	99.62	1077
3-4	82.59	53.44	1.00	16.99	6.87	0.14	5.13	7.92	4.52	0.74	0.17	0.17	0.07	2.97	0.06	817	98	100.20	1079
3-1_1	82.71	53.27	0.94	17.70	7.13	0.09	5.05	8.31	4.21	0.64	0.16	0.15	0.06	3.36	0.06	750	90	101.15	1069
3-1_2	83.71	53.31	1.00	17.49	7.21	0.12	5.00	8.23	4.51	0.64	0.17	0.16	0.07	3.33	0.01	729	87	101.33	1069
3-2	82.84	52.60	0.97	17.73	6.99	0.11	4.66	8.68	4.31	0.57	0.17	0.15	0.06	3.25	0.01	842	101	100.34	1064
3-5	84.03	51.93	1.03	17.93	7.01	0.10	5.44	8.82	4.20	0.60	0.19	0.15	0.06	3.08	0.03	799	96	100.61	1083
% Errors		0.4	3.8	0.6	0.7	14.6	1.1	1.0	1.5	1.9	2.8	1.8	6.9		9.0		11.1		

Appendix C. Continued Extended.

	Sc	V	Cr	Rb	Sr	Y	Zr	Nb	Ba	La	Ce	Pr	Nd	Sm	Eu	Gd	Dy	Er	Yb	Ta	Pb	Th	U
GB072																							
1-c	29	216	73	4.4	550	24	140	10.3	223	12	33.8	4.3	19.2	4.5	1.4	4.6	4.4	2.6	2.1	0.6	3	0.7	0.3
1-L	-	-	-	-	-	-	-	-	-	-	-	-	-	-	-	-	-	-	-	-	-	-	-
1-d	-	-	-	-	-	-	-	-	-	-	-	-	-	-	-	-	-	-	-	-	-	-	-
BLUE LAKE MAAR																							
BulkB1	22	169	95	8.3	614	15	80	4.2	230	9	16.8		10.3									0.7	
BulkB5	23	168	96	9.1	617	15	79	3.7	229	6	21.7		11.5									0.4	
BulkB21	22	170	94	9.2	618	16	83	4.2	240	9	22.1		13.3									1.7	
BL1																							
1-4	27	275	54	10.8	627	17	88	6.6	297	9	24.2	3.2	14.1	2.9	0.9	2.4	2.5	1.6	1.7	0.5	4	0.8	0.5
1-5	29	221	71	7.4	640	16	71	4.8	221	8	17.9	2.7	12.4	2.3	1.0	2.3	2.2	1.7	1.5	0.2	3	0.7	0.3
1-6_1	-	-	-	-	-	-	-	-	-	-	-	-	-	-	-	-	-	-	-	-	-	-	-
1-6_2	-	-	-	-	-	-	-	-	-	-	-	-	-	-	-	-	-	-	-	-	-	-	-
1-3_1	20	206	73	8.4	617	12	64	4.7	226	7	19.9	2.6	11.5	2.3	1.1	2.5	1.9	0.9	0.9	0.2	3	0.7	0.3
1-3_2	-	-	-	-	-	-	-	-	-	-	-	-	-	-	-	-	-	-	-	-	-	-	-
1-2	-	-	-	-	-	-	-	-	-	-	-	-	-	-	-	-	-	-	-	-	-	-	-
3																							
3-3	28	217	67	11.8	621	19	104	7.6	301	11	26.3	3.5	13.3	2.8	1.2	4.6	2.8	1.4	1.3	0.5	4	1.0	0.6
3-4	-	-	-	-	-	-	-	-	-	-	-	-	-	-	-	-	-	-	-	-	-	-	-
3-1_1	21	222	85	11.0	624	14	73	5.8	272	8	22.7	2.7	11.4	2.5	1.0	2.4	1.8	1.3	1.3	0.3	4	0.9	0.6
3-1_2	-	-	-	-	-	-	-	-	-	-	-	-	-	-	-	-	-	-	-	-	-	-	-
3-2	25	223	78	8.7	621	13	63	4.6	243	7	18.2	2.3	9.0	2.0	0.9	1.8	1.7	1.0	1.5	0.2	3	0.5	0.3
3-5	-	-	-	-	-	-	-	-	-	-	-	-	-	-	-	-	-	-	-	-	-	-	-
% Errors	4.8	2.7	17.5	3.8	2.5	4.1	3.1	4.1	3.4	4.2	3.8	5.2	6.7	14.3	12.1	15.1	11.9	15.6	15.5	19.1	9	13	14

[a] Temperature calculated after Sugawara (2000).

APPENDIX D

SUPPLEMENTARY FIGURES FOR CHAPTER III

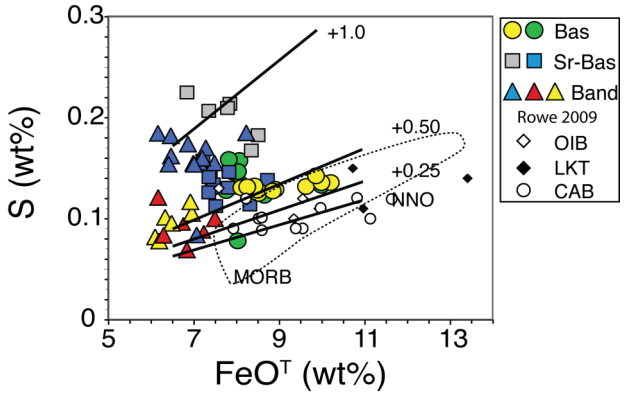

Figure S1. S vs. FeO^T, with the addition of MORB field (data from PetDB) and sulfide-saturation curves at NNO after Wallace and Carmichael (1992) modified using the temperature dependence from Mavrogenes & O'Neill (1999). Estimates of the total dissolved sulfur for NNO +0.25, +0.50, and +1.0 were calculated by combining S_{Total} calculated at NNO while assuming S^{6+}/S^{Total} ~0.21 (at NNO) and using equation (7) from Jugo (2009) (All calculations at T = 1100 °C).

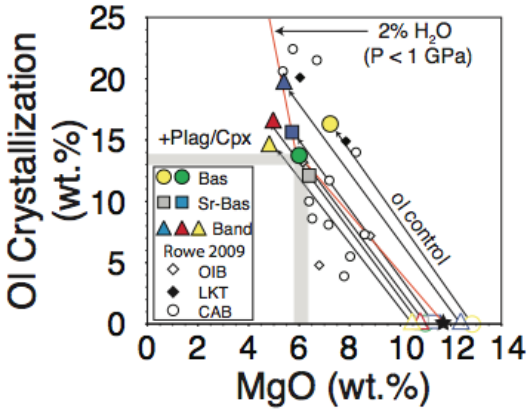

Figure S2. Restored melt inclusion MgO contents plotted against amount of olivine addition required to equilibrate with mantle olivine (see text). Thin red line represents isobaric pMELTS calculations using a primitive whole rock composition (black star) with2 wt.% H_2O at crustal pressures (200–800 MPa) (Ghiorso et al., 2002). Black arrows connecting melt inclusion symbols to corresponding open symbols at 0% crystallization show olivine crystallization trajectories for comparison. Gray bars show the range in MgO and crystallization extents at which plagioclase (P <200 MPa) or clinopyroxene (P >200 MPa) begins to crystallize in addition to olivine for magmas containing 1–2 wt.% H_2O. Black arrows connecting melt inclusion symbols to corresponding open symbols at 0% crystallization show olivine crystallization trajectories.

APPENDIX E

RESTORED MELT INCLUSION COMPOSITIONS

Sample	%Ol Add	(wt%) SiO_2	TiO_2	Al_2O_3	FeO^T	MnO	MgO	CaO	Na_2O	K_2O	P_2O_5	S	Cl	H_2O	1 s.d.	(ppm) CO_2	1 s.d.	(°C) T_{Sug}[a]	(MPa P^b
TWIN CRATERS																			
TC063Abottom																			
1-d1	2.8	51.07	1.54	17.90	8.76	0.14	5.69	9.99	3.68	0.69	0.32	0.13	0.03	1.71	0.21	1289	231	1126	201
1-f	2.7	51.85	1.46	17.29	8.88	0.12	5.83	9.65	3.70	0.66	0.34	0.15	0.03	1.65	0.17	991	100	1131	165
1-c	3.4	51.73	1.51	17.45	8.90	0.13	5.85	9.52	3.69	0.71	0.29	0.12	0.03	1.58	0.08	1023	77	1133	167
1-e	3.5	50.93	1.58	17.89	8.77	0.12	5.90	10.16	3.44	0.64	0.34	0.14	0.03	1.53	0.17	1080	122	1133	173
1-g2	3.5	50.76	1.45	17.83	8.86	0.14	6.14	9.92	3.74	0.63	0.31	0.12	0.03	1.81	0.15	1398	84	1135	215
1-g3	2.6	51.35	1.53	17.85	8.77	0.18	6.18	9.48	3.27	0.86	0.33	0.08	0.05	1.08	0.08	826	176	1149	133
1-i	3.4	52.56	1.32	16.19	8.77	0.16	6.27	9.68	3.92	0.62	0.31	0.14	0.03	1.65	0.08	900	45	1139	154
TC063Atop																			
1-e	2.0	50.43	1.43	18.37	8.86	0.14	5.77	10.22	3.59	0.65	0.31	0.13	0.04	1.27	0.10	590	34	1136	106
1-f1	3.4	50.70	1.45	17.87	8.81	0.14	6.03	10.16	3.65	0.66	0.32	0.15	0.03	1.42	0.09	786	47	1138	135
1-f2	4.1	50.89	1.64	18.39	8.77	0.13	6.27	10.24	2.48	0.65	0.33	0.13	0.03	1.40	0.09	931	56	1143	152
SAND MOUNTAIN CHAIN																			
SM2																			
1-g	2.4	50.72	1.36	17.26	8.76	0.15	5.94	9.98	4.14	1.08	0.39	0.18	0.10	1.07	0.15	112	41	1143	34
1-h	3.3	50.47	1.41	17.89	8.77	0.12	6.11	9.95	3.66	1.03	0.37	0.21	0.09	1.60	0.08	111	105	1138	44
1-c1	3.2	50.80	1.29	17.59	8.83	0.13	6.25	9.91	3.63	0.99	0.36	0.20	0.10	2.56	0.23	443	45	1124	119
1-c3	3.4	50.63	1.36	17.34	8.82	0.15	6.16	10.00	3.85	1.10	0.38	0.16	0.10	2.06	0.09			1102	36
1-i	1.7	50.64	1.46	17.60	8.74	0.14	6.40	9.89	3.56	0.97	0.40	0.20	0.08	2.18	0.15	1056	80	1129	189
1-f	6.0	50.78	1.51	17.18	8.74	0.09	6.51	10.05	3.59	0.97	0.36	0.21	0.08	2.06	0.34	835	119	1137	159
PALAGONITIZED TUFF (ISLAND FISSURE)																			
PT05																			
2-h1	-0.5	51.76	1.44	18.27	8.95	0.11	5.12	8.96	3.93	0.82	0.41	0.11	0.05	1.39	0.17	440	86	1124	99
1-b1	0.7	52.30	1.39	17.67	8.96	0.12	5.32	8.43	4.12	1.03	0.45	0.11	0.05	1.58	0.10	365	32	1126	90
2-b	2.8	51.68	1.40	17.75	8.98	0.16	5.46	8.98	3.95	0.96	0.46	0.14	0.05	1.93	0.14	1093	73	1121	201
P1-1	1.6	51.98	1.36	17.69	8.97	0.18	5.59	8.48	4.01	1.07	0.45	0.13	0.05	2.41	0.18	459	31	1118	124
P1-2	0.7	52.19	1.39	17.08	9.06	0.15	5.61	8.61	4.16	1.09	0.44	0.14	0.05	2.26	0.14	455	41	1120	120
1-h1	2.7	51.71	1.45	17.86	9.06	0.13	5.78	9.05	3.44	0.88	0.41	0.13	0.05	1.80	0.27	684	56	1130	144
1-h2	2.7	51.95	1.43	17.60	8.97	0.08	5.73	9.27	3.45	0.87	0.41	0.14	0.05	1.47	0.09	418	24	1133	96
1-g2	1.4	51.95	1.37	17.89	8.98	0.15	5.68	8.67	3.72	0.95	0.41	0.13	0.05	2.66	0.17	393	40	1115	120
P-5A	2.7	52.13	1.37	17.22	9.06	0.17	5.89	8.87	3.78	0.91	0.39	0.13	0.05	1.58	0.12	657	39	1136	135
2-d	2.5	51.67	1.41	17.69	8.98	0.12	5.85	8.92	3.81	0.91	0.42	0.14	0.04	1.62	0.13	893	88	1135	169

Appendix E. Continued.

Sample	%Ol Add	(wt%) SiO_2	TiO_2	Al_2O_3	FeO^T	MnO	MgO	CaO	Na_2O	K_2O	P_2O_5	S	Cl	H_2O	1 s.d.	(ppm) CO_2	1 s.d.	(°C) T_{Sug}	(MPa) P
PT05																			
2-c1	4.3	51.45	1.37	17.68	9.13	0.10	5.96	8.86	3.85	0.93	0.44	0.15	0.05	0.61	0.10	546	71	1156	102
2-f	1.6	51.95	1.38	17.35	8.97	0.17	5.87	8.79	3.91	0.95	0.43	0.14	0.05	2.14	0.43	815	90	1127	169
2-a1	2.8	51.49	1.35	17.84	9.03	0.16	6.11	8.79	3.72	0.86	0.43	0.12	0.04	1.18	0.29	804	185	1149	149
YAPOAH																			0
Yo061E																			0
1E-h	0.0	54.51	0.92	18.16	7.43	0.09	5.24	8.55	4.10	0.65	0.16	0.09	0.09	2.12	0.12	598	44	1113	124
1E-I	0.0	52.93	0.96	19.07	7.44	0.10	5.25	9.10	4.15	0.65	0.16	0.09	0.09	1.91	0.12	1	220	1161	34
Yo065D																			0
b1	2.6	54.23	0.84	18.65	7.72	0.05	4.79	8.08	4.52	0.77	0.16	0.08	0.10	2.28	0.55			1092	42
b2	1.6	55.49	1.00	17.58	7.76	0.15	4.81	7.26	4.48	1.08	0.19	0.07	0.12	3.08	0.26	292	54	1092	112
e	6.5	52.75	1.09	19.29	7.73	0.10	4.94	8.89	4.10	0.66	0.26	0.11	0.11	3.01	0.24	868	68	1093	188
a	-2.5	53.45	1.03	18.32	7.69	0.17	5.16	8.79	4.22	0.73	0.24	0.10	0.08	2.90	0.19	858	66	1098	180
COLLIER																			0
EJYo2 (Surface grab sample)																			0
c1	0.4	51.77	1.20	20.67	7.15	0.16	4.46	9.13	4.30	0.69	0.29	0.10	0.07	2.29	0.20	720	58	1095	136
c2	0.6	51.23	1.14	21.17	7.19	0.14	4.54	9.49	3.89	0.77	0.28	0.09	0.13	1.92	0.28	524	43	1101	101
i	-1.4	54.35	1.17	18.05	7.19	0.09	4.76	9.23	4.02	0.69	0.27	0.11	0.07	2.70	0.17	773	48	1091	155
a	-0.3	53.89	1.37	18.28	7.18	0.13	4.78	8.85	4.16	0.86	0.32	0.12	0.08	2.38	0.46	610	134	1098	125
g1	3.1	54.73	0.94	18.52	7.25	0.08	5.30	8.31	3.95	0.61	0.14	0.08	0.06	2.37	0.17	820	49	1110	147
g2	3.1	54.30	0.82	18.85	7.20	0.08	5.34	8.48	4.09	0.56	0.11	0.07	0.06	2.31	0.14	621	61	1112	124
GARRISON BUTTE CHAIN																			0
GB072																			0
1-g	2.9	50.21	1.47	16.52	10.51	0.18	6.66	9.82	3.40	0.64	0.34	0.13	0.07	1.16	0.08	266	40	1157	67
1-i	2.8	48.86	1.57	17.67	10.52	0.15	6.70	10.14	3.29	0.46	0.40	0.12	0.04	1.55	0.16	867	96	1151	161
1-a	4.1	49.59	1.54	17.22	10.47	0.13	6.85	9.95	3.06	0.51	0.42	0.12	0.09	1.21	0.10	707	42	1160	134
1-b	1.8	49.40	1.48	17.43	10.49	0.18	6.91	9.73	3.22	0.56	0.34	0.13	0.05	1.52	0.25	913	182	1157	166
1-h	3.0	50.01	1.39	16.40	10.47	0.20	7.31	9.52	3.50	0.62	0.33	0.13	0.08	1.17	0.24	231	37	1175	61
1-f	2.1	50.07	1.50	16.08	10.47	0.16	7.56	9.66	3.33	0.58	0.34	0.14	0.05	1.67	0.17	665	136	1167	137
1-k1	5.1	49.07	1.42	17.56	10.50	0.16	7.27	9.91	3.02	0.43	0.41	0.12	0.04	1.48	0.08	855	53	1165	158
1-k2	4.7	48.88	1.49	17.61	10.48	0.13	7.16	9.87	3.22	0.48	0.43	0.12	0.05	1.53	0.08			1162	24
1-c	4.7	48.99	1.49	17.40	10.47	0.17	7.43	9.77	3.16	0.49	0.38	0.12	0.05	1.52	0.14	427	31	1168	99
1-L	5.3	49.05	1.56	16.97	10.53	0.14	7.49	9.91	3.20	0.48	0.41	0.12	0.06	1.64	0.13	943	55	1166	172
1-d	6.0	48.17	1.39	17.94	10.51	0.14	7.47	9.95	3.22	0.49	0.46	0.12	0.06	1.44	0.13	947	86	1170	169
BLUE LAKE MAAR																			0
BL1																			0
1-4	-0.1	54.56	1.10	17.37	8.41	0.14	4.54	8.44	4.33	0.69	0.21	0.18	0.07	2.99	0.15	859	103	1084	192
1-5	2.4	53.50	0.95	17.87	8.42	0.11	5.20	8.73	4.30	0.57	0.15	0.15	0.07	2.92	0.07	791	95	1099	182

Appendix E. Continued.

Sample	%Ol Add	(wt%) SiO_2	TiO_2	Al_2O_3	FeO^T	MnO	MgO	CaO	Na_2O	K_2O	P_2O_5	S	Cl	H_2O	1 s.d.	(ppm) CO_2	1 s.d.	(°C) T_{Sug}	(MPa) P
BL1																			
1-6_1	7.8	54.17	1.13	17.53	8.43	0.11	5.24	8.02	4.29	0.68	0.19	0.17	0.07	3.59	0.28	732	88	1091	193
1-6_2	7.2	54.51	1.13	17.16	8.44	0.12	5.30	8.15	4.14	0.67	0.18	0.17	0.07	3.10	0.07	748	90	1099	181
1-3_1	6.7	53.72	0.96	17.65	8.43	0.12	5.69	8.34	4.13	0.62	0.14	0.15	0.06	3.47	0.04	807	97	1102	199
1-3_2	7.9	53.09	0.97	17.97	8.43	0.11	5.61	8.50	4.40	0.58	0.14	0.14	0.06	3.54	0.12			1099	82
1-2	2.3	51.82	0.93	19.08	8.43	0.11	5.83	8.57	4.34	0.52	0.16	0.08	0.10	2.75	0.05	670	80	1117	161
BL3																			0
3-3	1.6	54.46	1.12	17.14	8.43	0.14	5.19	8.10	4.27	0.74	0.20	0.17	0.07	2.82	0.20	721	86	1102	173
3-4	2.1	54.42	1.00	17.05	8.41	0.14	5.37	7.95	4.54	0.74	0.17	0.17	0.07	2.91	0.06	801	96	1105	187
3-1_1	2.3	53.95	0.94	17.62	8.43	0.09	5.50	8.27	4.19	0.64	0.16	0.15	0.06	3.29	0.06	732	88	1100	187
3-1_2	2.2	53.93	1.00	17.41	8.42	0.12	5.43	8.19	4.49	0.64	0.17	0.16	0.07	3.26	0.01	713	86	1100	184
3-2	3.6	53.48	0.96	17.57	8.49	0.11	5.57	8.60	4.27	0.57	0.17	0.15	0.06	3.13	0.01	813	98	1104	194
3-5	2.6	52.69	1.03	17.84	8.42	0.10	5.96	8.78	4.18	0.60	0.19	0.15	0.06	3.00	0.03	778	93	1114	186

[a] Temperature calculated after Sugawara (2000).

[b] Pressure calculated after Papale et al. (2006).

APPENDIX F

OTHER PRIMITIVE COMPOSITIONS

Source	1	2	2	2	2	2	2	2	2	2	2	2	2	2	2
Type	Shasta PBA	LKT	LKT	EIB	EIB	EIB	EIB	CAB	CAB	CAB	CAB	CAB	CAB	CAB	CAB
Sample	S173	FLR 031	NEF 031	WF 021	HL 031	BLW 031	NMB 031	TB 021	CC 021	BR 022	AIC0 21	SIC 021	LTB 022	DB 042	BC 021
(wt%)	n= 10														
SiO_2	53.83	46.90	47.48	48.28	46.29	47.24	46.88	49.83	49.69	48.84	49.47	49.12	49.39	49.57	47.56
TiO_2	0.57	1.53	1.69	1.84	1.82	1.54	1.84	1.40	1.02	1.23	1.33	1.26	1.21	1.26	1.17
Al_2O_3	12.70	15.27	14.31	17.86	15.85	16.09	15.57	17.66	17.00	15.97	16.98	17.18	16.95	16.03	15.31
FeO^T	7.00	11.09	11.08	7.73	9.85	10.00	9.68	8.02	8.71	9.64	8.47	8.77	8.79	9.62	11.21
MnO	0.07	0.14	0.15	0.11	0.12	0.15	0.13	0.10	0.12	0.14	0.11	0.13	0.12	0.13	0.13
MgO	13.03	13.03	12.90	8.74	11.00	11.50	11.04	9.35	10.17	11.32	9.85	10.27	10.21	11.49	13.13
CaO	10.36	9.13	8.74	11.09	10.74	9.71	10.75	9.85	9.43	9.30	9.89	9.81	9.26	8.48	7.94
Na_2O	1.63	2.21	2.89	3.35	3.34	2.97	2.91	2.95	3.07	2.86	3.14	2.86	3.25	2.65	2.81
K_2O	0.31	0.39	0.45	0.50	0.64	0.48	0.40	0.57	0.59	0.46	0.48	0.38	0.54	0.49	0.48
P_2O_5	0.27	0.31	0.32	0.49	0.36	0.34	0.79	0.29	0.20	0.22	0.29	0.22	0.29	0.26	0.26
S_{max} (ppm)	0.197	0.10	0.12	0.12	0.11	0.10	0.09	0.09	0.09	0.08	0.11	0.08	0.09	0.08	0.09
Cl_{max}	0.257	0.03	0.02	0.13	0.08	0.03	0.03	0.05	0.06	0.03	0.03	0.03	0.03	0.03	0.03
H_2O_{max} (wt%)	3.40	1.14	1.04	0.97	0.68	1.18	0.75	1.79	2.24	1.83	1.81	1.84	1.95	1.91	1.70
$T_{formation}$ (°C)	1250	1306	1304	1217	1263	1276	1263	1232	1249	1272	1241	1250	1251	1277	1312
Mg# Equilib	94	90.00	90.00	90.00	90.00	90.00	90.00	90.00	90.00	90.00	90.00	90.00	90.00	90.00	90.00
% OlAdd	20.8	15.0	20.2	4.9	13.3	7.3	13.6	4.0	5.6	7.4	8.7	8.2	10.1	11.8	14.1
LeeTemp (*C)	1260	1348	1346	1240	1318	1309	1310	1232	1244	1282	1246	1255	1252	1278	1333
Lee Press (GPa)	0.87	1.7	1.7	1.2	1.7	1.6	1.5	1.0	1.2	1.3	1.1	1.2	1.2	1.2	1.7

Appendix F. Continued.

Type	Shasta PBA	LKT	LKT	EIB	EIB	EIB	EIB	CAB	CAB	CAB	CAB	CAB	CAB	CAB	CAB
Sample	S173	FLR 031	NEF 031	WF 021	HL 031	BLW 031	NMB 031	TB 021	CC 021	BR 022	AIC 021	SIC 021	LTB 022	DB 042	BC 021
ppm	n= 10														
Sc	28.9	24.1	19.9	36.1	24.1	32.3	-	21.9	30.8	24.2	31.9	25.8	27.2	25.8	25.6
V	219	232	-	-	345	219	-	-	-	222	-	-	-	-	202
Cr	688	-	-	-	-	-	-	-	-	-	-	-	-	368	-
Rb	4.6	8.4	12.2	4.0	8.3	7.9	-	11.8	9.9	7.5	6.6	5.7	6.8	7.0	8.4
Sr	1036	343	405	996	598	302	-	416	455	358	366	321	425	391	413
Y	7.6	23.0	17.6	32.2	27.3	27.6	-	17.4	18.8	17.4	20.6	17.8	18.3	22.5	23.9
Zr	66	104	83	214	162	146	-	86	89	77	94	66	87	113	123
Nb	1.4	7.8	5.9	12.9	16.4	18.6	-	6.4	6.9	7.3	8.0	4.6	8.0	7.0	8.4
Ba	77	249	286	230	237	142	-	248	195	175	177	124	236	190	185
La	9.6	7.7	8.8	18.7	15.5	11.5	-	8.4	7.9	7.0	7.5	4.8	8.5	9.2	9.6
Ce	26.9	22.1	23.5	52.1	49.0	28.9	-	22.0	20.1	19.6	21.3	14.7	23.3	24.9	24.9
Pr	3.2	3.0	2.9	6.6	5.6	3.6	-	3.0	2.6	2.5	2.9	2.0	2.8	3.3	3.2
Nd	12.4	13.3	12.6	26.6	24.3	15.5	-	12.5	11.1	11.1	12.5	9.1	12.5	14.3	14.9
Sm	2.1	3.1	2.8	5.3	5.6	4.3	-	2.9	3.2	2.7	3.3	2.2	3.1	3.4	3.8
Eu	0.8	1.3	1.0	1.8	1.7	1.3	-	1.0	1.1	1.1	1.0	1.0	1.2	1.3	1.4
Gd	1.7	3.6	3.0	5.8	3.8	4.7	-	3.0	3.3	3.2	3.1	2.9	3.5	3.9	4.5
Dy	1.3	3.7	3.2	5.4	5.5	5.0	-	2.8	3.0	2.9	3.5	2.8	3.4	4.1	3.9
Er	0.8	2.1	1.6	3.1	2.1	2.9	-	1.7	1.9	1.9	1.9	1.8	1.8	2.1	2.5
Yb	0.8	2.5	1.4	2.8	1.9	2.6	-	1.5	1.8	1.8	1.8	1.8	1.7	2.1	2.5
Ta	0.1	0.5	0.3	0.8	1.1	1.0	-	0.4	0.4	0.4	0.5	0.3	0.5	0.4	0.5
Pb	2.9	2.4	3.4	3.2	2.7	1.7	-	3.4	2.5	2.3	2.2	1.6	2.6	2.8	2.6
Th	1.0	1.0	1.0	1.0	1.9	1.6	-	1.0	1.2	0.7	0.6	0.5	0.6	0.6	0.0
U	0.3	0.3	0.5	0.5		0.7	-	0.5	0.5	0.3	0.3	0.2	0.3	0.3	0.0

Appendix F. Extended

Source	2	2	2
Type	CAB	CAB	CAB
Sample	ELK021	KWB031	BB031
(wt%)			
SiO_2	47.31	50.37	48.65
TiO_2	1.28	1.18	1.35
Al_2O_3	14.12	14.21	13.95
FeO^T	11.84	10.50	11.23
MnO	0.15	0.12	0.13
MgO	13.84	12.45	13.26
CaO	7.74	6.86	7.56
Na_2O	2.80	3.22	2.88
K_2O	0.60	0.75	0.61
P_2O_5	0.31	0.34	0.35
S_{max} (ppm)	0.10	0.09	0.10
Cl_{max}	0.03	0.04	0.03
H_2O_{max} (wt%)	1.52	2.15	1.65
$T_{formation}$ (°C)	1326	1300	1314
Mg# Equilib	90.00	90.00	90.00
% OlAdd	21.6	20.7	22.5
LeeTemp (*C)	1358	1291	1331
LeePress (GPa)	1.9	1.3	1.6

[1] Ruscitto et al. (2008); [2] Rowe et al. (2009)

Note: 1 s.d. for H_2O (9%) and CO_2 (11%), 1 s.e. for S (1.8%) and Cl (6.9%), and 1 s.e. for Temp (~30 °C).

Appendix F. Extended Continued.

Type	CAB	CAB	CAB
Sample	ELK021	KWB031	BB031
ppm			
Sc	50.6	19.8	23.7
V	152	-	-
Cr	-	-	-
Rb	14.9	12.2	14.7
Sr	269	403	383
Y	23.9	17.5	23.9
Zr	111	83	105
Nb	6.4	5.9	6.9
Ba	312	285	255
La	8.2	8.8	9.2
Ce	20.4	23.4	25.4
Pr	2.6	2.9	3.3
Nd	11.1	12.6	15.1
Sm	3.5	2.8	3.8
Eu	1.3	1.0	1.3
Gd	6.9	3.0	3.9
Dy	3.9	3.1	3.8
Er	2.5	1.6	2.3
Yb	2.3	1.4	2.3
Ta	0.0	0.3	0.3
Pb	1.4	3.4	3.4
Th	0.9	1.0	1.1
U	0.3	0.5	0.6

APPENDIX G

MANTLE SOURCE COMPOSITIONS

		Enriched Mantle Compositions				Bulk Partition Coefficients		
		Average Mantle	WF021 Mantle	HF031 Mantle	BLW031 Mantle	Spl Lherz	Depleted Lherz	Harzburgite
Ba	ppm	10.20	11.55	11.94	7.12	0.00030	0.00025	0.00024
U	ppm	0.03	0.02	0.00	0.03	0.00103	0.00047	0.00037
Th	ppm	0.08	0.05	0.10	0.08	0.00212	0.00073	0.00035
K_2O	wt%	0.03	0.03	0.03	0.02	0.00097	0.00031	0.00009
Cl	ppm	0.00	0.01	0.00	0.00	0.00300	0.00300	0.00300
Nb	ppm	1.13	0.91	1.16	1.31	0.02155	0.01214	0.01228
La	ppm	0.86	1.05	0.87	0.65	0.00666	0.00174	0.00012
Rb	ppm	0.34	0.20	0.42	0.40	0.00038	0.00016	0.00010
H_2O	wt%	0.06	0.06	0.06	0.06	0.01200	0.00291	0.00022
Ce	ppm	2.62	3.16	2.96	1.75	0.01106	0.00291	0.00022
Sr	ppm	44.53	70.20	42.11	21.28	0.02155	0.00777	0.00399
Nd	ppm	1.50	1.80	1.64	1.05	0.01861	0.00504	0.00057
Zr	ppm	15.18	18.66	14.11	12.78	0.03933	0.02007	0.01690
Pb	ppm	0.15	0.19	0.16	0.10	0.00800	0.00800	0.00800
Sm	ppm	0.41	0.43	0.45	0.34	0.03136	0.00881	0.00136
Eu	ppm	0.14	0.15	0.14	0.11	0.03693	0.00987	0.00092
TiO_2	wt%	0.31	0.32	0.32	0.27	0.13277	0.10782	0.10013
Gd	ppm	0.44	0.54	0.36	0.44	0.04583	0.01359	0.00290
Dy	ppm	0.52	0.54	0.54	0.50	0.05133	0.01553	0.00366
Y	ppm	3.04	3.37	2.85	2.88	0.05745	0.02204	0.01038
Er	ppm	0.30	0.35	0.23	0.32	0.06400	0.02471	0.01158
Yb	ppm	0.24	0.27	0.19	0.26	0.05087	0.03415	0.02842

OIB and CAB magmas have trace element ratios permissive of source garnet (e.g., Leeman et al., 1990; 2005), however, the presence of garnet changes calculated extents of melting by <2% and results in substantially poorer fits for model HREE contents. Therefore, we assumed that all mantle melting occurred in the spinel stability field and used the modal mineralogy of Hughes & Taylor (1986) (Ol/Opx/Cpx/Spl: 53/30/12/5) to model OIB, LKT, and CAB (both basalt and Sr-rich basalt) petrogenesis. The depleted trace elements and higher SiO_2 contents in the basaltic andesite parents and high-Mg magmas from Mt. Shasta require more refractory sources (60/34/3/3 and 63/34/0/3, respectively).

APPENDIX H

PRELIMINARY SLAB COMPONENTS

		Twin Craters	Island Fissure	Yapoah	Collier	Garrison	Sand Mtn	Blue Lake
MODELING RESULTS								
residuals		0.75	0.52	0.97	0.99	0.45	0.55	1.05
PME		0.00	0.00	0.02	0.02	0.00	0.00	0.02
F		0.11	0.10	0.12	0.13	0.10	0.09	0.16
s.d. F		0.02	0.02	0.03	0.03	0.02	0.02	0.04
X SC wt%		0.17	0.27	0.40	0.37	0.13	0.24	0.56
X H_2O wt%		0.19	0.26	0.33	0.30	0.17	0.23	0.48
SUBDUCTION COMPONENT								
Ba	ppm	13225	13062	6684	6936	6251	10117	5960
U	ppm	9.57	11.43	9.88	11.16	2.11	1.27	9.92
Th	ppm	32.87	13.78	22.67	24.76	7.93	14.48	16.01
K_2O	wt%	22.78	22.06	19.24	20.31	15.19	22.96	15.01
Cl	ppm	28512	17217	30948	24531	63691	32970	25348
Nb	ppm	0	0	0	0	0	0	0
La	ppm	136.92	358.01	219.28	236.95	75.80	444.03	163.53
Rb	ppm	286.72	344.81	257.43	270.13	241.00	150.51	221.49
H_2O	wt%	74.05	72.90	76.68	75.86	80.60	69.98	81.29
Ce	ppm	372.00	993.73	480.14	497.14	24.81	1021.44	390.58
Sr	ppm	0.00	19883.15	12695.92	13131.48	0.00	32611.93	12947.92
Nd	ppm	220.40	516.30	225.02	252.33	35.15	554.98	190.89
Zr	ppm	0	0	0	0	0	0	0
Pb	ppm	83.76	184.89	87.28	88.42	93.52	108.62	79.17
Sm	ppm	89.30	53.96	26.56	32.93	38.92	95.91	21.32
Eu	ppm	25.46	39.76	13.21	16	21.29	27.59	11.52
TiO_2	wt%	0	0	0	0	0	0	0
Gd	ppm	29.77	29.88	10.00	18	0.00	40.47	11.06
Dy	ppm	0	0	0	0	0	0	0
Y	ppm	0	0	0	0	0	0	0
Er	ppm	0	0	0	0	0	0	0
Yb	ppm	0	0	0	0	0	0	0

APPENDIX I

RESTORED MELT INCLUSIONS OF ANDERSON 1974

HMA	%Fo Host	(wt%) SiO_2	TiO_2	Al_2O_3	FeO^T	MgO	CaO	Na_2O	K_2O	H_2O	S	Cl
S17-3	87.6	59.04	0.62	15.76	6.27	6.00	7.98	3.40	0.92	1.46	0.05	0.13
S17-3	87.9	58.61	0.62	15.91	6.19	6.13	8.44	3.20	0.90	1.36	0.02	0.12
S17-3	88.2	59.17	0.56	15.84	6.00	6.54	7.97	3.15	0.79	3.52	0.06	0.12
S17-3	88.4	59.27	0.63	16.02	5.75	5.90	8.11	3.42	0.90	1.17	0.03	0.12
S17-4	86.9	59.79	0.67	15.31	6.36	5.79	7.51	3.66	0.91	1.83	-	0.10
S17-4	87.4	58.10	0.66	15.86	6.58	6.46	8.07	3.38	0.89	1.97	-	0.10
S17-4	89.3	60.37	0.87	15.23	5.39	6.02	7.04	3.95	1.13	0.00	-	0.09
S17-4	89.3	60.92	1.11	13.88	6.16	7.25	6.11	3.33	1.24	0.00	-	0.09
S17-4	89.4	60.93	0.75	14.19	5.77	6.87	7.05	3.19	1.25	2.73	-	0.08
S17-L	89	59.49	0.64	15.56	6.04	6.95	7.69	2.63	1.01	0.75	0.04	0.10
S17-4	89.8	60.76	1.12	14.89	5.77	6.03	6.14	3.90	1.38	0.57	0.00	0.12
S17-4	90.4	60.47	0.93	14.76	5.77	6.73	6.87	3.34	1.13	-	-	0.15
S17-4	91.5	57.82	0.82	16.27	5.77	7.76	7.73	3.09	0.75	-	-	0.13
S17-4	91.9	58.18	0.73	15.57	5.77	8.05	7.33	3.39	0.97	-	-	0.06
S17-4	92	58.45	0.64	15.46	5.77	8.15	7.09	3.45	0.99	0.35	-	0.06
S17-4	92.3	58.63	0.64	15.03	5.77	8.50	6.96	3.48	0.99	1.23	-	0.08
S17-L	93.7	56.96	0.66	14.78	5.76	10.88	7.60	2.65	0.70	0.25	-	0.09
PBA												
S17-1	91.7	53.96	0.50	14.44	7.00	9.80	11.18	2.51	0.37	2.57	-	0.20
S17-3	91.8	55.88	0.55	12.37	7.00	10.33	11.42	1.98	0.24	5.63	0.29	0.21
S17-4	92.4	53.80	0.51	13.54	7.00	10.81	11.57	2.23	0.31	3.75	-	0.17
S17-4	92.4	55.33	0.44	12.74	7.01	11.17	10.88	1.95	0.26	4.52	-	0.16
S17-4	92.4	55.12	0.35	12.53	7.00	11.16	11.56	1.76	0.27	2.85	-	0.13
S17-1	92.6	52.54	0.78	14.03	7.00	10.83	11.87	2.43	0.29	0.09	-	0.19
S17-1	92.6	52.89	0.59	13.86	7.00	10.84	11.69	2.59	0.31	2.98	-	0.16
S17-1	92.7	53.29	0.50	15.16	7.00	11.08	9.58	2.83	0.34	1.79	-	0.20
S17-1	92.8	54.15	0.48	12.97	7.00	11.53	11.20	2.18	0.26	2.23	-	0.19
S17-3	92.8	55.83	0.53	11.78	7.00	11.86	10.52	1.94	0.31	4.74	0.19	0.17
S17-4	92.9	53.47	0.65	13.39	7.01	11.61	11.26	2.12	0.27	1.17	-	0.14
S17-4	92.9	52.98	0.74	13.63	7.00	11.44	11.40	2.32	0.26	0.43	-	0.17
S17-1	93.2	52.08	0.49	13.74	7.01	11.75	12.01	2.46	0.23	1.68	-	0.23
S17-1	93.2	53.14	0.55	13.35	7.00	12.02	11.07	2.20	0.45	3.95	-	0.26
S17-1	93.3	53.61	0.47	13.56	7.00	12.35	10.19	2.27	0.33	2.50	-	0.19
S17L	93.3	52.78	0.58	13.15	7.01	12.12	11.58	2.23	0.32	0.00	0.18	0.20
S17-1	93.7	52.65	0.55	12.79	7.00	12.96	11.45	2.06	0.31	1.80	-	0.22
S17L	94	52.97	0.55	12.64	7.01	13.82	10.16	2.09	0.40	1.76	0.18	0.16
S17-1	94.5	52.78	0.46	11.98	7.01	15.11	10.21	1.99	0.25	1.74	-	0.17

APPENDIX J

THERMOMECHANICAL MIXING MODEL

Model Description

A mixing model developed by Sparks & Marshall (1986) (S&M '86) was used to ascertain the validity of mixing between the primitive basaltic andesite (PBA) and the dacite. The model assumes that thermal equilibration between a mafic and silicic magma is achieved prior to chemical equilibration. The mixing equilibration temperature was calculated following equation 3 of S&M '86:

$$\theta = \frac{X_S L_S(1-x) + T_S C_S(x-1) - x\left(X_M L_M + C_M T_M\right)}{xC_S - xC_M - C_S}$$

Where M and S denote the mafic and silicic end members, respectively. $C_{M,S}$ (0.3 cal/g/ºC; S&M '86) are the heat capacities of both solid and liquid phases (which are assumed to be equal), $T_{M,S}$ are the initial magmatic temperatures, $L_{M,S}$ (100 and 70 cal/g, respectively; S&M '86) are the heats of fusion or crystallization of the solid phases, X_M is the mass fraction of new crystals formed in the mafic magma, X_S is the mass fraction dissolved in the silicic magma, θ is the equilibrium temperature and x is the fraction of mafic magma in the mixture.

The mafic end member used was the average PBA melt inclusion composition initially containing 4 wt.% H_2O and T_M = 1210 ºC. The silicic end member was a dacite (sample 82-92a; Grove et al., 2005) with 6–8 wt.% H_2O, 18 wt.% crystals, and T_S = 940 ºC (conditions of residual liquid 85-41c#9 with total crystal contents similar to other dacites; Grove et al., 2003; 2005). An isobaric (200 MPa) pMELTS calculation (Ghiorso et al., 2002) of the mafic end-member was used to derive approximate relationships between crystal content, liquid composition and temperature. Crystallinity and viscosity of the pMELTS model were approximated as 4th-order polynomial functions of temperature (coefficients in Table S1). The relationship between crystal content and temperature for the dacite was assumed linear and to be 1.8 wt.% crystallization for a 1 ºC temperature decrease with the dacite liquidus at 1040 ºC (slope based on linear fit through pMELTS model).

All liquid viscosities were calculated at the mixture equilibration temperature using the equations of Hui & Zhang (2007). Bulk viscosities were calculated using the Roscoe-Einstein equation (c = 1.67; exp = -2.5 as in S&M, '86).

Table S1. Coefficients for pMELTS model.

(T in ºC)	T^4	T^3	T^2	T	Constant
Xtals (M)	1.456e-11	-1.074e-7	2.529e-4	-0.2451	85.334
Liq Visc (M) (Pa s)	-1.971e-10	7.735-7	-1.107e-3	0.6675	-135.10
Xtals (S)	-	-	-	-0.0018	1.872

Supplementary References Cited

Ghiorso, M.S., M.M. Hirschmann, P.W. Reiners, and V.C. Kress III (2002) The pMELTS: An revision of MELTS aimed at improving calculation of phase relations and major element partitioning involved in partial melting of the mantle at pressures up to 3 GPa. Geochem Geophys Geosys 3(5), doi: 10.1029/2001GC000217

Grove, T.L., L. Elkins-Tanton, S. Parman, N. Chatterjee, O. Muntener, and G. Gaetani (2003) Fractional crystallization and mantle-melting controls on calc-alkaline differentiation trends. Contrib Mineral Petrol, 145(5): 515-533.

Grove, T.L., M.B. Baker, R.C. Price, S.W. Parman, L.T. Elkins-Tanton, N. Chatterjee, and O. Muntener (2005) Magnesian andesite and dacite lavas from Mt. Shasta, northern California: products of fractional crystallization of H2O-rich mantle melts. Contrib Mineral Petrol, 148: 542-565.

Hui, H. & Y. Zhang (2007) Toward a general viscosity equation for natural anhydrous and hydrous silicate melts. Geochim Cosmochim Acta 71: 403-416.

Sparks, R.S.J. & L.A. Marshall (1986) Thermal and mechanical constraints on mixing between mafic and silicic magmas. J Volcanol Geotherm Res, 29: 99-124.

REFERENCES CITED

Chapter I

Anderson, A.T., 1974. Evidence for a picritic, volatile-rich magma beneath Mt. Shasta, California. J. Petrol. 15, 243–267.

Bacon, C.R., Bruggman, P.E., Christiansen, R.L., Clynne, M.A., Donnelly-Nolan, J.M., Hildreth, W., 1997. Primitive Magmas at Five Cascade Volcanic Fields: Melts from Hot, Heterogeneous Subarc Mantle. Can. Mineral. 35, 397–423.

Conrey, R.M., Sherrod, D.R., Hooper, P.R., Swanson, D.A., 1997. Diverse Primitive Magmas in the Cascade Arc, Northern Oregon and Southern Washington. Can. Mineral. 35, 367–396.

Erlund, E.J., Cashman, K.V., Wallace, P.J., Pioli, L., Rosi, M., Johnson, E., Delgado Granados, H., 2009 Compositional evolution of magma from Parícutin Volcano, Mexico: the tephra record. J. Volcanol. Geotherm. Res. 197, 167–187.

Grove, T.L., Baker, M.B., Price, R.C., Parman, S.W., Elkins-Tanton, L.T., Chatterjee, N., Muntener, O., 2005. Magnesian andesite and dacite lavas from Mt. Shasta, northern California: products of fractional crystallization of H_2O-rich mantle melts. Contrib. Mineral. Petrol. 148, 542–565.

Hildreth, W., 2007. Quaternary magmatism in the Cascades — Geologic perspectives. U.S. Geological Survey Professional Paper 1744.

Holloway, J.R., Blank, J.G., 1994. Application of experimental results to C-O-H species in natural melts. In: Carrol, M.R., Holloway, J.R. (Eds.) Volatiles in Magmas, Reviews in Mineralogy and Geochemistry, Vol.30, pp. 187–230.

Hughes, S.S., 1990. Mafic Magmatism and Associated Tectonism of the Central High Cascade Range, Oregon. J. Geophys. Res. 95(B12): 19623–19638.

Johnson, E.R., Wallace, P.J., Cashman, K.V., Delgado Granados, H., Kent, A.J.R., 2008. Magmatic volatile contents and degassing-induced crystallization at Volcán Jorullo, Mexico: implications for melt evolution and the plumbing systems of monogenetic volcanoes. Earth Planet. Sci. Lett. 269, 477–486.

Kirby, S.H., Engdahl, E.R. & Villaseñor, A., 2002. Warm-slab subduction as a global process. In: Kirby, S.H., Wang, K., Dunlop, S.G. (eds.) The Cascadia Subduction Zone and Related Subduction systems, U.S. Geological Survey Open-File Report 02-328: 223–276

Leeman, W.P., Smith, D.R., Hildreth, W., Palacz, Z., Rogers, N., 1990. Compositional Diversity of Late Cenozoic Basalts in a Transect Across the Southern Washington Cascades: Implications for Subduction Zone Magmatism. J. Geophys. Res. 95(B12), 19561–19582.

Luhr, J.F., 2001. Glass inclusions and melt volatile contents at Parícutin Volcano, Mexico. Contrib. Mineralog. Petrol. 142, 261–283.

McBirney, A.R., 1978. Volcanic Evolution of the Cascade Range. Ann. Rev. Earth Planet. Sci. 6: 437–456.

Ort, M.H., Elson, M.D., Anderson, K.C., Duffield, W.A., Hooten, J.A., Champion, D.E., Waring, G., 2008. Effects of scoria-cone eruptions upon nearby human communities. Geol. Soc. Am. Bull., 120, 476–486.

Pioli, L., Erlund, E., Johnson, E., Cashman, K., Wallace, P., Rose, M., Delgado Granados, H., 2008. Explosive dynamics of violent Strombolian eruptions: The eruption of Parícutin Volcano 1943–1952 (Mexico). Earth Planet. Sci. Lett. 271, 359–368.

Plank, T., Cooper, L.B., Manning, C.E., 2009. Emerging geothermometers for estimating slab surface temperatures. Nature Geoscience. doi: 10.1038/NGEO614.

Schiano, P., 2003. Primitive mantle magmas recorded as silicate melt inclusions in igneous minerals. Earth Sci. Rev. 63(1–2), 121–144.

Schmidt, M.W., Poli, S., 1998. Experimentally based water budgets for dehydrating slabs and consequences for arc magma generation. Earth Planet. Sci. Lett. 163, 361–379.

Streck, M., Leeman, W.P., Chesley, J., 2007. High-magnesian andesite from Mount Shasta: a product of magma mixing and contamination, not a primitive mantle melt. Geology 35(4), 351–354.

Syracuse, E.M., van Keken, P.E., Abers, G.A., 2010. The global range of subduction zone thermal models. Phys. Earth Planet. Interior 183(1–2), 73-90.

Tatsumi, Y., 2005. The subduction factory: How it operates in the evolving Earth. GSA Today 15(7), doi:10:1130/1052-5173(2005)015<4:TSFHIO>2.0.CO;2.

Taylor, E.M., 1990. Volcanic History and Tectonic Development of the Central High Cascade Range, Oregon. J. Geophys. Res. 95(B12), 19611–19622.

Chapter II

Alletti, M., Baker, D.R., Scaillet, B., Aiuppa, A., Moretti, R., Ottolini, L., 2009. Chlorine partitioning between a basaltic melt and H_2O–CO_2 fluids at Mount Etna. Chem. Geol. 263, 37–50.

Anderson, A.T., 1974. Evidence for a picritic, volatile-rich magma beneath Mt. Shasta, California. J. Petrol. 15, 243–267.

Anderson, A.T., Brown, G.G., 1993. CO_2 contents and formation pressures of some Kilauean melt inclusions. Am. Mineralog. 78, 794–803.

Asimow, P.D., Ghiorso, M.S., 1998. Algorithmic modifications extending MELTS to calculate subsolidus phase relations. Am. Mineral. 83, 1127–1131.

Atlas, Z.D., Dixon, J.E., Sen, G., Finny, M., Martin-Del Pozzo, A.L., 2006. Melt inclusions from Volcan Popcatepetl and Volcan de Colima, Mexico: Melt evolution due to vapor-saturated crystallization during ascent. J. Volcanol. Geotherm. Res. 153, 221–240.

Benjamin, E.R., Plank, T., Wade, J.A., Kelley, K.A., Hauri, E.H., Alvarado, G.E., 2007. High water contents in basaltic magmas from Irazú Volcano, Costa Rica. J. Volcanol. Geoth. Res. 168, 68–92.

Blundy, J., Cashman, K., 2005. Rapid decompression-driven crystallization recorded by melt inclusions from Mount St. Helens volcano. Geology 33, 793–796.

Blundy, J., Cashman, K., 2008. Petrologic Reconstruction of Magmatic System Variables and Processes. In: Putirka, K.D., Tepley, F.J., III (Eds.) Reviews in mineralogy & geochemistry, Vol. 69, minerals, inclusions and volcanic processes. Mineralogical Society of America, Chantilly. pp. 179-240.

Blundy, J., Cashman, K.V., Rust, A., Witham, F., 2010. A case for CO_2-rich arc magmas. Earth Planet. Sci. Lett. 290, 289-301.

Cashman, K.V., Sturtevant, B., Papale, P., Navon, O., 2000. Magmatic Fragmentation. In: Sigurdsson, H. (Ed.), Encyclopedia of Volcanoes. Academic Press, New York. pp.421–430.

Cervantes, P., Wallace, P.J., 2003. Role of H_2O in subduction-zone magmatism: new insights from melt inclusions in high-Mg basalts from central Mexico. Geology 31, 235-238.

Connor, C.B., Conway, F.M., 2000. Basaltic Volcanic Fields. In: Sigurdsson, H. (Ed.), Encyclopedia of Volcanoes. Academic Press, New York. pp. 331-343.

Conrey, R.M., Sherrod, D.R., Donnelly-Nolan, J.M., Taylor, E.M. et al., 2000. The North-Central Oregon Cascade Margin: Exploring Petrologic and Tectonic Intimacy in a Propagating Intr-Arc Rift. MARGINS: Subduction Factory workshop. Eugene, OR.

Danyushevsky, L.V., Della-Pasqa, F.N., Sokolov, S., 2000. Re-equilibration of melt inclusions trapped by magnesian olivine phenocrysts from subduction-related magmas: petrological implications. Contrib. Mineral. Petrol. 138, 68–83.

Deardorff, N., Cashman, K.V., 2009. Morphologic measurements on an intermediate composition blocky lava flow field in Central Oregon using high resolution (~1m) LiDAR DEMs. Geolog. Soc. Am. Abstracts with Programs, 41(7), 432. Paper No. 165-7.

Dixon, J.E., Pan, V., 1995. Determination of the molar absorptivity of dissolved carbonate in basanitic glass. Am. Mineral. 80, 1339–1342.

Erlund, E.J., Cashman, K.V., Wallace, P.J., Pioli, L., Rosi, M., Johnson, E., Delgado Granados, H., 2009 Compositional evolution of magma from Parícutin Volcano, Mexico: the tephra record. J. Volcanol. Geotherm. Res. 197, 167–187.

Faure, F., Schiano, P., 2005. Experimental investigation of equilibration conditions during forsterite growth and melt inclusion formation. Earth Planet. Sci. Lett. 236(3–4), 882–898.

Ford, C.E., Russel, D.G., Craven, J.A., Fisk, M.R., 1983. Olivine-liquid equilibria: temperature, pressure and composition dependence of the crystal/liquid cation partition coefficients for Mg, Fe^{2+}, Ca, and Mn. J. Petrol. 24, 256–265.

Freda, C., Baker, D.R., Scarlato, P., 2005. Sulfur diffusion in basaltic melts. Geochim. Cosmochim. Acta. 69(21), 5061-5069.

Gaetani, G.A., Watson, E.B., 2000. Open system behavior of olivine-hosted melt inclusions. Earth Planet. Sci. Lett. 183, 27–41.

Ghiorso, M.S., Sack, R.O., 1995. Chemical mass transfer in magmatic processes. IV. A revised and internally consistent thermodynamic model for the interpolation and extrapolation of liquid–solid equilibria in magmatic systems at elevated temperatures and pressures. Contrib. Mineral. Petrol. 119, 197–212.

Ghiorso, M.S., Hirschmann, M.M., Reiners, P.W., Kress III, V.C., 2002. The pMELTS: a revision of MELTS aimed at improving calculation of phase relations and major element partitioning involved in partial melting of the mantle at pressures up to 3 GPa. Geochem. Geophys. Geosyst. 3(5). doi:10.1029/2001GC000217.

Gonnermann, H.M., Manga, M., 2005. Nonequilibrium magma degassing: Results from modeling of the ca. 1340 A.D. eruption of Mono Craters, California. Earth Planet. Sci. Lett. 238, 1–16.

Hildreth, W., 2007. Quaternary magmatism in the Cascades—geologic perspectives. U.S. Geological Survey Professional Paper 1744.

Holloway, J.R., Blank, J.G., 1994. Application of experimental results to C-O-H species in natural melts. In: Carrol, M.R., Holloway, J.R. (Eds.) Volatiles in Magmas, Reviews in Mineralogy and Geochemistry, Vol.30, Mineralogical Society of America, Chantilly, pp. 187–230.

Houghton, B.F., Gonnermann, H.M., 2008. Basaltic explosive volcanism: Constraints from deposits and models. Chemie der Erde, 68, 117–140.

Hughes, S.S., Taylor, E.M., 1986. Geochemistry, petrogenesis, and tectonic implications of central High Cascade mafic platform lavas. Geol. Soc. Am. Bull. 97, 1024–1036.

Jaggar, T.A., 1940. Magmatic Gases. Am. J. Sci., 238, 313–353.

Johnson, E.R., Wallace, P.J., Cashman, K.V., Delgado Granados, H., Kent, A.J.R., 2008. Magmatic volatile contents and degassing-induced crystallization at Volcán Jorullo, Mexico: implications for melt evolution and the plumbing systems of monogenetic volcanoes. Earth Planet. Sci. Lett. 269, 477–486.

Johnson, E.R., Wallace, P.J., Delgado Granados, H., Manea, V.C., Kent, A.J.R., Bindeman, I. N., Donegan, C.S., 2009. Subduction-related volatile recycling and magma generation beneath Central Mexico: insights from melt inclusions, oxygen isotopes and geodynamic models. J. Petrol. 50 (9), 1729–1764.

Johnson, E.R., Wallace, P.J., Cashman, K.V., Delgado Granados, H., 2010. Degassing of volatiles (H_2O, CO_2, S, Cl) during ascent, crystallization, and eruption at mafic monogenetic volcanoes in central Mexico. J. Volcanol. Geotherm. Res. 197, 225–238.

Jugo, P.J., 2009. Sulfur content at sulfide saturation in oxidized magmas. Geology 37, 415–418.

Kent, A.J.R., 2008. Melt inclusions in basaltic and related volcanic rocks. In: Putirka, K.D., Tepley, F.J., III (Eds.) Reviews in mineralogy & geochemistry, Vol. 69, minerals, inclusions and volcanic processes. Mineralogical Society of America, Chantilly. pp. 273–331.

Leeman, W.P., Smith, D.R., Hildreth, W., Palacz, Z., Rogers, N., 1990. Compositional Diversity of Late Cenozoic Basalts in a Transect Across the Southern Washington Cascades: Implications for Subduction Zone Magmatism J. Geophys. Res. 95(B12), 19561–19582.

Luhr, J.F., 2001. Glass inclusions and melt volatile contents at Parícutin Volcano, Mexico. Contrib. Mineralog. Petrol. 142, 261–283.

Mandeville, C.W., Webster, J.D., Rutherford, M.J., Taylor, B.E., Timbal, A., Faure, K., 2002. Determination of molar absorptivities for infrared absorption bands of H_2O in andesitic glasses. Am. Mineral. 87, 813–821.

Massare, D., Metrich, N., Clocchiatti, R., 2002. High-temperature experiments on silicate melt inclusions in olivine at 1 atm: inference on temperatures of homogenization and H_2O concentrations. Chem. Geol. 183, 87–98.

Mavrogenes, J.A., O'Neill, H., 1999. The relative effects of pressure, temperature and oxygen fugacity on the solubility of sulfide in mafic magmas. Geochim. Cosmochim. Acta. 63, 1173–1180.

McBirney, A.R., Taylor, H.P., Armstrong, R.L., 1987. Parícutin re-examined: a classic example of crustal assimilation in a calc-alkaline magma. Contributions to Mineralogy and Petrology 95, 4–20.

McKay, D. and K.V. Cashman, 2010. Interactions between mafic eruptions and glacial ice or snow: implications of the 2010 Eyjafjallajökull, Iceland, eruption for hazard assessments in the central Oregon Cascades. Abstract NH11B-1133 presented at 2010 Fall Meeting, AGU, San Francisco, CA.

Mercer, C.N., Johnston, A.D., 2008. Experimental studies of the P–T–H_2O near-liquidus phase relations of basaltic andesite from North Sister Volcano, High Oregon Cascades: constraints on lower-crustal mineral assemblages. Contrib. Mineralog. Petrol. 155, 571–592.

Moore, G., Carmichael, I.S.E., 1998. The hydrous phase equilibria (to 3 kbar) of an andesite and basaltic andesite from western Mexico: constraints on water content and conditions of phenocryst growth. Contrib. Mineral. Petrol. 130, 304–319.

Moore, G., 2008. Interpreting H_2O and CO_2 Contents in Melt Inclusions: Constraints from Solubility Experiments and Modeling. In: Putirka, K.D., Tepley, F.J., III (Eds.) Reviews in mineralogy & geochemistry, Vol. 69, minerals, inclusions and volcanic processes. Mineralogical Society of America, Chantilly. pp. 333–361.

Newman, S., Lowenstern, J.B., 2002. VolatileCalc: a silicate melt–H_2O–CO_2 solution model written in Visual Basic for excel. Computers Geosci. 28, 597–604.

Ort, M.H., Elson, M.D., Anderson, K.C., Duffield, W.A., Hooten, J.A., Champion, D.E., Waring, G., 2008. Effects of scoria-cone eruptions upon nearby human communities. Geol. Soc. Am. Bull., 120, 476–486.

Papale, P., Moretti, R., Barbato, D., 2006. The compositional dependence of the saturation surface of H_2O+CO_2 fluids in silicate melts. Chem. Geol. 229, 78–95.

Newman,S., Lowenstern, J.B., 2002. VolatileCalc: a silicate melt H_2O-CO_2 solution model written in Visual Basic for excel. Computers Geosci. 28, 597–604.

Parfitt, E.A., Wilson, L., 1995. Explosive volcanic eruptions: IX. The transition between Hawaiian-style lava fountaining and Strombolian explosive activity. Geophys. J. Int., 121, 226–232.

Pioli, L., Erlund, E., Johnson, E., Cashman, K., Wallace, P., Rosi, M., Delgado Granados, H., 2008. Explosive dynamics of violent Strombolian eruptions: The eruption of Parícutin Volcano 1943–1952 (Mexico). Earth Planet. Sci. Lett. 271, 359-368.

Portnyagin, M., Almeev, R., Matveev, S., Holtz, F., 2008. Experimental evidence for rapid water exchange between melt inclusions in olivine and host magma. Earth Planet. Sci. Lett. 272, 541–552.

Priest, G.R., 1990. Volcanic and Tectonic Evolution of the Cascade Volcanic Arc, Central Oregon. J. Geophys. Res. 95(B12), 19583–19599.

Putrirka, K.D., Perfit, M., Ryerson, F.J., Jackson, M.G., 2007. Ambient and excess mantle temperatures, olivine thermometry, and active vs. passive upwelling. Chem. Geol. 241:177–206.

Roggensack, K., Hervig, R.L., McKnight, S.B., Williams, S.N., 1997. Explosive basaltic volcanism from Cerro Negro volcano: influence of volatiles on eruptive style. Science 277, 1639–1642.

Rowe, M.C., Kent, A.J.R., Nielsen, R.L., 2009. Subduction influence on oxygen fugacity and trace and volatile elements in basalts across the Cascades volcanic arc. J. Petrol. 50 (1), 61–91.

Ruscitto, D.M., Wallace, P.J., Johnson, E.R., Kent, A.J.R., Bindeman, I.N., 2010a. Volatile contents of mafic magmas from cinder cones in the Central Oregon High Cascades: implications for magma formation and mantle conditions in a hot arc. Earth Planet. Sci. Lett. 298, 153–161. doi:10.1016/j.epsl.2010.07.037.

Ruscitto, D.M., Wallace, P.J., Kent, A.J.R., 2010b, in press. Revisiting the compositions and volatile contents of olivine-hosted melt inclusions from the Mount Shasta region: implications for the formation of high-Mg andesites. Contrib. Mineral. Petrol. doi: 10.1007/s00410-010-0587-y.

Rust, A.C., Cashman, K.V., Wallace, P.J., 2004. Magma degassing buffered by vapor flow through brecciated conduit margins. Geology 32(4), 349–352.

Scaillet, B., Pichavant, M., 2005. A model of sulfur solubility for hydrous mafic melts: application to the determination of magmatic fluid compositions of Italian volcanoes. Earth Prints Repository. http://hdl.handle.net/2112/9302005.

Schick, J.D., 1994. Origin of the Compositional Variability of the Lavas at Collier Cone, High Cascades, Oregon. M.S. Thesis, University of Oregon. Eugene, OR.

Schmidt, M.E., Grunder, A.L., 2009. The evolution of North Sister: A volcano shaped by extension and ice in the central Oregon Cascade Arc. Geol. Soc. Am. Bull. 121, 643–662.

Sherrod, D.R., Smith, J.G., 1990. Quaternary extrusion rates of the Cascade Range, Northwestern United States and Southern British Columbia. J. Geophys. Res. 95 (B12), 19465–19474.

Sherrod, D.R., Taylor, E.M., Ferns, M.L., Scott, W.E., Conrey, R.M., Smith, G.A., 2004. Geologic map of the Bend 30- × 60-Minute Quadrangle, Central Oregon. U.S. Geological Survey, Geologic Investigations Series I-2683.

Sisson, T.W., Layne, G.D., 1993. H_2O in basalt and basaltic andesite glass inclusions from four subduction-related volcanoes. Earth Planet. Sci. Lett. 177, 619–635.

Spilliaert, N., Allard, P., Métrich, N., Sobolev, A.V., 2006. Melt inclusion record of the conditions of ascent, degassing, and extrusion of volatile-rich alkali basalt during the powerful 2002 flank eruption of Mount Etna (Italy). J. Geophys. Res. 111. doi:10.1029/2005JB003934.

Taylor, E.M., 1990. Volcanic History and Tectonic Development of the Central High Cascade Range, Oregon. J. Geophys. Res. 95(B12), 19611–19622.

Valentine, G.A., Perry, F.V., Krier, D., Keating, G.N., Kelley, R.E., Cogbill, A.H., 2006. Small-volume basaltic volcanoes: Eruptive products and processes, and posteruptive geomorphic evolution in Crater Flat (Pleistocene), southern Nevada. Geol. Soc. Am. Bull. 118, 1313–1330.

Valentine, G.A., Gregg, T.K.P., 2008. Continental basaltic volcanoes – Processes and problems. J. Volcanol. Geotherm. Res., 177, 857–873.

Vigouroux, N., Wallace, P.J., Kent, A.J.R., 2008. Volatiles in high-K magmas from the western Trans-Mexican Volcanic Belt: evidence for fluid fluxing and extreme enrichment of the mantle wedge by subduction processes. J. Petrol. 49, 1589–1618.

Wade, J.A., Plank, T., Melson, W.G., Soto, G.J., Hauri, E.H., 2006. The volatile content of magmas from Arenal volcano, Costa Rica. J. Volcanol. Geoth. Res. 157, 94–120.

Walker, G.P.L., 1973. Explosive volcanic eruptions – a new classification scheme. Geol. Rundsch. 62, 432-446.

Wallace, P., Carmichael, I.S.E., 1992. Sulfur in basaltic magmas. Geochim. Cosmochim. Acta 56, 1863–1874

Wallace, P., Anderson, A.T., Jr., 2000. Volatiles in Magmas. In: Sigurdsson, H. (Ed.), Encyclopedia of Volcanoes. Academic Press, New York. pp. 149–170.

Wallace, P.J., 2005. Volatiles in subduction zone magmas: concentrations and fluxes based on melt inclusion and volcanic gas data. J. Volcanol. Geotherm. Res. 140, 217–240.

Wells, R.E., 1990. Paleomagnetic Rotations and the Cenozoic Tectonics of the Cascade Arc, Washington, Oregon, and California. J. Geophys. Res. 95(B12), 19409–19417.

Wells, R.E., Simpson, R.W., 2001. Northward migration of the Cascadia forearc in the northwestern U.S. and implications for subduction deformation. Earth Planets Space 53, 275–283.

Wyszocanski R, Tani K, 2006. Spectroscopic FTIR imaging of water species in silicic volcanic glasses and melt inclusions: an example from the Izu-Bonin arc. J. Volcanol. Geotherm. Res. 156(3–4), 302–314.

Chapter III

Anderson, A.T., 1974. Evidence for a picritic, volatile-rich magma beneath Mt. Shasta, California. J. Petrol. 15, 243–267.

Anderson, A.T., Brown, G.G., 1993. CO_2 contents and formation pressures of some Kilauean melt inclusions. Am. Mineralog. 78, 794–803.

Auer, S., Bindeman, I., Wallace, P., Ponomareva, V., Portnyagin, M., 2009. The origin of hydrous, high-$\delta^{18}O$ voluminous volcanism: diverse oxygen isotope values and high magmatic water contents within the volcanic record of Klyuchevsky volcano, Kamchatka, Russia. Contrib. Mineral. Petrol. 157, 209–230.

Baker, M.B., Grove, T.L., Price, R., 1994. Primitive basalts and andesites from the Mt. Shasta region, N. California: products of varying melt fraction and water content. Contrib. Mineral. Petrol. 118, 111–129.

Bacon, C.R., Bruggman, P.E., Christiansen, R.L., Clynne, M.A., Donnelly-Nolan, J.M., Hildreth, W., 1997. Primitive magmas at five Cascade volcanic fields: melts from a hot, heterogeneous sub-arc mantle. Can. Mineralog. 35, 397–423.

Benjamin, E.R., Plank, T., Wade, J.A., Kelley, K.A., Hauri, E.H., Alvarado, G.E., 2007. High water contents in basaltic magmas from Irazu Volcano, Costa Rica. J. Volcanol. Geotherm. Res. 168, 68–92.

Bezos, A., Escrig, S., Langmuir, C.H., Michael, P.J., Asimow, P.D., 2009. Origins of chemical diversity of back-arc basin basalts: a segment-scale study of the Eastern Lau Spreading Center. J. Geophys. Res. B114 (2008JB005924).

Brocher, T.M., Parson, T., Trehu, A.M., Snelson, C.M., Fisher, M.A., 2003. Seismic evidence for widespread serpentinized forearc upper mantle along the Cascadia margin. Geology 32 (3), 267–270.

Conrey, R.M., Sherrod, D.R., Hooper, P.R., Swanson, D.A., 1997. Diverse primitive magmas in the Cascade arc, Northern Oregon and Southern Washington. Can. Mineralog. 35, 367–396.

Conrey, R.M., Hooper, P.R., Larson, P.B., Chesley, J., Ruiz, J., 2001. Trace element and isotopic evidence for two types of crustal melting beneath a High Cascade volcanic center, Mt. Jefferson, Oregon. Contrib. Mineral. Petrol. 141, 710–732.

Currie, C.A., Wang, K., Hyndman, R.D., He, J., 2004. The thermal effects of steady-state slab-driven mantle flow above a subducting plate: the Cascadia subduction zone and backarc. Earth Planet. Sci. Lett. 223, 35–48.

Danyushevsky, L.V., Della-Pasqa, F.N., Sokolov, S., 2000. Re-equilibration of melt inclusions trapped by magnesian olivine phenocrysts from subduction-related magmas: petrological implications. Contrib. Mineral. Petrol. 138, 68–83.

Eiler, J.M., 2001. Oxygen isotope variations of basaltic lavas and upper mantle rocks. In: Valley, J.W., Cole, D.R. (Eds.), Stable Isotope Geochemistry: Rev. Mineral. Geochem., 43, pp. 319–364.

Elkins-Tanton, L., Grove, T., Donnelly-Nolan, J., 2001. Hot, shallow mantle melting under the Cascades volcanic arc. Geology 29 (7), 631–634.

Ghiorso, M.S., Hirschmann, M.M., Reiners, P.W., Kress III, V.C., 2002. The pMELTS: a revision of MELTS aimed at improving calculation of phase relations and major element partitioning involved in partial melting of the mantle at pressures up to 3 GPa. Geochem. Geophys. Geosys. 3 (5). doi:10.1029/2001GC000217.

Greene, A.R., DeBari, S.M., Kelemen, P.B., Blusztajn, J., Clift, P.D., 2006. A detailed geochemical study of island arc crust: the Talkeetna Arc section, South-Central Alaska. J. Petrol. 47 (6), 1051–1093.

Grove, T.L., Parman, S.W., Bowring, S., Price, R.C., Baker, M.B., 2002. The role of an H_2O rich fluid component in the generation of primitive basaltic andesites and andesites from the Mt. Shasta region, N. California. Contrib. Mineral. Petrol. 142, 375–396.

Grove, T.L., Elkins-Tanton, L., Parman, S., Chatterjee, N., Muntener, O., Gaetani, G., 2003. Fractional crystallization and mantle-melting controls on calc-alkaline differentiation trends. Contrib. Mineral. Petrol. 145 (5), 515–533.

Haugerud, R.A., 2004. Cascadia-physiography. U.S. Geological Survey, Geologic investigation series I-2689.

Hildreth, W., 2007. Quaternary magmatism in the Cascades—geologic perspectives. U.S. Geological Survey Professional Paper 1744.

Hildreth, W., Moorbath, S., 1988. Crustal contributions to arc magmatism in the Andes of Central Chile. Contrib. Mineral. Petrol. 98, 455–489.

Hughes, S.S., 1990. Mafic magmatism and associated tectonism of the Central High Cascade Range, Oregon. J. Geophys. Res. 95, 19623–19638.

Hughes, S.S., Taylor, E.M., 1986. Geochemistry, petrogenesis, and tectonic implications of central High Cascade mafic platform lavas. Geol. Soc. Am. Bull. 97, 1024–1036.

Hurwitz, S., Mariner, R.H., Fehn, U., Snyder, G.T., 2005. Systematics of halogen elements and their radioisotopes in thermal springs of the Cascade Range, Central Oregon, Western USA. Earth Planet. Sci. Lett. 235, 700–714.

Jagoutz, O.E., Burg, J.P., Hussain, S., Dawood, H., Pettke, T., Iizuka, T., Maruyama, S., 2009. Construction of the granitoid crust of an island arc part I: geochronological and geochemical constraints from the plutonic Kohistan (NW Pakistan). Contrib. Mineral. Petrol. 158, 739–755.

Jicha, B.R., Johnson, C.M., Hildreth, W., Beard, B.L., Hart, G.L., Shirey, S.B., Singer, B.S., 2009. Discriminating assimilants and decoupling deep- vs. shallow-level crystal records at Mount Adams using 238U–230Th and Os isotopes. Earth Planet. Sci. Lett. 277, 38–39.

Johnson, E.R., Wallace, P.J., Delgado Granados, H., Manea, V.C., Kent, A.J.R., Bindeman, I.N., Donegan, C.S., 2009. Subduction-related volatile recycling and magma generation beneath Central Mexico: insights from melt inclusions, oxygen isotopes and geodynamic models. J. Petrol. 50 (9), 1729–1764.

Jugo, P.J., 2009. Sulfur content at sulfide saturation in oxidized magmas. Geology 37, 415–418.

Kelemen, P.B., Honghoj, K., Greene, A.R., 2003. One view of the geochemistry of subduction-related magmatic arcs, with an emphasis on primitive andesite and lower crust. In: Rudnick, R.L. (Ed.), The Crust. : Treatise on Geochemistry, Vol. 3. Elsevier, pp. 593–659.

Kelley, K.A., Plank, T., Grove, T.L., Stolper, E.M., Newman, S., Hauri, E., 2006. Mantle melting as a function of water content beneath back-arc basins. J. Geophys. Res. 11 (B09208). doi:10.1029/2006JB003732.

Kent, A.J.R., Elliot, T.R., 2002. Melt inclusions from Marianas arc lavas: implications for the composition and formation of island arc magmas. Chem. Geol. 183, 263–286.

Kent, A.J.R., Norman, M.D., Hutcheon, I.D., Stolper, E.M., 1999. Assimilation of seawaterderived components in an oceanic volcano: evidence from matrix glasses and glass inclusions from Loihi seamount, Hawaii. Chem. Geol. 156, 299–319.

Kent, A.J.R., Stolper, E.M., Francis, D., Woodhead, J., Frei, R., Eiler, J., 2004. Mantle heterogeneity during the formation of the North Atlantic Tertiary Province: constraints from trace element and Sr–Nd–Os–O isotope systematics of Baffin Island picrites. Geochem. Geophys. Geosys. 5 (Q11004). doi:10.1029/2004GC000743.

Kessel, R., Schmidt, M.W., Ulmer, P., Pettke, T., 2005. Trace element signature of subduction-zone fluids, melts and supercritical liquids at 120–180 km depth. Nature 437. doi:10.0038/nature03971.

Lee, C.A., Luffi, P., Plank, T., Dalton, H., Leeman, W.P., 2009. Constraints on the depths and temperatures of basaltic magma generation on Earth and other terrestrial planets using new thermobarometers for mafic magmas. Earth Planet. Sci. Lett. 279, 2–33.

Leeman, W.P., Smith, D.R., Hildreth, W., Palacz, Z., Rogers, N., 1990. Compositional diversity of Late Cenozoic basalts in a transect across the Southern Washington Cascades: implications for subduction zone magmatism. J. Geophys. Res. 95 (B12), 19561–19582.

Leeman, W.P., Lewis, J.F., Evarts, R.C., Conrey, R.M., Streck, M.J., 2005. Petrologic constraints on the thermal structure of the Cascades arc. J. Volcanol. Geotherm. Res. 140, 67–105.

Mavrogenes, J.A., O'Neill, H., 1999. The relative effects of pressure, temperature and oxygen fugacity on the solubility of sulfide in mafic magmas. Geochim. Cosmochim. Acta. 63, 1173–1180.

Mercer, C.N., Johnston, A.D., 2008. Experimental studies of the P–T–H_2O near-liquidus phase relations of basaltic andesite from North Sister Volcano, High Oregon Cascades: constraints on lower-crustal mineral assemblages. Contrib. Mineral. Petrol. 155, 571–592.

Metrich, N., Wallace, P.J., 2008. Volatile abundances in basaltic magmas and their degassing paths tracked by melt inclusions. In: Putirka, K.D., Tepley III, F.J. (Eds.), Minerals, Inclusions and Volcanic Processes: Rev. Mineral. Geochem., 69, Min. Soc. Am., pp. 363–402.

Papale, P., Moretti, R., Barbato, D., 2006. The compositional dependence of the saturation surface of H_2O+CO_2 fluids in silicate melts. Chem. Geol. 229, 78–95.

Peacock, S.M., 2003. Thermal structure and metamorphic evolution of subducting slabs. In: Eiler, J. (Ed.), Inside the Subduction Factory, Geophysical Monograph 138: Am. Geophys. Union, pp. 7–22.

Plank, T., Cooper, L.B., Manning, C.E., 2009. Emerging geothermometers for estimating slab surface temperatures. Nat. Geosci. 2, 611–615. doi:10.1038/NGEO614.

Portnyagin, M., Hoernle, K., Plechov, P., Mironov, N., Khbunaya, S., 2007. Constraints on mantle melting and composition and nature of slab components in volcanic arcs from volatiles (H_2O, S, Cl, F) and trace elements in melt inclusions from the Kamchatka Arc. Earth Planet. Sci. Lett. 225, 53–69.

Portnyagin, M., Almeev, R., Matveev, S., Holtz, F., 2008. Experimental evidence for rapid water exchange between melt inclusions in olivine and host magma. Earth Planet. Sci. Lett. 272, 541–552.

Rapp, R.P., Watson, E.B., 1995. Dehydration melting of metabasalt at 8–32 kbar: Implications for continental growth and crust–mantle recycling. J. Petrol. 36 (4), 891–931.

Reiners, P.W., Hammond, P.E., McKenna, J.M., Duncan, R.A., 2000. Young basalts of the central Washington Cascades, flux melting of the mantle, and trace element signatures of primary arc magmas. Contrib. Mineral. Petrol. 138, 249–264.

Roggensack, K., Hervig, R.L., McKnight, S.B., Williams, S.N., 1997. Explosive basaltic volcanism from Cerro Negro Volcano: influence of volatiles on eruptive style. Science 277, 1639–1642.

Rondenay, S., Abers, G.A., van Keken, P.E., 2008. Seismic imaging of subduction zone metamorphism. Geology 36 (4), 275–278.

Rowe, M.C., Kent, A.J.R., Nielsen, R.L., 2009. Subduction influence on oxygen fugacity and trace and volatile elements in basalts across the Cascades volcanic arc. J. Petrol. 50 (1), 61–91.

Ruscitto, D., Wallace, P., 2008. Revisiting the compositions and volatile contents of olivine-hosted melt inclusions from the Mount Shasta region. Eos Trans. AGU 89 (53) Fall Meet. Suppl. Abstract V13F-06.

Sadofsky, S.J., Portnyagin, M., Hoernle, K., van den Bogaard, P., 2008. Subduction cycling of volatiles and trace elements through the Central American volcanic arc: evidence from melt inclusions. Contrib. Mineral. Petrol. 155, 433–456.

Schmidt, M.E., 2005. Deep crustal and mantle inputs to North Sister Volcano, Oregon High Cascade Range. PhD Thesis, Oregon State University. Corvallis, Oregon.

Schmidt, M.W., Poli, S., 1998. Experimentally based water budgets for dehydrating slabs and consequences for arc magma generation. Earth Planet. Sci. Lett. 163, 361–379.

Schmidt, M.E., Grunder, A.L., Rowe, M.C., 2008. Segmentation of the Cascade Arc as indicated by Sr and Nd isotopic variation among diverse primitive basalts. Earth Planet. Sci. Lett. 266, 166–181.

Shaw, A.M., Hilton, D.R., Macpherson, C.G., Sinton, J.M., 2004. The CO_2–He–Ar–H_2O systematics of the Manus back-arc basin: resolving source composition from degassing and contamination effects. Geochim. Cosmochim. Acta 68(8), 1837–1856.

Shaw, A.M., Hauri, E.H., Fischer, T.P., Hilton, D.R., Kelley, K.A., 2008. Hydrogen isotopes in Mariana arc melt inclusions: implications for subduction dehydration and the deep-Earth water cycle. Earth Planet. Sci. Lett. 275, 138–145.

Sherrod, D.R., Smith, J.G., 1990. Quaternary extrusion rates of the Cascade Range, Northwestern United States and Southern British Columbia. J. Geophys. Res. 95 (B12), 19465–19474.

Sherrod, D.R., Taylor, E.M., Ferns, M.L., Scott, W.E., Conrey, R.M., Smith, G.A., 2004. Geologic map of the Bend 30- × 60-Minute Quadrangle, Central Oregon. U.S. Geological Survey, Geologic Investigations Series I-2683.

Sisson, T.W., Grove, T.L., 1993. Experimental investigations of the role of H_2O in calcalkaline differentiation and subduction zone magmatism. Contrib. Mineral. Petrol. 113 (2), 143–166.

Sisson, T.W., Layne, G.D., 1993. H_2O in basalt and basaltic andesite glass inclusions from four subduction-related volcanoes. Earth Planet. Sci. Lett. 177, 619–635.

Stolper, E., Newman, S., 1994. The role of water in the petrogenesis of Mariana Trough magmas. Earth Planet. Sci. Lett. 121, 293–325.

Sugawara, T., 2000. Empirical relationshiops between temperature, pressure, and MgO content in olivine and pyroxene saturated liquid. J. Geophys. Res. 105(B4), 8457–8472.

Sun, S.-s., McDonough, W.F., 1989. Chemical and isotopic systematics of oceanic basalts: implications for mantle composition and processes. In: Saunders, A.D., Norry, M.J. (Eds.), Magmatism in the Ocean Basins: Geological Soc. Special Pub., 42, pp. 313–345.

Trehu, A.M., Asudeh, I., Brocher, T.M., Luetgert, J.H., Mooney, W.D., Nabelek, J.L., Nakamura, Y., 1994. Crustal architecture of the Cascadia forearc. Science 266, 237–243.

Wada, I., Wang, K., 2009. Common depth of slab–mantle decoupling: reconciling diversity and uniformity of subduction zones. Geochem. Geophys. Geosys. 10(10). doi:10.1029/2009GC002570.

Wade, J.A., Plank, T., Melson, W.G., Soto, G.J., Hauri, E.H., 2006. The volatile content of magmas from Arenal Volcano, Costa Rice. J. Volcanol. Geotherm. Res. 157, 94–120.

Walker, J.A., Roggensack, K., Patino, L.C., Cameron, B.I., Matias, O., 2003. The water and trace element contents of melt inclusions across an active subduction zone. Contrib. Mineral. Petrol. 146, 62–77.

Wallace, P.J., 2005. Volatiles in subduction zone magmas: concentrations and fluxes based on melt inclusion and volcanic gas data. J. Volcanol. Geotherm. Res. 140, 217–240.

Wallace, P., Carmichael, I.S.E., 1992. Sulfur in basaltic magmas. Geochim. Cosmochim. Acta 56, 1863–1874.

Wilson, D.S., 2002. The Juan de Fuca plate and slab — isochron structure and Cenozoic plate motions. U.S. Geological Survey Open-File Report 02-328, pp. 9–12.

Workman, R.K., Hart, S.R., 2005. Major and trace element composition of the depleted MORB mantle (DMM). Earth Planet. Sci. Lett. 231, 53–72.

Chapter IV

Anderson AT (1974) Evidence for a Picritic, Volatile-rich Magma beneath Mt. Shasta, California. J Petrol 15:243–267

Anderson AT (1991) Hourglass inclusions: theory and application to the Bishop Rhyolitic Tuff. Am Mineral 76(3–4):530–547

Bacon CR (1989) Crystallization of accessory phases in magmas by local saturation adjacent to phenocrysts. Geochim Cosmochim Acta 53:1055–1066

Bacon CR, Bruggman P, Christiansen RL, Clynne MA, Donnelly-Nolan JM, Hildreth W (1997) Primitive magmas at five Cascade volcanic fields: melts from hot, heterogeneous sub-arc mantle. Can Mineral 35:397–423

Baker MB, Grove TL, Price R (1994) Primitive basalts and andesites from the Mt. Shasta region, N. California: products of varying melt fractions and water content. Contrib Mineral Petrol 118:111–129

Barr J, Grove TL, Elkins-Tanton L (2007) High-magnesian andesite from Mount Shasta: a product of magma mixing and contamination, not a primitive melt: comment and reply. Geology. doi:10.1130/G24058C.1

Benjamin E, Plank T, Wade J, Kelley K, Hauri E, Alvarado G (2007) High water contents in basaltic magmas from Irazu volcano, Costa Rica. J Volcanol Geotherm Res 168:68–92

Borg LE, Brandon AD, Clynne MA, Walker RJ (2000) Re-Os isotopic systematics of primitive lavas from the Lassen region of the Cascade arc, California. Earth Planet Sci Lett 177:301–317

Chen Y, Zhang Y (2009) Olivine dissolution in basaltic melt. Geochim Cosmochim Acta 72:4756–4777

Cherniak DJ (2010) REE diffusion in olivine. Am Mineral 95:362–368

Clynne MA, Borg LE (1997) Olivine and chromian spinel in primitive calc-alkaline and tholeiitic lavas from the southernmost Cascade Range, California; a reflection of relative fertility of the source. Can Mineral 35(2):453–472

Cooper L, Plank Y, Arculus RJ, Hauri EH, Hall PS, Parman EW (2010) High-Ca boninites from the active Tonga arc. J Geophys Res. doi:10.1029/2009JB006661 (in press)

Crawford AJ, Falloon TJ, Green DH (1989) Classification, petrogenesis and tectonic setting of boninites. In: Crawford AJ (ed) Boninites and related rocks. Unwin Hyman Ltd, Winchester, pp 1–49

Danyushevsky LV, Della-Pasqa FN, Sokolov S (2000) Re-equilibration of melt inclusions trapped by magnesian olivine phenocrysts from subduction-related magmas: petrological implications. Contrib Mineral Petrol 138:68–83

Danyushevsky LV, McNeill AW, Sobolev AV (2002a) Experimental and petrological studies of melt inclusions in phenocrysts from mantle-derived magmas: an overview of techniques, advantages and complications. Chem Geol 183:5–24

Danyushevsky LV, Sokolov S, Falloon TJ (2002b) Melt inclusions in olivine phenocrysts: using diffusive re-equilibration to determine the cooling history of a crystal, with implications for the origin of olivine-phyric volcanic rocks. J Petrol 43(9):1651–1671

Defant MJ, Drummond MS (1990) Derivation of some modern arc magmas by melting of young subducted lithosphere. Nature 347:662–665

Dickinson WR (2004) Evolution of the North American Cordillera. Annu Rev Earth Planet Sci 32:13–45

Dixon JE, Pan V (1995) Determination of the molar absorptivity of dissolved carbonate in basanitic glass. Am Mineral 80:1339–1342

Dobson PF, Blank JG, Maruyama S, Liou JG (2006) Petrology and geochemistry of boninite series volcanic rocks, Chichi-jima, Bonin Islands, Japan. Lawrence Berkeley National Laboratory: Lawrence Berkeley National Laboratory. LBNL Paper LBNL- 57671

Dobson PF, O'Neil JR (1987) Stable isotope compositions and water contents of boninite series volcanic rocks from Chichi-Jima, Bonin Islands, Japan. Earth Planet Sci Lett 82:75–86

Donovan JJ, Tingle TN (1996) An improved mean atomic number correction for quantitative microanalysis. J Microscopy 2(1):1–7

Donovan JJ, Snyder DA, Rivers ML (1993) An improved interference correction for trace element analysis. Microbeam Analysis 2:23–28

Elkins-Tanton LT, Grove TL, Donnelly-Nolan JM (2001) Hot, shallow mantle melting under the cascades volcanic arc. Geol 29:631–634

Elliot T (2003) Tracers of the slab. In: Eiler, J (ed) Geophysical monograph 138, inside the subduction factory. American Geophysical Union, Washington, DC, pp 23–45

Falloon TJ, Danyushevsky LV (2000) Melting of refractory mantle at 1.5, 2 and 2.5 GPa under Anhydrous and H_2O-undersaturated conditions: implications for the petrogenesis of High-Ca boninites and the influence of subduction components on the mantle melting. J Petrol 41(2):257–283

Faure F, Schiano P (2005) Experimental investigation of equilibration conditions during forsterite growth and melt inclusion formation. Earth Planet Sci Lett 236(3–4):882–898

Gaetani GA, Hauri EH (2008) Timescales for re-equilibration of major elements in olivine-hosted melt inclusions. Eos Trans AGU 89(53) (Fall Meet. Suppl., Abstract V13F-01)

Gaetani GA, Watson EB (2000) Open system behavior of olivine-hosted melt inclusions. Earth Planet Sci Lett 183:27–41

Gaetani GA, Watson EB (2002) Modeling the major-element evolution of olivine-hosted melt inclusions. Chem Geol 183:25–41

Ghiorso MS, Hirschmann MM, Reiners PW, Kress III VC (2002) The pMELTS: An revision of MELTS aimed at improving calculation of phase relations and major element partitioning involved in partial melting of the mantle at pressures up to 3 GPa. Geochem Geophys Geosys 3(5). doi:10.1029/2001GC000217

Gill JB (1981) Orogenic andesites and plate tectonics. Springer, Berlin

Giordano D, Nichols ARL, Dingwell DB (2005) Glass transition temperatures of natural hydrous melts: a relationship with shear viscosity and implications for the welding process. J Volcanol Geotherm Res 142:105–118

Grove TL, Parman S, Bowring S, Price R, Baker M (2002) The role of an H_2O-rich fluid component in the generation of primitive basaltic andesites and andesites from the Mt. Shasta region, N California. Contrib Mineral Petrol 142:375–396

Grove TL, Elkins-Tanton L, Parman S, Chatterjee N, Muntener O, Gaetani G (2003) Fractional crystallization and mantle-melting controls on calc-alkaline differentiation trends. Contrib Mineral Petrol 145(5):515–533

Grove TL, Baker MB, Price RC, Parman SW, Elkins-Tanton LT, Chatterjee N, Muntener O (2005) Magnesian andesite and dacite lavas from Mt. Shasta, northern California: products of fractional crystallization of H_2O-rich mantle melts. Contrib Mineral Petrol 148:542–565

Hanson B, Delano JW, Lindstrom DJ (1996) High-precision analysis of hydrous rhyolitic glass inclusions in quartz phenocrysts using the electron microprobe and INAA. Am Mineral 81:1249–1262

Johnson ER, Wallace PJ, Cashman KV, Delgado-Granados H, Kent AJR (2008) Magmatic volatile contents and degassing-induced crystallization at Volcan Jorullo, Mexico: Implications for melt evolution and the plumbing systems of monogenetic volcanoes. Earth Planet Sci Lett 269:477–486

Johnson ER, Wallace PJ, Delgado-Granados H, Manea VC, Kent AJR, Bindeman IN, Donegan CS (2009) Subduction-related volatile recycling and magma generation beneath central Mexico: insights from melt inclusions, oxygen isotopes and geodynamic models. J Petrol 50(9):1729–1764

Kay RW (1978) Aleutian magnesian andesites: melts from subduction Pacific ocean crust. J Volcanol Geotherm Res 4(1–2):117–132

Kelemen PB (1995) Genesis of high Mg# andesites and the continental crust. Contrib Mineral Petrol 120:1–19

Kelemen PB, Yogodzinski G (2007) High-magnesian andesite from Mount Shasta: a product of magma mixing and contamination, not a primitive melt: comment and reply. Geology. doi: 10.1130/G24099C.1

Kelemen PB, Hanghoj K, Greene AR (2004) One view of the geochemistry of subduction-related magmatic arcs, with emphasis on primitive andesite and lower crust. In: Rudnick RL (ed) Treatise on geochemistry, vol 3, The Crust. Elsevier, Netherlands, pp 593–659

Kent AJR (2008) Melt inclusions in basaltic and related volcanic rocks. In: Putirka KD, Tepley FJ III (eds) Reviews in mineralogy & geochemistry, vol 69, minerals, inclusions and volcanic processes. Mineralogical Society of America, Chantilly, pp 273–331

Kent AJR, Elliot TR (2002) Melt inclusions from Marianas arc lavas: implications for the composition and formation of island arc magmas. Chem Geol 183:263–286

Kent AJR, Peate DW, Newman S, Stolper EM, Pearce JA (2002) Chlorine in submarine glasses from the Lau Basin: seawater contamination and constraints on the composition of slabderived fluids. Earth Planet Sci Lett 202:361–377

Kent AJR, Stolper EM, Francis D, Woodhead J, Frei R, Eiler J (2004) Mantle heterogeneity during the formation of the North Atlantic Tertiary Province: constraints from trace element and Sr-Nd-Os-O isotope systematics of Baffin Island picrites. Geochem Geophys Geosys 5:Q11004. doi:10.1029/2004GC000743

Lange RA (1994) The effect of H_2O, CO_2 and F on the density and viscosity of silicate melts. In: Carroll MR, Holloway JR (eds) Reviews in mineralogy, vol 30, Volatiles in Magmas. Mineralogical Society of America, Washington, DC, pp 331–369

Lange RA, Carmichael ISE (1987) Densities of Na_2O–K_2O-CaO-MgO-FeO-Fe_2O_3-Al_2O_3-TiO_2-SiO_2 liquids: new measurements and derived partial molar properties. Geochim Cosmochim Acta 51:2931–2946

Le Bas MJ (2000) IUGS reclassification of the high-Mg and picritic volcanic rocks. J Petrol 41(10):1467–1470

Le Voyer M, Rose-Koga EF, Shimizu N, Grove TL, Schiano P (2010) Two contrasting H_2O-rich components in primary melt inclusions from Mount Shasta. J Petrol 51(7):1571–1595

Lee CA, Luffi P, Plank T, Dalton H, Leeman WP (2009) Constraints on the depths and temperatures of basaltic magma generation on Earth and other terrestrial planets using new thermobarometers for mafic magmas. Earth Planet Sci Lett 279:20–33

Levander A, Niu F, Miller MS (2008) The Moho and the lithosphereasthenosphere boundary under the western U.S. from USArray PdS receiver functions. Eos Trans AGU 89(53) (Fall Meet. Suppl., Abstract S31D-05)

Li X, Yuan X, Kind R (2007) The lithosphere-asthenosphere boundary beneath the western United States. Geophys J Int 170(2):700–710

Lowenstern JB (1995) Applications of silicate-melt inclusions to the study of magmatic volatiles. In: Thompson JFH (ed) Mineralogical association of Canada short course vol. 23, Magmas, fluids, and ore deposits, pp 71–99

Luhr JF (2001) Glass inclusions and melt volatile contents at Paricutin Volcano, Mexico. Contrib Mineral Petrol 142:261–283

Magna T, Wiechert U, Grove TL, Halliday AN (2006) Lithium isotope fractionation in the Southern Cascadia subduction zone. Earth Planet Sci Lett 250:428–443

Mandeville CW, Webster JD, Rutherford MJ, Taylor BE, Timbal A, Faure K (2002) Determination of molar absorptivities for infrared absorption bands of H2O in andesitic glasses. Am Mineral 87:813–821

Martin H, Smithies RH, Rapp R, Moyen J-F, Champion D (2005) An overview of adakite, tonalite-trondhjemite-granodiorite (TTG), and sanukitoid: relationships and some implications for crustal evolution. Lithos 79:1–24

Martin E, Bindeman I, Grove T (2010) Magma genesis in a high fluid flux environment: Oxygen isotopes and geochemical investigation of high-Mg lavas from Mt. Shasta and Medicine Lake volcanoes, Cascade arc (California). Contrib Mineral Petrol (submitted)

Massare D, Metrich N, Clocchiatti R (2002) High-temperature experiments on silicate melt inclusions in olivine at 1 atm: inference on temperatures of homogenization and H_2O concentrations. Chem Geol 183:87–98

Metrich N, Wallace PJ (2008) Volatile abundances in basaltic magmas and their degassing paths tracked by melt inclusions. In: Putirka KD, Tepley FJ III (eds) Reviews in mineralogy & geochemistry, vol. 69. Minerals, inclusions and volcanic processes. Mineralogical Society of America, Chantilly, pp 363–402

Miller MS, Levander A, Xu Y, Jiang M, Collier M, Lee CA (2008) SdP receiver function images of the lithosphere-asthenosphere boundary beneath the Western U.S. using USArray data. Eos Trans AGU 89(53) (Fall Meet. Suppl., Abstract U43B-0061)

Morgan GB, London D (1996) Optimizing the electron microprobe analysis of hydrous alkali aluminosilicate glasses. Am Mineral 81:1176–1185

Muntener O, Kelemen PB, Grove TL (2001) The role of H_2O during crystallization of primitive arc magmas under uppermost mantle conditions and genesis of igneous pyroxenites: an experimental study. Contrib Mineral Petrol 141:643–658

Ochs FA III, Lange RA (1997) The partial molar volume, thermal expansivity, and compressibility of H_2O in $NaAlSi_3O_8$ liquid: new measurements and an internally consistent model. Contrib Mineral Petrol 129:155–165

Pallares C, Bellon H, Benoit M, Maury R (2008) Temporal geochemical evolution of Neogene volcanism in northern Baja California (27°-30' N): Insights on the origin of post-subduction magnesian andesites. Lithos 105:162–180

Papale P, Moretti R, Barbato D (2006) The compositional dependence of the saturation surface of $H_2O + CO_2$ fluids in silicate melts. Chem Geol 229:78–95

Parman SW, Grove TL (2004) Harzburgite melting with and without H_2O: experimental data and predictive modeling. J Geophys Res. doi:10.1029/2003JB002566

Perfit MR, Gust DA, Bence AE, Arculus RJ, Taylor SR (1980) Chemical characteristics of island-arc basalts: implications for mantle sources. Chem Geol 30:227–256

Portnyagin M, Hoernle K, Plechov P, Mironov N, Khubunaya S (2007) Constraints on mantle melting and composition and nature of slab components in volcanic arcs from volatiles (H_2O, S, Cl, F) and trace elements in melt inclusions from the Kamchatka Arc. Earth Planet Sci Lett 255:53–69

Portnyagin M, Almeev R, Matveev S, Holtz F (2008) Experimental evidence for rapid waterexchange between melt inclusions in olivine and host magma. Earth Planet Sci Lett 272(3–4):541–552

Putrirka KD, Perfit M, Ryerson FJ, Jackson MG (2007) Ambient and excess mantle temperatures, olivine thermometry, and active vs. passive upwelling. Chem Geol 241:177–206

Quick JE (1981) Petrology and petrogenesis of the trinity peridotite, an upper Mantle Diapir in the Eastern Klamath Mountains, Northern California. J Geophys Res 86(B12):11837–11863

Roberge J, Delgado-Granados H, Wallace PJ (2009) Mafic magma recharge supplies high CO_2 and SO_2 gas fluxes from Popocatepetl volcano, Mexico. Geology 37(2):107–110. doi:10.1130/G25242A.1

Roeder PL, Emslie RF (1970) Olivine-liquid equilibrium. Contrib Mineral Petrol 29(4):275–289

Roggensack K, Hervig RL, McKnight SB, Williams SN (1997) Explosive basaltic volcanism from Cerro Negro volcano: influence of volatiles on eruptive style. Science 277:1639–1642

Rudnick RL, Fountain DM (1995) Nature and composition of the continental crust: a lower crustal perspective. Rev Geophys 33(3):267–309

Ruscitto DM, Wallace PJ, Johnson ER, Kent AJR, Bindeman IN (2010) Volatile contents of mafic magmas from cinder cones in the Central Oregon High Cascades: implications for magma formation and mantle conditions in a hot arc. Earth Planet Sci Lett. doi:10.1016/j.epsl.2010.07.037 (in press)

Schiano P (2003) Primitive mantle magmas recorded as silicate melt inclusions in igneous minerals. Earth Sci Rev 63(1–2):121–144

Shaw AM, Hauri EH, Fischer TP, Hilton DR, Kelley KA (2008) Hydrogen isotopes in Mariana arc melt inclusions: implications for subduction dehydration and the deep-Earth water cycle. Earth Planet Sci Lett 275:138–145

Shimoda G, Tatsumi Y, Nohda S, Ishizaka K, Jahn BM (1998) Setouchi high-Mg andesites revisited: geochemical evidence for melting of subducting sediments. Earth Planet Sci Lett 160(3–4):479–492

Silver PG, Holt WE (2002) The mantle flow field beneath Western North America. Science 295:1054–1057

Sisson TW, Layne GD (1993) H_2O in basalt and basaltic andesite glass inclusions from four subduction-related volcanoes. Earth Planet Sci Lett 117:619–635

Smith AL, Carmichael ISE (1968) Quaternary Lavas from the Southern Cascades. Western U.S.A. Contrib Mineral Petrol 19:212–238

Sobolev AV, Chaussidon M (1996) H_2O concentrations in primary melts from island arcs and mid-ocean ridges: implications for H_2O storage and recycling in the mantle. Earth Planet Sci Lett 137:47–55

Sobolev AV, Danyushevsky LV (1994) Petrology and geochemistry of boninites from the north termination of the Tonga trench: constraints on the generation conditions of primary high-Ca boninite magmas. J Petrol 35(5):1183–1211

Spandler C, St H, O'Neill C, Kamenetsky VS (2007) Survival times of anomalous melt inclusions from element diffusion in olivine and chromite. Nature 447:303–306

Sparks RSJ, Marshall LA (1986) Thermal and mechanical constraints on mixing between mafic and silicic magmas. J Volcanol Geotherm Res 29:99–124

Spilliaert N, Metrich N, Allard P (2006) S-Cl-F degassing pattern of water-rich alkali basalt: Modeling and relationship with eruption styles on Mount Etna volcano. Earth Planet Sci Lett 248:772–786

Streck M, Leeman WP, Chesley J (2007a) High-magnesian andesite from Mount Shasta: a product of magma mixing and contamination, not a primitive mantle melt. Geol 35(4):351–354

Streck M, Leeman WP, Chesley J (2007b) Reply to Barr et al., doi:10.1130/G24058C.1. Geology. doi:10.1130/G24177Y.1

Streck M, Leeman WP, Chesley J (2007c) Reply to Kelemen & Yogodzinski, doi: 10.1130/G24099C.1. Geology. doi:10.1130/G24356Y.1

Sun S-S, McDonough WF (1989) Chemical and isotopic systematics of oceanic basalts: implications for mantle composition and processes. In: Saunders AD, Norry MJ (eds) Magmatism in the ocean basins. Geological Society of London Special Publication No. 42, pp 313–345

Toplis MJ (2005) The thermodynamics of iron and magnesium partitioning between olivine and liquid: criteria for assessing and predicting equilibrium in natural and experimental systems.Contrib Mineral Petrol 149:22–39

Umino S (1986) Magma mixing in boninite sequence of Chichjima, Bonin islands. J Volcanol Geotherm Res 29:125–157

Vigouroux N, Wallace PJ, Kent ARJ (2008) Volatiles in high-K Magmas from the Western trans-Mexican volcanic belt: evidence for fluid fluxing and extreme enrichment of the mantle wedge by subduction processes. J Petrol 49(9):1589–1618. doi:10.1093/petrology/egn039

Wade J, Plank T, Melson W, Soto G, Hauri E (2006) The volatile content of magmas from Arenal volcano, Costa Rica. J Volcanol Geotherm Res 157(1–3):94–120

Wallace PJ (2005) Volatiles in subduction zone magmas: concentrations and fluxes based on melt inclusion and volcanic gas data. J Volcanol Geotherm Res 140:217–240

Wallace PJ, Carmichael ISE (1994) S speciation in submarine basaltic glasses as determined by measurements of SKa X-ray wavelength shifts. Am Mineral 79:161–167

Watson EB, Sneeringer MA, Ross A (1982) Diffusion of dissolved carbonate in magmas: experimental results and applications. Earth Planet Sci Lett 61:346–358

Wood BJ, Turner SP (2009) Origin of primitive high-Mg andesite: constraints from natural experiments. Earth Planet Sci Lett 248:59–66. doi:10.1016/j.epsl.2009.03.032

Wyszocanski R, Tani K (2006) Spectroscopic FTIR imaging of water species in silicic volcanic glasses and melt inclusions: an example from the Izu-Bonin arc. J Volcanol Geotherm Res 156(3–4):302–314

Yogodzinski G, Lees JM, Churikova TG, Dorendorf F, Woerner G, Volynets ON (2001) Geochemical evidence for the melting of subducting oceanic lithosphere at plate edges. Nature 409:500–504

Zandt G, Humphreys, E (2008) Toroidal mantle flow through the western U.S. slab window. Geology 36:295–298. doi:10.1130/G24611A.1

Zieg MJ, Lofgren GE (2006) An experimental investigation of texture evolution during continuous cooling. J Volcanol Geotherm Res 154:74–88

Chapter V

Auer, S., Bindeman, I., Wallace, P., Ponomareva, V., Portnyagin, M., 2009. The origin of hydrous, high-$\delta^{18}O$ voluminous volcanism: diverse oxygen isotope values and high magmatic water contents within the volcanic record of Klyuchevskoy volcano, Kamchatka, Russia. Contrib. Mineral. Petrol. 157, 209–230.

Benjamin, E.R., Plank, T., Wade, J.A., Kelley, K.A., Hauri, E.H., Alvarado, G.E., 2007. High water contents in basaltic magmas from Irazu Volcano, Costa Rice. J. Volcanol. Geotherm. Res. 168, 68–92.

Bezos, A., Escrig, S., Langmuir, C.H., Michael, P.J., Asimow, P.D., 2009. Origins of chemical diversity of back-arc basin basalts: a segment-scale study of the Eastern Lau Spreading Center. J. Geophys. Res. B114 (2008JB005924).

Borg, L.E., Blichert-Toft, J., Clynne, M.A., 2002. Ancient and Modern Subduction Zone Contributions to the Mantle Sources of Lavas from the Lassen Region of California Inferred from Lu-Hf Isotopic Systematics. J. Petrol. 43(4), 704–723.

Bouvier, A.-S., Metrich, N., Deloule, E., 2008. Slab-derived fluids in magma sources of St. Vincent (Lesser Antilles Arc): Volatile and light element imprints. J. Petrol. 49, 1427–1448.

Bouvier, A.,-S., Deloule, E., Metrich, N., 2010. Fluid Inputs to Magma Sources of St. Vincent and Grenada (Lesser Antilles): New Insights from Trace Elements in Olivine-hosted Melt Inclusions. J. Petrol. 51(8), 1597–1615.

Cervantes, P., Wallace, P.J., 2003. Role of H_2O in subduction-zone magmatism: New insights from melt inclusions in high-Mg basalts from central Mexico. Geology 31(3), 235–238.

Cooper, L., Plank, T., Arculus, R.J., Hauri, E.H., Hall, P.S., Parman, S.W., 2010, in press. High-Ca Boninites from the active Tonga arc. J Geophys Res., doi: 10.1029/2009JB006661.

Dixon, J.E., Leist, L., Langmuir, C., Schilling, J.G., 2002. Recycled dehydrated lithosphere observed in plume-influenced mid-ocean-ridge basalt. Nature 420, 385–389.

Eiler, J.M., Carr, M.J., Reagan, M., Stolper, E., 2005. Oxygen isotope constraints on the sources of Central American arc lavas. Geochem. Geophys. Geosys. 6(7), doi: 10.1029/2004GC000804.

Elliot, T., Plank, T., Zindler, A., White, W., Bourdon, B., 1997. Element transport from slab to volcanic front at the Mariana arc. J. Geophys. Res. 102(B7), 14991–15019.

Elliot, T., 2003. Tracers of the Slab. In: J. Eiler (Ed.) Inside the Subduction Factory. Geophysical Monograph 138. Am. Geophys. Union, Washington, D.C. pp. 23–45.

George, R.M.M., Turner, S.P., Hawkesworth, C.J., Morris, J.D., Nye, C.J., Ryan, J.G., Zheng, S.-H., 2003. Melting processes and fluid and sediment transport rates along the Alaska-Aleutian arc from an integrated U-Th-Ra-Ba isotope study. J. Geophys. Res. B108 (2002JB001916).

Gill, J.B., 1981. Orogenic Andesites and Plate Tectonics. Springer, Berlin.

Gribble, R.F., Stern, R.J., Bloomer, S.H., Stuben, D., O'Hearn, T., Newman, S., 1996. MORB mantle and subduction components interact to generate basalts in the southern Mariana Trough back-arc basin. Geochim. Cosmchim. Acta 60(12), 2153–2166.

Grove, T.L., Parman, S., Bowring, S., Price, R., Baker, M., 2002. The role of an H_2O-rich fluid component in the generation of primitive basaltic andesites and andesites from the Mt. Shasta region, N California. Contrib. Mineral. Petrol. 142, 375–396.

Gorbatov, A., Kostoglodov, V., 1997. Maximum depth of seismicity and thermal parameter of the subducting slab: general empirical relation and its application. Tectonophysics 277, 165–187.

Gurenko, A.A., Belousov, A.B., Trumbull, R.B., Sobolev, A.B., 2005. Explosive basaltic volcanism of the Chikurachki volcano (Kurile arc, Russia): Insights on pre-eruptive magmatic conditions and volatile budget revealed from phenocryst-hosted melt inclusions and groundmass glasses. J. Volcanol. Geotherm. Res. 147, 203–232.

Haase, K.M., Worthington, T.J., Stoffers, P., Garbe-Schonberg, C.-D., Write, I.C., 2002. Mantle dynamics, element recycling and magma genesis beneath the Kermadec Arc-Havre Trough. Geochem. Geophys. Geosys. 3(11), 1071, doi: 10.1029/2002GC000335.

Hacker, B.R., 2008. H_2O subduction beyond arcs. Geochem. Geophys. Geosys. 9(3), Q03001, doi: 10.1029/2007GC001707.

Hamada, M., Fujii, T., 2007. H_2O-rich island arc low-K tholeiite magma inferred from Ca-rich plagioclase melt inclusion equilibria. Geochem. J. 41, 437–461.

Hauri, E.H., Gaetani, G.A., Green, T.H., 2006. Partitioning of water during melting of the Earth's upper mantle at H_2O-undersaturated conditions. Earth Planet. Sci. Lett. 248, 715–734.

Hawkins, J.W., Jr., Lonsdale, P.F., MacDougall, J.D., Volpe, A.M., 1990. Petrology of the axial ridge of the Mariana Trough backarc spreading center. Earth Planet. Sci. Lett. 100, 226–250.

Helsel, D.R., Hirsch, R.M., 2002. Statistical methods in water resources: Techniques of Water-Resources Investigations of the United State Geological Survey, Book 4. USGS. Reston, VA. P.266–274.

Hermann, J., Spandler, C., Hack, A., Korsakov, A.V., 2006. Aqueous fluids and hydrous melts in high-pressure and ultra-high pressure rocks: Implications for element transfer in subduction zones. Lithos 92, 399–417.

Hermann, J., Spandler, C.J., 2008. Sediment melts at sub-arc depths: an experimental study. J. Petrol. 49(4), 717–740.

Jicha, B.R., Singer, B.S., Brophy, J.G., Fournelle, J.H., Johnson Clark, M., Beard, B.M., Lapen, T.J., Mahlen, N.J., 2004. Variable impact of the subducted slab on Aleutian island arc magma sources: evidence from Sr, Nd, Pb, and Hf isotopes and trace element abundances. J. Petrol. 45, 1845–1875.

Johnson, K.E., Harmon, R.S., Richardson, J.M., Moorbath, S., Strong, D.F., 1996. Isotope and trace element geochemistry of Augustine volcano, Alaska: implications for magmatic evolution. J. Petrol. 37, 95–115.

Johnson, E.R., Wallace, P.J., Delgado Granados, H., Manea, V.C., Kent, A.J.R., Bindeman, I. N., Donegan, C.S., 2009. Subduction-related volatile recycling and magma generation beneath Central Mexico: insights from melt inclusions, oxygen isotopes and geodynamic models. J. Petrol. 50 (9), 1729–1764.

Johnson, E.R., Wallace, P.J., Cashman, K.V., Delgado Granados, H., 2010. Degassing of volatiles (H_2O, CO_2, S, Cl) during ascent, crystallization, and eruption at mafic monogenetic volcanoes in central Mexico. J. Volcanol. Geotherm. Res. 197, 225–238.

Kay, R.W. (1978) Aleutian magnesian andesites: Melts from subduction Pacific ocean crust. J Volcanol Geotherm Res, 4(1-2): 117–132.

Kelley, K.A., Plank, T., Ludden, J., Staudigel, H., 2003. Composition of altered oceanic crust at ODP Sites 801 and 1149. Geochem. Geophys. Geosys. 4(6), 8910, doi: 10.1029/2002GC000435.

Kelley, K.A., Plank, T., Grove, T.L., Stolper, E.M., Newman, S., Hauri, E., 2006. Mantle melting as a function of water content beneath back-arc basins. J. Geophys. Res. 11(B09208), doi: 10.1029/2006JB003732.

Kelley, K.A., Plank, T., Newman, S., Stolper, E.M., Grove, T.L., Parman, S., Hauri, E.H., 2010. Mantle melting as a function of water content beneath the Mariana arc. J. Petrol. doi: 10.1093/petrology/egq036

Kent, A.J.R., Norman, M.D., Hutcheon, I.D., Stolper, E.M., 1999. Assimilation of seawater-derived components in an oceanic volcano: evidence from matrix glasses and glass inclusions from Loihi seamount, Hawaii. Chem. Geol. 156: 299–319.

Kent, A.J.R., Elliot, T.R., 2002. Melt inclusions from Marianas arc lavas: implications for the composition and formation of island arc magmas. Chem. Geol. 183: 263–286.

Kessel, R., Schmidt, M.W., Ulmer, P., Pettke, T., 2005. Trace element signature of subduction-zone fluids, melts and supercritical liquids at 120–180 km depth. Nature 437, doi: 10.0038/nature03971.

Kirby, S.H., Stein, S., Okal, E.A., Rubie, D.C., 1996. Metastable mantle phase transformations and deep earthquakes in subducting oceanic lithosphere. Rev. Geophys. 34, 261–306.

Klimm, K., Blundy, J.D., Green, T.H., 2008. Trace Element Partitioning and Accessory Phase Saturation during H_2O-Saturated Melting of Basalt with Implications for Subduction Zone Chemical Fluxes. J. Petrology (2008) 49 (3): 523–553. doi: 10.1093/petrology/egn001

Leeman, W.P., Smith, D.R., Hildreth, W. Palacz, Z., Rogers, N., 1990. Compositional diversity of Late Cenozoic basalts in a transect across the Southern Washington Cascades: Implications for subduction zone magmatism. J. Geophys. Res. 95(B12): 19561–19582.

Le Roux, P.J., Shirey, S.B., Hauri, E.H., Perfit, M.R., Bender, J.F., 2006. The effects of variable sources, processes and contaminants on the composition of northern EPR MORB (8–10°N and 12–14°N): Evidence from volatiles (H_2O, CO_2, S) and halogens (F, Cl). Earth Planet. Sci. Lett. 251, 209–231.

Mangan, M.T., Miller, T.P., Waythomas, C.F., Trusdell, F.A., Calvert, A.T., Layer, P.W., 2009. Diverse lavas from closely spaced volcanoes drawing from a common parent: Emmons Lake Volcanic Center, Eastern Aleutian Arc. Earth Planet. Sci. Lett. 287, 363–372.

Manning, C.E., 2004. The chemistry of subduction-zone fluids. Earth Planet. Sci. Lett. 223, 1–16, doi:10.1016/j.epsl.2004.04.030.

Marsh, B.D., 1982. The Aleutians. In: Orogenic Andesites. John Wiley. pp. 99-114.

Massare, D., N. Metrich, and R. Clocchiatti (2002) High-temperature experiments on silicate melt inclusions in olivine at 1 atm: inference on temperatures of homogenization and H_2O concentrations. Chem. Geol., 183: 87–98.

McBirney, A.R., 2007. Igneous Petrology, 3rd Edition. Jones and Bartlett Publishers, Boston. pp. 196–197.

McDonough, W.F. and Sun, S.-S., 1995. Composition of the Earth. Chem. Geol. 120, 223–253. doi: 10.1016/0009-2541(94)00140-4.

Miller, D.M., Langmuir, C.H., Goldstein, S.L., Franks, A.L., 1992. The importance of parental magma composition to calc-alkaline and tholeiitic evolution: evidence from Umnak Island in the Aleutians. J. Geophys. Res. B97, 321–343.

Myers, J.D., Marsh, B.D., Frost, C.D., Linton, J.A., 2002. Petrologic constraints on the spatial distribution of crustal magma chambers, Atka Volcanic Center, Central Aleutian Arc. Contrib. Mineral. Petrol. 143, 567–586.

Newman, S., Stolper, E.M., Stern, R.J., 2000. H_2O and CO_2 in magmas from the Mariana arc and back arc systems. Geochem. Geophys. Geosys. 1 (1999GC000027).

Nye, C.J., Reid, M.R., 1986. Geochemistry of primary and least fractionated lavas from Okmok Volcano, Central Aleutians: Implications for arc magmagenesis. J. Geophys. Res. B91, 10271–10287.

Peacock, S.M., 2003. Thermal structure and metamorphic evolution of subducting slabs. In: Eiler, J. (Ed.), Inside the Subduction Factory, Geophysical Monograph 138. Am. Geophys. Union, Washington, D.C. pp. 7–22.

Plank, T., Langmuir, C.H., 1988. An evaluation of the global variations in the major element chemistry of arc basalts. Earth Planet. Sci. Lett. 90, 349–370.

Plank, T., Langmuir, C.H., 1993. Tracing trace elements from sediment input to volcanic output at subduction zones. Nature 362, 739–742.

Plank, T., Langmuir, 1998. The chemical composition of subducting sediment and its consequences for the crust and mantle. Chem. Geol. 145, 325–394.

Plank, T., Cooper, L.B., Manning, C.E., 2009. Emerging geothermometers for estimating slab surface temperatures. Nature Geoscience. doi: 10.1038/NGEO614.

Portnyagin, M., Hoernle, K., Plechov, P., Mironov, N., Khbunaya, S., 2007. Constraints on mantle melting and composition and nature of slab components in volcanic arcs from volatiles (H_2O, S, Cl, F) and trace elements in melt inclusions from the Kamchatka Arc. Earth Planet. Sci. Lett. 225: 53–69.

Portnyagin, M., Almeev, R., Matveev, S., Holtz, F., 2008. Experimental evidence for rapid water exchange between melt inclusions in olivine and host magma. Earth Planet. Sci. Lett. 272: 541–552.

Roberge, J., Delgado-Granados, H., Wallace, P.J., 2009. Mafic magma recharge supplies high CO_2 and SO_2 gas fluxes from Popocatepetl volcano, Mexico. Geology 37(2), 107–110. doi:10.1130/G25242A.1.

Roggensack, K., Hervig, R.L., McKnight, S.B., Williams, S.N., 1997. Explosive basaltic volcanism from Cerro Negro Volcano: Influence of volatiles on eruptive style. Science 277: 1639–1642.

Roggensack, K., 2001. Unraveling the 1974 eruption of Fuego volcano (Guatemala) with small crystals and their young melt inclusions. Geology 29(10), 911–914.

Romick, J.D., Perfit, M.R., Swanson, S.E., Shuster, R.D., 1990. Magmatism in the Eastern Aleutian arc: temporal characteristic of igneous activity on Akutan Island. Contrib. Mineral. Petrol. 104, 700–721.

Rowe, M.C., Kent, A.J.R., Nielsen, R.L., 2007. Determination of sulfur speciation and oxidation state of olivine hosted melt inclusions. Chem. Geol. 236, 303–322.

Rowe, M.C., Kent, A.J.R., Nielsen, R.L., 2009. Subduction influence on oxygen fugacity and trace and volatile elements in basalts across the Cascades volcanic arc. J. Petrol. 50(1), 61–91.

Ruscitto, D.M., Wallace, P.J., Johnson, E.R., Kent, A.J.R., Bindeman, I.N., 2010a. Volatile contents of mafic magmas from cinder cones in the Central Oregon High Cascades: implications for magma formation and mantle conditions in a hot arc. Earth Planet Sci Lett. 298, 153–161. doi:10.1016/j.epsl.2010.07.037

Ruscitto, D.M., Wallace, P.J., Kent, A.J.R., 2010b, in press. Revisiting the compositions and volatile contents of olivine-hosted melt inclusions from the Mount Shasta region: implications for the formation of high-Mg andesites. Contrib. Mineral. Petrol. doi: 10.1007/s00410-010-0587-y.

Sadofsky, S.J., Portnyagin, M., Hoernle, K., van den Bogaard, P., 2008. Subduction cycling of volatiles and trace elements through the Central American volcanic arc: evidence from melt inclusions. Contrib. Mineral. Petrol. 155: 433–456.

Saito, G., Morishita, Y., Shinohara, H., 2010. Magma plumbing system of the 2000 eruption of Miyakejima volcano, Japan, deduced from volatile and major component contents of olivine-hosted melt inclusions. J. Geophys. Res. 115, B11202, doi:10.1029/2010JB007433.

Schmidt, M.W., Poli, S., 1998. Experimentally based water budgets for dehydrating slabs and consequences for arc magma generation. Earth Planet. Sci. Lett. 163, 361–379.

Schmidt, M.W., Vielzeuf, D., Auzanneau, 2004. Melting and dissolution of subducting crust at high pressures: the key role of white mica. Earth Planet. Sci. Lett. 228, 65–84.

Shaw, A.M., Hauri, E.H., Fischer, T.P., Hilton, D.R., Kelley, K.A., 2008. Hydrogen isotopes in Mariana arc melt inclusions: Implications for subduction dehydration and the deep-Earth water cycle. Earth Planet. Sci. Lett. 275, 138–145.

Singer, B.S., Jicha, B.R., Leeman, W.P., Rogers, N.W., Thirlwall, M.F., Ryan, J., Nicolaysen, K.E., 2007. Along-strike trace element and isotopic variation in Aleutian Island arc basalt: Subduction melts sediments and dehydrates serpentine. J. Geophys. Res. 112, B06206, doi:10.1029/2006JB004897.

Sisson, T.W., Bronto, S. 1998. Evidence for pressure-release melting beneath magmatic arcs from basalt at Galunggung, Indonesia. Nature 391, 883–886.

Sisson, T.W., Layne, G.D., 1993. H_2O in basalt and basaltic andesite glass inclusions from four subduction-related volcanoes. Earth Planet. Sci. Lett. 177: 619–635.

Spilliaert, N., Allard, P., Métrich, N., Sobolev, A.V., 2006. Melt inclusion record of the conditions of ascent, degassing, and extrusion of volatile-rich alkali basalt during the powerful 2002 flank eruption of Mount Etna (Italy). J. Geophys. Res. 111. doi:10.1029/2005JB003934.

Stolper, E., Newman, S., 1994. The role of water in the petrogenesis of Mariana Trough magmas. Earth Planet. Sci. Lett. 121: 293–325.

Sun, S.-s., McDonough, W.F., 1989. Chemical and isotopic systematics of oceanic basalts: implications for mantle composition and processes. In: Saunders, A.D., Norry, M.J. (Eds.), Magmatism in the Ocean Basins. Geological Soc. Special Pub. 42: 313–345.

Syracuse, E.M., van Keken, P.E., Abers, G.A., 2010. The global range of subduction zone thermal models. Phys. Earth Planet. Interior 183(1–2), 73–90.

Tolstykh, M.L., Naumov, V.B., Babansky, A.D., Bogoyavlenskaya, G.E., Khubunaya, S., 2003. Chemical composition, volatile components, and trace elements in andesitic magmas of the Kurile-Kamchatka region. Petrol. 16(1), 1–18, doi: 10.1134/S0869591108010013.

van Keken, P.E., Hacker, B.R., Syracuse, E.M., Abers, G.A., 2011. Subduction factory: 4. Depth-dependent flux of H_2O from subducting slabs worldwide. J. Geophys. Res. 116, B01401, doi:10.1029/2010JB007922.

Vielzeuf, D., Schmidt, M.W., 2001. Melting relations in hydrous systems revisited: application to metapelites, metagreywackes and metabasalts. Contrib. Mineral. Petrol. 141, 251–267.

Wade, J.A., Plank, T., Melson, W.G., Soto, G.J., Hauri, E.H., 2006. The volatile content of magmas from Arenal volcano, Costa Rica. J. Volcanol. Geoth. Res. 157, 94–120.

Walker, J.A., Roggensack, K., Patino, L.C., Cameron, B.I., Matias, O., 2003. The water and trace element contents of melt inclusions across an active subduction zone. Contrib. Mineral. Petrol. 146, 62–77.

Wallace, P.J., 2005. Volatiles in subduction zone magmas: concentrations and fluxes based on melt inclusion and volcanic gas data. J. Volcanol. Geotherm. Res. 140, 217–240.

Winter, J.D., 2001. An Introduction to Igneous and Metamorphic Petrology. Prentice-Hall. pp. 155–180.

Wyszocanski R, Tani K, 2006. Spectroscopic FTIR imaging of water species in silicic volcanic glasses and melt inclusions: an example from the Izu-Bonin arc. J. Volcanol. Geotherm. Res. 156(3–4), 302–314.

Zimmer, M.M., Plank, T., Hauri, E.H., Yogodzinski, G.M., Stelling, P., Larsen, J., Singer, B.S., Jicha, B.R., Mandeville, C.W., Nye, C.J., 2010 (in press). The role of water in generating the calc-alkaline trend: new volatile data for Aleutian magmas and a new Tholeiitic Index. J. Petrol. doi:10.1093/petrology/egq062.

Chapter VI

Hermann, J., Spandler, C.J., 2008. Sediment melts at sub-arc depths: an experimental study. J. Petrol. 49(4), 717–740.

Johnson, E.R., Wallace, P.J., Cashman, K.V., Delgado Granados, H., Kent, A.J.R., 2008. Magmatic volatile contents and degassing-induced crystallization at Volcán Jorullo, Mexico: implications for melt evolution and the plumbing systems of monogenetic volcanoes. Earth Planet. Sci. Lett. 269, 477–486.

Johnson, E.R., Wallace, P.J., Cashman, K.V., Delgado Granados, H., 2010. Degassing of volatiles (H_2O, CO_2, S, Cl) during ascent, crystallization, and eruption at mafic monogenetic volcanoes in central Mexico. J. Volcanol. Geotherm. Res. 197, 225–238.

Kessel, R., Schmidt, M.W., Ulmer, P., Pettke, T., 2005. Trace element signature of subduction-zone fluids, melts and supercritical liquids at 120–180 km depth. Nature 437, doi: 10.0038/nature03971.